AD_____

Award Number: W81XWH-06-1-0149

TITLE: VatuximabTM: Optimizing Therapeutic Strategies for Prostate Cancer Based on Dynamic MR Tumor Oximetry

PRINCIPAL INVESTIGATOR: Ralph P. Mason, Ph.D.

CONTRACTING ORGANIZATION: UT Southwestern Medical Center at Dallas
Dallas, TX 75390-9058

REPORT DATE: December 2007

TYPE OF REPORT: Annual

PREPARED FOR: U.S. Army Medical Research and Materiel Command
Fort Detrick, Maryland 21702-5012

DISTRIBUTION STATEMENT: Approved for Public Release;
Distribution Unlimited

The views, opinions and/or findings contained in this report are those of the author(s) and should not be construed as an official Department of the Army position, policy or decision unless so designated by other documentation.

REPORT DOCUMENTATION PAGE

Form Approved
OMB No. 0704-0188

Public reporting burden for this collection of information is estimated to average 1 hour per response, including the time for reviewing instructions, searching existing data sources, gathering and maintaining the data needed, and completing and reviewing this collection of information. Send comments regarding this burden estimate or any other aspect of this collection of information, including suggestions for reducing this burden to Department of Defense, Washington Headquarters Services, Directorate for Information Operations and Reports (0704-0188), 1215 Jefferson Davis Highway, Suite 1204, Arlington, VA 22202-4302. Respondents should be aware that notwithstanding any other provision of law, no person shall be subject to any penalty for failing to comply with a collection of information if it does not display a currently valid OMB control number. **PLEASE DO NOT RETURN YOUR FORM TO THE ABOVE ADDRESS.**

1. REPORT DATE *(DD-MM-YYYY)*	**2. REPORT TYPE**	**3. DATES COVERED** *(From - To)*
01-12-2007	Annual	15 NOV 2006 - 14 NOV 2007

4. TITLE AND SUBTITLE

VatuximabTM: Optimizing Therapeutic Strategies for Prostate Cancer Based on Dynamic MR Tumor Oximetry

5a. CONTRACT NUMBER

5b. GRANT NUMBER
W81XWH-06-1-0149

5c. PROGRAM ELEMENT NUMBER

6. AUTHOR(S)
Ralph P. Mason, Ph.D.

E-Mail: Ralph.Mason@UTSouthwestern.edu

5d. PROJECT NUMBER

5e. TASK NUMBER

5f. WORK UNIT NUMBER

7. PERFORMING ORGANIZATION NAME(S) AND ADDRESS(ES)

UT Southwestern Medical Center at Dallas
Dallas, TX 75390-9058

8. PERFORMING ORGANIZATION REPORT NUMBER

9. SPONSORING / MONITORING AGENCY NAME(S) AND ADDRESS(ES)
U.S. Army Medical Research and Materiel Command
Fort Detrick, Maryland 21702-5012

10. SPONSOR/MONITOR'S ACRONYM(S)

11. SPONSOR/MONITOR'S REPORT NUMBER(S)

12. DISTRIBUTION / AVAILABILITY STATEMENT
Approved for Public Release; Distribution Unlimited

13. SUPPLEMENTARY NOTES

14. ABSTRACT

Targeting the vasculature of tumors promises a new effective therapy for prostate cancer. We propose a new approach targeting the blood vessels in the tumor. Specifically, a novel antibody 3G4, which targets phosphatidylserine (PS) expressed on tumor vasculature was developed by Thorpe et al. and is being developed by Peregrine Pharmaceuticals for clinical trials. Normally, PS exclusively resides on the cytosolic leaflet of the plasma membrane. However, in tumors PS becomes externalized and provides a viable target. The agent not only targets various tumors, but also induces vascular damage and tumor regression with minimal accompanying toxicity. In developing a new therapy, critical issues include scheduling, optimal combination with other interventions to achieve synergy and early assessment of efficacy. Magnetic resonance imaging allows us to follow the induction and development of tumor vascular damage providing new insight into spatial and temporal activity and facilitating effective combination with the hypoxic cell selective cytotoxin tirapazamine. Importantly, this therapy may be effective at any stage of tumor development, and could be most effective for advanced disease. Success will confirm the potential of this new therapeutic approach to prostate cancer in man and lay the foundation for future clinical trials.

15. SUBJECT TERMS
No subject terms provided.

16. SECURITY CLASSIFICATION OF:			**17. LIMITATION OF ABSTRACT**	**18. NUMBER OF PAGES**	**19a. NAME OF RESPONSIBLE PERSON**
a. REPORT	**b. ABSTRACT**	**c. THIS PAGE**			USAMRMC
U	U	U	UU	186	**19b. TELEPHONE NUMBER** *(include area code)*

Table of Contents

	Page
Introduction…….	**4**
Body……..	**4**
Key Research Accomplishments……..	**20**
Reportable Outcomes……	**20**
Conclusion……	**21**
References……	**22**
Appendices……	**24**

Introduction

Targeting tumor vasculature promises new effective therapy for prostate cancer (1, 2). It avoids issues of drug delivery and is potentiated by massive downstream effects where one blood vessel may supply the nutrients for thousands of tumor cells. Thus, disrupting the vascular supply should generate magnified tumor cell kill. This research combines the expertise of three laboratories (Pharmacology, Urology, and Radiology) to investigate and optimize a novel therapeutic approach to prostate cancer. Thorpe *et al.* pioneered the concept of targeting tumor vasculature for therapeutic gain using antibodies (3). Recently, they generated a novel antibody 3G4, which targets phosphatidylserine (PS) expressed on tumor vasculature. 3G4 is a naked antibody, which recruits host defense cells to attack tumor vasculature (4-6). In collaboration with Peregrine Pharmaceuticals, this agent has been chimerized and is now being developed for clinical trials as Bavituximab (it should be noted that until last year the name Vatuximab^{TM} had been proposed) (7). Normally, PS exclusively resides on the cytosolic leaflet of the plasma membrane. However, in tumors PS becomes externalized and provides a viable target. The agent not only targets various tumors, but also induces vascular damage and tumor regression with minimal accompanying toxicity. In developing any new therapy, critical issues include scheduling, optimal combination with other interventions to achieve synergy and early assessment of efficacy. Magnetic resonance imaging will allow us to follow the induction and development of tumor vascular damage *in vivo* providing new insight into spatial and temporal activity and facilitating effective combination with the hypoxic cell selective cytotoxin tirapazamine.

This research program will evaluate the ability of the agent Bavituximab to generate damage in tumor vasculature and induce prostate tumor growth delay. MRI will be used to assess the onset and distribution of tumor vascular damage in a series of Dunning prostate rat tumors (R3327- AT1, MAT-Lu, HI, and H) (8, 9) (10-14). This will provide an indication of the efficacy with respect to tumors exhibiting diverse histologies (anaplastic to well differentiated), a range of volume doubling times (1.5 to 20 days). Importantly, all these tumors are subclones of the original R3327-H tumor, and hence, together they represent a strong analogy for the clinical situation of advanced multi focal multi clonal prostate cancer. We will assess tumor response at different sizes and the value of repeated doses. Ultimately, we will investigate the synergistic application of Bavituximab with the hypoxia selective cell cytotoxin, tirapazamine (15-17). The experience in diverse subcutaneous models will be translated to human tumor xenografts in intraosseous models of advanced metastatic prostate cancer (18). Here, PSA levels and bioluminescence will provide primary indications of tumor growth and MRI will be applied to examine the tumor pathophysiolology.

Successful completion of this project will confirm the potential of this new therapeutic approach to prostate cancer in man. It will lay the foundation for future clinical trials and promises a highly effective novel therapy obviating the need for radical prostatectomy, with its inherent costs, risks, and complications. Ultimately, this approach could lead not only to increased survival time with quality of life, but also cure of the prostate cancer patient.

It should be noted that the antibody Bavituximab was formerly variously called Vatuximab^{TM} or Tarvacin.

Body and Progress

Phase 1 Evaluate efficacy of Bavituximab to control diverse syngeneic rat prostate tumors: assess physiological parameters (*e.g.*, pO_2) as surrogate markers of prostate tumor control and mechanisms of response.

Task 1 Months 1-3

Implant tumors of the four Dunning prostate sublines R3327- MAT-Lu, AT1, HI, and H in Copenhagen rats.

Completed Year 1

Task 2 Months 2-15

Measure baseline pO_2 (*FREDOM*), perfusion characteristics (DCE MRI), and ADC (Apparent diffusion coefficient) of tumors and changes with respect to Bavituximab infusion to assess acute response over two hours.

Investigations completed Year 2, with ongoing data analysis

Tumor oximetry

FREDOM (Fluorocarbon Relaxometry using Echo Planar imaging for Dynamic Oxygen Mapping) (19) was successfully applied to measure tumor pO_2 and dynamic response to interventions. Under baseline air breathing conditions all tumors show quite similar oxygenation patterns typically ranging from regions of hypoxia to others with pO_2 ~ 40 torr (Figure 1). Comparison of pO_2 values using ANOVA (Analysis of Variance) with Fisher's post hoc test showed that the H tumors had significantly lower pO_2 than the AT1 or HI tumors (Tables 1&2). Following bavituximab administration MAT-Lu, AT1 and H tumors showed no particular change. However, several HI tumors showed hypoxiation over about 1 h. One week later both HI and H tumors showed elevated pO_2 (Figs 6 &6).

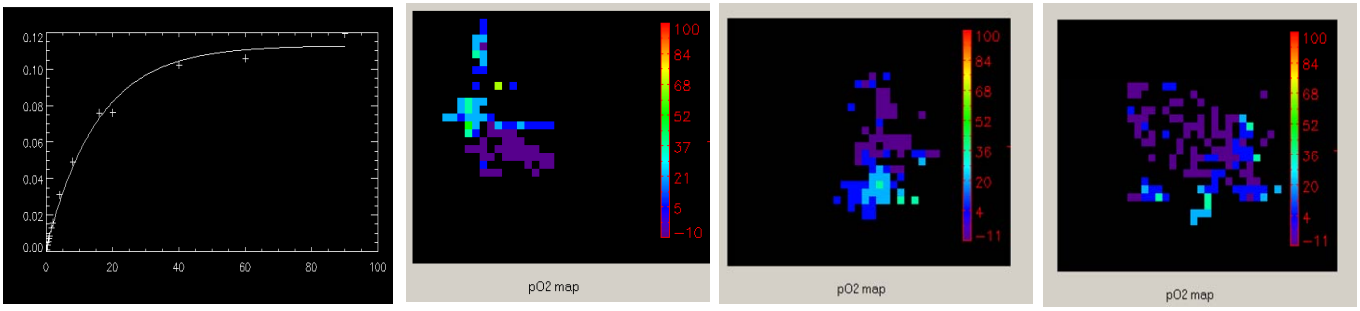

Relaxation curve **MAT-Lu** **HI** **H**

Figure 1 Oximetry in Dunning prostate tumors. Left A typical ^{19}F NMR T1 relaxation curve for the signal intensity of the reporter molecule hexafluorobenzene from a single voxel within a tumor. The relaxation rate is directly proportional to pO_2. Based on such curves maps were generated for representative MAT-LU, HI and H tumors growing on anesthetized rats breathing air with isoflurane anesthesia. Voxel dimension 1.25 mm in plane with 10 mm thickness.

	Count	Mean	Std. Dev.	Std. Err.
AT1	15	10.459	9.635	2.488
H	12	1.751	2.610	.753
HI	24	8.233	9.258	1.890
MAT-LU	18	5.283	8.079	1.904

	Mean Diff.	Crit. Diff	P-Value	
AT1, H	8.708	6.404	.0085	S
AT1, HI	2.226	5.442	.4170	
AT1, MAT-LU	5.176	5.781	.0784	
H, HI	-6.482	5.846	.0303	S
H, MAT-LU	-3.533	6.162	.2565	
HI, MAT-LU	2.950	5.156	.2574	

Tables 1 (left) and 2 (right) Baseline oxygenation of four Dunning prostate R3327-tumor lines.

ANOVA showed that H tumors had significantly lower pO_2 than AT1 or HI. This is contrary to our previous observations and we are examining histology and repeating tests to further clarify the pO_2 values observed in the H tumors.

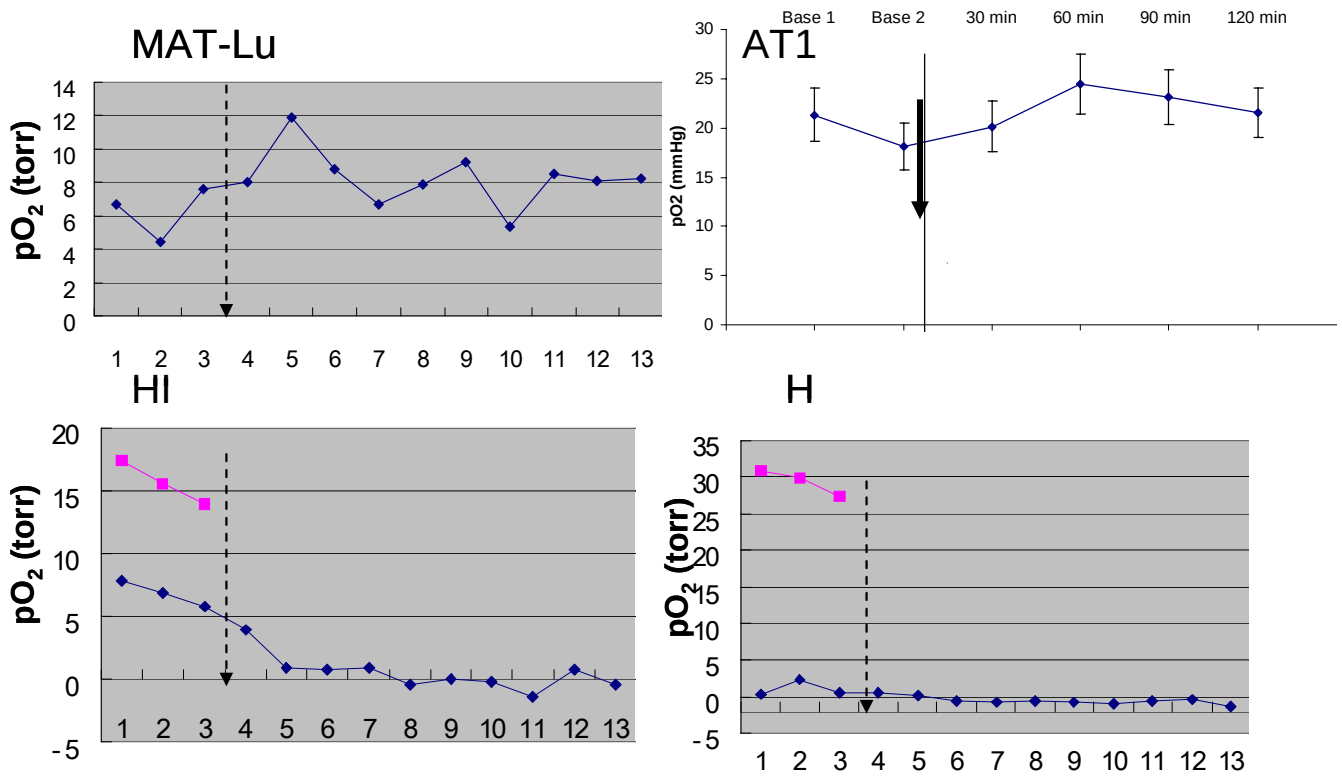

Figure 2 Oxygen dynamic in Dunning prostate R3327 tumors with respect to bavituximab infusion.

Two or three baseline pO_2 maps were generated in individual tumors and then bavituximab was infused IP (arrow). Further pO_2 maps were generated over the following 2 hours. Only HI tumors showed significant change (hypoxiation) following infusion (Fig 5). Pink lines show pO_2 measurements seven days later. For HI tumors the decline in pO_2 was significant within 30 mins.

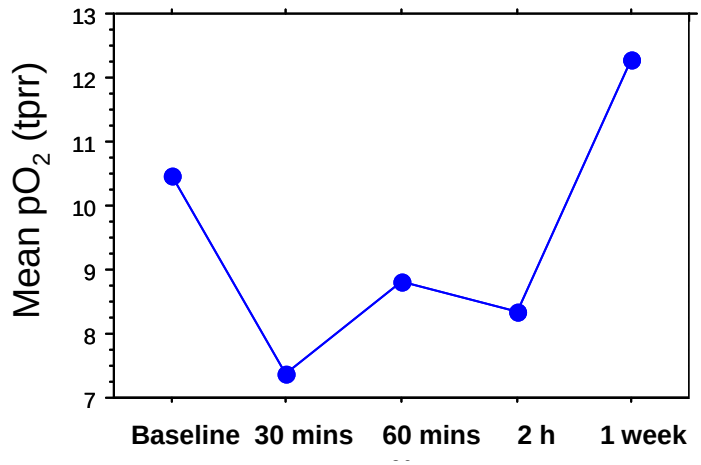

	Mean Diff.	Crit. Diff	P-Value
Base vs 30 mins	3.097	9.258	.5046
Base vs 60 mins	1.633	9.258	.7246
Base vs 2 h	2.113	7.516	.5746
Base vs 7 d	-1.838	8.029	.6476
30 vs 60 mins	-1.465	10.811	.7866
30 mins vs 2 h	-.984	9.363	.8336
30 mins vs 7 d	-4.935	9.779	.3155
60 mins vs 2 h	.481	9.363	.9183
60 mins vs 7 d	-3.470	9.779	.4791
2 h vs 7 d	-3.951	8.149	.3347

AT1

Figure 3 Oxygen dynamics in Dunning prostate R3327-AT1 tumors with respect to bavituximab infusion. Variation in mean pO_2 for a group of 7 small AT1 tumors with respect to infusion of bavituximab IP at 2.5 mg/kg. No significant changes were seen.

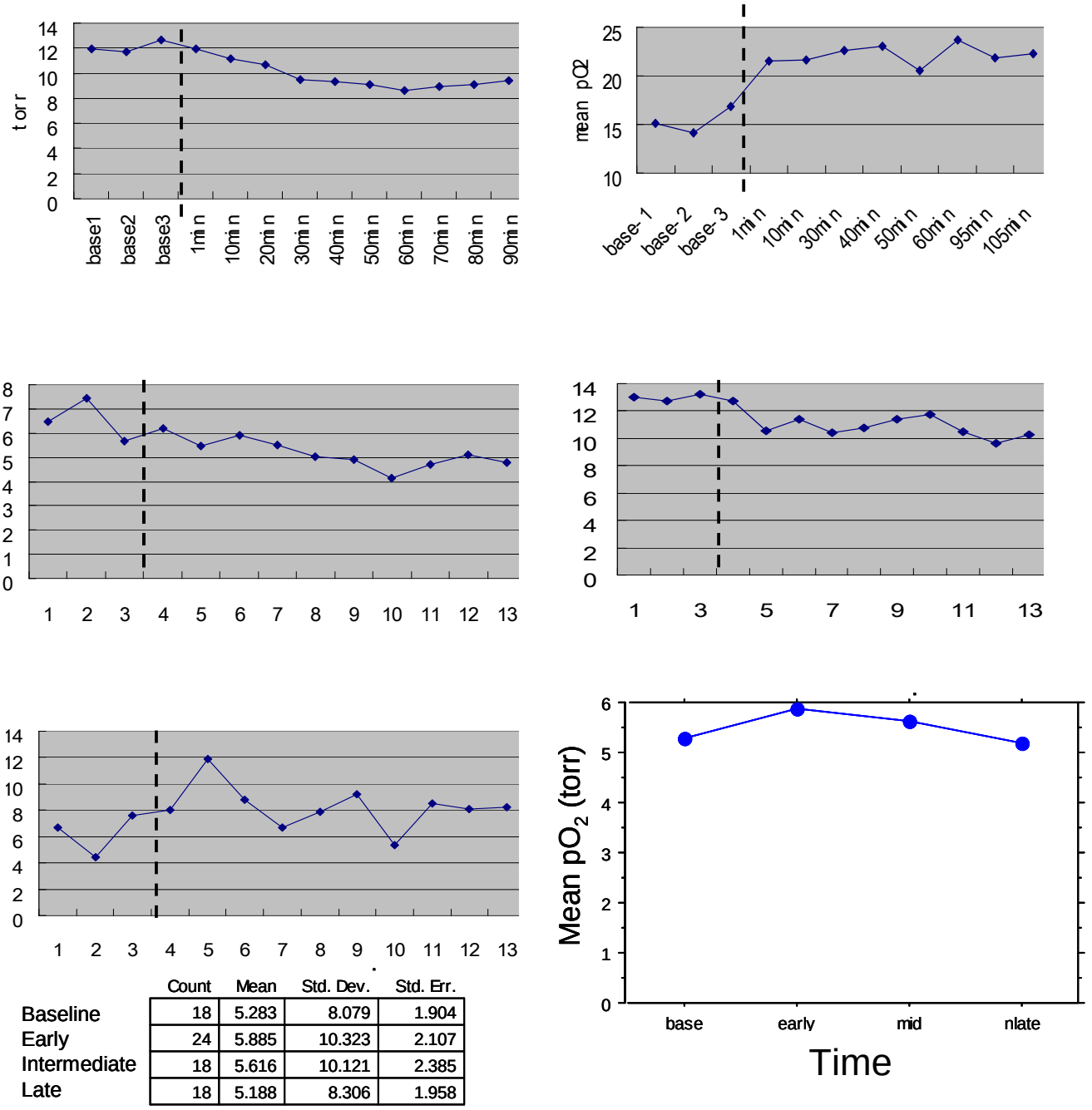

	Count	Mean	Std. Dev.	Std. Err.
Baseline	18	5.283	8.079	1.904
Early	24	5.885	10.323	2.107
Intermediate	18	5.616	10.121	2.385
Late	18	5.188	8.306	1.958

Figure 4 Oxygen dynamics in Dunning prostate R3327-MAT-Lu tumors with respect to bavituximab infusion. Variation in mean pO_2 for each of a group of 5 small MAT-Lu tumors with respect to infusion of bavituximab IP at 2.5 mg/kg. Vertical dashed lines indicate time of bavituximab administration. Data are summarized (bottom right) for a group of six tumors. No significant changes were seen.

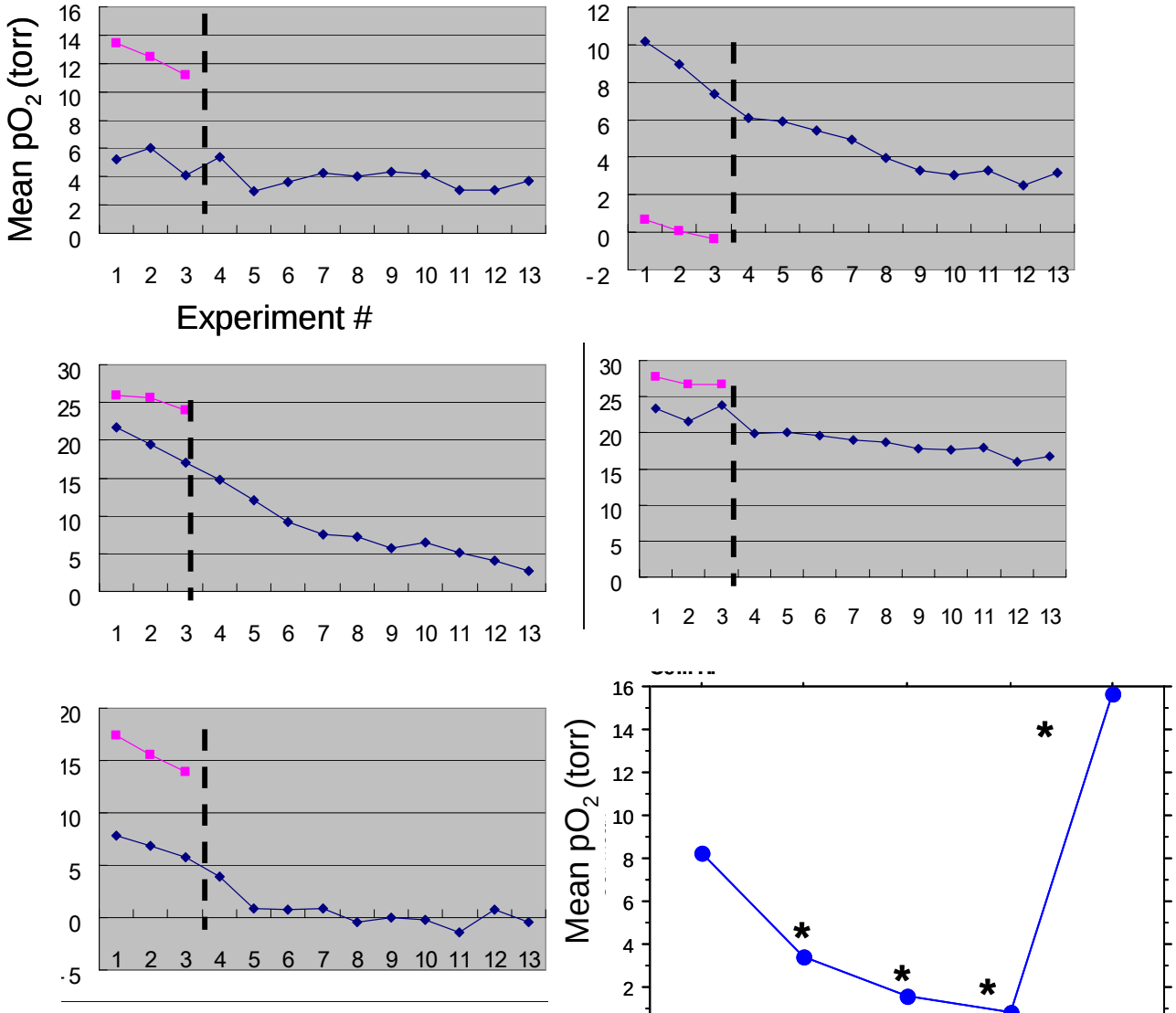

	Mean Diff.	Crit. Diff	P-Value	
base, early	4.837	4.583	.0388	S
base, mid	6.684	4.899	.0079	S
base, nlate	7.389	4.899	.0034	S
base, w 1-base	-7.427	5.292	.0063	S
early, mid	1.847	4.583	.4264	
early, nlate	2.552	4.583	.2724	
early, w 1-base	-12.264	5.000	<.0001	S
mid, nlate	.705	4.899	.7762	
mid, w 1-base	-14.111	5.292	<.0001	S
nlate, w 1-base	-14.816	5.292	<.0001	S

Figure 5 Oxygen dynamics in Dunning prostate R3327-HI tumors with respect to bavituximab infusion. Variation in mean pO_2 for each of a group of 5 small HI tumors with respect to infusion of bavituximab IP at 2.5 mg/kg. Data are summarized for a group of eight tumors in graph. Significant decreases in mean pO_2 were seen over the following two hours as shown in Table based on Fisher's PLSD test and indicated by asterisks on graph. One week later pO_2 had risen significantly.

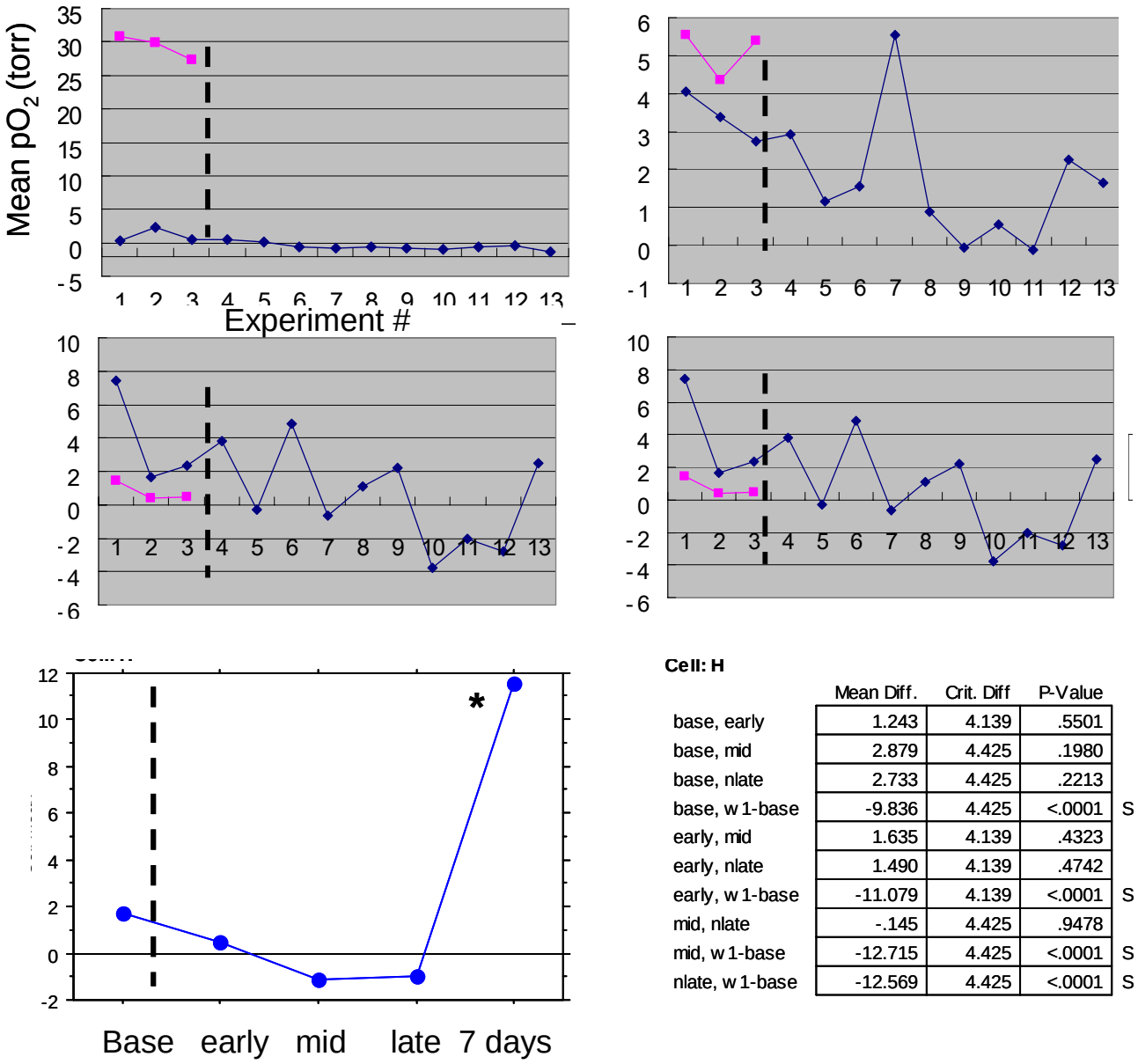

Cell: H

	Mean Diff.	Crit. Diff	P-Value	
base, early	1.243	4.139	.5501	
base, mid	2.879	4.425	.1980	
base, nlate	2.733	4.425	.2213	
base, w 1-base	-9.836	4.425	<.0001	S
early, mid	1.635	4.139	.4323	
early, nlate	1.490	4.139	.4742	
early, w 1-base	-11.079	4.139	<.0001	S
mid, nlate	-.145	4.425	.9478	
mid, w 1-base	-12.715	4.425	<.0001	S
nlate, w 1-base	-12.569	4.425	<.0001	S

Figure 6 Oxygen dynamics in Dunning prostate R3327-H tumors with respect to bavituximab infusion. Variation in mean pO_2 for each of a group of 4 small H tumors with respect to infusion of bavituximab IP at 2.5 mg/kg. Data are summarized for a group of six tumors in graph. No significant acute changes were seen, but 1 week later pO_2 was significantly elevated.

Dynamic contrast enhanced MRI

DCE was performed using ^{1}H MRI at 4.7 T with the small paramagnetic contrast agent Omniscan (0.1 umol /kg (~250 ul) infused IV in tail using catheter vein by hand rapidly (~ 1 s). Data were examined in terms of ΔSI (max change in signal intensity). There was distinct heterogeneity between center and periphery of each tumor type as shown in Figures 7-12. In some cases we have compared regional differences and undertaken measurements of the exchange function kep. Baseline data have been submitted for publication (see appendix)

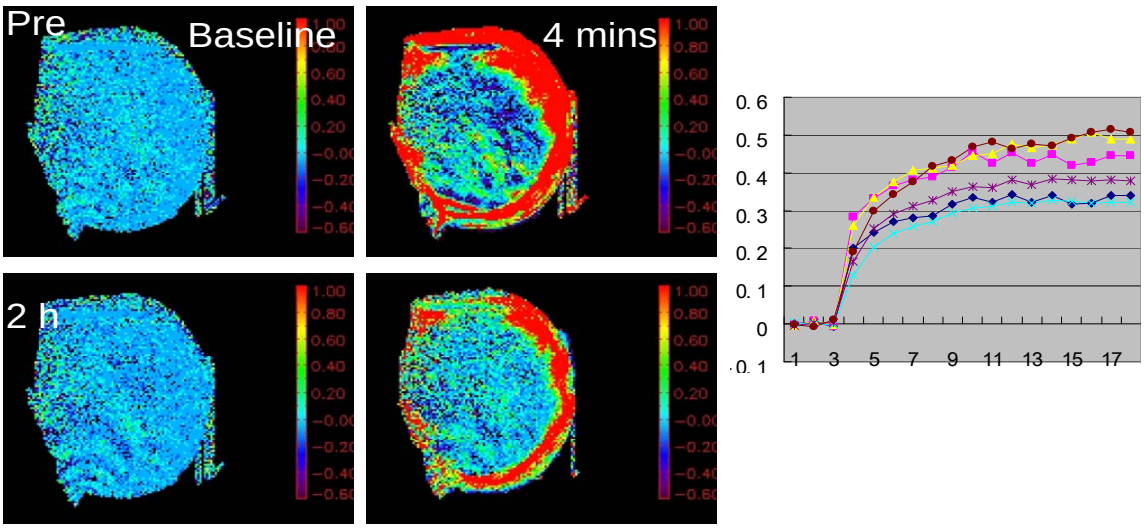

Figure 7 DCE for MAT-Lu tumor. Top left Relative signal intensity map for T1 weighted MRI pre therapy and before contrast agent. Top center: 4 mins after contrast showing strong peripheral enhancement; Bottom left baseline MRI 2 h after administration of bavituximab; Bottom center 4 mins post contrast, 2 h after bavituximab. Right curves show mean signal enhancement for three representative image slices before and 2 h after bavituximab. There were no significant changes. Clearly, further analyses will be required on a regional signal intensity basis.

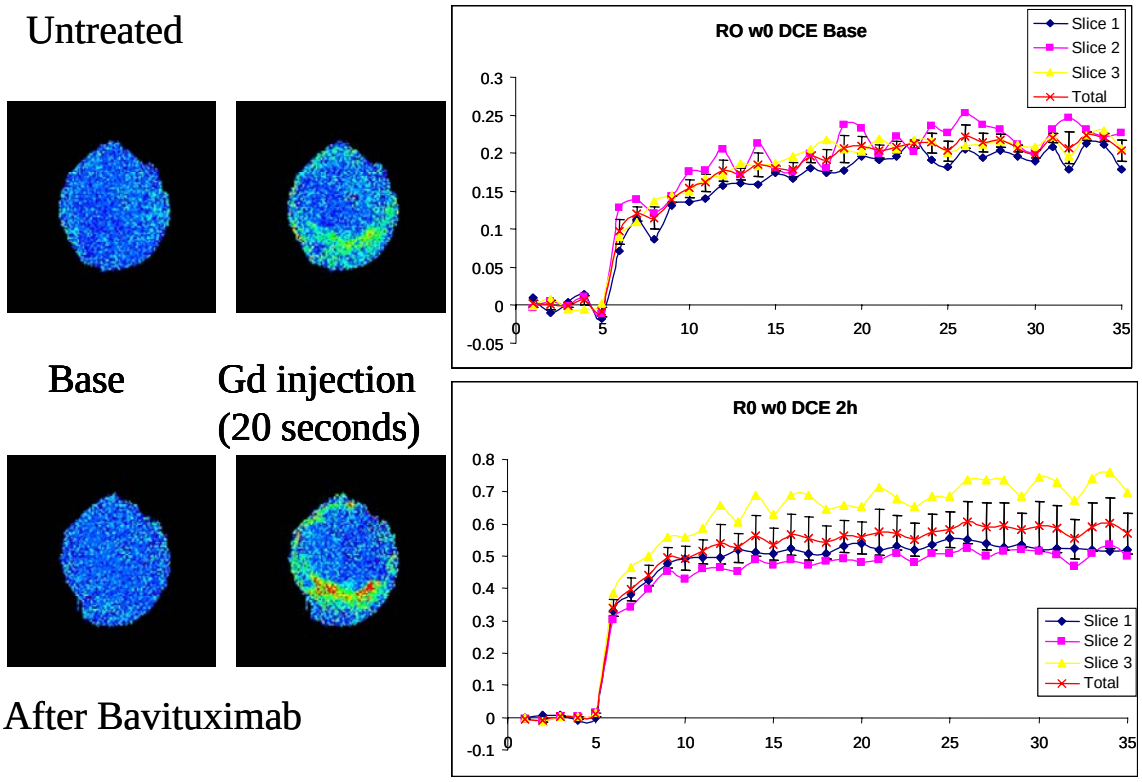

Figure 8 DCE for AT1 tumor. Top left Relative signal intensity map for T1 weighted MRI pre therapy and before contrast agent. Top center: 20 s after contrast showing strong peripheral enhancement; Bottom left baseline MRI 2 h after administration of bavituximab; Bottom center 20 s post contrast, 2 h after bavituximab.

Right curves show mean signal enhancement for three representative image slices before (top) and 2 h after (bottom) bavituximab.

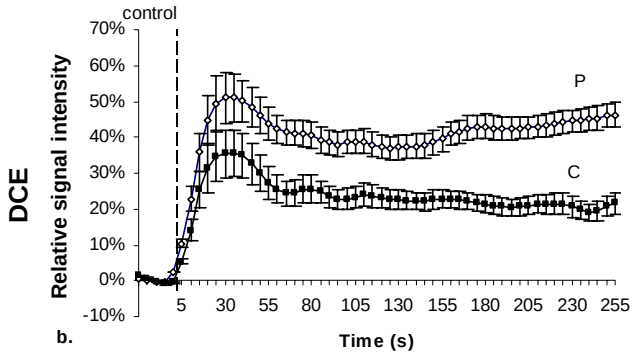

Figure 9 Comparison of signal intensity during DCE experiments for a group of AT1 tumors. A significant difference in signal response was observed between central and peripheral regions of tumor.

	Mean	36±1
(ΔSI) DCE	Periphery	43±1*
%response	Center	24±1
K_{ep} (min^{-1})	Mean	3.05±0.37
	Periphery	3.11±0.44
	Center	2.59±0.51

Table 3 Comparison of DCE parameters. For a group of AT1 tumors showing significant difference in signal response between central and peripheral regions of tumor (*). No differences were observed for Kep.

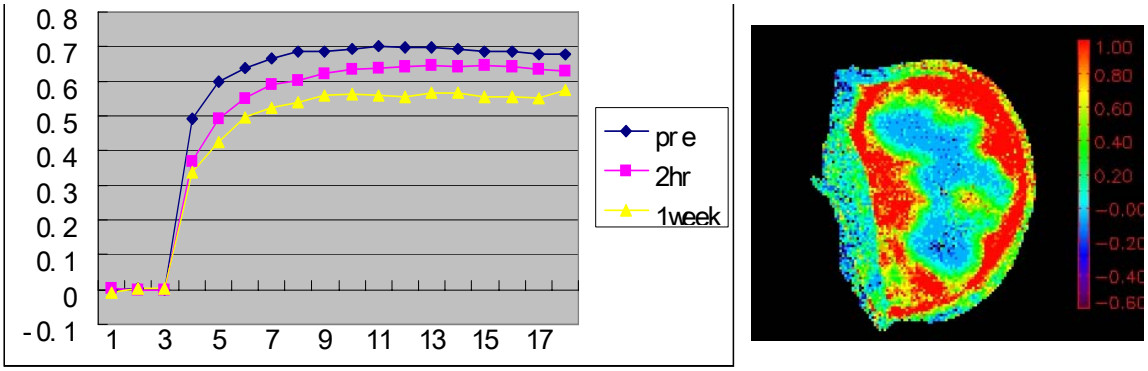

Figure 10 DCE for HI tumor. Left Mean signal intensity kinetics following infusion of contrast agent. Right: Relative signal intensity map for T1 weighted MRI 2 h post therapy (4 minutes after contrast agent) showing heterogeneous perfusion.

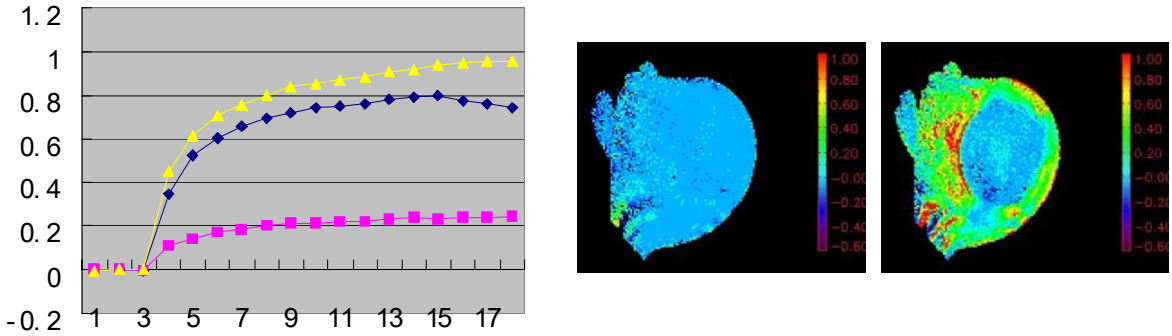

Figure 11 DCE for H tumor. Left Mean signal intensity kinetics following infusion of contrast agent. Pre (blue), 2h post bavituximab (pink), 7 days post (yellow). On most occasions DCE indicated considerably lower signal response in the H tumors 2 h after bavituximab. To verify this result we will both use histology following administration of Hoechst perfusion dye and ensure that future studies include normal tissue following assessment of arterial input function. This is cruel to verify that the contrast agent injections are all similarly successful. Right: Relative signal intensity map for T1 weighted MRI pre and 4 minutes after contrast agent showing heterogeneous perfusion pre bavituximab.

$(\Delta SI)\,\mathrm{DCE}^{+}$ %response	Mean	55±2‡
	Periphery	31±1
	Center	124±6*‡
K_{ep} (min^{-1})	Mean	3.20±0.39
	Periphery	3.34±0.46
	Center	2.95±0.54

Table 4 Comparison of DCE parameters. For a group of H tumors there was a significant difference in signal response between central and peripheral regions of tumor. No differences were observed for Kep.

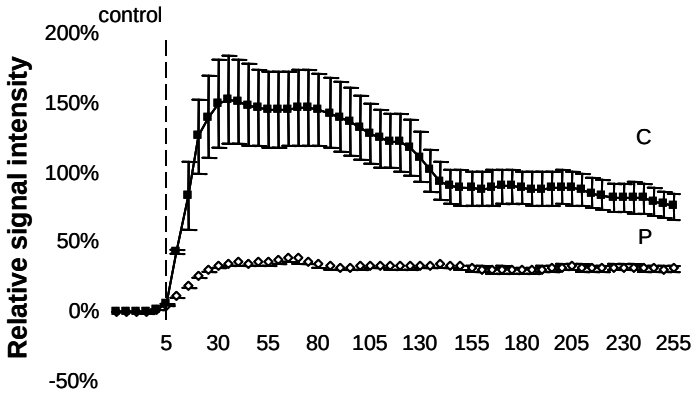

Figure 12 Comparison of signal intensity during DCE experiments for a group of H tumors. A significant difference in signal response was observed between central and peripheral regions of tumor, but here the center showed a larger change, whereas for AT1 tumors in Figure 9, the opposite was observed.

Apparent diffusion coefficient (ADC) maps are shown for thin slices from representative Dunning prostate tumors of each subline in Figures 13 and 14. Each tumor shows some heterogeneity. In Figure 14 color representations are provided for a representative AT1 tumor, with 3 selected slices before and two hours after administration of Bavituximab. Table 5 provides mean values and compares the statistical significance of difference between the sublines. While the maps showed no significant differences between the AT1 and MAT-

Lu tumor types, all the other comparisons revealed significantly differences and the H showed much lower ADC values.

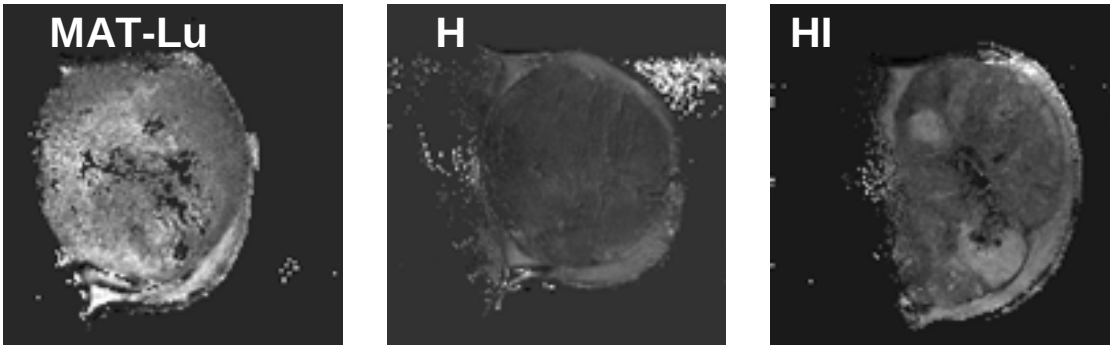

Figure 13 Apparent diffusion maps obtained by proton MRI at 4.7 T of Dunning prostate R3327 tumors growing in rats. Each image represents a slice of a tumor observed *in vivo* presenting diffusion maps obtained with 4 b-value diffusion gradients (MR parameters, FOV = 30 mm, TR = 2,300 ms, TE= 50 ms, in plane resolution 230 um, slice thickness 2 mm with a total acquisition time of 20 mins)

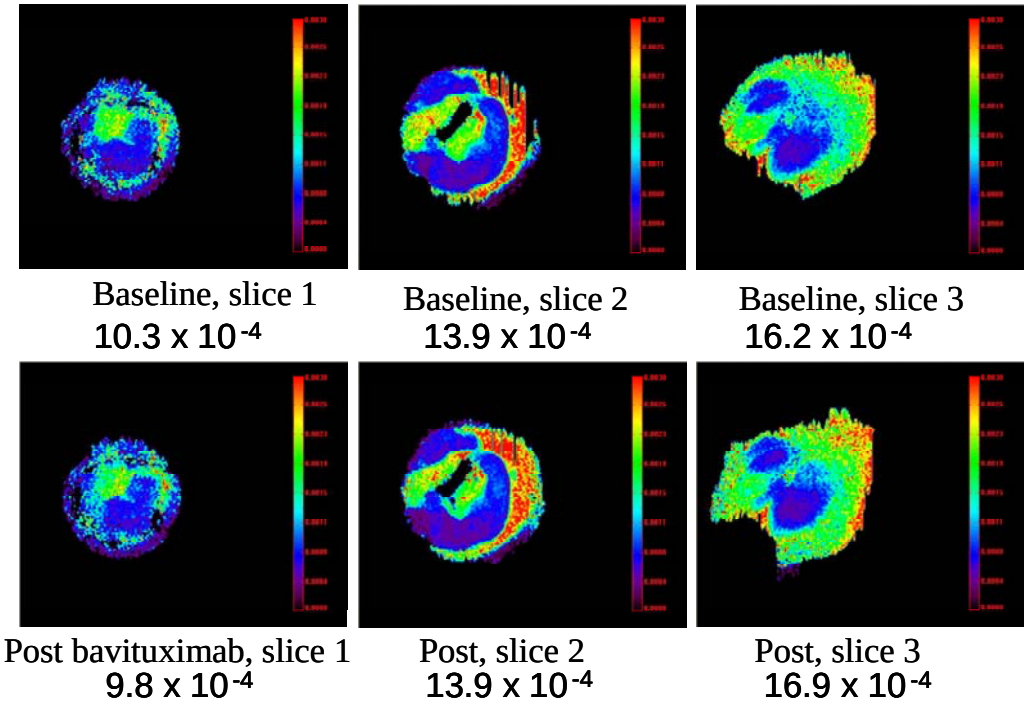

Figure 14 Apparent diffusion maps obtained by proton MRI at 4.7 T of Dunning prostate R3327-AT1 tumor. Data as for Figure 9, but showing three consecutive image slices in representative AT1 tumor. Distinct baseline heterogeneity is apparent with mean ADC ranging from 10.2×10^{-4} to 16.2×10^{-4} mm^2/s. The lower image shows the same slices 2 h after administration of 2.5 mg/kg bavituximab. There were no significant acute changes.

	Mean	Std. Dev.
AT1	12.9	.92
H	2.6	3.83
HI	16.7	2.80
MAT-Lu	11.8	2.44

Fisher's PLSD for ADC pre
Effect: Tumor type
Significance Level: 5 %

	Mean Diff.	Crit. Diff	P-Value	
AT1, H	10.292	3.710	<.0001	S
AT1, HI	-3.839	3.153	.0196	S
AT1, MAT-Lu	1.079	3.349	.5083	
H, HI	-14.130	3.387	<.0001	S
H, MAT-Lu	-9.213	3.570	<.0001	S
HI, MAT-Lu	4.918	2.987	.0027	S

Table 5 Left Relative ADC values for groups of Dunning prostate tumors. **Right** Statistical comparison of ADC values for tumor types showing levels of significance for analysis of variance based on Fisher's test

For HI tumors below:

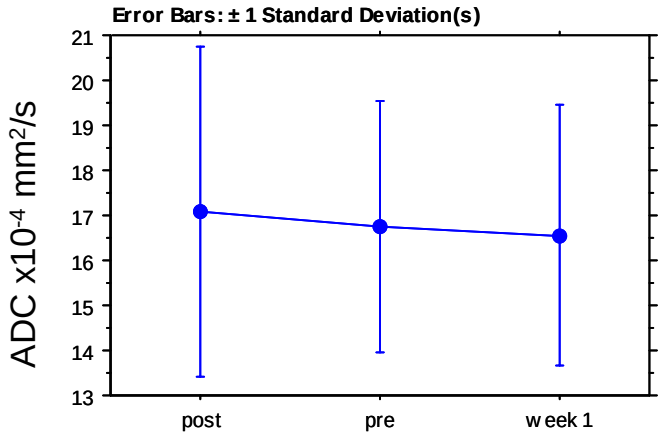

Fisher's PLSD for ADC
Effect: Time
Significance Level: 5 %

	Mean Diff.	Crit. Diff	P-Value
post, pre	.337	3.314	.8335
post, week 1	.525	3.580	.7622
pre, week 1	.188	3.580	.9139

Figure 15 Variation in ADC with respect to bavituximab administration Data shown for a group of 7 HI tumors. No significant changes were observed.

Task 3 Months 3-15

Response to multiple doses of Bavituximab. Use MRI to measure pO_2, perfusion characteristics and diffusion characteristics of tumors with respect to repeated Bavituximab administration (assess response over a period of weeks/months by MRI and tumor volume).

MAT-Lu tumors show heterogeneous baseline pO_2, but generally minimal acute response to administration of bavituximab.

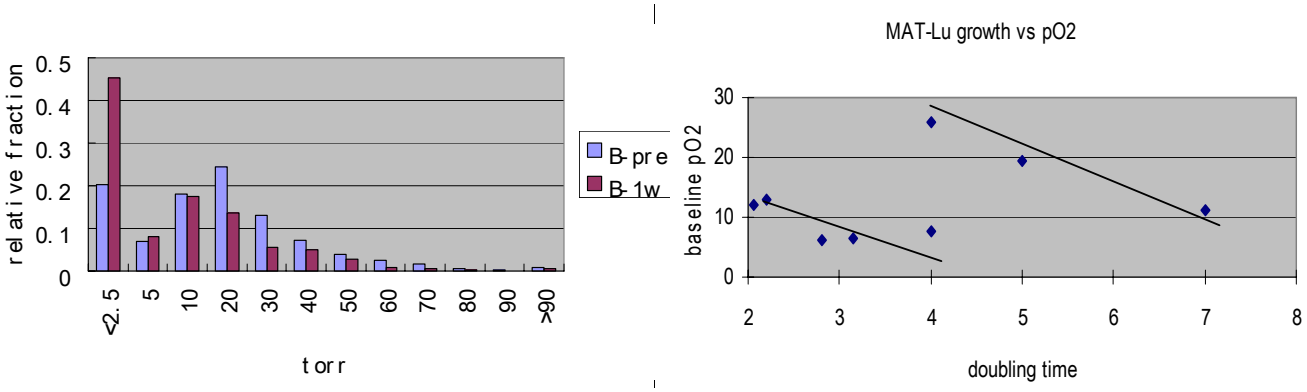

Figure 16 Chronic changes in pO_2 accompanying multiple doses of bavituximab in MAT-Lu tumors. Left: Histogram presents distribution of pO_2 values measured using ^{19}F MR oximetry for a group of 8 small tumors. Blue bars are pre therapy and purple 7 days later after 3 doses (2.5 mg/kg) of bavituximab. Distinct hypoxiation of these tumors is apparent. This may be due to the drug, but is likely attributable to rapid growth

seen in the tumor which has about 2 day volume doubling time (VDT). Further tests are underway to verify the cause of the hypoxiation. **Right:** There appear to be correlations between pre-therapy baseline pO_2 and time to double in volume during bavituximab therapy (thrice weekly). However, tumors appear to fall into two separate groups, requiring further evaluation.

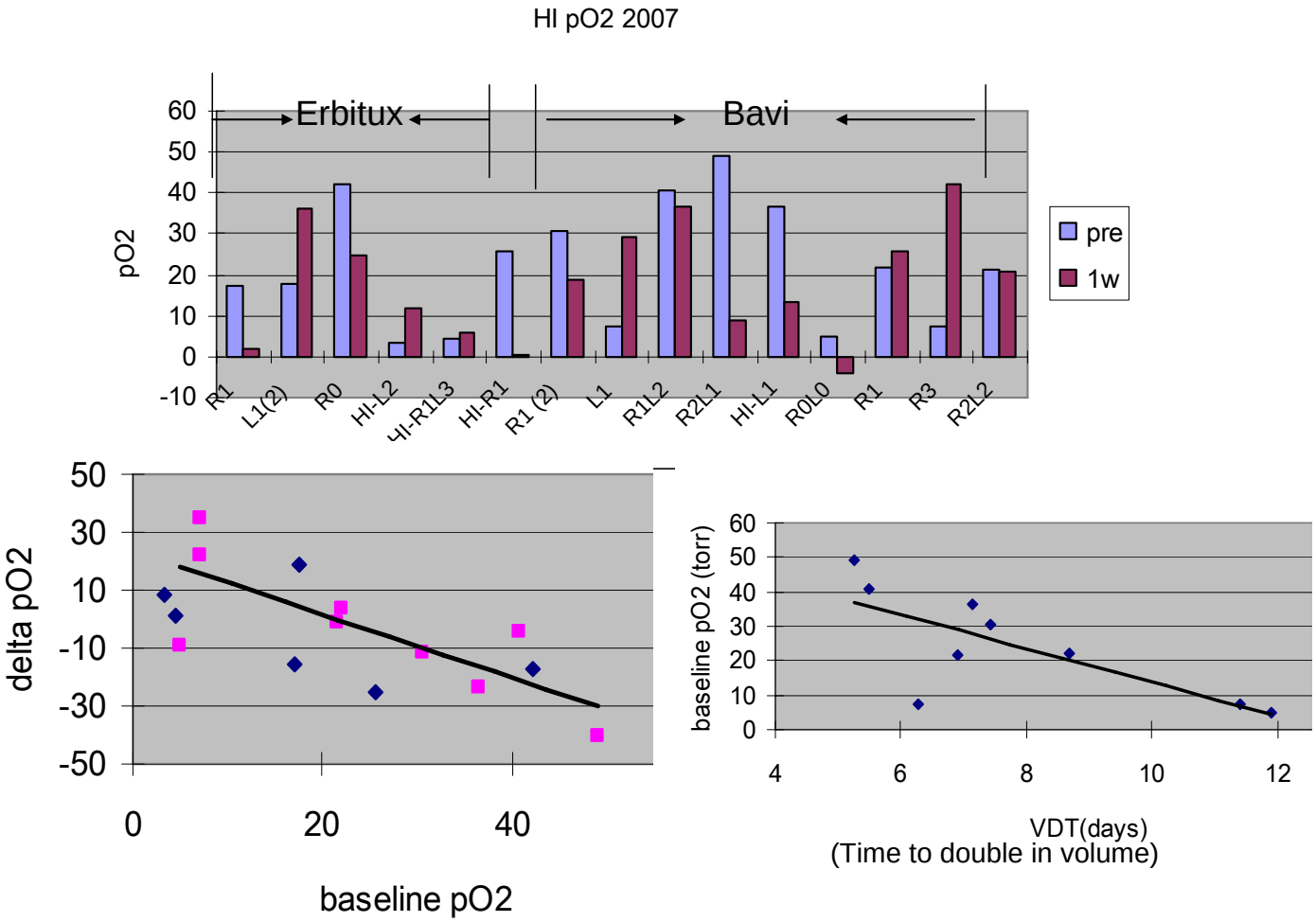

Figure 17 Chronic changes in pO_2 accompanying multiple doses of bavituximab in HI tumors.

Upper: Histogram comparing pO_2 pre treatment and after 7 days (3 doses) of bavituximab or erbitux.

Lower graphs- left- Change in pO_2 over 7 days of treatment (ΔpO_2) with erbitux (pink) or bavituximab (blue) appears to be related to baseline pO_2 prior to therapy. Right: Time to double in volume during therapy appears to be related to baseline pO_2, as also seen for MAT-Lu tumors in Figure 16.

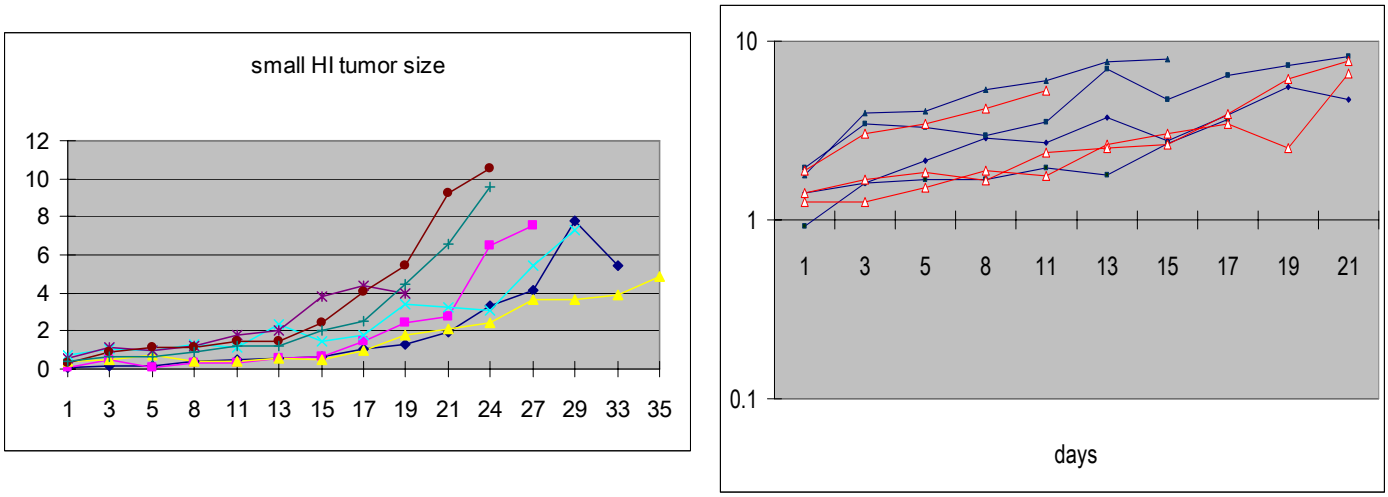

Figure 18 Growth curves for HI tumors with respect to bavituximab therapy.

Left: individual small tumors all receiving bavituximab; **right**: individual medium sized tumors receiving treatment (thrice weekly) with erbitux (red) or bavituximab (blue).

H tumors indicated strong therapeutic response (Figure 19). Each tumor showed either reduction in growth or tumor shrinkage. Tumors of the faster growing cell lines appeared to respond less well to therapy. However, they generally develop massive central necrosis with only a thin peripheral rim of viable tumors. In many cases this was revealed as ulceration leaving a donut cavity. Thus, there is extensive tumor control, but volume measurement based on respective dimensions alone does not appropriately reveal the control.

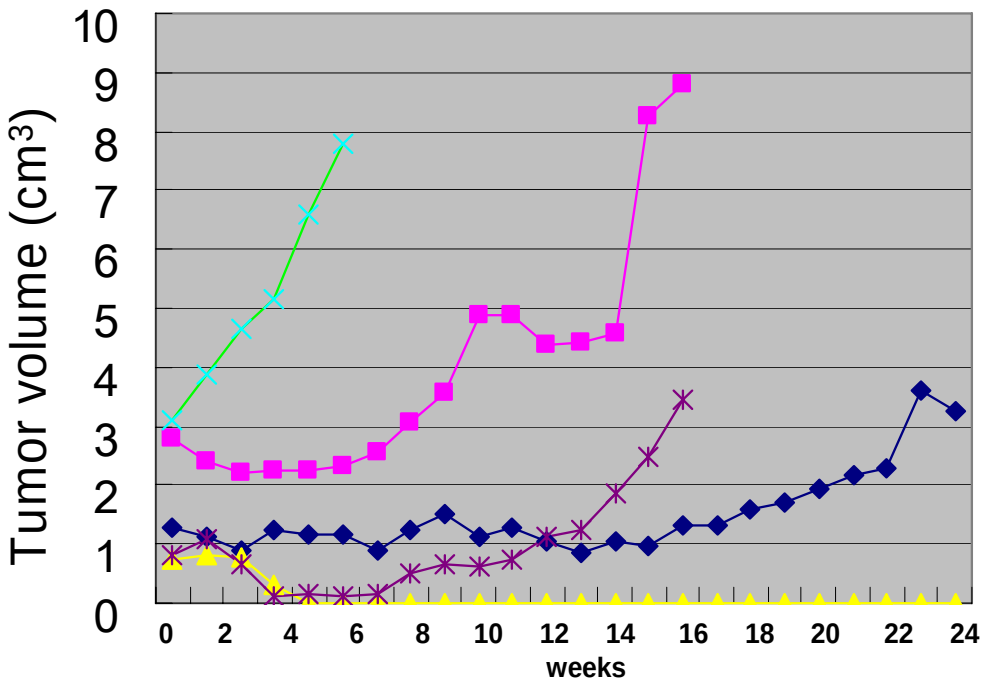

Figure 19 Growth curves for H tumors with respect to bavituximab therapy. Growth curves for groups of control and bavituximab treated H tumors. Separate curves are shown for highly responsive small H tumors (yellow; n=2); responsive small tumors (blue; 1 tumor) and somewhat less responsive large tumors (pink; 2 tumors). Bavituximab treated tumors received 2.5 mg/kg IP thrice weekly starting on day 1. For comparison a large tumor designated by green label received equivalent dose of control, antibody rituximab.

Task 4 Months 3-18

Histological analysis- assess distribution of Bavituximab, necrosis, hypoxia, perfusion based on dyes and antibodies.

Treated tumors have been stored and histology is underway. Data were included in the manuscript accepted for publication in Clinical Cancer research (appended).

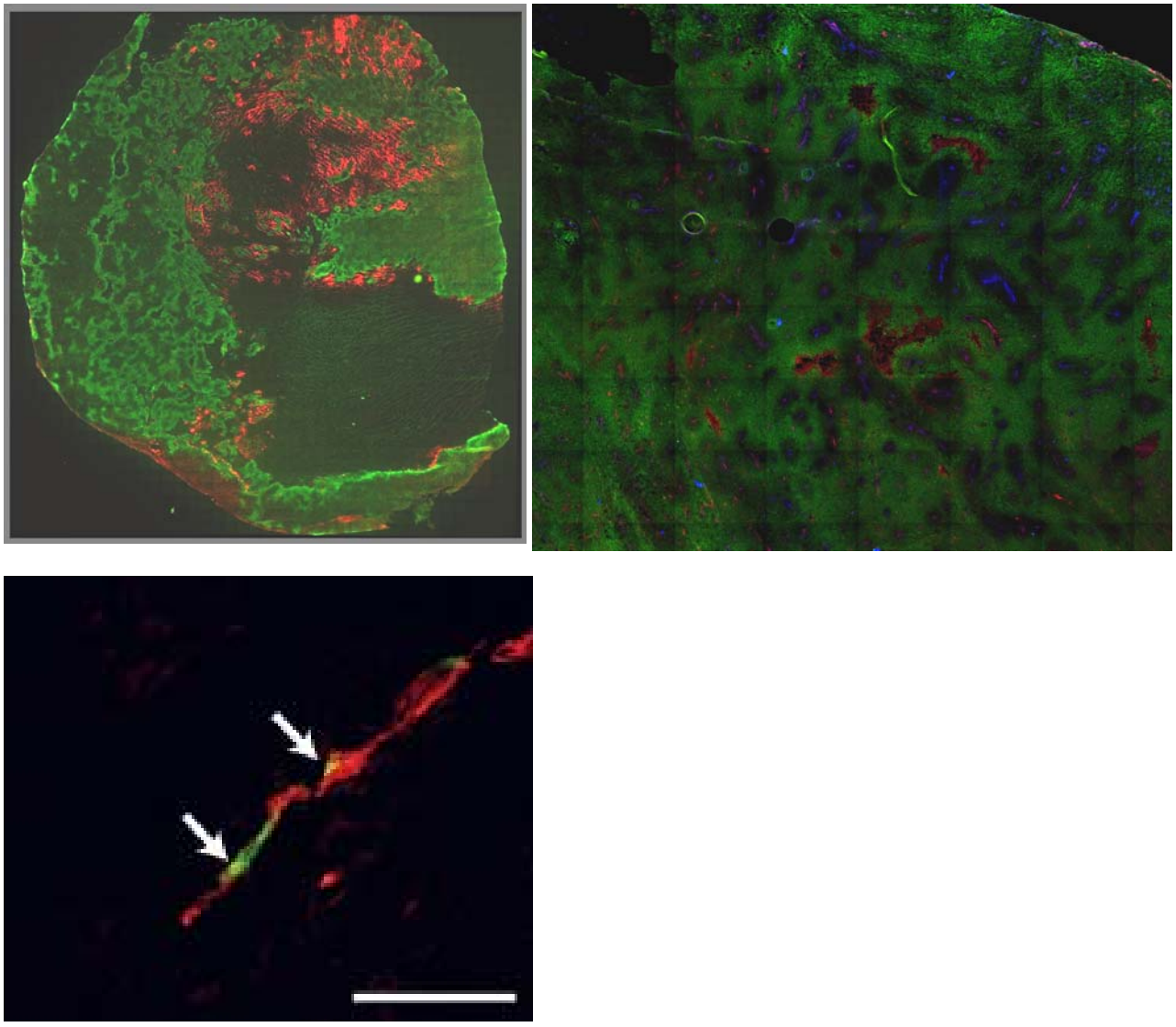

Figure 20 Histology of poorly differentiated Dunning prostate AT1 tumors.

Top left Staining with antiCD31 (vasculature) represented in red and bavituximab (anti-PS) in green.

Top right: Triple staining shows extensive hypoxia (pimonidazole-green), few blood vessels (CD31-red), and some perfused vessels (Hoechst- blue).

Bottom Staining showing coincidence of CD31 and PS with overlay of green and red generating yellow.

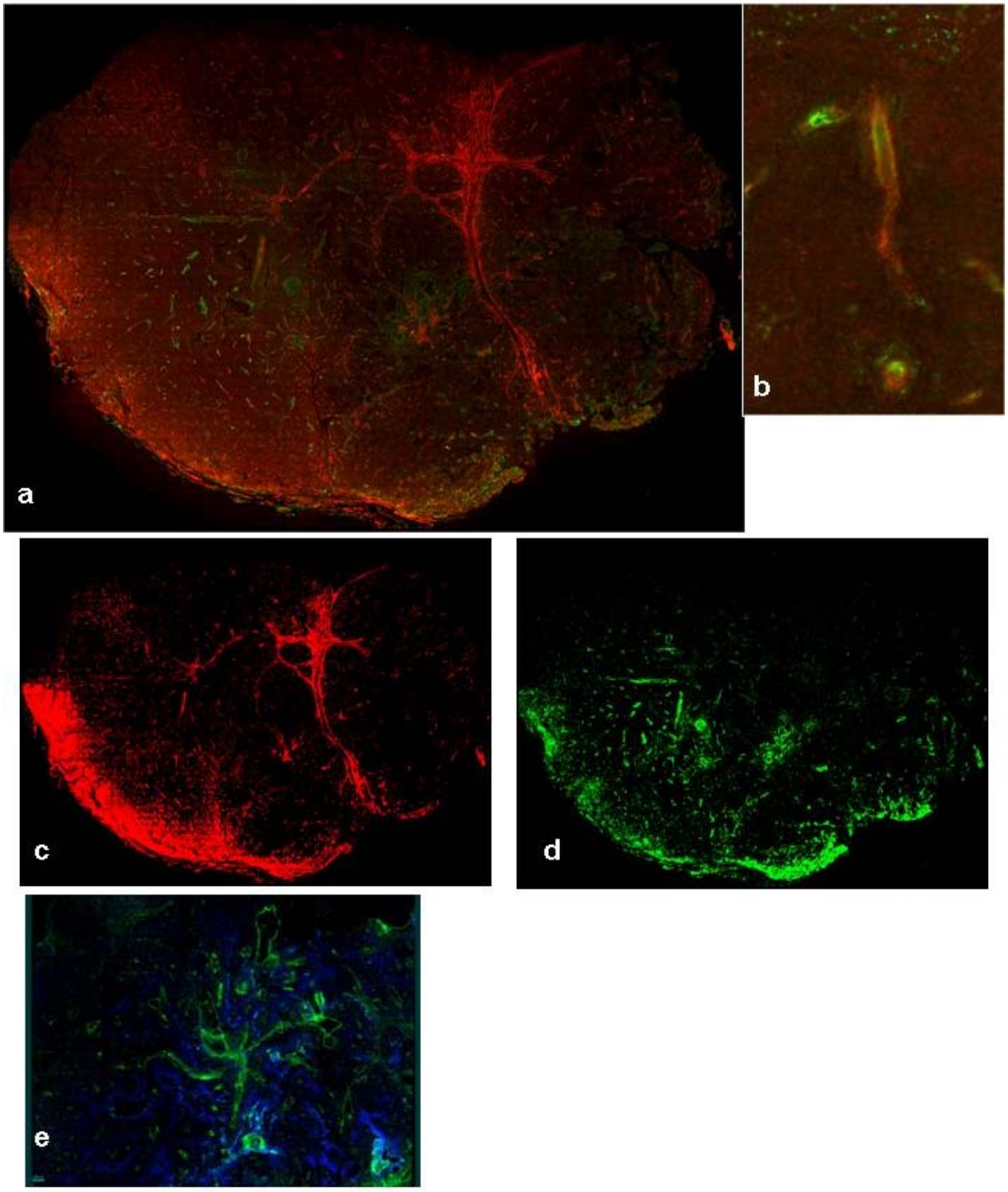

Figure 21 Histology of moderately differentiated Dunning prostate HI tumors.

Whole mount hosing bavituximab (PS) green on CD31 red; b) magnification showing overlap in blood vessel. c) Color separation of a showing CD31 in red; d) color separation of a showing bavituximab in green; and e) PS I green and hypoxia based on pimonidazole in blue.

Task 5 Month 12

Prepare annual report and manuscript.

Completed and approved for Year 1- manuscripts in appendix.

Task 6 Months 15-18

Implant tumors of the four sublines R3327- MAT-Lu, AT1, HI and H (6 tumors of each of 4 sublines with 3 treatment sizes (0.5 cm, 1 cm, 1.5 cm diameter; respectively 0.06 cm^3, 0.5 cm^3, 1.7 cm^3) = 144 experimental rat tumors: Tasks 7 and 8 are based on these rats))
Completed year 2

Task 7 Months 16-30

Assess tumor growth delay in response to combined Vatuximab™ with tirapazamine (SR4233: 3-amino-1,2,4-benzotriazine 1,4 dioxide). Use MRI to assess differential response to therapy compared with tumors receiving Vatuximab™ alone.
Growth of small AT1 tumors based on external caliper measurements with respect to various drug combinations. Bavituximab from Task 3 for comparison with Figures 18 and 19. Since tumors are expected to be hypoxic the hypoxia selective cytotoxin tirapazamine was added. For comparison data are shown for the standard chemotherapeutic docetaxel. These studies are ongoing.

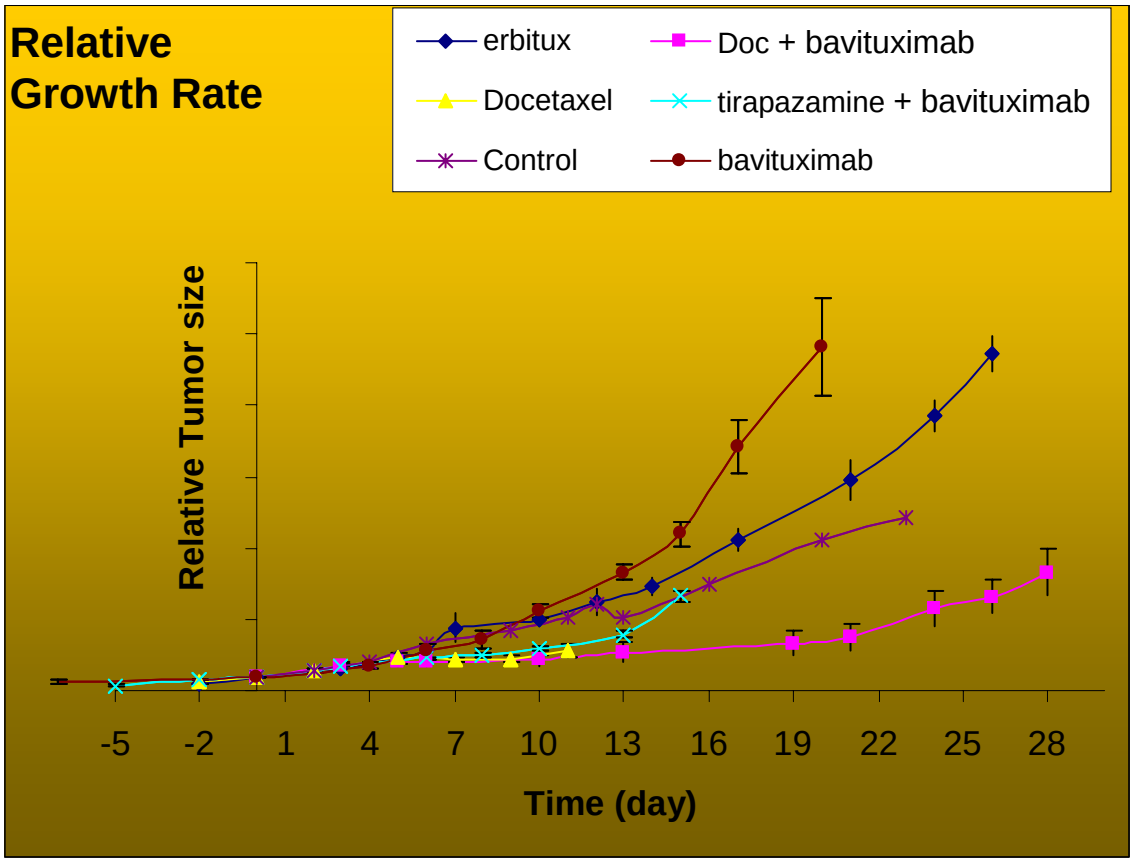

Figure 22 Growth curves for groups of treated AT1 tumors
Purple * control untreated tumors; brown ● bavituximab at 2.5 mg/kg thrice weekly; cyan x bavituximab (2.5 mg/kg IP thrice weekly) + tirapazamine (25 mg/kg IP weekly); blue ◆ control antibody –erbitux (2.5 mg/kg thrice weekly); yellow ▲- docetaxel (5 mg/kg, ip- only 4 doses due to toxicity) pink ■ bavituximab (2.5 mg/kg IP thrice weekly) + docetaxel (2.5 mg/kg, ip - only 4 doses due to toxicity)

Task 8 Month 24
Prepare annual report and manuscript.
Report enclosed here. Manuscripts submitted and more in preparation (appendix).

KEY RESEARCH ACCOMPLISHMENTS:

- Examined changes in tumor oxygenation in response to bavituximab administration. Only HI tumors showed significant hypoxiation.
- Examined changes in tumor perfusion following bavituximab. Only H tumor showed significant change (reduction)
- No changes in apparent diffusion coefficients were found following batuximab administration.
- Most H tumors showed significant reduction in growth rate (based on tumor volume) and growth delay (or shrinkage) were maintained over many weeks wile additional doses of bavituximab were administered.
- The faster growing tumors showed central necrosis and tumor control based on histological examination, but simply measuring whole tumor volume did not readily reveal tumor control due to peripheral rim which continued to grow.
- Preliminary data suggest that addition of tirapazamine to bavituximab enhances therapeutic growth delay.
- By comparison bavituximab + docetaxel gives strongest growth delay, but docetaxel causes weight loss and severe toxicity.

REPORTABLE OUTCOMES:

1 Peer-reviewed Papers

During this second year two significant peer reviewed manuscripts have been accepted for publication. Each credits this grant and is based in part on studies funded by the grant. The papers are included in the appendix.

- Kodibagkar VD, Wang X, Mason RP. "Physical principles of quantitative nuclear magnetic resonance oximetry." *Front Biosci.* 13:1371-84 (2008).
- Jennewein M, Lewis MA, Zhao D, Tsyganov T, Slavine N, He J, Watkins L, Kodibagkar VD, O'Kelly S, Kulkarni P, Antich PP, Hermanne A, Rösch F, Mason RP and Thorpe PE," Vascular imaging of solid tumors in rats with a radioactive arsenic-labeled antibody that binds exposed phosphatidylserine" *Clin. Cancer Res.*, accepted (2007).

2 Book Chapter

- "Non-Invasive Physiology and Pharmacology Using ^{19}F Magnetic Resonance", J.X. Yu, W. Cui, D. Zhao, and R. P. Mason, CHAPTER 5, In FLUORINE AND HEALTH, A. Tressaud & G. Haufe (Eds) 2008 Elsevier B.V.

3 Peer-reviewed Grants

Research results and the needs of this current grant have directly assisted in UT Southwestern winning two significant grants for infrastructure from the NCI. These will both enhance the current studies and future prostate cancer research at UT Southwestern and the surrounding community.

- 1S10RR024757-01 (PI Mason) 04/01/08 – 03/31/09 0.00 calendar

NIH/National Cancer Institute $334,600
Small Animal Bioluminescence and Fluorescence Imaging System (with 3D capability)
Major Goal: Purchase a commercial bioluminescence imaging system to accelerate development of new therapies in cancer research

- 1U24CA126608-01 (PI Mason) 03/01/07 – 02/28/12 2.40 calendar

NIH – SAIR $300,000 annual
UT Southwestern Small Animal Imaging Resource Program
Major Goal: Oversight of multi-modality imaging resource

4 Submitted manuscript

"Blood Oxygen Level Dependent (BOLD) and Gd-DTPA dynamic contrast enhanced (DCE) MRI: comparison of two prostate tumor sublines exhibiting different vascular development", L. Jiang, D. Zhao, E. W. Hahn, A. J. van der Kogel, J. Bussink, P. Peschke, and R. P. Mason

5 Conference proceedings

- "Differential physiological response to carbogen of two diverse prostate tumor lines detected by tissue water ^{1}H MRI", J. Pacheco-Torres, D. Zhao, J. McAnally, and R. P. Mason, *Second International Conference of European Society for Molecular Imaging*, Naples, Italy , June 14-15, 2007
- "Vatuximab™: Optimizing Therapeutic Strategies For Prostate Cancer Based on Dynamic MR Tumor Oximetry", R. P. Mason; W. Cui; D. Zhao; A. J. van der Kogel; J. Bussink; J. Pacheco Torres; J. McAnally; L. Watkins; P. Peschke; and P. Thorpe. *Innovative Minds in Prostate Cancer Today - IMPaCT* meeting, September 5-8, Atlanta, Georgia, 2007, (poster appended). It may also be viewed at

http://www.utsouthwestern.edu/vgn/images/portal/cit_56417/62/36/410903DOD_poster_for_ralph_pdf.pdf

- "*DOCENT*-Dynamic Oxygen Challenge Evaluated by NMR T1 and T2* of Tumors", D. Zhao, J. Pacheco Torres, P. Peschke and R. P. Mason, Imaging in 2020 2007 Jackson Hole (poster appended). It may also be viewed at

http://www.utsouthwestern.edu/vgn/images/portal/cit_56417/15/33/416771Imaging2020-2007.pdf

- "*DOCENT*- Dynamic Oxygen Challenge Evaluated by NMR T1 and T2* of Tumors", J. Pacheco-Torres, D. Zhao, A. Contero, P. Peschke and R. P. Mason ISMRM Toronto, submitted

CONCLUSIONS: As expected based on previous observations all prostate tumors show considerable hypoxia. However, only HI tumors showed significant acute increased hypoxia following administration of bavituximab. Thus, the hypoxia selective cytotoxin tirapazamine is expected to be effective on the prostate tumors, but in terms of combined effects and potential synergy, we now only expect this for the HI tumors, where additional hypoxia is induced by bavituximab. It appears that the faster growing sublines have a rapidly proliferating edge, which escapes control from bavituximab alone.

References

1. Thorpe, P. E., Chaplin, D. J., and Blakey, D. C. The first international conference on vascular targeting: meeting overview. *Cancer Res., 63: 1144-1147, 2003*.
2. Thorpe, P. E. Vascular Targeting Agents as Cancer Therapeutics. Clin. Cancer Res., *10:* 415-427, 2004.
3. Burrows, F. J. and Thorpe, P. E. Vascular-targeting- a new approach to the therapy of solid tumors. *Pharmacol. Ther.*, ***64:*** 155-174, 1994.
4. Ran, S., Downes, A., and Thorpe, P. E. Increased exposure of anionic phospholipids on the surface of tumor blood vessels. *Cancer Res., 62:* 6132-6140, 2002.
5. Ran, S., He, J., Huang, X., Soares, M., Scothorn, D., and Thorpe, P. E. Anti-tumor effects of a monoclonal antibody directed against anionic phospholipids on the surface of tumor blood vessels in mice. Clin. Cancer Res., *11:* 1551-1562, 2005.
6. Ran, S. and Thorpe, P. E. Phosphatidylserine is a marker of tumor vasculature and a potential target for cancer imaging and therapy. Int. J. Radiat. Oncol. Biol. Phys., *54:* 1479-1484, 2002.
7. Peregrine http://ir.peregrineinc.com/phoenix.zhtml?c=74236&p=irol-newsArticle&ID=696919&highlight=.
8. Zhao, D., Constantinescu, C., Hahn, E. W., and Mason, R. P. Differential oxygen dynamics in two diverse Dunning prostate R3327 rat tumor sublines (MAT-Lu and HI) with respect to growth and respiratory challenge. Int. J. Radiat. Oncol. Biol. Phys., *53:* 744-756, 2002.
9. Zhao, D., Ran, S., Constantinescu, A., Hahn, E. W., and Mason, R. P. Tumor oxygen dynamics: correlation of in vivo MRI with histological findings. Neoplasia, *5:* 308-318, 2003.
10. Lohr, F., Wenz, F., Flentje, M., Peschke, P., and Hahn, E. Measurement of proliferative activity of three different sublines of Dunning rat prostate tumor R3327. Strahlenther. Onkol., *169:* 438-445, 1993.
11. Eble, M. J., Wenz, F., Bachert, K. B., Lohr, F., and Peschke, P. Invasive pO_2 histography in Dunning prostate tumor R-3327-AT1 and R3327-HI: Correlation with ^{31}P-MR spectroscopy and in-vivo radiosensitivity. *In:* P. W. Vaupel, D. K. Kelleher, and M. Günderoth (eds.), Tumor Oxygenation, pp. 95-105. Stuttgart: Gustav Fischer, 1995.
12. Peschke, P., Hahn, E. W., Wenz, F., Lohr, F., Brauschweig, F., Wolber, G., Zuna, I., and Wannenmacher, M. Differential sensitivity of three sublines of the rat Dunning prostate tumor system R3327 to radiation and/or local tumor hyperthermia. Radiat. Res., *150:* 423-430, 1998.
13. Isaacs, J. T., Isaac, W. B., Feitz, W. F. J., and Scheres, J. Establishment and characterization of 7 Dunning prostate cancer cell lines and their use in developing methods for predicting metastatic ability of prostate cancer. Prostate, *9:* 261-281, 1986.
14. Tennant, T. R., Kim, H., Sokoloff, M., and Rinker-Schaeffer, C. W. The Dunning model. Prostate, *43:* 295-302, 2000.
15. Bedikian, A. Y., Legha, S. S., Eton, O., Buzaid, A. C., Papadopoulos, N., Coates, S., Simmons, T., Neefe, J., and von Roemeling, R. Phase II trial of tirapazamine combined with cisplatin in chemotherapy of advanced malignant melanoma. Annal. Oncol., *8:* 363-367, 1997.
16. Rischin, D., Peters, L., Fisher, R., Macann, A., Denham, J., Poulsen, M., Jackson, M., Kenny, L., Penniment, M., Corry, J., Lamb, D., and B., M. Tirapazamine, Cisplatin, and Radiation versus Fluorouracil, Cisplatin, and Radiation in patients with locally advanced head and neck cancer: a randomized phase II trial of the Trans-Tasman Radiation Oncology Group (TROG 98.02). *J Clin Oncol, 23:* 79-87, 2005.
17. Lara, P. N. J., Frankel, P., Mack, P. C., Gumerlock, P. H., Galvin, I., Martel, C. L., Longmate, J., Doroshow, J. H., Lenz, H. J., Lau, D. H., and Gandara, D. R. Tirapazamine plus carboplatin and paclitaxel in advanced malignant solid tumors: a california cancer consortium phase I and molecular correlative study. *Clin Cancer Res, 9:* 4356-4362, 2003.
18. Wu, T. T., Sikes, R. A., Cui, Q., Thalmann, G. N., Kao, C., Murphy, C. F., Yang, H., Zhau, H. E., Balian, G., and Chung , L. W. K. Establishing human prostate cancer cell xenografts in bone: induction

of osteoblastic reaction by prostate-specific antigen-producing tumors in athymic and scid/bg mice using LNCaP and lineage-derived metastatic sublines. *Int. J. Cancer:*, *77:* 887-894, 1998.
19. Zhao, D., Jiang, L., and Mason, R. P. Measuring Changes in Tumor Oxygenation. *Methods Enzymol*, *386:* 378-418, 2004.

APPENDICES:

[Frontiers in Bioscience 13, 1371-1384, January 1, 2008]

Physical principles of quantitative nuclear magnetic resonance oximetry

Vikram D. Kodibagkar[1], Xianghui Wang[1] , Ralph P. Mason[1]

[1]Cancer Imaging Program, Department of Radiology, UT Southwestern, Dallas TX

TABLE OF CONTENTS

1. *Abstract*
2. *Introduction*
    - *2.1. Tissue oxygenation and hypoxia*
    - *2.2. Measurement of tissue oxygenation*
    - *2.3. Magnetic Resonance in Bioscience*
3. *NMR and MRI oximetry*
    - *3.1. Dependence of spin lattice relaxation rate of reporter molecules on pO_2*
    - *3.2. Diamagnetic contributions to R_1*
    - *3.3. Paramagnetic contribution of oxygen*
    - *3.4. Measuring pO_2*
    - *3.5. New development: ^{1}H MRI based oximetry using hexamethyldisiloxane*
4. *Perspective and Conclusion*
5. *Acknowledgements*
6. *References*

1. ABSTRACT

Over the years many techniques have been devised for the measurement of tissue oxygenation (oximetry). Oximetry using polarographic needle electrodes has long been considered a gold standard. Nuclear Magnetic Resonance (NMR) based oximetry uses exogenously administered reporter molecules such as perfluorocarbons to quantitatively interrogate oxygen tension (pO_2). This technique has been successfully used *in vivo* in the preclinical setting and shows promise for clinical applications. NMR pO_2 reporter molecules display a linear dependence of the spin lattice relaxation rate on pO_2, which forms the basis of this technique. Physical principles of spin lattice relaxation of pO_2 reporter molecules and the pO_2 dependence of relaxation rate are discussed in this review. Practical considerations for choice of reporter molecules for *in vivo* measurements, general methodology and new developments are also described.

2. INTRODUCTION

2.1. Tissue oxygenation and hypoxia

Oxygen is essential for tissue health and any reduction in its supply can lead to rapid cellular dysfunction and cell death. It is also an important variable in the treatment of many medical conditions including tumors, peripheral vascular disease, and stroke. In solid tumors, oxygen delivery is impaired by structural abnormalities present in the tumor vasculature such as chaotic vessel architecture. In addition, the altered tumor cell metabolism with elevated metabolic rates contributes to the occurrence of low tissue oxygenation (hypoxia). Hypoxia can adversely affect the efficacy of radiation therapy, chemotherapy, and photodynamic therapy (1). These therapies rely on creation of reactive oxygen species, which can kill cancer cells by damaging DNA and sub cellular organelles (2). Reactive oxygen species are also formed as a natural byproduct of normal metabolism of

oxygen and have important roles in cell signaling (3). Production of reactive oxygen species from molecular oxygen by macrophages and neutrophils probably plays a key role in cell-mediated immunity and microbiocidal activity (4). Measurements of pO_2 in tumors have been found to have prognostic value and the probability of disease-free survival is significantly lower for patients with hypoxic tumors (5-8). Given the importance of oxygen, the ability to measure tissue oxygen tension non-invasively may have a significant impact in understanding mechanisms of tissue function and in clinical prognosis of disease. Quantitative tissue oximetry remains a challenge, especially *in vivo* and this review will consider progress in magnetic resonance approaches and the physical foundations underpinning the method.

2.2. Measurement of tissue oxygenation

Many techniques have been used to assess tissue oxygenation *in vivo*, both qualitative and quantitative as reviewed extensively (1, 9, 10). Direct measurement methods include those using electrodes and fiber-optic probes. These methods have been used for *in vivo* research and also in the clinical setting, but are invasive and may be unsuitable for routine human use. Indirect methods such as those based on Magnetic Resonance (MR) measure parameters that report on local oxygenation status (see section 3).

Measurements of pO_2 using polarographic needle electrodes have long been considered a gold standard (1, 11, 12). Typically, an anode is placed on the skin and polarized with a constant voltage. The polarographic needle electrode (cathode) consists of a gold filament embedded within a flexible stainless steel housing with an oxygen permeable membrane covering the opening. The cathode is inserted into the tissue of interest and electrical current is generated at the tip of the electrode, which is proportional to the tissue oxygen pressure. Polarographic electrodes are calibrated in phosphate buffered normal saline, bubbled with gases with a range of pO_2s. Multiple electrodes may be placed at different locations in tissue in order to measure spatial heterogeneity and one can make dynamic measurements to gauge the response to intervention (13). The invasiveness of this technique can be minimized by use of electrode tips as fine as a few microns (14), but these are fragile and are susceptible to stray electromagnetic fields. The Eppendorf Histograph is an improved version of this technique that can make multiple successive measurements along tracks in tissue using a stepwise motion of the needle electrode under computer control (15). It has been successfully used in the clinical setting and revealed hypoxia in many tumor types that are externally accessible (6-8, 12, 16-19). The drawbacks of polarographic electrodes are that measurements can be affected by changes in pH, salinity, and ionic strength. Electrodes also consume oxygen, and thus, may bias readings especially under hypoxic conditions (such as found in tumors) and over long measurement periods.

Another quantitative method for measuring the partial pressure of dissolved or gaseous oxygen utilizes fiber-optic oxygen sensors based on fluorescence. Typically, an optical fiber carries excitation light to the fluorophore coating at the probe tip. Fluorescence generated at the tip is returned by the optical fiber to a spectrometer. When oxygen in the gas or liquid sample diffuses into the fluorophore coating, it quenches the fluorescence. Commercial instruments exploit various parameters such as fluorescence lifetime (OxyLite™) or relative fluorescence intensity (FOXY™), which are correlated with pO_2, and hence, a calibration curve can be used to measure pO_2 *in vivo*. The fluorophores used in commercial systems may be platinum based (OxyLite™) or ruthenium based (FOXY™). This method does not consume oxygen during measurement, but the fluorophore coating may wear off after several measurements and needs to be re-applied to the fiber. Weak detected fluorescence intensity is a clear sign that fluorophore coating needs to be re-applied. Probes can be coated with oxygen permeable coatings to further protect the fluorophore. This usually slows the response time of measurement. Several recent applications have been reported (20-31). Fiber optic probes are more fragile than the Eppendorf Histograph.

Qualitative methods have been used to non-invasively identify tumor regions that are hypoxic based on selective accumulation of specially designed reporter molecules in such regions (32). Following intravenous infusion, these reporter molecules are trapped in tissues in the absence of oxygen, very much like molecules such as pimonidazole and EF5 that are widely used in histological assessment of hypoxia (33). Many such reporter molecules have been developed for different modalities such as NMR (34-36), positron emission tomography (PET) (37-40) and single photon emission computed tomography (SPECT) (41, 42). The red shift of the fluorescence of green fluorescent protein (GFP) under hypoxic conditions has also been used to image hypoxia by fluorescence imaging (43). Exploiting various biochemical pathways that are under oxygen regulation such as induction of hypoxia-inducible factor 1 (HIF-1) or introduction of transgenes with hypoxic response elements (HREs) coupled to reporter genes has enabled the visualization of hypoxia by optical imaging (44-47).

2.3. Magnetic Resonance in Bioscience

In biomedicine, the abundant hydrogen nuclei from tissue water can be utilized to obtain high-resolution anatomical images using Magnetic Resonance Imaging (MRI) to probe living systems non-invasively. Of all medical imaging modalities, MRI provides the best combination of spatial and temporal resolution to yield superb anatomical detail and functional information. It has become an invaluable clinical tool for diagnosis of many diseases. Using tricks of nuclear spin physics it is possible to obtain information beyond structural anatomy. Routinely, one can study diverse aspects of physiology, such as vasculature and blood flow (48-50), cellularity and apparent diffusion (51-54), vascular and tissue oxygenation (9, 55-59) as well as tissue perfusion and endothelial permeability (60, 61). The development of contrast agents and reporter molecules has pushed the limits of detection and established MRI as a tool for molecular imaging (62-64). Assessment of key metabolites such as lactate, choline

and N-acetyl aspartate (NAA) by proton NMR has enabled the assessment of metabolic changes at onset of disease (65-71).

Magnetic Resonance (MR) based techniques to measure oxygenation may be divided into quantitative and qualitative methods. Qualitative MR techniques, such as BOLD (Blood Oxygen Level Dependant) contrast use blood oxygenation status as a surrogate marker for tissue oxygenation. BOLD can provide high spatial and temporal resolution and can assess dynamic changes in vascular oxygenation using endogenous deoxyhemoglobin, and is the basis for functional MRI. For large blood vessels where imaging voxels are wholly within a vessel quantitative oximetry has been reported (55, 72, 73). However, since BOLD contrast (changes in T_2*) depends on the amount of deoxyhemoglobin it is influenced by hematocrit, vascular volume, pH and flow. While signal changes are sensitive to changes in vascular oxygenation, the relationship with tissue pO_2 is neither straightforward nor direct in tissues (58). Quantitative MR oximetry techniques have been developed based on reporter molecules for nuclear magnetic resonance (NMR) (9, 74-76) and electron paramagnetic resonance (EPR) (10, 77-81). EPR is a technique that is very similar to NMR in that they both result from the Zeeman interaction of a spin with an external magnetic field. Unlike NMR where nuclei like protons with non-zero nuclear spin give rise to the signal, EPR relies on unpaired electrons. EPR oximetry, much like NMR oximetry, relies on the indirect methods that exploit the paramagnetic properties of molecular oxygen. Paramagnetic oxygen not only relaxes nuclear spins, but also is effective in electronic T_1 and T_2 relaxation of other paramagnetic species or radicals. The EPR linewidth of the radical is broadened and the change in the relaxation rate is often proportional to the concentration of oxygen over a wide range of oxygen tensions. Similar to NMR oximetry, *in vivo* EPR oximetry also requires prior intravenous or intramuscular infusion of free radicals, or direct implantation of particulate spin probes into the tissue of interest. This technique has been reviewed extensively elsewhere (81, 82). The method can offer exceptional sensitivity at very low pO_2 values. A primary shortcoming is the lack of widespread EPR instrumentation for small animal investigations, l*et al*one clinical studies.

Although extensive reviews exist on NMR oximetry (9, 76), they have generally focused on applications. Here, we focus on the underlying physical principles. NMR based oximetry uses exogenously administered reporter molecules to interrogate oxygen tension (pO_2). Such exogenous agents, which can quantitatively report tissue oxygenation, have been successfully used *in vivo* in the preclinical setting. NMR pO_2 reporter molecules are often perfluorocarbons, which display a linear dependence of the ^{19}F spin lattice relaxation rate R_1 (=$1/T_1$) on pO_2. We will also describe an analogous ^1H NMR approach using a recently identified ^1H pO_2 reporter molecule hexamethyldisiloxane (83).

3. NMR AND MRI OXIMETRY

3.1. Dependence of spin lattice relaxation rate of reporter molecules on pO_2

Molecular oxygen is paramagnetic and therefore tends to shorten nuclear spin-lattice relaxation times, T_1 and T_2, in solution or *in vivo*. Most of the NMR oximetry applications utilize the linear dependence of the ^{19}F longitudinal (spin-lattice) relaxation rate (R_1=$1/T_1$) of fluorine nuclei of perfluorocarbons (PFC) on the partial pressure of oxygen (9, 84, 85). PFCs exhibit specific characteristics that are critical for *in vivo* oximetry: high oxygen solubility and hydrophobicity. Hydrophobicity ensures the exchange of gases between the PFC and surrounding tissue, while preventing the exchange of aqueous ions, which could perturb R_1. The linear dependence of PFC R_1 on pO_2 can be understood as follows. One can visualize two types of PFC molecules in the PFC pool, those with and without oxygen in their vicinity. If those free of oxygen have a **diamagnetic** longitudinal relaxation rate of R_{1d}, the ones with oxygen in their immediate vicinity have a longitudinal relaxation rate of $R_{1d} + R_{1p}$, where R_{1p} is the **paramagnetic** contribution of oxygen. Since the oxygen molecules rapidly diffuse in the solvent, the observed relaxation rate for each type of fluorine atom is a molar weighted average:

$$R_1 = (1-x)\, R_{1d} + x\,(R_{1d} + R_{1p}) = R_{1d} + x*R_{1p} \quad (1)$$

where x is the mole fraction of oxygen. Since PFCs behave as essentially ideal liquids, the solubility of oxygen in the PFCs obeys Henry's law,

$$pO_2 = k*x \quad (2)$$

where k is a constant that reflects solubility of oxygen in the PFC. It is therefore different for different PFCs. Combining eqs. 1 and 2

$$R_1 = R_{1d} + pO_2*R_{1p}/k \quad (3)$$

Thus, the plot of R_1 vs. pO_2 at a given temperature should be linear, with an intercept of R_{1d} and a slope of R_{1p}/k. R_{1d} is the anoxic relaxation rate, *i.e*., the relaxation rate in absence of oxygen, and R_{1p} is the relaxation rate due to the paramagnetic contribution of oxygen dissolved in the solution or tissue.

3.2. Diamagnetic contributions to R_1

The diamagnetic contribution R_{1d} to the total relaxation rate of PFCs generally results from a combination of ^{19}F-^{19}F dipole-dipole (DD) interactions and ^{19}F chemical-shift anisotropy (CSA) at high magnetic fields. When molecular motions are in the extreme narrowing region the DD contribution to R_{1d} (R_{1DD}) is independent of the magnetic-field strength (86), but the CSA contribution to R_{1d} (R_{1CSA}) varies directly as the square of the magnetic-field strength (87). Thus, at relatively low magnetic fields, the CSA contribution to relaxation is negligible, while at high

magnetic fields it is comparable to the contribution of DD interactions. In general, we can treat DD and CSA interactions as independent and additive contributions to R_{1d}, but they can be correlated in some cases. DD and CSA interactions within a CF_2 or CF_3 group can interfere with each other because they both are fixed to the same physical structure and this correlation can cause the relaxation curve to be multi exponential by introducing a slow relaxing component (88-90) in some cases. Generally such effects on R_{1d} are negligible. Any inter-molecular DD contribution can be assimilated into the intramolecular DD contribution and represented by an effective ^{19}F-^{19}F distance r_{FF}. An exact expression for the DD and CSA relaxation times depends on the structure and the molecular dynamics of the functional group under consideration (*i.e.*, CF_3, CF_2, or CF) and can be quite complicated. Some knowledge of the molecular dynamics may allow assumptions to compute an exact expression, which can then be compared with experimental observations. For example, internal rotation of the CF_2 groups in a linear chain PFC may be sterically hindered and considered to be fixed motionless in a rigid sphere that undergoes isotropic rotational diffusion. For the terminal CF_3 group, reorientation results from the same isotropic rotational diffusion of the rigid sphere and random internal 120° jumps about the three-fold symmetry axis fixed in the sphere. It is reasonable to assume that the principle component of the chemical shift tensor lies along the C-F bond and one can use chemical-shielding anisotropy ($\Delta\sigma$) and asymmetry (η_σ) values from literature. Such internal motion will lead to extra terms and the angular dependence in the equations for the CF_3 group compared to the CF_2 group. Shukla *et al.* (91) calculated the DD and CSA relaxation rates for the CF_2 and CF_3 groups of perfluorotributylamine (PFTB) and compared theory with experimental measurements of R_{1a} (= R_{1DD} + R_{1CSA}). For the CF_2 group,

$$R_{1DD} = \frac{(N-1)3\gamma^4\hbar^2}{10{r_{FF}}^6}\left[j_1(\omega_0) + 4j_2(2\omega_0)\right] \quad (4)$$

$$R_{1CSA} = \frac{2(\gamma B_0 \Delta\sigma)^2}{15}\left(1 + \frac{{\eta_\sigma}^2}{3}\right) j_1(\omega_0) \quad (5)$$

while for the CF_3 groups,

$$R_{1DD} = \frac{(N-1)3\gamma^4\hbar^2}{10{r_{FF}}^6} \times \left\{ \left[\frac{1}{4}(3\cos^2\Delta_{DD} - 1)^2 \right] \left[j_1(\omega_0) + 4j_2(2\omega_0) \right] + \left[1 - \frac{1}{4}(3\cos^2\Delta_{DD} - 1)^2 \right] \left[j_{1j}(\omega_0) + 4j_{2j}(2\omega_0) \right] \right\} \quad (6)$$

$$R_{1CSA} = \frac{2(\gamma B_0 \Delta\sigma)^2}{15}\left(1 + \frac{\eta_\sigma^2}{3}\right) \left\{ \left[\frac{1}{4}(3\cos^2\Delta_{CSA} - 1)^2 \right] j_1(\omega_0) + \left[1 - \frac{1}{4}(3\cos^2\Delta_{CSA} - 1)^2 \right] j_{1j}(\omega_0) \right\} \quad (7)$$

where N is the number of ^{19}F nuclei in the group (2 for CF_2 and 3 for CF_3), γ is the gyromagnetic ratio of ^{19}F, B_0 is the spectrometer magnetic-field strength and ω_0 is the corresponding ^{19}F Larmor frequency (= γB_0). Δ_{DD} is the angle between the F-F vector and the internal rotation axis and Δ_{CSA} is the angle between the principle axis of the chemical-shift tensor and the internal rotation axis. The spectral density functions $j_n(n\omega_0)$ and $j_{nj}(n\omega_0)$ are related to the correlation times of isotropic rotational diffusion of the molecule (τ_c) and internal rotation of the CF_3 group around the symmetry axis (τ_{ci}), respectively, by

$$j_n(n\omega_0) = \frac{\tau_c}{1 + (n\omega_0\tau_c)^2} \quad (8)$$

$$j_{nj}(n\omega_0) = \frac{\tau_{cj}}{1 + (n\omega_0\tau_{cj})^2} \quad (9)$$

where

$$1/\tau_{ci} = 1/\tau_c + 1/\tau_{ci} \quad (10)$$

Assuming that all bond angles for the CF_3 groups are tetrahedral (Δ_{DD}=90°, Δ_{CSA}= 71°),
eqns. 6 and 7 reduce to

$$R_{1DD} = \frac{3\gamma^4\hbar^2}{5{r_{FF}}^6} \times \left\{ 0.25\left[j_1(\omega_0) + 4j_2(2\omega_0) \right] + 0.75\left[j_{1j}(\omega_0) + 4j_{2j}(2\omega_0) \right] \right. \quad (11)$$

$$R_{1CSA} = \frac{2(\gamma B_0 \Delta\sigma)^2}{15}\left(1 + \frac{\eta_\sigma^2}{3}\right) \left\{ 0.11 j_1(\omega_0) + 0.89 j_{1j}(\omega_0) \right\} \quad (12)$$

In the motional narrowing limit $j_n(n\omega_0) \rightarrow \tau_c$ and $j_{nj}(n\omega_0) \rightarrow \tau_{ci}$, and further simplification of the above equations is possible. The relative contributions of DD and CSA to R_{1d} can vary with temperature and magnetic field. In the case of perfluorotributylamine (PFTB), R_{1CSA} was found to be greater than R_{1DD} for CF_2 groups at high fields, while R_{1DD} dominates over R_{1CSA} for the CF_3 group (91). Internal molecular rotation of the CF_3 group results in a greater fractional decrease in R_{1CSA} compared to the fractional decrease in R_{1DD}. From eqns. 4, 5, 11 and 12, in the limit where internal rotation is extremely fast (*i.e.*, τ_{ci}, $\tau_{ci} \rightarrow 0$), $R_{1DD}(CF_3) = R_{1DD}(CF_2)/2$ and $R_{1CSA}(CF_3) = R_{1CSA}(CF_2)/9$.

The anoxic contribution to the relaxation rate, R_{1d}, represents the lower limit of R_1 with respect to pO_2 reporter molecules. Accurate determination is essential for calibration, as it represents "0 torr". In the case of a molecule like hexafluorobenzene (HFB), the expression for R_{1DD} will be similar to eqn. 4. However, three different F-F distances must be taken into account. Each F nucleus has two ortho (r_{FF} ~2.91Å), two meta (r_{FF} ~5.04 Å) and one para (r_{FF} ~5.82 Å) F neighbors and the total R_{1DD} will be a sum of these three components. Due to the strong $1/{r_{FF}}^6$ dependence, the para and the meta contributions may be small (1/27 and 1/128 of the ortho

contribution, respectively, accounting for the distances and number of atoms), but this has not been verified. Compared to CF_3 (r_{FF} ~2.41Å) and CF_2 (r_{FF} ~2.38Å) groups the closest FF distance in HFB is larger, and hence, one might expect R_{1DD} to be smaller. Indeed, the anoxic relaxation rate of HFB (~0.08 s^{-1}) is smaller than those of the α-CF_2 (~1.35 s^{-1}) and CF_3 (~0.88 s^{-1}) resonances in PFTB (91, 92). Of course, the differences in R_{1d} for different perfluorocarbons cannot be accounted for by considering the F-F distances only; molecular dynamics and CSA contributions play a major role as well.

3.3. Paramagnetic contribution of oxygen

The presence of dissolved oxygen affects the chemical shift as well as the relaxation rates of the PFC molecules in their vicinity. The measured paramagnetic chemical shift, $\Delta\sigma_P$, in presence of oxygen results from a Fermi contact interaction between molecular oxygen and PFC nuclei and is given by (86, 93)

$$\Delta\sigma_P = \frac{Axn_M hS(S+1)\gamma^2 g_e{}^2 \beta_e{}^2}{g_N{}^2 \beta_N{}^2 kT} \quad (13)$$

where A is the hyperfine constant, x is the mole fraction of oxygen, n_M is the number of PFC molecules surrounding an oxygen molecule, h and k are Planck and Boltzmann constants, γ is the nuclear gyromagnetic ratio, $g_e\beta_e$ and $g_N\beta_N$ are the electron and nuclear magnetic moments, *S* is the total electron spin of the paramagnetic species (S = 1 for O_2), and T is the absolute temperature. Using eqns. 2 and 13 one could try to measure pO_2 from the chemical shift using a predetermined calibration curve. However, $\Delta\sigma_P$ is usually small and is superimposed upon chemical shifts induced by changes in bulk magnetic susceptibility due to the presence of oxygen. Separating the two effects would require the ability to apply B_0 perpendicular, as well as parallel to the sample(93). For *in vivo* imaging, shimming could also affect the measurement of $\Delta\sigma_P$ and this method has not been used to measure pO_2.

The presence of any dissolved oxygen results in a paramagnetic contribution, R_{1p}, which is given by (93, 94)

$$R_{1p} = \frac{2S(S+1)\gamma^2 g^2 \beta^2}{15r^6}\left[\frac{3\tau_c}{1+\omega_I{}^2\tau_c{}^2} + \frac{7\tau_c}{1+\omega_S{}^2\tau_c{}^2}\right] \quad (14)$$

where r is the distance between the paramagnetic center and the nucleus concerned, ω_S is the angular frequency of electron resonance, and ω_I is the angular frequency of nuclear resonance. Here, we ignore the contribution due to contact interaction as oxygen does not form a complex with the PFCs, and hence the hyperfine interaction would be very small. The correlation time for the reorientation of the coupled magnetic moment vectors, τ_c, is given by

$$1/\tau_c = 1/\tau_s + 1/\tau_r + 1/\tau_e \quad (15)$$

where τ_s is the electron spin relaxation time, τ_r, is the rotational correlation time, and τ_e, is the residence time of the paramagnetic species. In the motional narrowing limit, $\omega_S\tau_c << 1$ and $\omega_S\tau_c << 1$ so eqn. 11 simplifies to

$$R_{1p} = \frac{8\gamma^2 g^2 \beta^2 \tau_c}{3r^6} \quad (16) \text{ for S=1.}$$

R_{1p} determines the sensitivity of the PFC spin lattice relaxation rate to the presence of oxygen. PFCs with multiple ^{19}F atoms (with unique chemical shifts) generally exhibit a different R_1 response of each resonance to pO_2 (*i.e.*, different slopes on an R_1 vs. pO_2 graph). These differences are a result of the inverse dependence of R_{1p} on r^6 and imply that oxygen has a preferred approach to each PFC molecule. If the average distances between the oxygen molecule and various fluorine atoms in a PFC are different, R_{1p} would be larger for the fluorine nuclei that are closer to the oxygen molecule. Effective spin diffusion within the molecule can lead to the reduction of differences in the slopes. The preferences of the approach of oxygen to different parts of the PFCs are most likely due to steric factors rather than specific binding as formation of complexes or preferential binding would manifest itself as a very high R_1 of a particular fluorine atom compared to its neighbors. The oxygen molecule may prefer to approach the ends of the PFCs simply because there is more space available at the ends than in the bridgehead positions or the middle of a chain. This is clearly seen by comparing the slopes of different fluorine atoms of the cis and trans isomers of perfluorodecalin (PFD) (94). In the case of trans-perfluorodecalin, the larger difference in oxygen access to the end chain fluorine atoms compared to bridgehead fluorine atoms leads to a larger variability in the slopes compared to cis-perfluorodecalin. The slope does not vary greatly between terminal CF_3 groups of perfluorotributylamine (PFTB), perfluorotripropylamine (PFTP) and perfluorooctyl bromide (PFOB or perflubron) (91), and thus, relative pO_2 sensitivity of this resonance is determined by R_{1d}, which is different in all three cases. The CF_2 resonances from these PFCs show high sensitivity to temperature within the temperature range 5-50 °C. The terminal trifluoromethyl groups have greater sensitivity to oxygen and lower sensitivity to temperature (compared to CF_2 groups). The CF_3 resonance of PFOB exhibits greater sensitivity to pO_2 than PFTB or PFTP. Internal motion also aids R_{1p}, and hence pO_2 sensitivity. For example, the bulky CF_2Br group of PFOB is less sensitive to pO_2 than the CF_3 group on the other end of the molecule.

In general, each contribution (R_{1d} and R_{1p}) to R_1 is temperature dependent at a given field and exhibits a maximum at a temperature at which the inverse of corresponding correlation time matches the Larmor frequency. The constant k, which represents the oxygen solubility of the PFC, is also temperature dependent. On increasing the temperature, oxygen solubility in the PFC decreases and both R_{1p} and R_{1d} decrease for liquids in the motional narrowing regime ($\omega_0\tau_c << 1$). The temperature dependence of these relaxation rates can reveal information of the molecular dynamics that dominate these relaxation processes. In case of both anoxic and oxic PFTB the R_1 maxima were observed to occur at similar temperatures (91). This implies that in this case the τ_c that

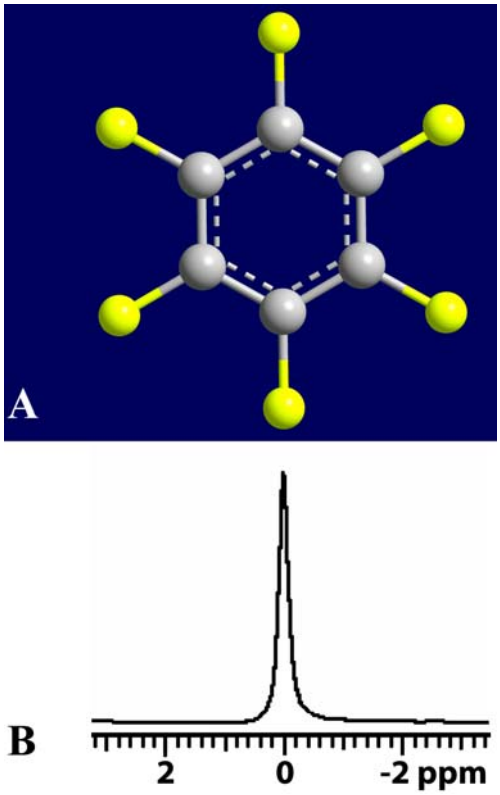

Figure 1. (a) Hexafluorobenzene and (b) its ^{19}F NMR spectrum.

determine R_{1p} and R_{1d} are approximately equal. Therefore, the residence time of an oxygen molecule near a given PFTB molecule may be comparable to the molecular rotational correlation time of PFTB. This represents a strong influence of residence time on R_{1p}, possibly as important as the inter-nuclear fluorine-oxygen distance.

3.4. Measuring pO_2

Although there is no theoretical reason to expect linearity in R_{1d} and R_{1p} with temperature, a linear approximation can be made for R_{1d} and R_{1p}/k from a purely practical standpoint within the biologically relevant temperature range (*e.g.*, 30-42 ^{o}C). If the respective relaxation rate maxima occur in the middle of this range, the slope and intercept may "appear" to be temperature independent). For characterizing the pO_2 and temperature dependence, the neat PFC or emulsion is typically placed in gas-tight NMR glass tubes, saturated by bubbling for 20-30 minutes with a range of standard gases (*e.g.*, 0%, 5%, 10%, 21% and 100 % O_2 -balance N_2) and sealed. Each sealed tube is inserted in a circulating water bath and the T_1 is measured as a function of temperature. The data at each temperature is fit to eqn. 3

$$R_1\,[s^{-1}] = A' + B' * pO_2 \quad (12)$$

where A' (=R_{1d}) and B' (=R_{1p}/k) are constants at a given temperature. If we assume a linear dependence of A' and B' on temperature T, then A'= A+C*T and B'= B+D*T, giving a temperature-dependent model (95):

$$R_1\,[s^{-1}] = A + B * pO_2 + C * T + D * pO_2 * T \quad (13)$$

where A, B, C and D are constants. For PFCs with multiple resonances theses constants are usually different for each resonance, discussed earlier. For such PFCs pO_2 and temperature can be estimated simultaneously by solving two simultaneous equations (corresponding to eqn. 13 for 2 resonances) using the measured values of R_1 for each resonance (95). In graphical terms, in a 3-dimensional variable space (R_1= f(pO_2, T)) the ordinates corresponding to the intersection of R_1 iso-contours of the two resonances are pO_2 and T, respectively. Multi resonance PFC spectra can provide multiple estimates of pO_2, if temperature is known, or pO_2 and temperature by solving simultaneous equations, as needed.

For imaging, multiple resonances could lead to chemical shift artifacts or reduced signal-to-noise following selective excitation or editing (96, 97). In practice, a PFC such as hexafluorobenzene (HFB) with a single resonance (Figure 1 a, b), high pO_2 sensitivity and minimal temperature sensitivity is preferable (75). Perfluoro-15-crown-5-ether (15-C-5) also has quite similar characteristics, and shorter absolute T_1s making data acquisition potentially faster, but a higher R_1 sensitivity to temperature and it is less readily available (9, 74). While a smaller A' value represents greater sensitivity, it also implies that the PFC has longer T_1 values (smaller R_1) under hypoxic conditions, where R_1 may be close to A'. Indeed, the T_1 of HFB at 4.7 T may reach 12 s, limiting the current temporal resolution of pO_2 measurements using HFB to 6 ½ min (98). However, use of echo planar imaging as in the *FREDOM* (Fluorocarbon Relaxometry using Echo planar imaging for Dynamic Oxygen Mapping) approach allows images, and hence, spatially resolved oxygen distributions to be acquired in the same time as spectroscopy (9). Following a direct intra-tissue injection, dynamic changes in oxygenation in response to hyperoxic intervention can be monitored *in vivo* (Figure 2). A further improvement in temporal resolution is possible by using other approaches such as those based on the Look-Locker technique (99, 100). Even then, a complete sampling of the relaxation curve would require at least 1 min (~ 5*T_1 for HFB under hypoxic conditions). The slope B' represents the effect of oxygen and hence a greater slope is desirable for measurement accuracy. A greater slope would result in a wider separation of measured T_1 values especially at low pO_2 values. A high slope could result from higher R_{1p} or a smaller k (higher O_2 solubility). From eqn. 2 we can see that for a given pO_2, a smaller k reflects a larger O_2 mole fraction x.

The solubility of oxygen (and gases in general) in perfluorocarbons and hydrofluorocarbons is three to ten times higher than observed in the parent hydrocarbons or in water (101, 102). It was shown that a model of continuous diffusion of oxygen, that accounts for the T_1 and T_2 relaxation of benzene, fails in the case of HFB, leading to either impossibly short residence times for oxygen or

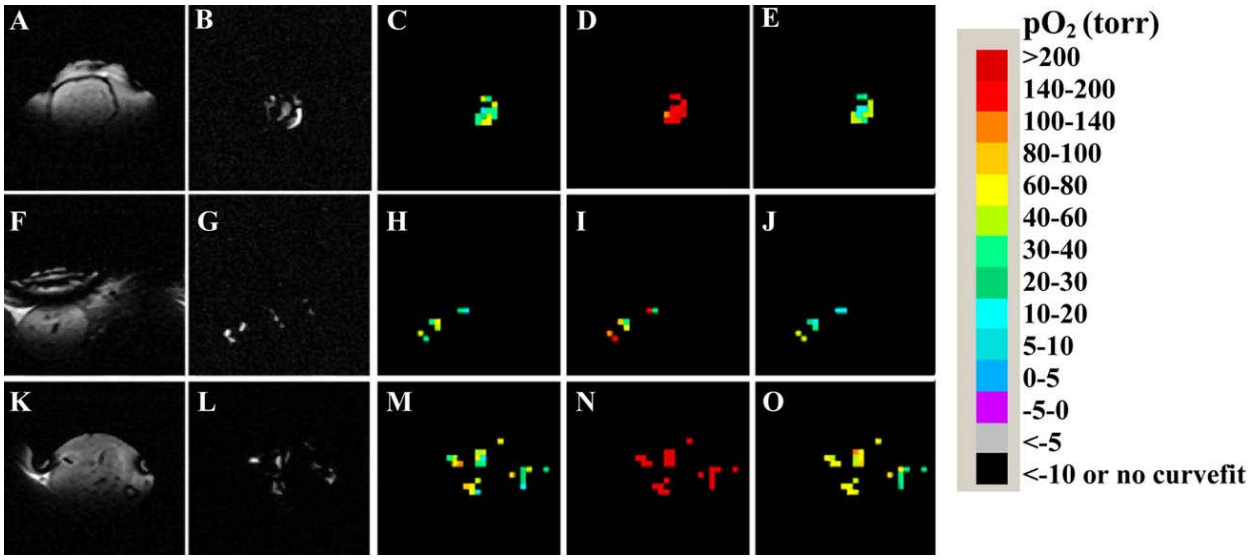

Figure 2. Dynamic ^{19}F MR oximetry. Monitoring changes in oxygenation at locations in the brain (a-e), kidney and liver (f-j) and thigh (k-o) of Sprague Dawley rat with respect to oxygen challenge following direct intra-tissue injection of HFB (50 µl) at discrete locations. Spin-echo anatomical images (a,f,k), spin-echo images of hexafluorobenzene injected into the tissue (b,g,l) and the corresponding time course *FREDOM* pO_2 maps (c,h,m: baseline air breathing, d,i,n: 30 min oxygen and e,j,o: 30 min after return to air breathing) showing the response to hyperoxic gas intervention. Data obtained in collaboration with Dr. Mark Rollins and Dr. Lisa Wilmes of UCSF.

impossibly small distance of closest approach between fluorine and oxygen (93). The presence of the larger fluorine atoms appears to result in the existence of numerous large "vacancies" or "channels" in the liquid "lattice", which the oxygen molecules occupy successively by random jumps. The oxygen solubility of long chained aliphatic fluorocarbons are observed to be higher than that of cyclic or aromatic fluorocarbons (102), which suggests that aliphatic chains form large channels in the liquid state, which accommodate more oxygen molecules unlike planar aromatic structures that may result in tighter "packing" with smaller vacancies. This exceptionally high solubility motivated the use of perfluorocarbons as blood substitutes for oxygen delivery to tissues (103, 104). Fluosol-DA (Green Cross Corp., Osaka, Japan) a perfluorotripropylamine based emulsion was the first PFC emulsion clinically tested and approved for clinical use as perfusate for percutaneous coronary angioplasty, but was later withdrawn from the market because of low oxygen delivery capacity under physiologic conditions, lack of clear clinical benefit and development of flow-through catheters (105-108). More recently, Oxygent^{TM} (Alliance Corp., San Diego, CA), an emulsion of perfluorooctyl bromide (perflubron) with a higher oxygen solubility and improved emulsion stability has been tested in clinical trials (109, 110). In terms of *in vivo* oximetry, due to their high oxygen solubility and hydrophobicity, PFCs essentially act as molecular amplifiers by displaying extra sensitivity to oxygen and insensitivity to variations in ionic constituents compared to the surrounding tissue water.

^{19}F MR based oximetry has several strengths and a few weaknesses. The nuclear spin ½ ^{19}F nucleus has γ of 40.05 MHz/T (compared to 42.58 MHz/T for ^{1}H) and about 83% NMR sensitivity compared to ^{1}H. It is 100 % abundant (isotopically) and the amount of endogenous fluorine in the body is very small (mostly present in form of solid fluorides in bones and teeth). Due to a very short T_2 relaxation time, the NMR signal from endogenous fluorine is undetectable in most biological systems. Given the absence of background signals, the exogenously administered PFC is readily observed. ^{19}F MR oximetry has been used as a research tool for many years (9, 74, 75, 84, 85, 98, 111-136). However, to date the method has not been translated to the routine clinical setting, since most clinical MRI scanners lack a ^{19}F capability. PFCs have been observed in patients following administration as adjuvant to radiotherapy and as residues in the eye, where they are used as tamponades during retinal surgery (127, 137, 138). A ^{1}H pO_2 reporter molecule could have greater immediate applicability and higher potential for clinical translation.

3.5. New development: ^{1}H MRI based oximetry using hexamethyldisiloxane

The ^{1}H R_1 of tissue water has been shown to be sensitive to tissue oxygenation (139), but many other factors like metal ions, cellularity, pH, ionic strength can also affect relaxation of tissue water. This makes quantitative measurements impossible except in tissues such as the vitreous humor in the eye and cerebrospinal fluid, where ionic and protein content is low or known and constant (140-143). Even then, R_1 sensitivity to oxygen is low (B'= 0.0002 s^{-1}/torr) and to temperature is high. We have recently identified hexamethyldisiloxane (HMDSO, Figure 3) as a ^{1}H NMR probe of pO_2 (analogous to PFCs) and shown the feasibility of tissue oximetry using ^{1}H-NMR spectroscopic relaxometry (83). We have also implemented

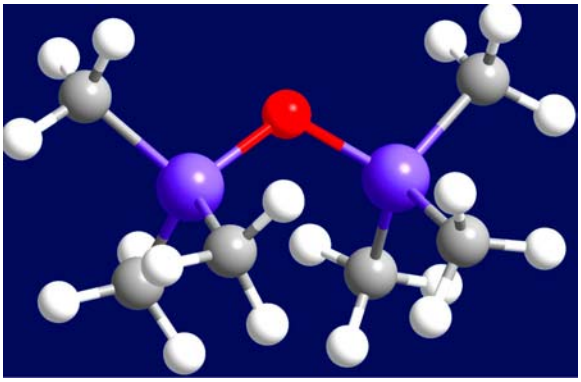

Figure 3. Structure of hexamethyldisiloxane (HMDSO).

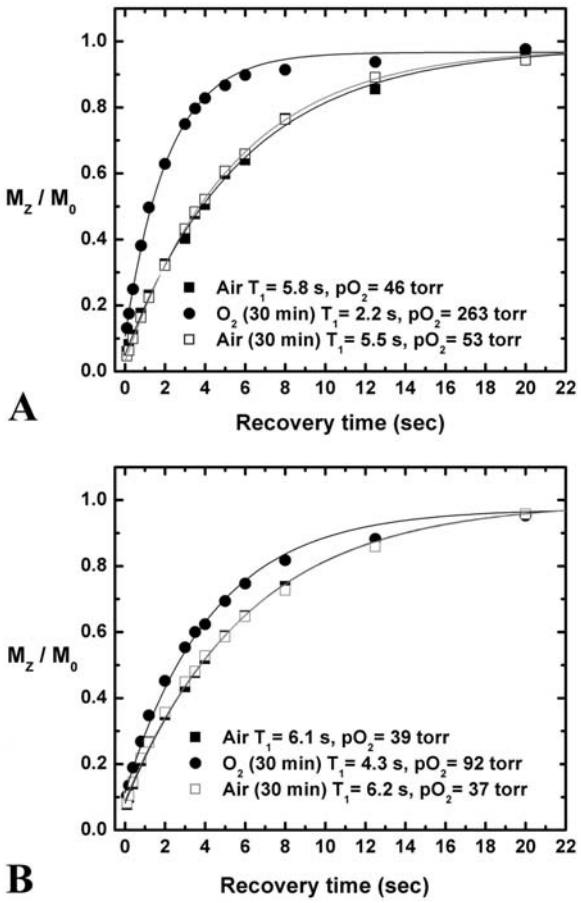

Figure 4. Dynamic ^{1}H oximetry. HMDSO magnetization recovery curves *in vivo* in response to hyperoxic challenge following direct intra-tissue injection of HMDSO (50 µl) at discrete locations. Chemical shift selective spectroscopy with suppression of fat and water signals permitted relaxometry of HMDSO. On switching breathing gas from air (■) to oxygen for 30 min (●) a larger change in T_1 (corresponding to a larger change in pO_2) is observed in thigh muscle **(a)** compared to AT1 prostate tumor **(b)** which is reversed in both cases by switching back to air breathing (□).

an imaging based method: Proton Imaging of Silanes to map Tissue Oxygenation Levels (*PISTOL*) for spatial mapping of pO_2 (144).

HMDSO is a symmetric molecule with a single NMR signal close to that of the chemical shift standard tetramethylsilane (TMS) (83). It is therefore well separated from water and reasonably separated from fat. HMDSO has many characteristics similar to PFCs: it is a highly hydrophobic mobile liquid, non-toxic, with high gas solubility and is readily available and cheap. At a given temperature, R_1 of HMDSO showed a linear dependence on pO_2, with constants A'= 0.1126 ± 0.0010[s^{-1}] and B'= 0.00130 ± 0.00002 [(torr*s)$^{-1}$] at 37 ^{o}C. The T_1 values range from 8.7 s (pO_2= 0 torr) to 1 s (pO_2= 760 torr) at 37 ^{o}C. A small temperature dependence was observed in the temperature range 26-46 ^{o}C. Fitting the calibration data to the temperature–dependant model (eqn. 13) yielded constants A = 0.1479 ± 0.0028 s^{-1}, B = (1.79 ± 0.05) X 10^{-3} (s torr)$^{-1}$, C = (-9.57 ± 0.81) X 10^{-4} (s ^{o}C)$^{-1}$, and D = (-1.23 ± 0.13) X 10^{-5} (s torr ^{o}C)$^{-1}$. In this temperature range, linear approximation resulted in errors < 3%. The pO_2 and temperature sensitivities of HMDSO are similar to 15-C-5.

Using a spectroscopic approach, pO_2 was measured in rat thigh muscle and Dunning prostate R3327 AT1 adenocarcinomas in response to an oxygen challenge (83). Changes in relaxation times in response to hyperoxia and differential response in tumor versus healthy thigh muscle can be easily seen from the HMDSO magnetization recovery curves (Figure 4). Clearance of HMDSO from muscle was seen to be slow with a half-life ~ 35 h, so that minimal change would be observed during typical MR studies of oxygen dynamics in response to acute interventions. HMDSO is quite inert and it has been reported that no treatment-related signs of toxicity or mortality or other statistically significant deleterious effects were noted in studies where Fisher rats were exposed to up to 6000 ppm HMDSO by inhalation (145, 146).

Like PFCs, HMDSO is lipophilic and is essentially immiscible in aqueous solutions. The boiling point and hydrophobicity of HMDSO suggest that it could be emulsified for intravenous delivery, as popular for several PFCs (147) and such an attempt is currently underway. HMDSO is readily and cheaply available from many commercial vendors and easy to store. One key difference in this ^{1}H MR approach compared to ^{19}F oximetry is the need to effectively suppress water and fat signals and perform relaxometry on the silane signal. In PISTOL, we have developed an effective approach using a combination of frequency selective excitation of the silane resonance and CHESS (148) suppression of the water and fat resonances is used followed by EPI detection for measuring T_1 values (144). As with HFB, ARDVARC (*A*lternating *R*elaxation *D*elays with *V*ariable *A*cquisitions for *R*eduction of *C*learance effects) protocol (98) is used in conjunction with this sequence to obtain T_1 values.

4. PERSPECTIVE AND CONCLUSION

An important advantage of MR oximetry compared to hypoxia imaging using nuclear and optical imaging agents is that one can quantitatively measure tissue pO_2 as opposed to qualitatively labeling hypoxic regions. Thus issues such as hypoxia specificity, oxygen dependency of agent binding and clearance of unbound agents do not come into play and affect interpretation. Dynamic measurements with transient interventions such as hyperoxia (9) or acute effects of vascular targeting (149) are not possible with nuclear and optical techniques. Optical imaging methods to image hypoxia to date rely on transfection to express bioluminescent (45, 47) or fluorescent proteins (44, 46) and are thus inappropriate for clinical application. In any case light penetration in tissue would be a problem for human use.

MR oximetry has found extensive use in pre clinical studies because it provides essentially unique insight into tissue oxygenation- specifically spatial and temporal resolution revealing heterogeneity and dynamic response to intervention. Moreover, precision achieved is appropriate for radiobiological studies of tumors. To date ^{19}F NMR approaches have been used to examine vascular oxygenation following i.v. administration of PFC emulsion or tissue oxygenation following vascular clearance and sequestration in tissue. However, accumulation occurs predominantly in tumor periphery biasing measurements towards well-perfused regions. Moreover, there is substantial uptake by the reticuloendothelial system (RES). While this allows effective measurements of pO_2 in liver, spleen and bone marrow, it is less satisfactory for oncological investigations. An alternate approach is direct injection of the reporter molecule into the tissue of interest. The possibility of targeting emulsion to specific antigens such fibrin for cardiovascular imaging opens further possibilities (150).

The development of PISTOL, a quantitative ^1H MR method for dynamic imaging of pO_2 opens further opportunities for *in vivo studies*. This method has a high potential of translation to the clinical setting. With current state-of-the-art MR hardware, it would be easy to generate effective water and fat suppression needed for PISTOL as used in detection of metabolites by Magnetic Resonance Spectroscopy (MRS). In both the research and clinical setting, it will now be possible to add quantitative oximetry to a protocol consisting of other ^1H-MR based functional techniques such as dynamic contrast enhancement, diffusion measurements, and MRS, but the minimal invasiveness of the technique has to be taken into account. Development of targeted nano-emulsions for intravenous delivery might help circumvent the need for direct intra-tissue injections, if high targeting specificity is achieved. Other ^1H pO_2 reporter molecules could be identified or synthesized, which could have higher oxygen sensitivity than HMDSO. We foresee MR oximetry as a valuable tool for assessing tissue oxygenation status in various disease states, helping to evaluate the acute and chronic response of therapeutic interventions and aiding in the screening of new drugs, such as vascular targeting and anti angiogenic agents which can perturb tissue oxygenation.

5. ACKNOWLEDGMENTS

Investigations discussed here have been supported by the Texas Affiliate of the American Heart Association, the Whitaker Foundation, the American Cancer Society, the Department of Defense Breast and Prostate Cancer Initiatives and the National Institute of Health. Most recent funding is from the NCI SAIRP U24 CA126608 and the work in Figure 2 was supported by the Foundation for Anesthesia Education and Research.

6. REFERENCES

1. Tatum, J. L., G. J. Kelloff, R. J. Gillies, J. M. Arbeit, J. M. Brown, K. S. Chao, J. D. Chapman, W. C. Eckelman, A. W. Fyles, A. J. Giaccia, R. P. Hill, C. J. Koch, M. C. Krishna, K. A. Krohn, J. S. Lewis, R. P. Mason, G. Melillo, A. R. Padhani, G. Powis, J. G. Rajendran, R. Reba, S. P. Robinson, G. L. Semenza, H. M. Swartz, P. Vaupel, D. Yang, B. Croft, J. Hoffman, G. Liu, H. Stone & D. Sullivan: Hypoxia: importance in tumor biology, noninvasive measurement by imaging, and value of its measurement in the management of cancer therapy. *Int J Radiat Biol*, 82, 699-757 (2006)

2. Okunieff, P., B. Fenton & Y. Chen: Past, present, and future of oxygen in cancer research. *Adv Exp Med Biol*, 566, 213-22 (2005)

3. Poli, G., G. Leonarduzzi, F. Biasi & E. Chiarpotto: Oxidative stress and cell signalling. *Curr Med Chem*, 11, 1163-82 (2004)

4. Bergamini, C. M., S. Gambetti, A. Dondi & C. Cervellati: Oxygen, reactive oxygen species and tissue damage. *Curr Pharm Des*, 10, 1611-26 (2004)

5. Brizel, D. M., G. S. Sibly, L. R. Prosmitz, R. L. Scher & M. W. Dewhirst: Tumor hypoxia adversely affects the prognosis of carcinoma of the head and neck. *Int. J. Radiat. Oncol. Biol. Phys.*, 38, 285-289 (1997)

6. Rofstad, E. K., K. Sundfor, H. Lyng & C. G. Trope: Hypoxia-induced treatment failure in advanced squamous cell carcinoma of the uterine cervix is primarily due to hypoxia-induced radiation resistance rather than hypoxia-induced metastasis. *Br. J. Cancer*, 83, 354-9 (2000)

7. Fyles, A., M. Milosevic, D. Hedley, M. Pintilie, W. Levin, L. Manchul & R. P. Hill: Tumor hypoxia has independent predictor impact only in patients with node-negative cervix cancer. *J Clin Oncol*, 20, 680-7 (2002)

8. Fyles, A., M. Milosevic, M. Pintilie, A. Syed, W. Levin, L. Manchul & R. P. Hill: Long-term performance of interstial fluid pressure and hypoxia as prognostic factors in cervix cancer. *Radiother Oncol*, 80, 132-7 (2006)

9. Zhao, D., L. Jiang & R. P. Mason: Measuring changes in tumor oxygenation. *Methods Enzymol*, 386, 378-418 (2004)

10. Swartz, H. M. & J. F. Dunn: Measurements of oxygen in tissues: overview and perspectives on methods. In: Oxygen Transport to Tissue XXIV. Eds: J. F. Dunn&H. M. Swartz. Kluwer Academic, New York (2003)

11. Stone, H. B., J. M. Brown, T. Phillips & R. M. Sutherland: Oxygen in human tumors: correlations between

methods of measurement and response to therapy. *Radiat. Res.*, 136, 422-434 (1993)
12. Vaupel, P., K. Schlenger, C. Knoop & M. Hockel: Oxygenation of human tumors: evaluation of tissue oxygen distribution in breast cancers by computerized O_2 tension measurements. *Cancer Res*, 51, 3316-22 (1991)
13. Cater, D. B. & I. A. Silver: Quantitative measurements of oxygen tension in normal tissues and in the tumours of patients before and after radiotherapy. *Acta radiol*, 53, 233-56 (1960)
14. Crawford, D. W. & M. A. Cole: Performance evaluation of recessed microcathodes: criteria for tissue pO_2 measurement. *J Appl Physiol*, 58, 1400-5 (1985)
15. Nozue, M., I. Lee, F. Yuan, B. A. Teicher, D. M. Brizel, M. W. Dewhirst, C. G. Milross, L. Milas, C. W. Song, C. D. Thomas, M. Guichard, S. M. Evans, C. J. Koch, E. M. Lord, R. K. Jain & H. D. Suit: Interlaboratory variation in oxygen tension measurement by Eppendorf "Histograph" and comparison with hypoxic marker. *J Surg Oncol*, 66, 30-8 (1997)
16. Brizel, D. M., S. P. Scully, J. M. Harrelson, L. J. Layfield, J. M. Bean, L. R. Prosnitz & M. W. Dewhirst: Tumor oxygenation predicts for the likelihood of distant metastases in human soft tissue sarcoma. *Cancer Res.*, 56, 941-3 (1996)
17. Movsas, B., J. D. Chapman, E. M. Horwitz, W. H. Pinover, R. E. Greenberg, A. L. Hanlon, R. Iyer & G. E. Hanks: Hypoxic regions exist in human prostate carcinoma. *Urology*, 53, 11-8 (1999)
18. Rudat, V., B. Vanselow, P. Wollensack, C. Bettscheider, S. Osman-Ahmet, M. J. Eble & A. Dietz: Repeatability and prognostic impact of the pretreatment pO_2 histography in patients with advanced head and neck cancer. *Radiother Oncol*, 57, 31-7 (2000)
19. Aquino-Parsons, C., A. Green & A. I. Minchinton: Oxygen tension in primary gynaecological tumours: the influence of carbon dioxide concentration. *Radiother Oncol*, 57, 45-51 (2000)
20. Griffiths, J. R. & S. P. Robinson: The OxyLite: a fibre-optic oxygen sensor. *British Journal of Radiology*, 72, 627-630 (1999)
21. Bussink, J., J. H. A. M. Kaanders, A. M. Strik, B. Vojnovic & A. J. van der Kogel: Optical sensor-based oxygen tension measurements correspond with hypoxia marker binding in three human tumor xenograft lines. *Radiation Research*, 154, 547-555 (2000)
22. Mason, R. P., D. Zhao, A. Constantinescu & A. Obeid: Tumor oximetry: comparison of ^{19}F MR EPI (FREDOM) and the fiber-optic OxyLite™. *Proc Intl Soc Magn Reson Med*, 8, 1040 (2000)
23. Braun, R. D., J. L. Lanzen, S. A. Snyder & M. W. Dewhirst: Comparison of tumor and normal tissue oxygen tension measurements using OxyLite or microelectrodes in rodents. *Am J Physiol Heart Circ Physiol*, 280, H2533-44 (2001)
24. Seddon, B. M., D. J. Honess, B. Vojnovic, G. M. Tozer & P. Workman: Measurement of tumor oxygenation: *in vivo* comparison of a luminescence fiber-optic sensor and a polarographic electrode in the p22 tumor. *Radiat Res*, 155, 837-46 (2001)
25. Jarm, T., G. Sersa & D. Miklavcic: Oxygenation and blood flow in tumors treated with hydralazine: evaluation with a novel luminescence-based fiber-optic sensor. *Technol Health Care*, 10, 363-80 (2002)
26. Urano, M., Y. Chen, J. Humm, J. A. Koutcher, P. Zanzonico & C. Ling: Measurements of tumor tissue oxygen tension using a time-resolved luminescence-based optical oxylite probe: comparison with a paired survival assay. *Radiat Res*, 158, 167-73 (2002)
27. Gu, Y. Q., V. A. Bourke, J. G. Kim, A. Constantinescu, R. P. Mason & H. L. Liu: Dynamic response of breast tumor oxygenation to hyperoxic respiratory challenge monitored with three oxygen-sensitive parameters. *Applied Optics*, 42, 2960-2967 (2003)
28. Brurberg, K. G., H. K. Skogmo, B. A. Graff, D. R. Olsen & E. K. Rofstad: Fluctuations in pO_2 in poorly and well-oxygenated spontaneous canine tumors before and during fractionated radiation therapy. *Radiother Oncol*, 77, 220-6 (2005)
29. Brurberg, K. G., M. Thuen, E. B. Ruud & E. K. Rofstad: Fluctuations in pO_2 in irradiated human melanoma xenografts. *Radiat Res*, 165, 16-25 (2006)
30. Elas, M., K. H. Ahn, A. Parasca, E. D. Barth, D. Lee, C. Haney & H. J. Halpern: Electron paramagnetic resonance oxygen images correlate spatially and quantitatively with Oxylite oxygen measurements. *Clin Cancer Res*, 12, 4209-17 (2006)
31. Wen, B., M. Urano, J. A. O'Donoghue & C. C. Ling: Measurements of partial oxygen pressure pO_2 using the OxyLite system in R3327-AT tumors under isoflurane anesthesia. *Radiat Res*, 166, 512-8 (2006)
32. Ballinger, J. R.: Imaging hypoxia in tumors. *Semin Nucl Med*, 31, 321-9 (2001)
33. Ljungkvist, A. S., J. Bussink, J. H. Kaanders & A. J. van der Kogel: Dynamics of tumor hypoxia measured with bioreductive hypoxic cell markers. *Radiat Res*, 167, 127-45 (2007)
34. Maxwell, R. J., P. Workman & J. R. Griffiths: Demonstration of tumor-selective retention of fluorinated nitroimidazole probes by ^{19}F magnetic resonance spectroscopy *in vivo*. *Int J Radiat Oncol Biol Phys*, 16, 925-9 (1989)
35. Raleigh, J. A., A. J. Franko, D. A. Kelly, L. A. Trimble & P. S. Allen: Development of an *in vivo* ^{19}F magnetic resonance method for measuring oxygen deficiency in tumors. *Magn Reson Med*, 22, 451-66 (1991)
36. Aboagye, E. O., R. J. Maxwell, M. R. Horsman, A. D. Lewis, P. Workman, M. Tracy & J. R. Griffiths: The relationship between tumour oxygenation determined by oxygen electrode measurements and magnetic resonance spectroscopy of the fluorinated 2-nitroimidazole SR-4554. *Br J Cancer*, 77, 65-70 (1998)
37. Jerabek, P. A., T. B. Patrick, M. R. Kilbourn, D. D. Dischino & M. J. Welch: Synthesis and biodistribution of ^{18}F-labeled fluoronitroimidazoles: potential *in vivo* markers of hypoxic tissue. *Int J Rad Appl Instrum [A]*, 37, 599-605 (1986)
38. Rasey, J. S., Z. Grunbaum, S. Magee, N. J. Nelson, P. L. Olive, R. E. Durand & K. A. Krohn: Characterization of radiolabeled fluoromisonidazole as a probe for hypoxic cells. *Radiat Res*, 111, 292-304 (1987)
39. Lewis, J. S., D. W. McCarthy, T. J. McCarthy, Y. Fujibayashi & M. J. Welch: Evaluation of 64Cu-ATSM *in*

vitro and *in vivo* in a hypoxic tumor model. *J Nucl Med*, 40, 177-83 (1999)
40. Dolbier, W. R., Jr., A. R. Li, C. J. Koch, C. Y. Shiue & A. V. Kachur: [18F]-EF5, a marker for PET detection of hypoxia: synthesis of precursor and a new fluorination procedure. *Appl Radiat Isot*, 54, 73-80 (2001)
41. Mannan, R. H., V. V. Somayaji, J. Lee, J. R. Mercer, J. D. Chapman & L. I. Wiebe: Radioiodinated 1- (5-iodo-5-deoxy-beta-D-arabinofuranosyl)-2-nitroimidazole (iodoazomycin arabinoside: IAZA): a novel marker of tissue hypoxia. *J Nucl Med*, 32, 1764-70 (1991)
42. Li, L., J. M. Yu, L. G. Xing, G. R. Yang, X. D. Sun, J. Xu, H. Zhu & J. B. Yue: Hypoxic imaging with 99mTc-HL91 single photon emission computed tomography in advanced nonsmall cell lung cancer. *Chin Med J (Engl)*, 119, 1477-80 (2006)
43. Takahashi, E., T. Takano, Y. Nomura, S. Okano, O. Nakajima & M. Sato: *In vivo* oxygen imaging using green fluorescent protein. *Am J Physiol Cell Physiol*, 291, C781-7 (2006)
44. Vordermark, D., T. Shibata & J. M. Brown: Green fluorescent protein is a suitable reporter of tumor hypoxia despite an oxygen requirement for chromophore formation. *Neoplasia*, 3, 527-34 (2001)
45. Payen, E., M. Bettan, A. Henri, E. Tomkiewitcz, A. Houque, I. Kuzniak, J. Zuber, D. Scherman & Y. Beuzard: Oxygen tension and a pharmacological switch in the regulation of transgene expression for gene therapy. *J Gene Med*, 3, 498-504 (2001)
46. Raman, V., D. Artemov, A. P. Pathak, P. T. Winnard, Jr., S. McNutt, A. Yudina, A. Bogdanov, Jr. & Z. M. Bhujwalla: Characterizing vascular parameters in hypoxic regions: a combined magnetic resonance and optical imaging study of a human prostate cancer model. *Cancer Res*, 66, 9929-36 (2006)
47. Safran, M., W. Y. Kim, F. O'Connell, L. Flippin, V. Gunzler, J. W. Horner, R. A. Depinho & W. G. Kaelin, Jr.: Mouse model for noninvasive imaging of HIF prolyl hydroxylase activity: assessment of an oral agent that stimulates erythropoietin production. *Proc Natl Acad Sci U S A*, 103, 105-10 (2006)
48. Abramovitch, R., D. Frenkiel & M. Neeman: Analysis of subcutaneous angiogenesis by gradient echo magnetic resonance imaging. *Magn. Reson. Med.*, 39, 813-24 (1998)
49. Brasch, R. C., K. C. Li, J. E. Husband, M. T. Keogan, M. Neeman, A. R. Padhani, D. Shames & K. Turetschek: *In vivo* monitoring of tumor angiogenesis with MR imaging. [Review]. *Acad. Radiol.*, 7, 812-23 (2000)
50. Cao, Y., Z. Shen, T. L. Chenevert & J. R. Ewing: Estimate of vascular permeability and cerebral blood volume using Gd-DTPA contrast enhancement and dynamic T2*-weighted MRI. *J Magn Reson Imaging*, 24, 288-96 (2006)
51. Roberts, T. P. & H. A. Rowley: Diffusion weighted magnetic resonance imaging in stroke. *Eur J Radiol*, 45, 185-94 (2003)
52. Sotak, C. H.: Nuclear magnetic resonance (NMR) measurement of the apparent diffusion coefficient (ADC) of tissue water and its relationship to cell volume changes in pathological states. *Neurochem Int*, 45, 569-82 (2004)
53. Sykova, E.: Diffusion properties of the brain in health and disease. *Neurochem Int*, 45, 453-66 (2004)
54. Charles-Edwards, E. M. & N. M. deSouza: Diffusion-weighted magnetic resonance imaging and its application to cancer. *Cancer Imaging*, 6, 135-43 (2006)
55. Foltz, W. D., N. Merchant, E. Downar, J. A. Stainsby & G. A. Wright: Coronary venous oximetry using MRI. *Magnetic Resonance in Medicine*, 42, 837-48 (1999)
56. Neeman, M., H. Dafni, O. Bukhari, R. D. Braun & M. W. Dewhirst: *In vivo* BOLD contrast MRI mapping of subcutaneous vascular function and maturation: validation by intravital microscopy. *Magn. Reson. Med.*, 45, 887-98 (2001)
57. Howe, F. A., S. P. Robinson, D. J. McIntyre, M. Stubbs & J. R. Griffiths: Issues in flow and oxygenation dependent contrast (FLOOD) imaging of tumours. *NMR in Biomed.*, 14, 497-506 (2001)
58. Baudelet, C. & B. Gallez: How does blood oxygen level-dependent (BOLD) contrast correlate with oxygen partial pressure (pO_2) inside tumors? *Magn. Reson. Med.*, 48, 980-986 (2002)
59. Baudelet, C. & B. Gallez: Current issues in the utility of blood oxygen level dependent MRI for the assessment of modulations in tumor oxygenation *Curr Med Imaging Rev.*, 1, 229-243 (2005)
60. Bhujwalla, Z. M., D. Artemov, E. Aboagye, E. Ackerstaff, R. J. Gillies, K. Natarajan & M. Solaiyappan: The physiological environment in cancer vascularization, invasion and metastasis. *Novartis Found Symp*, 240, 23-38; discussion 38-45, 152-3 (2001)
61. Gillies, R. J., Z. M. Bhujwalla, J. Evelhoch, M. Garwood, M. Neeman, S. P. Robinson, C. H. Sotak & B. Van Der Sanden: Applications of magnetic resonance in model systems: tumor biology and physiology. *Neoplasia*, 2, 139-51 (2000)
62. Yu, J. X., V. Kodibagkar, W. Cui & R. P. Mason: ^{19}F: a versatile reporter for non-invasive physiology and pharmacology using magnetic resonance. *Curr. Med. Chem.*, 12, 818-848 (2005)
63. Evans, S. M., S. Hahn, D. R. Pook, W. T. Jenkins, A. A. Chalian, P. Zhang, C. Stevens, R. Weber, G. Weinstein, I. Benjamin, N. Mirza, M. Morgan, S. Rubin, W. G. McKenna, E. M. Lord & C. J. Koch: Detection of hypoxia in human squamous cell carcinoma by EF5 binding. *Cancer Res*, 60, 2018-24 (2000)
64. Aime, S., C. Cabella, S. Colombatto, S. Geninatti Crich, E. Gianolio & F. Maggioni: Insights into the use of paramagnetic Gd (III) complexes in MR-molecular imaging investigations. *JMRI*, 16, 394-406 (2002)
65. Kurhanewicz, J., D. B. Vigneron, R. G. Males, M. G. Swanson, K. K. Yu & H. Hricak: The prostate: MR imaging and spectroscopy. Present and future. [Review]. *Radiol. Clin. North Amer.*, 38, 115-38 (2000)
66. Minati, L., M. Grisoli & M. G. Bruzzone: MR spectroscopy, functional MRI, and diffusion-tensor imaging in the aging brain: a conceptual review. *J Geriatr Psychiatry Neurol*, 20, 3-21 (2007)
67. Cecil, K. M.: MR spectroscopy of metabolic disorders. *Neuroimaging Clin N Am*, 16, 87-116, viii (2006)
68. Horn, M.: Cardiac magnetic resonance spectroscopy: a window for studying physiology. *Methods Mol Med*, 124, 225-48 (2006)
69. Shah, N., A. Sattar, M. Benanti, S. Hollander & L. Cheuck: Magnetic resonance spectroscopy as an imaging

tool for cancer: a review of the literature. *J Am Osteopath Assoc*, 106, 23-7 (2006)
70. De Stefano, N. & M. Filippi: MR spectroscopy in multiple sclerosis. *J Neuroimaging*, 17 Suppl 1, 31S-35S (2007)
71. Martin, W. R.: MR Spectroscopy in Neurodegenerative Disease. *Mol Imaging Biol* (2007)
72. Li, K. C. P., G. A. Wright, L. R. Pelc, R. L. Dalamn, J. H. Brittain, H. Wegmueller, J. T. Lin & C. K. Song: Oxygen saturation of blood in the superior mesenteric vein. *Radiology*, 194, 321-325 (1995)
73. Wright, G. A., B. S. Hu & A. Macovski: Estimating oxygen saturation of blood *in vivo* with MR imaging at 1.5 T. *JMRI*, 1, 275-283 (1991)
74. Dardzinski, B. J. & C. H. Sotak: Rapid tissue oxygen tension mapping using ^{19}F inversion-recovery echo-planar imaging of perfluoro-15-crown-5-ether. *Magn Reson Med*, 32, 88-97 (1994)
75. Mason, R. P., W. Rodbumrung & P. P. Antich: Hexafluorobenzene: a sensitive ^{19}F NMR indicator of tumor oxygenation. *NMR Biomed.*, 9, 125-134 (1996)
76. Mason, R. P.: Non-invasive physiology: ^{19}F NMR of perfluorocarbons. *Artif Cells Blood Substit Immobil Biotechnol*, 22, 1141-53 (1994)
77. Glockner, J. F. & H. M. Swartz: *In vivo* EPR oximetry using two novel probes: fusinite and lithium phthalocyanine. *Adv Exp Med Biol*, 317, 229-34 (1992)
78. Swartz, H. M., K. J. Liu, F. Goda & T. Walczak: India ink: a potential clinically applicable EPR oximetry probe. *Magn. Reson. Med.*, 31, 229-232 (1994)
79. Zweier, J. L. & P. Kuppusamy: Electron paramagnetic resonance measurements of free radicals in the intact beating heart: A technique for detection and characterization of free radicals in whole biological tissues. *Proc. Natl. Acad. Sci. (USA)*, 85, 5703-5707 (1988)
80. Matsumoto, A., S. Matsumoto, A. L. Sowers, J. W. Koscielniak, N. J. Trigg, P. Kuppusamy, J. B. Mitchell, S. Subramanian, M. C. Krishna & K. Matsumoto: Absolute oxygen tension (pO_2) in murine fatty and muscle tissue as determined by EPR. *Magn Reson Med*, 54, 1530-5 (2005)
81. Gallez, B., C. Baudelet & B. F. Jordan: Assessment of tumor oxygenation by electron paramagnetic resonance: principles and applications. *NMR Biomed*, 17, 240-62 (2004)
82. Gallez, B. & H. M. Swartz: *In vivo* EPR: when, how and why? *NMR Biomed*, 17, 223-5 (2004)
83. Kodibagkar, V. D., W. Cui, M. E. Merritt & R. P. Mason: Novel 1H NMR approach to quantitative tissue oximetry using hexamethyldisiloxane. *Magn Reson Med*, 55, 743-8 (2006)
84. Thomas, S. R.: The biomedical applications of Fluorine-19 NMR. In: Magnetic Resonance Imaging. Eds: C. L. Partain, R. R. Price, J. A. Patton, M. V. Kulkarni&A. E. J. James. W.B. Saunders Co., London (1988)
85. Mason, R. P.: Non-invasive physiology: ^{19}F NMR of perfluorocarbon. *Art. Cells, Blood Sub. & Immob. Biotech.*, 22, 1141-1153 (1994)
86. Abragam, A.: The Principles of Nuclear Magnetism. Oxford University Press, New York (1961)
87. McConnell, H. M. & C. H. Holm: Anisotropic chemical shielding and nuclear magnetic relaxation in liquids. *J. Chem. Phys.*, 25, 1289 (1956)
88. Blicharski, J. S.: Interference effect in nuclear magnetic relaxation. *Phys. Lett. A*, 24, 608 (1967)
89. Farrar, T. C. & J. D. Decatur: Temperature-Dependent NMR Relaxation Studies of Na_2PHO_3 in Solution. *J Phys Chem*, 94, 7395-7401 (1990)
90. Matson, G. B.: Methyl NMR relaxation: the effects of spin rotation and chemical shift anisotropy mechanisms. *J. Chem. Phys.*, 67, 5152 (1977)
91. Shukla, H. P., R. P. Mason, D. E. Woessner & P. P. Antich: A comparison of three commercial perfluorocarbon emulsions as high field NMR probes of oxygen tension and temperature. *J. Magn. Reson. Series B*, 106, 131-141 (1995)
92. Hunjan, S., R. P. Mason, A. Constantinescu, P. Peschke, E. W. Hahn & P. P. Antich: Regional tumor oximetry: ^{19}F NMR spectroscopy of hexafluorobenzene. *Int J Radiat Oncol Biol Phys*, 41, 161-71 (1998)
93. Delpuech, J. J., M. A. Hamza, G. Serratrice & M. J. Stebe: Fluorocarbons as Oxygen Carriers .1. Nmr-Study of Oxygen Solutions in Hexafluorobenzene. *J Chem Phys*, 70, 2680-2687 (1979)
94. Parhami, P. & B. M. Fung: F-19 Relaxation Study of Perfluoro Chemicals as Oxygen Carriers. *J Phys Chem*, 87, 1928-1931 (1983)
95. Mason, R. P., H. Shukla & P. P. Antich: *In vivo* oxygen tension and temperature: simultaneous determination using ^{19}F NMR spectroscopy of perfluorocarbon. *Magn Reson Med*, 29, 296-302 (1993)
96. Mason, R. P., P. P. Antich, E. E. Babcock, J. L. Gerberich & R. L. Nunnally: Perfluorocarbon imaging *in vivo*: A ^{19}F MRI study in tumor-bearing mice. *Magn. Reson. Imaging*, 7, 475-485 (1989)
97. Babcock, E. E., R. P. Mason & P. P. Antich: Effect of homonuclear J modulation on ^{19}F spin-echo images. *Magn. Reson. Med.*, 17, 178-188 (1991)
98. Hunjan, S., D. Zhao, A. Constantinescu, E. W. Hahn, P. P. Antich & R. P. Mason: Tumor oximetry: demonstration of an enhanced dynamic mapping procedure using fluorine-19 echo planar magnetic resonance imaging in the Dunning prostate R3327-AT1 rat tumor. *Int J Radiat Oncol Biol Phys*, 49, 1097-108 (2001)
99. Look, D. C. & D. R. Locker: Time saving in measurement of NMR and EPR relaxation times. *Rev. Sci. Instrum.*, 41, 250 (1970)
100. Caruthers, S. D., P. J. Gaffney, F. D. Hockett, R. Lamerichs, G. M. Lanza, A. M. Neubauer, M. J. Scott, S. A. Wickline & P. M. Winter: 19F MR techniques augment quantitative molecular imaging with paramagnetic perfluorocarbon nanoparticles at 1.5 T. *Proc Intl Soc Magn Reson Med*, 14, 1834 (2006)
101. Hamza, M. A., G. Serratrice, M. J. Stebe & J. J. Delpuech: Fluorocarbons as Oxygen Carriers .2. An Nmr-Study of Partially or Totally Fluorinated Alkanes and Alkenes. *J Magn Reson*, 42, 227-241 (1981)
102. Hamza, M. A., G. Serratrice, M. J. Stebe & J. J. Delpuech: Solute-Solvent Interactions in Perfluorocarbon Solutions of Oxygen - an Nmr-Study. *JACS*, 103, 3733-3738 (1981)
103. Kim, H. W. & A. G. Greenburg: Artificial oxygen carriers as red blood cell substitutes: a selected review and current status. *Artif Organs*, 28, 813-28 (2004)

104. Riess, J. G.: Perfluorocarbon-based oxygen delivery. *Artif Cells Blood Substit Immobil Biotechnol*, 34, 567-80 (2006)
105. Tremper, K. K., G. M. Vercellotti & D. E. Hammerschmidt: Hemodynamic Profile of Adverse Clinical Reactions to Fluosol-Da 20-Percent. *Critical Care Medicine*, 12, 428-431 (1984)
106. Gould, S. A., A. L. Rosen, L. R. Sehgal, H. L. Sehgal, L. A. Langdale, L. M. Krause, C. L. Rice, W. H. Chamberlin & G. S. Moss: Fluosol-Da as a Red-Cell Substitute in Acute Anemia. *New England Journal of Medicine*, 314, 1653-1656 (1986)
107. Bell, M. R., R. A. Nishimura, D. R. Holmes, K. R. Bailey, R. S. Schwartz & R. E. Vlietstra: Does Intracoronary Infusion of Fluosol-Da 20-Percent Prevent Left-Ventricular Diastolic Dysfunction During Coronary Balloon Angioplasty. *J Am Coll Cardiol*, 16, 959-966 (1990)
108. Kent, K. M., M. W. Cleman, M. J. Cowley, M. B. Forman, C. C. Jaffe, M. Kaplan, S. B. King, M. W. Krucoff, T. Lassar, B. McAuley, R. Smith, C. Wisdom & D. Wohlgelernter: Reduction of Myocardial-Ischemia During Percutaneous Transluminal Coronary Angioplasty with Oxygenated Fluosol. *Am J Cardiol*, 66, 279-284 (1990)
109. Spahn, D. R., K. F. Waschke, T. Standl, J. Motsch, L. Van Huynegem, M. Welte, H. Gombotz, P. Coriat, L. Verkh, S. Faithfull & P. Keipert: Use of perflubron emulsion to decrease allogeneic blood transfusion in high-blood-loss non-cardiac surgery: results of a European phase 3 study. *Anesthesiology*, 97, 1338-49 (2002)
110. Hill, S. E., B. J. Leone, N. S. Faithfull, K. E. Flaim, P. E. Keipert & M. F. Newman: Perflubron emulsion (AF0144) augments harvesting of autologous blood: a phase II study in cardiac surgery. *J Cardiothorac Vasc Anesth*, 16, 555-60 (2002)
111. Thomas, S. R., R. W. Millard, R. G. Pratt, Y. Shiferaw & R. C. Samaratunga: Quantitative pO_2 imaging *in vivo* with perfluorocarbon F-19 NMR: tracking oxygen from the airway through the blood to organ tissues. *Art Cells, Blood Subst. Immob. Biotechnol.*, 22, 1029-1042 (1994)
112. Thomas, S. R., R. G. Pratt, R. W. Millard, R. C. Samaratunga, Y. Shiferaw, L. C. Clark Jr. & R. E. Hoffmann: Evaluation of the Influence of the Aqueous Phase Bioconstituent Environment on the F-19 T1 of Perfluorocarbon Blood Substitute Emulsions. *JMRI*, 4, 631-635 (1994)
113. Thomas, S. R., R. G. Pratt, R. W. Millard, R. C. Samaratunga, Y. Shiferaw, A. J. McGoron & K. K. Tan: *In vivo* pO_2 imaging in the porcine model with perfluorocarbon F-19 NMR at low field. *Magn. Reson. Imaging*, 14, 103-114 (1996)
114. Zhao, D., A. Constantinescu, C.-H. Chang, E. W. Hahn & R. P. Mason: Correlation of Tumor Oxygen Dynamics with Radiation Response of the Dunning Prostate R3327-HI Tumor. *Radiat. Res.*, 159, 621-631 (2003)
115. Zhao, D., A. Constantinescu, L. Jiang, E. W. Hahn & R. P. Mason: Prognostic Radiology: quantitative assessment of tumor oxygen dynamics by MRI. *Am. J. Clin. Oncol*, 24, 462-466 (2001)
116. Zhao, D., S. Ran, A. Constantinescu, E. W. Hahn & R. P. Mason: Tumor oxygen dynamics: correlation of *in vivo* MRI with histological findings. *Neoplasia*, 5, 308-18 (2003)
117. Mason, R. P., P. P. Antich, E. E. Babcock, A. Constantinescu, P. Peschke & E. W. Hahn: Non-invasive determination of tumor oxygen tension and local variation with growth. *Int. J. Radiat. Oncol. Biol. Phys.*, 29, 95-103 (1994)
118. Mason, R. P., F. M. H. Jeffrey, C. R. Malloy, E. E. Babcock & P. P. Antich: A noninvasive assessment of myocardial oxygen tension: ^{19}F NMR spectroscopy of sequestered perfluorocarbon emulsion. *Magn. Reson. Med.*, 27, 310-317 (1992)
119. Mason, R. P., H. P. Shukla & P. P. Antich: Oxygent: a novel probe of tissue oxygen tension. *Biomater. Artif. Cells Immob. Biotechnol.*, 20, 929-935 (1992)
120. Hunjan, S., R. P. Mason, A. Constantinescu, P. Peschke, E. W. Hahn & P. P. Antich: Regional tumor oximetry: ^{19}F NMR spectroscopy of hexafluorobenzene. *Int. J. Radiat. Oncol. Biol. Phys.*, 40, 161-71 (1998)
121. Song, Y., A. Constantinescu & R. P. Mason: Dynamic Breast tumor oximetry: the development of Prognostic Radiology. *Technol. Cancer Res. Treat.*, 1, 471-478 (2002)
122. Xia, M., V. Kodibagkar, H. Liu & R. P. Mason: Tumour oxygen dynamics measured simultaneously by near infrared spectroscopy and ^{19}F magnetic resonance imaging in rats. *Phys. Med. Biol.*, 51, 45-60 (2006)
123. Barker, B. R., R. P. Mason, N. Bansal & R. M. Peshock: Oxygen tension mapping by ^{19}F echo planar NMR imaging of sequestered perfluorocarbon. *JMRI*, 4, 595-602 (1994)
124. Sotak, C. H., P. S. Hees, H.-H. Huang, M.-H. Hung, C. G. Krespan & S. Reynolds: A new perfluorocarbon for use in fluorine-19 magnetic resonance spectroscopy. *Magn. Reson. Med.*, 29, 188-195 (1993)
125. Sotak, C. H., P. S. Hees, H. N. Huang, M. H. Hung, C. G. Krespan & S. Raynolds: A new perfluorocarbon for use in fluorine-19 MRI and MRS. *Magn. Reson. Med*, 29, 188-95 (1993)
126. Berkowitz, B. A., C. A. Wilson, D. L. Hatchell & R. E. London: Quantitative determination of the partial oxygen pressure in the vitrectomized rabbit eye *in vivo* using ^{19}F NMR. *Magn Reson Med*, 21, 233-41 (1991)
127. Wilson, C., B. Berkowitz, B. McCuen & C. Charles: Measurement of preretinal pO2 in the vitrectomized human eye using ^{19}F NMR. *Arch. Ophthalmol*, 110, 1098-100 (1992)
128. Noth, U., S. P. Morrissey, R. Deichmann, H. Adolf, C. Schwarzbauer, J. Lutz & A. Haase: *In vivo* measurement of partial oxygen pressure in large vessels and in the reticuloendothelial system using fast ^{19}F-MRI. *Magn Reson Med*, 34, 738-45 (1995)
129. Noth, U., P. Grohn, A. Jork, U. Zimmermann, A. Haase & J. Lutz: ^{19}F-MRI *in vivo* determination of the partial oxygen pressure in perfluorocarbon-loaded alginate capsules implanted into the peritoneal cavity and different tissues. *Magn Reson Med*, 42, 1039-47 (1999)
130. Mattrey, R. F., D. J. Schumacher, H. T. Tran, Q. Guo & R. B. Buxton: The use of Imagent BP in diagnostic imaging research and ^{19}F magnetic resonance for PO2

measurements. *Biomaterials, Artificial Cells, & Immobilization Biotechnology.*, 20, 917-20 (1992)
131. McIntyre, D. J. O., C. L. McCoy & J. R. Griffiths: Tumour oxygenation measurements by ^{19}F MRI of perfluorocarbons. *Curr. Sci.*, *76*, 753-762 (1999)
132. Bellemann, M. E., J. Bruckner, P. Peschke, G. Brix & R. P. Mason: [Quantification and visualization of oxygen partial pressure *in vivo* by 19F NMR imaging of perfluorocarbons]. *Biomed Tech (Berl)*, 47 Suppl 1 Pt 1, 451-4 (2002)
133. Lutz, J., U. Noth, S. P. Morrissey, H. Adolf, R. Deichmann & A. Haase: Measurement of oxygen tensions in the abdominal cavity and in the skeletal muscle using ^{19}F-MRI of neat PFC droplets. *Adv Exp Med Biol*, 428, 569-72 (1997)
134. Zimmermann, U., U. Noth, P. Grohn, A. Jork, K. Ulrichs, J. Lutz & A. Haase: Non-invasive evaluation of the location, the functional integrity and the oxygen supply of implants: 19F nuclear magnetic resonance imaging of perfluorocarbon-loaded Ba2+-alginate beads. *Artif Cells Blood Substit Immobil Biotechnol*, 28, 129-46 (2000)
135. Lutz, J., U. Noth, S. P. Morrissey, H. Adolf, R. Deichmann & A. Haase: *In vivo* measurement of oxygen pressure using ^{19}F-NMR imaging. *Adv Exp Med Biol*, 388, 53-7 (1996)
136. Jager, L. J., U. Noth, A. Haase & J. Lutz: Half-life of perfluorooctylbromide in inner organs determined by fast ^{19}F-NMR imaging. *Adv Exp Med Biol*, 361, 129-34 (1994)
137. Nunnally, R., P. Antich, P. Nguyen, E. Babcock, G. McDonald & R. Mason: Fluosol adjuvant therapy in human cancer: examinations *in vivo* of perfluorocarbons by F-19 NM. *Proc. SMRM 7th Meeting San Francisco*342 (1988)
138. Gewiese, B., W. Noske, A. Schilling, D. Stiller, K. Wolf & M. Foerster: Human eye: visualization of perfluorodecalin with F-19 MR imaging. *Radiology*, 185, 131-3 (1992)
139. Tadamura, E., H. Hatabu, W. Li, P. V. Prasad & R. R. Edelman: Effect of oxygen inhalation on relaxation times in various tissues. *J Magn Reson Imaging*, 7, 220-5 (1997)
140. Berkowitz, B. A., Y. Ito, T. S. Kern, C. McDonald & R. Hawkins: Correction of early subnormal superior hemiretinal DeltaPO (2) predicts therapeutic efficacy in experimental diabetic retinopathy. *Invest Ophthalmol Vis Sci*, 42, 2964-9 (2001)
141. Berkowitz, B. A., C. McDonald, Y. Ito, P. S. Tofts, Z. Latif & J. Gross: Measuring the human retinal oxygenation response to a hyperoxic challenge using MRI: eliminating blinking artifacts and demonstrating proof of concept. *Magn Reson Med*, 46, 412-6 (2001)
142. Zaharchuk, G., A. J. Martin, G. Rosenthal, G. T. Manley & W. P. Dillon: Measurement of cerebrospinal fluid oxygen partial pressure in humans using MRI. *Magnetic Resonance in Medicine*, 54, 113-121 (2005)
143. Zaharchuk, G., R. F. Busse, G. Rosenthal, G. T. Manley, O. A. Glenn & W. P. Dillon: Noninvasive oxygen partial pressure measurement of human body fluids *in vivo* using magnetic resonance imaging. *Academic Radiology*, 13, 1016-1024 (2006)
144. Kodibagkar, V. D. & R. P. Mason: Proton Imaging of Silanes to map Tissue Oxygenation Levels (PISTOL): a new tool for quantitative tissue oximetry. *Proc Intl Soc Magn Reson Med*, 14, 928 (2006)
145. Cassidy, S. L., A. Dotti, G. B. Kolesar, L. W. Dochterman, R. G. Meeks & H. J. Chevalier: Hexamethyldisiloxane: A 13-week subchronic whole-body vapor inhalation toxicity study in Fischer 344 rats. *Int J Toxicol*, 20, 391-9 (2001)
146. Dobrev, I. D., M. B. Reddy, K. P. Plotzke, S. Varaprath, D. A. McNett, J. Durham & M. E. Andersen: Closed-chamber inhalation pharmacokinetic studies with hexamethyldisiloxane in the rat. *Inhal Toxicol*, 15, 589-617 (2003)
147. Riess, J. G.: Overview of progress in the fluorocarbon approach to *in vivo* oxygen delivery. *Biomater Artif Cells Immobilization Biotechnol*, 20, 183-202 (1992)
148. Haase, A., J. Frahm, W. Hanicke & D. Matthaei: ^{1}H NMR chemical shift selective (CHESS) imaging. *Phys Med Biol*, 30, 341-4 (1985)
149. Zhao, D., L. Jiang, E. W. Hahn & R. P. Mason: Tumor physiologic response to combretastatin A4 phosphate assessed by MRI. *Int J Radiat Oncol Biol Phys*, 62, 872-80 (2005)
150. Wickline, S. A., A. M. Neubauer, P. M. Winter, S. D. Caruthers & G. M. Lanza: Molecular imaging and therapy of atherosclerosis with targeted nanoparticles. *J Magn Reson Imaging*, 25, 667-80 (2007)

Key Words: Oximetry, hypoxia, perfluorocarbons, MRI, ^{19}F, hexamethyldisiloxane, Review

Send correspondence to: Vikram Kodibagkar, Ph.D., Assistant Professor of Radiology, UT Southwestern Medical Center at Dallas, 5323 Harry Hines Blvd., Dallas, TX 75390-9058, Tel: 214-648-7612, Fax: 214-648-4538, E-mail: vikram.kodibagkar@utsouthwestern.edu

http://www.bioscience.org/current/vol13.htm

Vascular imaging of solid tumors in rats with a radioactive arsenic-labeled antibody that binds exposed phosphatidylserine

Marc Jennewein[1,2], Matthew A. Lewis[2,3], Dawen Zhao[2], Edward Tsyganov[2], Nikolai Slavine[2], Jin He[3,5], Linda Watkins[3,5], Vikram D. Kodibagkar[2], Sean O'Kelly[6], Padmakar Kulkarni[2], Peter P. Antich[2], Alex Hermanne[4], Frank Rösch[1], Ralph P. Mason[2,3] and Philip E. Thorpe[3,5]

[1]Institute of Nuclear Chemistry, Johannes Gutenberg-University of Mainz, Fritz-Strassmann-Weg 2, 55128 Mainz, Germany

[2]Cancer Imaging Program, Department of Radiology, University of Texas Southwestern Medical Center at Dallas, Dallas, Texas, USA

[3]Simmons Cancer Center, University of Texas Southwestern Medical Center at Dallas, Dallas, Texas, USA

[4]VUB Cyclotron, University of Brussels, Laarbeeklaan 103, 1090 Brussels, Belgium

[5]Department of Pharmacology and Hamon Cancer Center, University of Texas Southwestern Medical Center at Dallas, Dallas, Texas, USA

[6]Department of Nuclear Engineering, University of Texas at Austin, Pickle Research Campus, Austin, Texas, USA

Running title: Vascular imaging with arsenic-labeled antibody

Key words: tumor microcirculation and microenvironment, new targets, phosphatidylserine, radioactive arsenic, PET

This work was conducted with the support of a grant from the Gillson Longenbaugh Foundation, an NCI SPORE grant in lung cancer research (CA70907), a sponsored research agreement with Peregrine Pharmaceuticals Inc (Tustin, CA), the Boehringer Ingelheim Fonds for Basic Research in Biomedicine, the Deutsche Forschungsgemeinschaft (DFG-Grant Ro 985/17), the NoE 'European Molecular Imaging Laboratories: EMIL', DOD Prostate IDEA awards PC050766 (W81XWH-06-1-0149) and PC050301 (W81XWH-06-1-0050), the NCI Pre-ICMIC P20 CA086334 and SAIRP U24 CA126608. MRI was performed at the AIRC an NIH BTRP Facility P41-RR02584.

Address correspondence to: Philip E. Thorpe, Department of Pharmacology and Simmons and Hamon Cancer Centers, University of Texas Southwestern Medical Center at Dallas, 2201 Inwood Road NC7.304, Dallas, Texas 75390-8794, USA. Phone: (214) 648-1499; Fax: (214) 648-1613; E-mail: Philip.Thorpe@utsouthwestern.edu

Abbreviations: (FBS) fetal bovine serum; (MRI) magnetic resonance imaging; (nca) no-carrier-added; (PBS) phosphate buffered saline; (PET) positron emission tomography; (PS) phosphatidylserine; (ROI) region of interest; (T½) half life.

ABSTRACT

Purpose: We recently reported that anionic phospholipids, principally phosphatidylserine, become exposed on the external surface of vascular endothelial cells in tumors, probably in response to oxidative stresses present in the tumor microenvironment. In the present study, we tested the hypothesis that a chimeric monoclonal antibody that binds phosphatidylserine could be labeled with radioactive arsenic isotopes and used for molecular imaging of solid tumors in rats. **Experimental Design:** Bavituximab was labeled with ^{74}As (β+, T½ 17.8d) or ^{77}As (β-, T½ 1.6d) using a novel procedure. The radionuclides of arsenic were selected because their long half-lives are consistent with the long biological half lives of antibodies *in vivo* and because their chemistry permits stable attachment to antibodies. The radiolabeled antibodies were tested for the ability to image subcutaneous Dunning prostate R3227–AT1 tumors in rats. **Results:** Clear images of the tumors were obtained using planar γ-scintigraphy and positron emission tomography (PET). Biodistribution studies confirmed the specific localization of bavituximab to the tumors. The tumor to liver ratio 72 h after injection was 22 for bavituximab as compared with 1.5 for an isotype-matched control chimeric antibody of irrelevant specificity. Immunohistochemical studies showed that the bavituximab was labeling the tumor vascular endothelium. **Conclusions:** These results demonstrate that radioarsenic labeled bavituximab has potential as a new tool for imaging the vasculature of solid tumors.

INTRODUCTION

Imaging offers non-invasive perspective on tumor development and therapy, providing information on receptor expression, targeting, and drug pharmacokinetics. Imaging technologies include PET, SPECT, MRI, ultrasound and optical imaging, as reviewed extensively elsewhere (1, 2). Nuclear medicine approaches are particularly relevant, since extremely low concentrations of tracer/reporter are permissible. Several radionuclides are in clinical use and many more are under development (3-5). However, many isotopes decay rapidly limiting shelf life and preventing investigation of long term biological phenomena. A particular problem arises with antibodies, which usually have a long biological half life and not reach optimal target to background selectivity for several days. For PET, common radionuclides such as ^{64}Cu (18% β^+ positron branching, T½ 12.7 h) or ^{86}Y (32% β^+, T½ 17.8 h) have too short half-lives for following antibody localization, while ^{124}I (24% β^+, T½ 4.18 d) has a suitable T½, but undergoes metabolic dehalogenation and release of iodine.

Arsenic radioisotopes include long lived positron emitters having favorable characteristics for PET: ^{71}As (T½ 64 h, 30% β^+, 104 keV average kinetic energy of the positrons), ^{72}As (T½ 26 h, 88% β^+, 1024 keV) and ^{74}As (T½ 17.8 d, 29% β^+, 128 keV). Other arsenic isotopes are high energy β^- emitters that could potentially be used for tumor therapy: ^{77}As (T½ 38.8 h, $\bar{E}_{\beta^-}$ 226 keV) and ^{76}As (T½ 26.3 h, $\bar{E}_{\beta^-}$ 1068 keV). The decay characteristics of the arsenic isotopes that are most relevant for imaging or therapy are presented as supplementary information in the Table. ^{74}As was used in some of the earliest radionuclide imaging studies for the development of PET, at that time called positrocephalography (6). However, inefficient isotope production, difficulty in isolating pure nuclides, and lack of effective derivatization processes handicapped

the exploitation of arsenic isotopes. Radiochemistry has now evolved and several isolation procedures for arsenic isotopes have been reported. Most recently, Jennewein and Rösch developed efficient methods for isolating pure radionuclides from irradiated GeO_2 targets on the basis of a solid phase extraction system (7, 8). Moreover, Jennewein and Rösch proposed chemistry for the effective labeling of biologically relevant molecules, as we have now exploited.

Bavituximab, a chimeric antibody targeting exposed vascular phosphatidylserine (PS), was chosen to develop the labeling procedure and demonstrate the first *in vivo* use of arsenic isotopes for PET imaging of solid tumors. Bavituximab binds to PS by stabilizing a complex of two β2-glycoprotein I molecules attached to PS on the cell surface (9-12). PS is normally tightly segregated to the internal surface of the plasma membrane in most cell types, including the vascular endothelium (10, 11, 13, 14). PS asymmetry is maintained by an ATP-dependent aminophospholipid translocase (a Mg^{2+}-ATPase) that catalyzes the transport of aminophospholipids from the external to the internal leaflet of the plasma membrane (15). Loss of PS asymmetry occurs during apoptosis (16), necrosis (17), cell activation (18) and transformation (19), resulting in the exposure of PS on the external surface of the cells. PS exposure occurs when the aminophospholipid translocase becomes inhibited (20) or when transporters such as scramblase (21) and the floppases (22) become activated by Ca^{2+} fluxes into the cytosol (23, 24).

We previously demonstrated that anionic phospholipids become exposed on the vascular endothelium of blood vessels in mice bearing various types of solid tumors probably in response to oxidizing stresses in the tumor (10, 11). There was no detectable exposure on vascular endothelium in normal tissues including the ovary, a site of physiological angiogenesis, and the

pancreas, a site of high vascular permeability. PS is one of the most specific markers of tumor vasculature yet discovered. The murine version of bavituximab, 3G4, retards tumor growth in multiple rodent models, by stimulating host cells to bind to, and destroy tumor blood vessels. Bavituximab is currently in Phase I clinical trials in patients with various solid tumors[†]. Despite its proven ability to target tumor endothelium, bavituximab has not yet been explored as an imaging agent. The vascular location of PS ensures ready access by radiolabeled antibody in the blood. Imaging techniques could not only enable the detection of tumors and their metastases, but also verify the presence of antigen before bavituximab therapy.

In the present study, we tested the hypothesis that bavituximab can be labeled with radioactive arsenic isotopes and used for vascular targeting and molecular imaging of solid tumors in rats. Doses of bavituximab were used that are ten-fold below the doses that have significant vascular damaging activity (14) in order to prevent occlusion of tumor vasculature from impeding effective imaging. Clear tumor imaging was obtained by planar γ-scintigraphy and PET.

MATERIALS AND METHODS

Antibodies. Bavituximab was provided by Peregrine Pharmaceuticals Inc. (Tustin, CA). Bavituximab is a chimeric antibody composed of the Fv regions of the mouse antibody 3G4 (14) and the constant regions of human IgG1. Bavituximab binds to PS through a cofactor protein, β2-glycoprotein I. Bavituximab recognizes rat β2-glycoprotein I as strongly as it does human β2-glycoprotein I, avoiding the need for supplementation with exogenous human β2-glycoprotein I

[†] Peregrine Pharmaceuticals Inc. See: http://www.clinicaltrials.gov/ct/show/nct00129337

which is necessary in the mouse (14). Bavituximab binds to human β2-glycoprotein I with an affinity of 1.7 x 10^{-8}M (monovalent interaction) and an avidity of approximately 10^{-10}M (divalent interaction) in Biacore experiments.

Hamster anti-mouse CD31 monoclonal antibody was from BD Pharmingen (San Diego, CA). Secondary antibodies were from Jackson Immunoresearch Labs (West Grove, PA). Rituximab (Monoclonal antibody Thera®, CD20) was purchased from Roche.

Isotopes. ^{74}As for PET imaging was produced by ^{nat}Ge(p,x)^{74}As reaction [E_p= 20 MeV, 3 h irradiation at 15 μA] giving a yield of about 370 MBq. ^{77}As for scintigraphy was produced in a no-carrier-added (nca) state via the ^{76}Ge(n,γ)^{77}Ge, T½ 11.30 h → β^- → ^{77}As processes in a TRIGA reactor ($\Phi = 4.0 \cdot 10^{13}$ n/cm^2·s).

Radiochemical separations. Nuclear reactions were typically performed on 100 mg of $^{nat}GeO_2$ (99.9999 % grade, PURA TREM, Strem Chemicals Inc.). Irradiated germanium oxide targets were dissolved in 5 ml HF_{conc}. and extracted, as described in detail previously (7) providing nca [*As]AsI_3 fixed to the solid phase of the extraction cartridge (Varian BOND ELUT ENV solid phase extraction cartridges with a sorbent mass of 50 mg and a volume of 1 ml). Excess $HF_{conc.}$ was removed with a high pressure nitrogen-flow over the cartridge for 5 min. When required for labeling, nca [*As]AsI_3 was eluted with 500 μl ethanol and concentrated to 50 μl under a gentle N_2-flow. The radioarsenic separation yield and efficacy of nca [*As]AsI_3 was >90%.

Antibody conjugation and testing. Antibodies were SATA-modified according to the protocol of Pierce Endogen (25). Deprotection of the sulfhydryl groups of the monoclonal antibody derivative using hydroxylamine was performed directly before the labeling. The number of free thiol groups per antibody molecule was measured using Ellman's reagent and by comparison with cysteine based standards. Thiolated antibody (100 µg) in PBS (3 ml, pH = 7.5) was combined with the nca [*As]AsI_3 solution at 37°C for 30 min. [*As]AsI_3 couples to one SH functionality with elimination of HI, as illustrated in Fig. 1. Quality control of the antibody labeling was performed by HPLC, using an Agilent 1100 Series HPLC system, with an LDC/Milton Roy UV-Monitor III at 254 nm and a 'Gabi' NaI-radiation Monitor from Raytest. The HPLC column was a Bio-Silect Sec 250-5, 300x7.8 mm and PBS + 0.01 M NaN_3 was used as solvent at a flow of 0.8 ml/min. Retention time of the *As[SATA] labeled antibodies was 11.5±0.5 min. To keep the thiols from forming disulfide bridges, all solutions were kept out of contact with air and contained 1 mM EDTA.

***In vitro* stability.** The radioarsenic-labeled bavituximab was tested for possible transfer of radioarsenic to proteins present in blood plasma. This was done by incubating the labeled antibody in fetal bovine serum (FBS) and examining the mixture by HPLC at various time points up to 72 h. Radioarsenic labeled bavituximab (10 µg) in PBS (50 µl) was added to undiluted FBS (500 µl) and incubated at 37°C. Samples (50 µl) were taken at 30 min, 24, 48, and 72 h, diluted with 200 µl water, and examined by HPLC.

Binding of bavituximab antibody to plastic-immobilized phospholipids. Phospholipids were dissolved in *n*-hexane to a concentration of 50 µg/ml. 100 µl of this solution was added to wells

of 96-well microtiter plates. After evaporation of the solvent in air, the plates were blocked for 2 h with 1% BSA diluted in PBS (binding buffer). Bavituximab was diluted in the binding buffer containing 10% FBS at an initial concentration of 33 nM. Serial two-fold dilutions were prepared in the plates (100 µl per well). The plates were then incubated for 1 h at room temperature. After washing with PBS, HRP goat anti-human IgG (diluted 1:2000) was used to detect bavituximab. Secondary reagents were detected by using chromogenic substrate *o*-phenyldiamine followed by reading plates at 490 nm using a microplate reader (Molecular Devices, Palo Alto, CA). Binding of [^{77}As]-bavituximab to PS-coated plates was determined using unmodified bavituximab as the positive control and [^{77}As]-rituximab as the negative control. The concentrations of [^{77}As]-bavituximab and unmodified bavituximab that gave half-maximal binding were determined. Since the association rate of bavituximab with PS on the plate is rapid and its dissociation is negligible over the time course of the experiment, the half-maximal binding concentrations allow the antigen-binding capacities of the labeled and unmodified antibodies to be compared under conditions that approximate equilibrium.

Growth of tumors. All experiments were conducted in accordance with recommendations of the UTSW Institutional Animal Care and Use Committee. A Dunning prostate R3327-AT1 tumor (originally provided by Dr. Peter Peschke, German Cancer Center, Heidelberg, Germany) was excised from a donor animal (26, 27). Small pieces were implanted subcutaneously into the left thigh of male Copenhagen rats (Charles River, Wilmington, MA) and allowed to grow to a size of 15-25 mm diameter.

Biodistribution and planar imaging studies. Three animals each were injected with [^{74}As]-bavituximab or with [^{74}As]-rituximab in PBS (5 MBq in 500 µl) into a tail vein. The animals were sedated using isoflurane (Baxter Healthcare) and imaged on a 25.2 x 30.3 cm phosphor imaging plate (Fuji CR ST-VN, Fuji Photo Film, Tokyo). The photostimulable plates were read on a Molecular Dynamics Storm (Amersham Biosciences) scanner and regions of interest drawn around the tumors and upper body for quantification. In a second study, four animals were injected with 3 MBq of [^{77}As]-bavituximab or [^{77}As]-rituximab were imaged at 48 and 72 h using a 30 min exposure time. Prior studies have established that [^{74}As]-bavituximab and [^{77}As]-bavituximab have identical pharmacological parameters, *i.e*. independent of the isotope of arsenic. In a further study, rats were injected with with 3 MBq of [^{77}As]-bavituximab or [^{77}As]-rituximab and were sacrificed without exsanguination 48 or 72 h later. Tumors were excised, frozen and 1mm sections were cut. Tumor sections were autoradiographed with exposure times of 12 h for [^{77}As]-bavituximab and 48 h for [^{77}As]-rituximab to visualize the distribution of radioactivity within the tumors.

PET studies. Four animals each were injected with 10 MBq of [^{74}As]-bavituximab or [^{74}As]-rituximab in 500 µl of PBS (pH 7.4, 1 mM EDTA) via a tail vein. The animals were anesthetized with isoflurane and imaged over 2 h after 24, 48, and 72 h using a small animal PET system built at UT Southwestern (28, 29). The images were reconstructed using the maximum Likelihood - Expectation Maximization (ML-EM) algorithm for 3D reconstruction (28) After 72 h, the animals were sacrificed by exsanguination and perfusion via cardiac puncture under general anesthesia and major organs and tumors were collected and their radioactivity measured in a gamma counter.

MRI. T1 weighed spin- echo MR images were obtained from rats with size matched tumors for anatomical comparison. The images were acquired with TR/TE = 450 ms/14 ms. The acquisition matrix was 128x256 zero-filled to 512x1024 with field of view 10 x 20 cm and a slice thickness of 1 mm

Detection of localized bavituximab in tumor bearing rats *in vivo.* Groups of two male Copenhagen rats (200 g weight) bearing AT1 tumors (s.c., 15 mm diameter) were injected i.v.. with 1 mg bavituximab or control antibody (rituximab). Twenty four h later, rats were anesthetized and their blood circulation was perfused with heparinized saline to clear it of free antibody, as described above. Organs and tumors were removed and snap-frozen for preparation of cryosections. Sections were fixed with 4% paraformaldehyde in PBS and blocked with PBS containing 1% BSA. To prevent loss of phospholipids during slide processing, detergents and organic solvents were omitted from blocking and washing buffers. Chimeric IgG was detected using biotinylated goat anti-human IgG followed by Cy2-streptavidin. Vascular endothelium was detected by mouse anti-rat CD31 antibody followed by Cy3-goat anti-mouse antibody (minimally reactive with rat serum). Tumor sections derived from rats injected with rituximab served as negative controls. Single images, taken with appropriate filters for Cy2 (green) and Cy3 (red) fluorescence, respectively, were captured by digital camera and transferred to a computer. Images of 10 random fields (0.317 mm^2/field) were merged with the aid of Metaview software. When bavituximab was bound to tumor endothelium, the green and red fluorescence often merged to give a yellow color. The percentage of vessels with localized bavituximab was calculated.

RESULTS

^{74}As and ^{77}As were produced, radiochemically separated, and transformed into the labeling synthon *AsI_3. Isotopes were chosen depending on the goal of each study, so that ^{74}As was used for *ex vivo* organ distribution, whole body planar imaging (*in vivo* and *ex vivo*), and *in vivo* PET imaging. ^{77}As was used to develop the radiochemistry and labeling procedures and used to label bavituximab for whole body planar imaging *in vivo* and biodistribution.

Babituximab was modified with SATA to introduce an average of 3.5 free thiol groups per molecule of antibody (Fig. 1a). Arsenic has a high affinity for sulfur and AsI_3 is able to bind covalently to sulfhydryl groups (7). *AsI_3 conjugation to the SATA-modified antibodies was achieved quantitatively (Fig. 1b). The specific activity of the [*As]-labeled antibodies was > 100 GBq / µmol. Incubation in serum for up to 72 h did not cause release of radioarsenic from the labeled monoclonal antibody or formation of antibody fragments (Fig. 1c). Complexes of bavituximab and β2-glycoprotein I were not observed, probably because the complex is not stable in the absence of an anionic phospholipid surface upon which to dimerize. Immunoreactivity of the labeled bavituximab was verified by ELISA. Little or no loss of PS-binding activity was observed after SATA-modification and subsequent labeling with nca [^{77}As] AsI_3 (Fig. 1d). The concentration of [^{77}As]-bavituximab giving half-maximal binding was less than twice that for unmodified bavituximab, indicating that the labeling procedure had caused no more than a two-fold reduction in the antigen binding capacity of the antibody.

Rats bearing Dunning R3227-ATI prostate tumors of approximately 15 mm diameter were injected i.v. with [^{74}As]-bavituximab or with the isotype-matched control antibody, [^{74}As]-rituximab. The radioactivity present in various organs was measured 48 and 72 h after injection.

These time points were selected because they gave good tumor localization in the imaging studies below. Tumor to normal tissue ratios were highest for bavituximab at 72 h after injection, consistent with the imaging results. Tumor to liver and tumor to muscle ratios at 72 h were 22 and 470, respectively (Fig. 2a and b). Bavituximab localized to tumors to a greater extent than did the control antibody, rituximab. The ratios of bavituximab to rituximab were 28 and 52 at 48 h and 72 h, respectively (Fig. 2c). The percentage of the injected dose per gram of tumor was 0.25 and 0.65 for [^{74}As]-bavituximab at 48 and 72 h, respectively. This level of localization is respectable given the inverse relationship between animal weight and %ID/gram in different species. Significant uptake of radioactivity was observed in the stomach 48 h after injection of [^{74}As]-bavituximab, but had decreased by 72 h. In most organs (heart, liver, kidney, muscle, bone), the two antibodies showed similar low uptake. Uptake of [^{74}As]-labeled bavituximab and rituximab was observed in the spleen.

Fig. 3a shows the whole body scintigraphy of a representative rat imaged at 72 h after injection with [^{74}As]-bavituximab. Fig. 3b compares the radioactivity in the tumor to that in the upper organs (liver, lung, heart) at various time points after injection of [^{74}As]-bavituximab. At 24 h, the tumor was barely distinguishable because of the high body background. At 48 h, the tumor was clearly localized, but some signal attributable to blood pool was observed in the upper organs. At 72 h, labeled bavituximab had substantially cleared from the blood and antibody localization to the tumor was most visible. Thereafter, tumor to background ratios declined. Images are also shown for rats injected with [^{77}As]-bavituximab or [^{77}As]-rituximab (Fig. 3c and d) and imaged 72 h after injection. Relatively little [^{77}As]-rituximab (about one-eighth as much) localized to the tumor as compared with [^{77}As]-bavituximab, showing that the localization of [^{77}As]-bavituximab was antigen-specific.

Distribution of radioactivity within the tumor was heterogeneous. Slices of tumors were examined by autoradiography (Fig 4). Extensive localization of [^{77}As]-bavituximab was observed in the tumor periphery and throughout the central regions, though quite heterogeneously. For rituximab, activity was limited to the tumor periphery. PET images from a 3D data set of a tumor-bearing rat obtained 48 h after injection of [^{74}As]-bavituximab again showed strong localization to the tumor periphery with similar heterogeneity of activity in central regions (Fig. 5).

Frozen sections of tumor and normal tissues were stained for the presence of human immunoglobulin to identify the cells to which the bavituximab had localized. Sections were counterstained with anti-rat CD31 to detect vascular endothelium (Fig. 6). The images were merged. Coincidence of staining between localized bavituximab and CD31 indicated specific localization of bavituximab to tumor endothelium. (Fig. 6). Coincident staining appeared yellow, unless dominated by a particularly intense green or red fluorescence in that region. Labeled vessels were visible in all regions of the tumors with an average of 40$\pm$10% labeled vessels. Labeled vessels were particularly abundant in and around regions of necrosis. Larger vessels sometimes had regions where the vascular endothelium was positive for localized bavituximab and other regions where it was not, showing heterogeneity of PS exposure within a single vessel. Regions where bavituximab had leaked into the tumor interstitium were also visible around the endothelium of some vessels. Non-vascular staining of dead and dying tumor cells in and around necrotic tumor regions was only occasionally observed. The antigen specificity of bavituximab localization to vessels was confirmed by the lack of endothelial cell staining in tumors from rats injected with rituximab. Localization of bavituximab to vascular endothelium in normal tissues was not detectable in rat heart, lung, liver, pancreas, kidney, spleen, brain, and testis.

DISCUSSION

This study demonstrates the feasibility of using arsenic radioisotopes to label a monoclonal antibody directed against anionic phospholipids on the surface of tumor vascular endothelium. Tumor selective targeting was observed *in vivo* and confirmed by biodistribution analysis and histology.

The two isotopes we selected for the present studies were ^{74}As, a potential clinical PET imaging isotope, and ^{77}As, a potential therapeutic isotope. ^{74}As (β^+, T½ 17.8 d) has a long half life that allows imaging several days after administration of labeled antibody. Optimal tumor imaging in humans is often achieved three or more days after administration of a labeled antibody, when the levels of free antibody have declined relative to those specifically bound or retained by the tumor (30, 31). ^{77}As (β^-, T½ 38.8) has a high energy β^- emission suitable for anti-tumor therapy. Both isotopes, like other isotopes of arsenic, can be attached through stable covalent linkages to antibodies. In addition, arsenic does not accumulate in the thyroid or undergo transchelation to metal-binding blood and tissue proteins.

Jennewein and Rösch have developed efficient methods for isolating arsenic from irradiated germanium oxide targets to provide arsenic in a form that is useful for labeling sensitive biomolecules (7, 8). They have also developed novel methods for linking arsenic to biomolecules. Here, we demonstrate that monoclonal antibodies can be labeled efficiently with ^{74}As or ^{77}As to produce radioimmunoconjugates having full antigen-binding activity and high *in vitro* and *in vivo* stability. [*As]-bavituximab was stable for several days when incubated in serum. Very little non-specific uptake of radioactivity by the liver was seen in rats injected with [*As]-bavituximab or [*As]-rituximab, indicating that the labeled antibodies have high *in vivo*

stability and that transfer of *As to serum proteins and uptake by the liver is minimal. This contrasts with the use of radioiodine for antibody labeling, where dehalogenation and high thyroid uptake are considerable. Instability is less of a problem for antibodies labeled with metal ions (e.g. ^{64}Cu) since the advent of improved chelating agents.

Biodistribution studies showed high selectivity of bavituximab toward tumor tissue. Within 48 h, the tumor to muscle ratio approached 10 and reached almost 500 by 72 h (Fig. 2). The tumor to liver ratio exceeded 20 by 72 h. [^{74}As]-bavituximab showed 30 to 50-fold higher absolute uptake in tumor than did the control antibody, [^{74}As]-rituximab. The *ex vivo* biodistribution matches the tumor uptake observed by imaging, with higher localization of bavituximab being seen in the tumor than in any normal tissues. Both *As-labeled bavituximab and rituximab accumulated in the spleen, possibly due to non-specific capture of immunoglobulin or metabolites by the reticuloendothelial system. We did not observe preferential accumulation of [*As]-bavituximab in the liver or spleen, which would be expected if bavituximab bound to PS-expressing blood cells being cleared by these organs.

The PET and planar scintigraphy studies showed pronounced localization of bavituximab to solid Dunning prostate R3227-AT1 tumors. Localization was seen in the periphery of the tumor and in various central regions, in agreement with prior PET studies with FDG or perfusion MRI (32-34). We have previously observed that PS positive vessels are present in both the periphery and the core of tumors. It is likely that the peripheral location of the radioactivity seen with [*As]-bavituximab in the present study is because this is the region of tumors that typically has the most abundant and functional blood supply. Some of the bavituximab was probably free in the blood of peripheral vessels, or had diffused into peripheral tumor regions, because a similar peripheral distribution was seen with the non-binding rituximab control antibody.

Heterogeneous localization of bavituximab was also observed throughout the central regions of the tumor. This central localization was antigen-specific since relatively little localization was seen in central tumor regions with the rituximab control antibody. Immunohistochemical examination confirmed that the bavituximab was bound to the endothelium of the central tumor regions with little staining of necrotic regions being visible. The heterogeneous staining with bavituximab is probably because some tumor regions have more hypoxia, acidity or inflammatory cytokines than others, leading to variable levels of PS exposure on the tumor endothelium. We have previously examined multiple different types of mouse and human tumors growing in mice and all have PS-expressing tumor vascular endothelium (10, 14, 35, 36). The percentage of PS-positive vessels ranged from 16 to 41%. Thus, we anticipate that vascular imaging observed with bavituximab in the present studies will extend to other tumor types. The Dunning prostate R3227-AT1 tumor has small areas of focal necrosis scattered throughout the tumor (37). The lack of strong localization of bavituximab to these necrotic regions could be related to difficulties of access associated with high interstitial pressure and inadequate lymphatic drainage. However, in a previous study using a different anti-PS antibody (9D2) and different tumors, staining of necrotic tumor tissue was observed in addition to the endothelium at later time points (10). The apparent difference in the ability of the two antibodies to localize to necrotic regions may relate to idiosyncrasies of the tumor models or to differences in the ability of the two antibodies to resist proteolysis after binding. It is also possible that the cofactor protein, β2-glycoprotein I, which is needed for PS binding by bavituximab but not 9D2, does not efficiently penetrate into extravascular tissues or is degraded rapidly by proteolytic enzymes within the tumor interstitium.

The present labeling chemistry can also be applied to other radioarsenic isotopes. ^{72}As has a half life of 26 h, suitable for imaging with antibody Fab' and F(ab')$_2$ fragments and other biomolecules having intermediate half lives. The abundance of positrons for ^{72}As is 88%, which is higher than for other commonly-used positron emitters, such as ^{64}Cu (18.0 % β^+, T½ 12.7 h) or ^{124}I (23.0 % β^+, T½ 4.2 d). Arsenic provides two potentially therapeutic isotopes: ^{77}As (T½ 38.8 h, $\bar{E}_{\beta^-}$ 226 keV), as used in the present study, and ^{76}As (T½ 26.3 h, $\bar{E}_{\beta^-}$ 1068 keV) (see Table in supplementary information). The multiple isotopes of arsenic potentially offer additional applications such as combined imaging/dosimetry and radioimmunotherapy. Another advantage of arsenic is that, unlike iodine, it does not subject the thyroid to high irradiation. The doses of arsenic used for imaging with [^{74}As]-bavituximab are also several orders of magnitude below toxic levels, so that even if ^{74}As were released from the antibody no toxicity would be expected. However, the arsenic isotopes do not include alpha emitters, which, because of their short path length, could be advantageous for vascular targeted therapies.

In conclusion, we have exploited the unique properties of arsenic radioisotopes to achieve clear imaging of tumors with an antibody, bavituximab, directed against a tumor vessel marker. Radioarsenic-labeled bavituximab shows promise as a vascular imaging agent for tumor detection and dosimetry in man.

LEGENDS

Figure 1.

a) Reaction scheme for the labeling of SATA-modified antibody with radioactive arsenic isotopes. **b) Quality control of bavituximab labeling with radioactive arsenic.** After a labeling time of 30 min, a sample of [^{74}As]-bavituximab (20 µl) was resolved on a size-exclusion column for radio-HPLC. The UV-spectrum (upper trace) and corresponding radioactivity-progression (lower trace) confirm the absence of aggregates and of free ^{74}As. Labeling yield is > 99.9 %. **c) *In vitro* stability of [^{74}As]-bavituximab.** [^{74}As]-bavituximab was incubated in undiluted FBS for 24, 48, and 72 h. Size exclusion radio-HPLC was performed. The UV spectrum (upper graph) shows a typical FBS profile because the amount of [^{74}As]-bavituximab is too small to detect. The lower graphs show the corresponding radioactivity peak. Aggregates and breakdown products were not observed, indicating that the product is stable in serum. **d) Immunoreactivity.** ELISA was used to analyze the immunoreactivity of [^{77}As]-bavituximab (●). Unlabeled and unmodified bavituximab was used as the positive control (o) and [^{77}As]-rituximab as the negative control (▼). Little or no reduction of immunoreactivity was detected following SATA-modification and radioarsenic labeling.

Figure 2.

Biodistribution. Dunning prostate R3327-AT1 tumor bearing rats were injected with 185 kBq of [^{74}As]-bavituximab or [^{74}As]-rituximab i.v. Groups of four animals were sacrificed by exsanguination and perfusion 48 h or 72 h after injection. a) Tumor to liver ratios for rats sacrificed after 48 and 72 h after injection with [^{74}As]-rituximab (black) or [^{74}As]-bavituximab (dots). b) Corresponding tumor to muscle ratios. c) Specific localization of bavituximab:

rituximab in major organs after 48 h (narrow hatched) and 72 h (broad hatched). Specific localization is calculated as the ratio of the %ID/g for [^{74}As]-bavituximab to the %ID/g for [^{74}As]-rituximab in tumor and normal tissues. At 72 h the uptake of bavituximab was significantly higher in tumor than liver or muscle ($p<0.001$).

Figure 3.

Whole-body planar scintigraphy of Dunning prostate R3227-AT1 tumor bearing rats.

a) Rats bearing approximately 20 mm diameter tumors were injected i.v. with 5 MBq of [^{74}As]-bavituximab. The rats were imaged on a phosphor plate at various time points after injection. The Figure shows a representative image 72 h after injection. The image is overlaid on an X-ray picture to provide anatomical correlation. b) Ratio of uptake of [^{74}As]-bavituximab in tumor versus upper organs (liver, lung, heart) at various time points after injection. ●, outer tumor regions; ○, entire tumor. At 24 h after injection, no obvious contrast was observed, but at 48 h the tumor became clearly visible and by 72 h, the tumor to organ ratio was the highest. c-d) Scintigraphy of rats injected with 3 MBq [^{77}As]-bavituximab or [^{77}As]-rituximab (negative control). Images acquired with 30 min exposure time at 72 h. Eight-fold higher uptake of bavituximab than of the control antibody was observed in the tumor.

Figure 4.

Autoradiography of excised tumor sections. a-b) Autoradiographs of 1mm sections of Dunning prostate R3227-AT1 tumors from rats 48 h or 72 h after injection with [^{77}As]-bavituximab. Localization of bavituximab was observed in the tumor periphery and heterogeneously throughout the tumor core. c) [^{77}As]-rituximab showed relatively little

accumulation in the tumor, particularly in the central regions. The autoradiograph was exposed for 4 times longer with [^{77}As]-rituximab to visualize the distribution. Scale shows arbitrary storage phosphor units.

Figure 5.

Small Animal PET. a-b) Small animal PET images obtained from a Dunning prostate R3227-AT1 tumor-bearing rat 48 h after injection of 10 MBq of [^{74}As]-bavituximab a) coronal; b) transaxial. PET intensity is overlaid on slices obtained by 3D MRI. [^{74}As]-bavituximab localized to the tumor (arrows) and was also visible in the blood pool of normal organs. The PET field of view (FOV) is indicated by the bracket. c) Images of 1mm sequential tumor slices from the 3D data sets.

Figure 6.

Localization of bavituximab to tumor vessels after injection into rats bearing syngeneic Dunning R3227-AT1 prostate tumors. Rats were injected i.v. with bavituximab or rituximab. After 24 h the rats were exsanguinated and their tumors were removed. Panels a, b and c show blood vessels in a frozen section of tumor at low magnification. a) Stained with biotinylated goat anti-human IgG followed by Cy2-streptavidin (green) to detect localized bavituximab; b) Stained with mouse anti-rat CD31 followed by Cy3-labeled goat anti-mouse IgG (red) to detect vascular endothelium. c) A merged image of bavituximab localized on CD31 positive endothelium (thick arrows). d) A merged image of blood vessels in the tumor of a rat injected with rituximab. No binding of rituximab was detected. e-f) Higher magnification merged images of blood vessels in

tumors from rats injected with rituximab (e) or bavituximab (f). Bars in the panels represent 100 μm.

References

1. Rudin M, Weissleder R. Molecular imaging in drug discovery and development. Nature Rev Drug Discov 2003;2:123-31.
2. Massoud TF, Gambhir SS. Molecular imaging in living subjects: seeing fundamental biological processes in a new light. Genes & Development 2003;17:545-80.
3. Kumar R, Jana S. Positron emission tomography: an advanced nuclear medicine imaging technique from research to clinical practice. Methods Enzymol 2004;385:3-19.
4. McQuade P, J. RD, Lewis JS, Welch MJ. Positron-Emitting Isotopes Produced on Biomedical Cyclotrons. Curr Med Chem 2005;12:807-18.
5. Boerman OC, Kopp MJ, Postema EJ, Corstens FH, Oyen WJ. Radionuclide therapy of cancer with radiolabeled antibodies. Current Medicinal Chemistry-Anti Cancer Agents 2007;7:335-343.
6. Burnham CA, Aronow S, Brownell GL. A hybrid positron scanner. Phys Med Biol 1970;15:517-28.
7. Jennewein M, Qaim SM, Hermanne A, et al. A New Method for the Radiochemical Separation of Arsenic from Reactor and Cyclotron Irradiated Germanium Oxide. Appl Rad Isoto 2005;63:343 -51.
8. Jennewein M, Schmidt A, Novgorodov AF, Qaim SM, Roesch F. A no-carrier-added ^{72}Se/^{72}As radionuclide generator based on distillation. Radiochim Acta 2004;92:245-9.
9. Huang X, Bennett M, Thorpe PE. A Monoclonal Antibody that Binds Anionic Phospholipids on Tumor Blood Vessels Enhances the Antitumor Effect of Docetaxel on Human Breast Tumors in Mice. Cancer Res 2005;65:4408-16.
10. Ran S, Downes A, Thorpe PE. Increased exposure of anionic phospholipids on the surface of tumor blood vessels. Cancer Res 2002;62:6132-40.
11. Ran S, Thorpe PE. Phosphatidylserine is a marker of tumor vasculature and a potential target for cancer imaging and therapy. Int J Radiat Oncol Biol Phys 2002;54:1479-84.
12. Luster TA, He J, Huang X, et al. Plasma protein beta-2-glycoprotein 1 mediates interaction between the anti-tumor monoclonal antibody 3G4 and anionic phospholipids on endothelial cells. J Biol Chem 2006;281:29863-71.
13. Ran S, Gao B, Duffy S, Watkins L, Rote N, Thorpe PE. Infarction of solid Hodgkin's tumors in mice by antibody-directed targeting of tissue factor to tumor vasculature. Cancer Res 1998;58:4646-53.
14. Ran S, He J, Huang X, Soares M, Scothorn D, Thorpe PE. Anti-tumor effects of a monoclonal antibody directed against anionic phospholipids on the surface of tumor blood vessels in mice. Clin Cancer Res 2005;11:1551-62.
15. Seigneuret M, Devaux PF. ATP-dependent asymmetric distribution of spin-labeled phospholipids in the erythrocyte membrane: relation to shape changes. Proc Natl Acad Sci U S A 1984;81:3751–5.
16. Bombeli T, Karsan A, Tait JF, Harlan JM. Apoptotic vascular endothelial cells become procoagulant. Blood 1997;89:2429-42.
17. Boyle EM, Jr., Pohlman TH, Cornejo CJ, Verrier ED. Endothelial cell injury in cardiovascular surgery: ischemia-reperfusion. Ann Thorac Surg 1996;62:1868-75.
18. Bevers EM, Comfurius P, Zwaal RF. Changes in membrane phospholipid distribution during platelet activation. Biochim Biophys Acta 1983;736:57-66.

19. Rote NS, Ng AK, Dostal-Johnson DA, Nicholson SL, Siekman R. Immunologic detection of phosphatidylserine externalization during thrombin-induced platelet activation. Clin Immunol Immunopathol 1993;66:193-200.
20. Bitbol M, Fellmann P, Zachowski A, Devaux PF. Ion regulation of phosphatidylserine and phosphatidylethanolamine outside-inside translocation in human erythrocytes. Biochim Biophys Acta 1987;904:268-82.
21. Zhao J, Zhou Q, Wiedmer T, Sims PJ. Level of expression of phospholipid scramblase regulates induced movement of phosphatidylserine to the cell surface. J Biol Chem 1998;273: 6603-6.
22. Hamon Y, Broccardo C, Chambenoit O, et al. ABC1 promotes engulfment of apoptotic cells and transbilayer redistribution of phosphatidylserine. Nat Cell Biol 2000;2:399-406.
23. Pradhan D, Williamson P, Schlegel RA. Phosphatidylserine vesicles inhibit phagocytosis of erythrocytes with a symmetric transbilayer distribution of phospholipids. Mol Membr Biol 1994;11:181-7.
24. Balasubramanian K, Schroit AJ. Aminophospholipid asymmetry: a matter of life and death. Annu. Rev. Phydiol. 2003;65:701-34
25. Duncan RJ, Weston PD, Wrigglesworth R. A new reagent which may be used to introduce sulfhydryl groups into proteins, and its use in the preparation of conjugates for immunoassay. Anal Biochem 1983;132:68-73.
26. Henke K, Hartmann GH, Peschke P, Hahn EW. Stereotactic radiosurgery of the rat Dunning R3327-AT1 prostate tumor. Int J Radiat Oncol Biol Phys 1996;36:385-91
27. Zhao D, Ran S, Constantinescu A, Hahn EW, Mason RP. Tumor oxygen dynamics: correlation of in vivo MRI with histological findings. Neoplasia 2003;5:308-18.
28. Modestou M, Puig-Antich V, Korgaonkar C, Eapen A, Quelle DE. The alternative reading frame tumor suppressor inhibits growth through p21-dependent and p21-independent pathways. Cancer Research 2001;61:3145-50.
29. Tsyganov EN, Anderson J, Arbique G, et al. UTSW Small Animal Positron Emission Imager. IEEE Trans Nucl Inst 2006; 53:2591-2600
30. Bischof Delaloye A, Delaloye B. Tumor imaging with monoclonal antibodies. Semin Nucl Med 1995;25:144-64.
31. Von Kleist S. Ten years of tumor imaging with labelled antibodies. In Vivo 1993;7:581-4.
32. Karam JA, Mason RP, Koeneman KS, Antich PP, Benaim EA, Hsieh JT. Molecular imaging in prostate cancer. J Cell Biochem 2003;90:473-83.
33. Jiang L, Zhao D, Constantinescu A, Mason RP. Comparison of BOLD contrast and Gd-DTPA Dynamic Contrast Enhanced imaging in rat prostate tumor. Magn Reson Med 2004;51: 953-60.
34. Zhao D, Jiang L, Hahn EW, Mason RP. Continuous low-dose (Metronomic) chemotherapy on rat prostate tumors evaluated using MRI in vivo and comparison with histology. Neoplasia 2005;7:678-87.
35. Beck, A.W., Luster, T.A., Miller, A.F., Holloway, S.E., Conner, C.R., Barnett, C.C., Thorpe, P.E., Fleming, J.B., and Brekken, R.A. (2006) Combination of a monoclonal anti-phosphatidylserine antibody with gemcitabine strongly inhibits the growth and metastasis of orthotopic pancreatic tumors. Int. J. Cancer 118, 10:2639-2643.
36. He, J., Luster, T.A., and Thorpe, P.E. Radiation-enhanced vascular targeting of human lung cancers in mice with a monoclonal antibody that binds anionic phospholipids.

(2007) Clin. Cancer Res. 207, 5211-8.
37. Hahn EW, Peschke P, Mason RP, Babcock EE, Antich PP. Isolated tumor growth in a surgically formed skin pedicle in the rat: a new tumor model for NMR studies. Magn. Reson. Imaging 1993; 11:1007-1017.

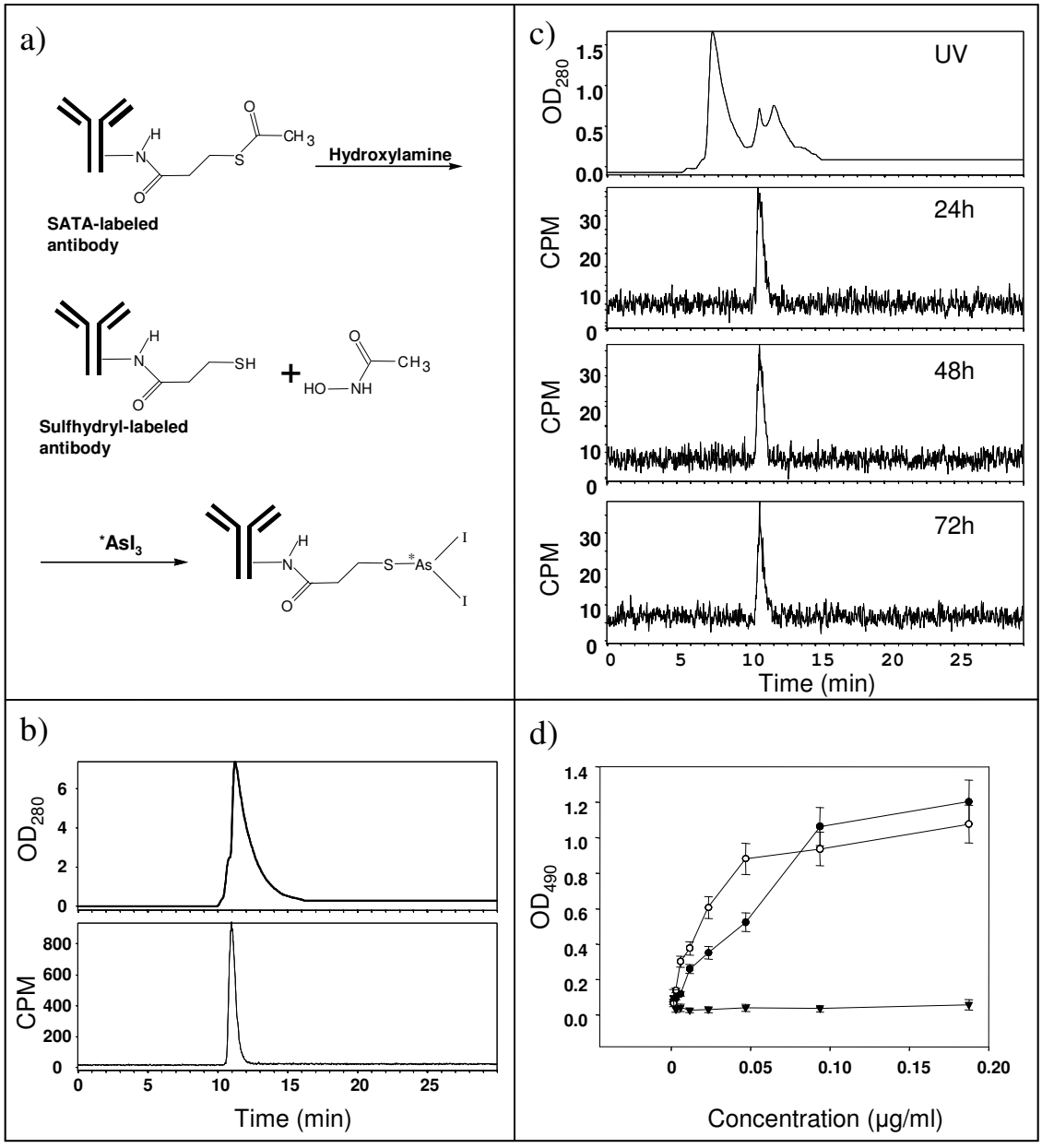
a)
Hydroxylamine
SATA-labeled antibody
Sulfhydryl-labeled antibody
*AsI3
b)
OD280
CPM
Time (min)
c)
UV
24h
48h
72h
OD280
CPM
Time (min)
d)
OD490
Concentration (µg/ml)

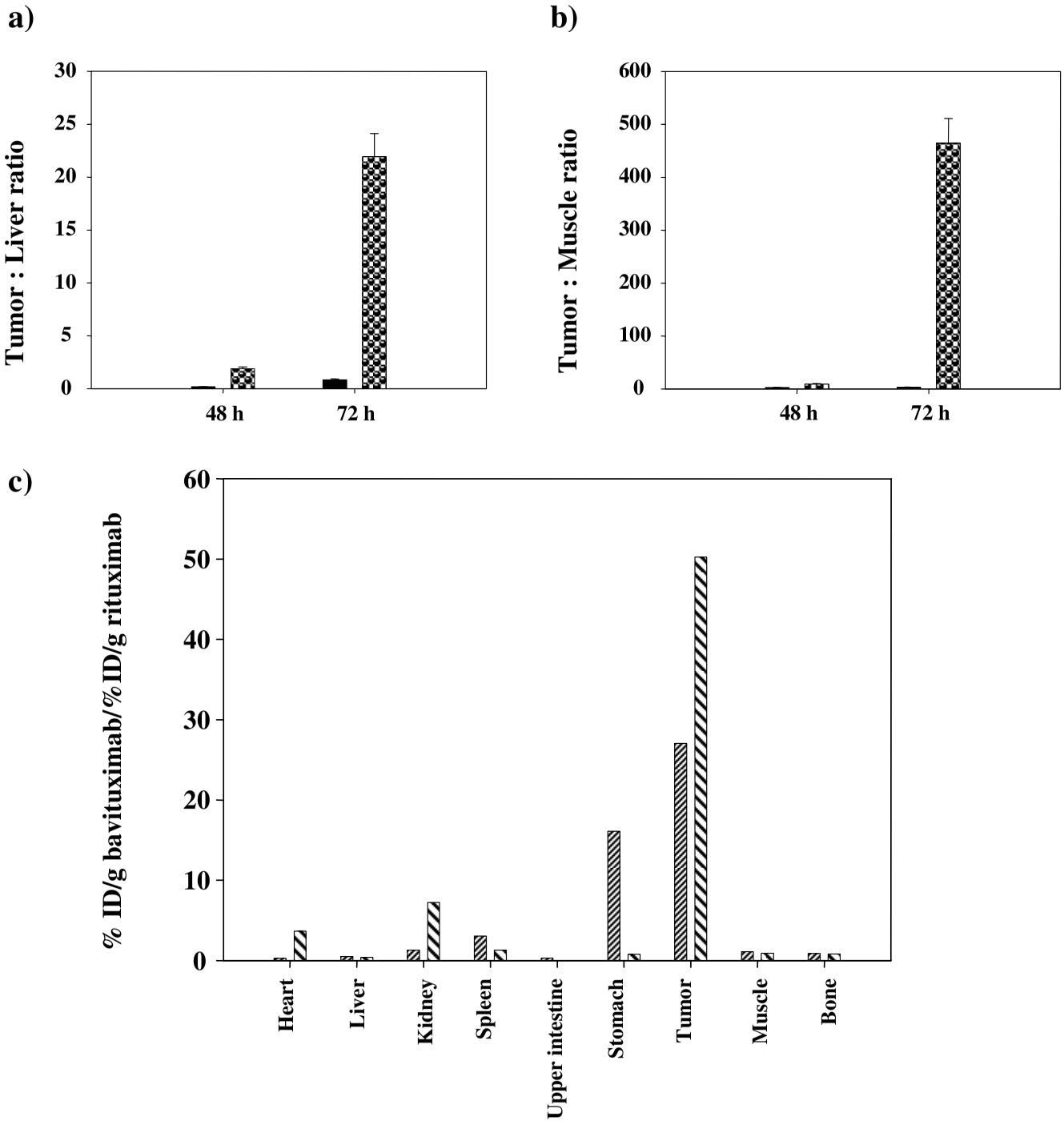
a)
Tumor : Liver ratio
30
25
20
15
10
5
0
48 h
72 h
b)
Tumor : Muscle ratio
600
500
400
300
200
100
0
48 h
72 h
c)
% ID/g bavituximab/%ID/g rituximab
60
50
40
30
20
10
0
Heart
Liver
Kidney
Spleen
Upper intestine
Stomach
Tumor
Muscle
Bone

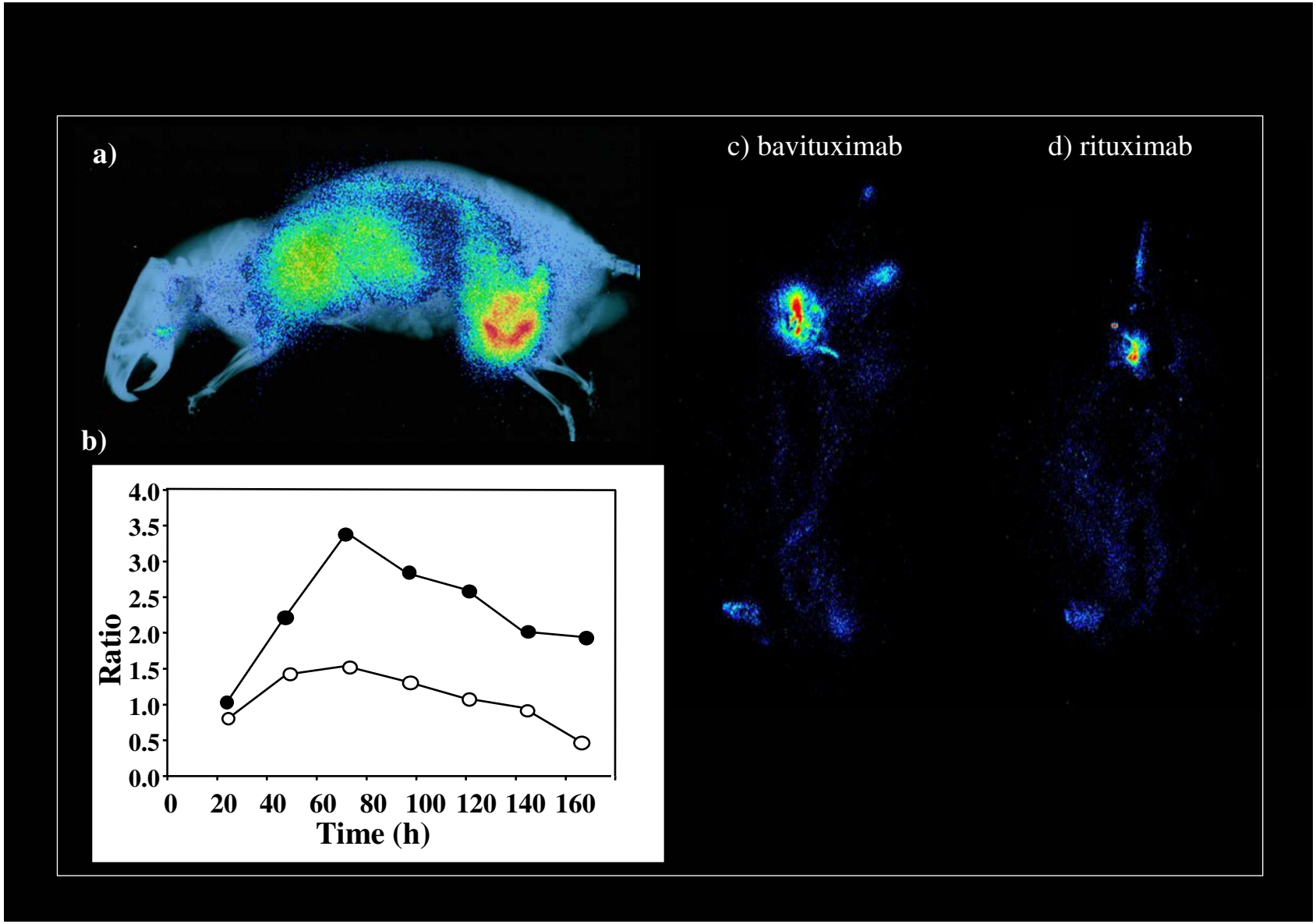
a)
b)
c) bavituximab
d) rituximab
Ratio
4.0
3.5
3.0
2.5
2.0
1.5
1.0
0.5
0.0
0
20
40
60
80
100
120
140
160
Time (h)

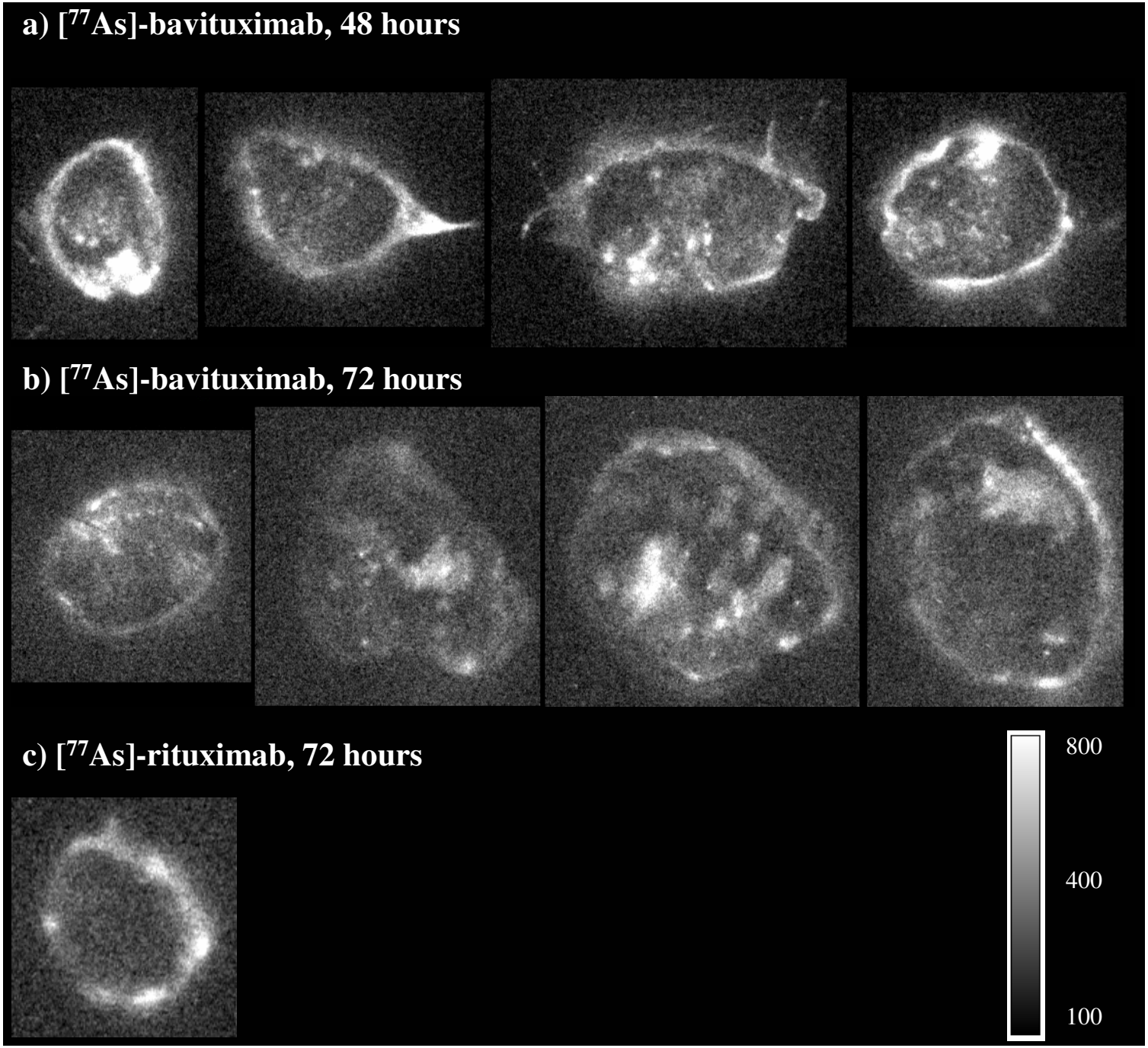
a) [77As]-bavituximab, 48 hours
b) [77As]-bavituximab, 72 hours
c) [77As]-rituximab, 72 hours
800
400
100

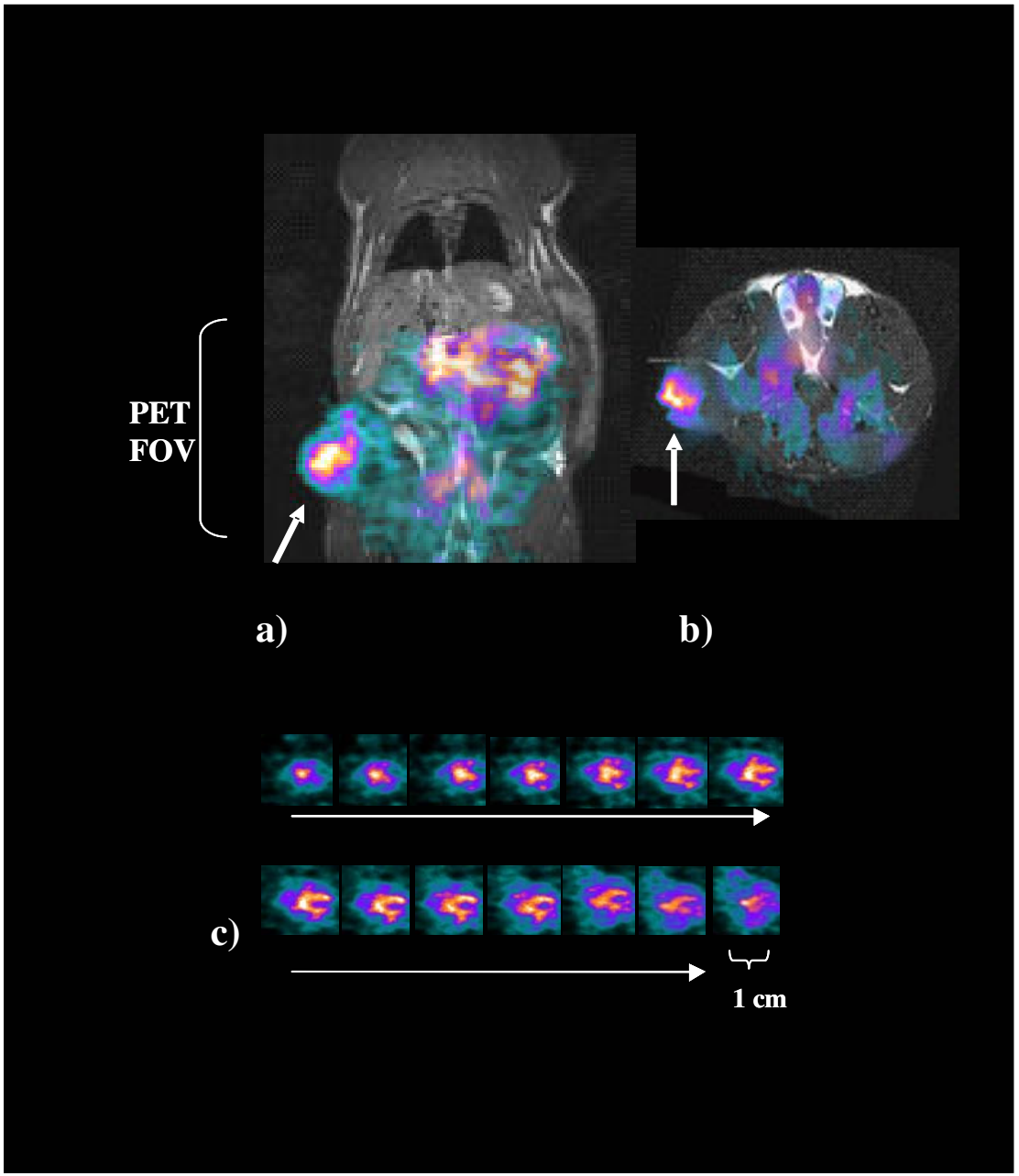
PET
FOV
a)
b)
c)
1 cm

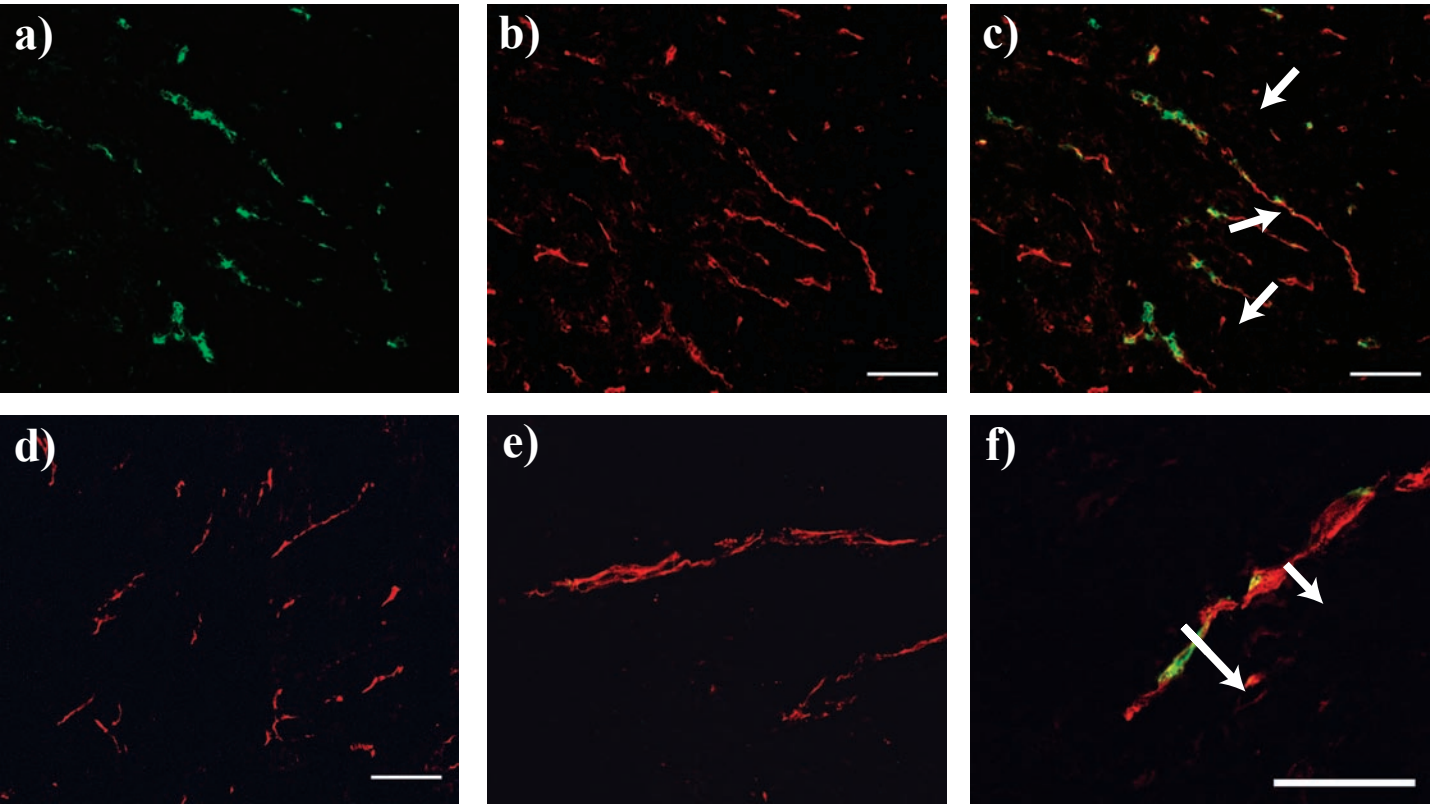
a)
b)
c)
d)
e)
f)

Supplementary Information

Table 1:

Decay characteristics of the most relevant arsenic isotopes for molecular imaging or therapy

	^{71}As	^{72}As	^{73}As	^{74}As	^{76}As	^{77}As
T½ [d]	2.70	1.08	80.3	17.78	1.1	1.62
Mode of decay (%)	EC (70) β^+ (30)	EC (12) β^+ (88)	EC(100)	EC (42) β^+ (29) β^- (29)	β^- (100)	β^- (100)
Most abundant γ-lines [keV]	175.0 (83.1%)	834.0 (79.5%) 630.0 (7.9%)	53.4 (10.5%)	595.9 (60.2%) 634.8 (15.4%)	559.1 (45.0%) 657.1 (6.2%)	239.0 (1.6%) 520.6 (0.5%)
Mean particle energies [keV]	β^+: 104	β^+: 1024		β^+: 128 β^-: 137	β^-: 1068	β^-: 226
Application	PET	PET		PET	SPECT	SPECT Therapy

EC electron capture

Comp. by: RMervin Date:19/11/07 Time:18:07:48 Stage:First Proof File Path://
pchns1301/WOMAT/Production/PRODENV/0000000001/0000006424/0000000016/
0000749453.3D Proof by: QC by: ProjectAcronym:bs:AFS Volume:00005

CHAPTER 5

Non-Invasive Physiology and Pharmacology Using ^{19}F Magnetic Resonance

Jian-Xin Yu, Weina Cui, Dawen Zhao, and Ralph P. Mason*

Laboratory of Prognostic Radiology, Department of Radiology, The University of Texas Southwestern Medical Center at Dallas, TX 75390, USA

Contents

1. Introduction 198
   1.1. Context and perspective 199
   1.2. ^{19}F as an *in vivo* NMR probe 201
2. ^{19}F NMR for pharmacology 215
   2.1. Cancer chemotherapeutics 216
      2.1.1. Fluoropyrimidines 216
      2.1.2. Other anticancer drugs 217
   2.2. Other drugs 218
3. Active reporter molecules 220
   3.1. Physical interactions 220
      3.1.1. *In vivo* oximetry 220
      3.1.2. pH 231
      3.1.3. Metal ions 235
      3.1.4. Caveats 242
   3.2. Chemical interactions 243
      3.2.1. Metabolism of FDG 243
      3.2.2. Hypoxia 244
      3.2.3. Enzyme reporters 245
4. Passive reporter molecules 252
5. Potential innovations and improvements 253
6. Conclusions 253
References 254

Abstract

^{19}F provides a powerful tool for nuclear magnetic resonance (NMR) investigations. It has been widely exploited for both spectroscopic studies and increasingly for magnetic resonance imaging (MRI). The ^{19}F atom has high NMR sensitivity while there is essentially no background signal in the body. Many diverse reporter molecules have been designed, which exploit the unique sensitivity of the fluorine atom to its microenvironment and these

*Corresponding author. Tel.: +1-(214)-648-8926; Fax: +1-(214)-648-2991;
E-mail: Ralph.Mason@UTSouthwestern.edu

FLOURINE AND HEALTH
A. Tressaud & G. Haufe (Editors)
DOI: 10.1016/B978-0-444-53086-8.00005-9

© 2008 Elsevier B.V.
All rights reserved.

UNCORRECTED PROOF

Comp. by: RMervin Date:19/11/07 Time:18:07:52 Stage:First Proof File Path://
pchns1301/WOMAT/Production/PRODENV/0000000001/0000006424/0000000016/
0000749453.3D Proof by: QC by: ProjectAcronym:bs:AFS Volume:00005

cover such diverse aspects as pO_2, pH, metal ion concentrations (e.g., calcium, magnesium), gene reporter molecules, hypoxia reporters, vascular flow, and volume. There are also numerous drugs in clinical use (e.g., the cancer chemotherapeutics 5-fluorouracil and gemcitabine, anesthetics, and psychoactive drugs such as fluoxetine) and agrochemicals, which include a fluorine atom. This review examines the properties of the fluorine atom that make it an ideal tool for NMR, consider the many properties that are available for interrogation and examine applications. NMR is a particularly flexible technology, since it can provide information through multiple parameters including chemical shift, relaxation processes (R_1 and R_2), scalar coupling, and chemical exchange. Moreover, fluorine NMR has a very large chemical shift range ($\sim$300 ppm) allowing multiple agents to be examined simultaneously.

1. INTRODUCTION

MRI has become the technology of choice for radiology and detection of many diseases. Today, clinical MRI uses almost exclusively the proton nucleus of the hydrogen atom, which occurs naturally in tissue water. Thus, there is a particularly strong signal, which is sensitive to tissue status and provides exquisite indications of soft tissue anatomy. Increasingly, the development of specific contrast agents and selective pulse sequences allows more detailed analysis of tissue properties such as diffusion, flow, and changes in vascular oxygenation [1,2]. Much information may also be obtained from metabolites; however, these typically occur at millimolar concentrations (or less) requiring prodigious water suppression [3]. Heteronuclei can provide metabolic tracers and physiological reporters while avoiding the intense water and lipid signals. The ^{19}F atom has sensitivity of the order of 80% of that of proton, but there is essentially no endogenous signal from tissues. Most of the fluorine in the body is in the form of solid state fluoride ions, which give very broad lines, essentially undetectable using standard NMR equipment. There are also a few fluorine containing molecules that occur in nature, but these are almost exclusively in plants, are highly toxic, and thought to be part of inherent defense mechanisms [4]. Thus, any molecular fluorine introduced into the body in the form of reporter molecules or drugs is readily detected with high sensitivity.

The importance of fluorine in the Life Sciences continues to be recognized in journals such as the *Journal of Fluorine Chemistry*, reviews in regular journals devoted to technology, and the current series Advances in Fluorine Science. Many reviews beginning in the 1980s were devoted to fluorine NMR with seminal work from Thomas, Selinsky and Burt, Prior, and London [5–8]. More recently, Mason reviewed the use of perfluorocarbons (PFCs) for measuring tissue oxygenation [9,10] and fluorinated derivatives of vitamin B6 as probes of pH *in vivo* [11]. McSheehy *et al*. [12] discussed applications of fluorine NMR to oncology, Menon [13] examined fluorinated anesthetics, and Passe *et al.* [14] reviewed neuropsychiatric applications. Several reviews have concerned the pharmacokinetics of

UNCORRECTED PROOF

Comp. by: RMervin Date:19/11/07 Time:18:07:53 Stage:First Proof File Path://
pchns1301/WOMAT/Production/PRODENV/0000000001/0000006424/0000000016/
0000749453.3D Proof by: QC by: ProjectAcronym:bs:AFS Volume:00005

fluoropyrimidine drugs based on fluorine NMR including notable contributions from Bachert, Martino, and Wolf [15–17] and, indeed, Wolf *et al*. contributed the succeeding article in this volume. Use of fluorine NMR to investigate physiology and pharmacology from an organic chemical perspective was the focus of a review by us [18]. Given the continuing appearance of novel applications in the field and developing interest in fluorine NMR, this current article will provide both a historical perspective and review state of the art. Readers are also directed to many relevant reviews that consider pharmacology, organic chemistry, or synthetic methods relating to fluorine [19–30]. Examples include recent reviews from Jescke [26]: on the unique role of fluorine in the design of active ingredients for modern crop protection, Dolbie: a review of fluorine chemistry at the millennium [21], Shimizu and Hiyama [24]: examining modern synthetic methods for fluorine substituted target molecules, Isanbor and O'Hagan [28]: reviewing fluorinated anticancer agents, Jäckel and Koksch [23]:on fluorine in peptide design approaching engineering, and Plenio: on the coordination chemistry of fluorine in fluorocarbons [25].

1.1. Context and perspective

In many disciplines, investigators have a deep understanding of their own speciality, but lack perspective of competing technologies. Historically, NMR investigators were physicists, who could develop sophisticated pulse sequences to manipulate nuclear spins, or radiofrequency engineers specialized in wave propagation and coil design. Alternatively, NMR investigators were chemists who could design new reporter molecules and assess metabolic processes. Today, the field is far more diverse. Beyond the integration of multiple disciplines into NMR, increasingly, there is recognition that often no single technology will optimally solve a problem, but multidisciplinary teams need to understand the strengths and weakness of diverse technologies and exploit multiple modalities. This review will promote the virtues and unique capabilities of ^{19}F NMR, but it is important to recognize competing technologies. In the United States, increased emphasis on multimodality imaging and cross-disciplinary research is now driven by the formation of the National Institute for Biomedical Imaging and Bioengineering (NIBIB) [31] and Cancer Imaging Program (CIP) of the NCI [32]. Moreover, new learned societies are dedicated to imaging in general, for example, Society of Molecular Imaging (SMI) [33], as opposed to being devoted to a specific modality (e.g., International Society of Magnetic Resonance in Medicine (ISMRM) [34] or Society of Nuclear Medicine [35]) and many journals have published issues reviewing diverse imaging methods [36–39].

Proton MRI has the great advantage of using spin physics to interrogate tissue water revealing anatomy and pathophysiology based on cellular and tissue properties. Nonetheless, it is often enhanced by the introduction of paramagnetic contrast agents at micromolar concentrations. Fluorine MRI typically requires

UNCORRECTED PROOF

Comp. by: RMervin Date:19/11/07 Time:18:07:54 Stage:First Proof File Path://
pchns1301/WOMAT/Production/PRODENV/0000000001/0000006424/0000000016/
0000749453.3D Proof by: QC by: ProjectAcronym:bs:AFS Volume:00005

millimolar concentrations of reporter molecules. In this respect, radionuclide and optical imaging techniques can offer far superior sensitivity, potentially with pico to nanomolar requirements. Fluorescence imaging is becoming more attractive with the commercial availability of many labeling kits [40] and new instrumentation, which allows spectral deconvolution [41]. However, fluorescence imaging can suffer from signal quenching and is generally a two-dimensional technique. Recently, 3D fluorescence is becoming feasible in small animals [42,43]. Nanoparticles (quantum dots) offer particularly high sensitivity although current generations would be inappropriate for human application, since they use highly toxic elements, such as cadmium and mercury [44]. Fluorescent proteins can also be generated *in situ*; cellular transfection can generate green fluorescent protein (GFP) or longer wavelength proteins [45]. Alternatively, cells may be transfected with a bioluminescent imaging (BLI) reporter such as luciferase, which emits light upon interaction with luciferin substrate [38,46]. Again, this is becoming feasible in three dimensions in small animals [47]. Generally, optical imaging technologies can use relatively cheap instrumentation.

Radionuclide imaging has similar sensitivity to optical imaging and is routinely used for studies of biodistribution, planar γ-scintigraphy, positron emission tomography (PET), and single photon emission computed tomography (SPECT) [48,49]. A major drawback with radionuclides is the limited shelf life of substrates, which may either decay (short half-life) or be subject to long-term radiolysis. Radioactivity also poses specific safety issues during production, reagent preparation, and ultimate disposal. Nonetheless, several PET and SPECT agents are in routine clinical use (e.g., fluorodeoxyglucose [FDG], Prostascint, ^{99m}Tc [50–52]). Other materials are effective for tracing the pharmacokinetics of labeled substrates. A major problem is ensuring that the label remains part of the molecule, since radioactivity provides no molecular characterization and unless specific analytical techniques such as high performance liquid chromatography (HPLC) are applied, only experience can indicate whether metabolic transformation has occurred.

Ultrasound and X-ray imaging are routine in the clinic and examine endogenous molecules based on signal reflection and/or absorption. These are starting to find application in small animal research [53]. Currently, they provide primarily anatomical information, although addition of contrast agents promises new applications [54].

Relatively, ^{19}F NMR has multiple strengths and virtues as described in the following sections. Briefly, fluorine containing molecules tend to be metabolically stable and have indefinite shelf life. The fluorine nucleus offers sufficient sensitivity for imaging, but also provides a very large chemical shift range immediately revealing metabolic transformations and allowing multiple molecules to be observed and identified simultaneously with potential applications to metabolomics. Fluorine MRI is readily combined with anatomical proton MRI providing high spatial resolution anatomy.

UNCORRECTED PROOF

Comp. by: RMervin Date:19/11/07 Time:18:07:55 Stage:First Proof File Path://
pchns1301/WOMAT/Production/PRODENV/0000000001/0000006424/0000000016/
0000749453.3D Proof by: QC by: ProjectAcronym:bs:AFS Volume:00005

1.2. ^{19}F as an *in vivo* NMR probe

^{19}F is 100% naturally abundant and the only stable isotope of fluorine. The nucleus has a nuclear spin $I = ½$ and a gyromagnetic ratio of 40.05 MHz/T, providing a sensitivity approximately 83% that of protons. The high gyromagnetic ratio generally allows the use of existing proton NMR instrumentation with the minimum of component adjustments. NMR has multiple strengths and virtues. Modern NMR instrumentation can be user friendly allowing a well-trained technician to undertake studies. However, NMR is intrinsically a complex tool providing potentially a multitude of information based on diverse parameters including signal intensity (SI), chemical shift (δ), and changes of chemical shift ($\Delta\delta$). In addition, signals are characterized by the transverse dephasing rate ($R_2^* = 1/T_2^*$), spin–spin or transverse relaxation rate ($R_2 = 1/T_2$) and spin–lattice or longitudinal relaxation rate ($R_1 = 1/T_1$). Indeed, each of these parameters have been exploited for specific ^{19}F NMR reporter molecules (Table 1). With care, the NMR signal can be quantitative, so that the integral (area under the peak) of a signal is directly proportional to the amount of material being interrogated. However, NMR may be considered relatively insensitive compared with some other modalities. Typically, millimolar concentrations are required to achieve a good signal in a reasonable amount of time. The precise detection sensitivity is governed by numerous parameters including the volume of interrogation, the required spatial resolution, and relaxation properties of the molecule, and its tendency to accumulate or disperse from a region of interest. Perhaps, most important is the temporal resolution since signals may be averaged over many hours. Increasingly, there are attempts to target fluorinated agents to accumulate at a site of interest, for example, using specific antibodies [55,56] and low-molecular weight ligands [57].

The simplest concept of NMR is that of chemical shift. In this context, ^{19}F is exceptionally sensitive to molecular and microenvironmental changes. Fluorine NMR has a chemical shift range of approximately 300 ppm, as opposed to approximately 10 ppm for proton. Multiple different fluorinated agents may readily be detected simultaneously with minimal danger of signal overlap. To allow comparison between data from different molecules and different investigators, chemical shifts must be referred to a standard. The International Union of Pure and Applied Chemistry (IUPAC) ^{19}F NMR chemical shift standard is fluorotrichloromethane ($CFCl_3$) [58]. Using this agent, the range of chemical shifts of most organic fluorinated compounds is 0–250 ppm. However, this volatile solvent is not convenient for most biomedical applications and thus, secondary standards are usually preferred. We favor sodium trifluoroacetate (CF_3CO_2Na or NaTFA). This has the advantage of being readily available, quite nontoxic, and may be used as either an external, or indeed, internal chemical shift standard in biological investigations. It should be noted that fluorine chemical shifts can be strongly solvent dependent and vary with dilution [59]. Fluorine may ultimately be described on a ϕ scale, extrapolated to infinite dilution, under which

UNCORRECTED PROOF

Comp. by: RMervin Date:19/11/07 Time:18:08:00 Stage:First Proof File Path://pchns1301/WOMAT/Production/PRODENV/000000001/000000424/000000016/0000749453.3D Proof by: QC by: ProjectAcronym:bs:AFS Volume:00005

UNCORRECTED PROOF

Table 1. Fluorinated reporter molecules

Parameter	Indicator (example)	NMR parameter	References (representative)
Physical interactions			
pO_2	Perfluorocarbons	R_1 (R_2)	[9,10,222,351,407]
	For example, hexafluorobenzene	$\Delta\delta$	[408]
pH	FPOL, DFMO, ZK150471	$\Delta\delta$, J	[11,280,301,303,409]
$[Na^+]$	F-cryp-1	δ, ratio	[410]
$[Ca2^+]$	5F-BAPTA	δ, ratio	[8,295,311]
$[Mg2^+]$	5F-APTRA	δ, ratio	[321]
Membrane/chloride potential	TFA	ratio	[287,411]
Chemical interactions			
Gene activity	PFONPG, 5FC	$\Delta\delta$	[147,294,374,378]
Nitric oxide	NN•[a]	$\Delta\delta$	[412]
Hypoxia	F-misonidazoles	Integral	[351,413]
Glycolysis	FDG	Integral	[331]
Drug metabolism	5FU, gemcitabine	Integral	[17,63]
Protein catabolism	DLBA	Integral	[414]
Disease specific receptors	Nanoparticles	Integral	[56,57]
Passive reporters			
Temperature	PFCs	Ratio	[5,207,415]
Blood flow	Freon FC-23	Integral	[401]
Cell volume	TFM	integral	[287]
Diffusion	FDG	ADC	[416]
Vascular volume	Fluorocarbon emulsion	Integral	[398,417]
Lung function	PFC; SF_6	Integral	[384,386,387]
GI function	PFC	Integral	[69,392]
Myocardial infarction	MP-312	Integral	[418]

[a] 2-(2,6-Difluorophenyl)-4,4,5,5-tetramethyl-4,5-dihydro-1*H*-imidazol-3-oxide-1-oxyl.

Comp. by: RMervin Date:19/11/07 Time:18:08:01 Stage:First Proof File Path://
pchns1301/WOMAT/Production/PRODENV/0000000001/0000006424/0000000016/
0000749453.3D Proof by: QC by: ProjectAcronym:bs:AFS Volume:00005

conditions CF_3CO_2H is quoted as -76.530 ppm. For precise measurements, it may be critical for both the chemical shift standard and molecule of investigation to be under precisely the same conditions (necessitating an internal standard). External standards, for example, in glass capillaries, may be subject to small susceptibility effects causing errors in estimation of absolute chemical shift. However, they provide more reliable quantitation standards for SI. Chemical shift is the mainstay of detecting and classifying molecules and detecting and identifying metabolic products of agents. While there have been many theoretical exercises on fluorine chemical shift it can often be quite unpredictable and occurs across an exceptionally large range. In 1971, Emsley and Phillips [60] published a 520-page review of the theory relating to ^{19}F NMR chemical shifts followed by a 673 page compilation of coupling constants [61].

Scalar coupling constants of fluorine are typically much larger than proton. For geminal fluorine atoms, $^2J_{FF}$ may be in the range of 200–800 Hz, while $^3J_{FF}$ is often less than 1 Hz, yet $^4J_{FF}$ may reach 20 Hz: such nonmonotonicity can be confusing and large long range couplings $^{6or7}J_{FF}$ are also encountered [18,59,61,62]. Proton fluorine coupling constants are $^2J_{FH} \sim 45$–90 Hz and $^3J_{FH}$: 0–53 Hz. While fluorine carbon coupling is typically large ($^1J_{CF} > 200$ Hz), it generally not observed unless the carbon is enriched with ^{13}C. However, as a corollary, fluorine coupling is observed clearly and extensively in ^{13}C NMR spectra. To avoid complexity of fluorine–fluorine coupling, it may be important to include fluorine as a symmetrical moiety, for example, a trifluoromethyl group, as opposed to asymmetric geminal fluorine atoms or a single fluorine atom. Likewise, a CF_3 moiety will generally avoid fluorine–hydrogen couplings. Since ^{19}F NMR is often detected by retuning a proton channel, proton decoupling may not be available.

Representative drugs, which include fluorine atoms and for which *in vivo* NMR has been reported are shown in Fig. 1 [17,63–73]. Furthermore, many drugs in early preclinical testing include fluorine atoms: the prevalence of fluorine atoms may reach 20% of all candidate agents [19]. Introduction of fluorine requires care. While the carbon fluorine bond is particularly strong, any release of fluoride or metabolites such as mono- or difluoroacetate can lead to exceedingly toxic products. For reporter molecules or pharmacological drugs, it is clearly important to minimize inadvertent toxicity. In this respect, the trifluoromethyl (CF_3) group is particularly suitable, since it resists degradation and for NMR avoids fluorine–fluorine couplings. In pharmaceuticals and agrochemicals, fluorine occurs in many forms ranging from a single fluorine atom to as many as six or nine identical fluorines (Table 2). In terms of NMR detection, the more equivalent fluorines, the stronger the signal. However, fluorine will modulate the properties of a molecule, since the fluorine atom is exceedingly electronegative and the CF bond strongly polarized. While the van der Waals radius of a fluorine atom is quite similar to a proton, the electronegativity alters electronic configuration modulating pK_a. For the series of acetic acids p$K_a(CH_3CO_2H) = 4.76$, p$K_a(CH_2FCO_2H) = 2.59$, p$K_a(CHF_2CO_2H) = 1.24$, and p$K_a(CF_3CO_2H) = 0.23$ [19]. Similar changes have been reported for a

UNCORRECTED PROOF

Comp. by: RMervin Date:19/11/07 Time:18:08:03 Stage:First Proof File Path://
pchns1301/WOMAT/Production/PRODENV/0000000001/0000006424/0000000016/
0000749453.3D Proof by: QC by: ProjectAcronym:bs:AFS Volume:00005

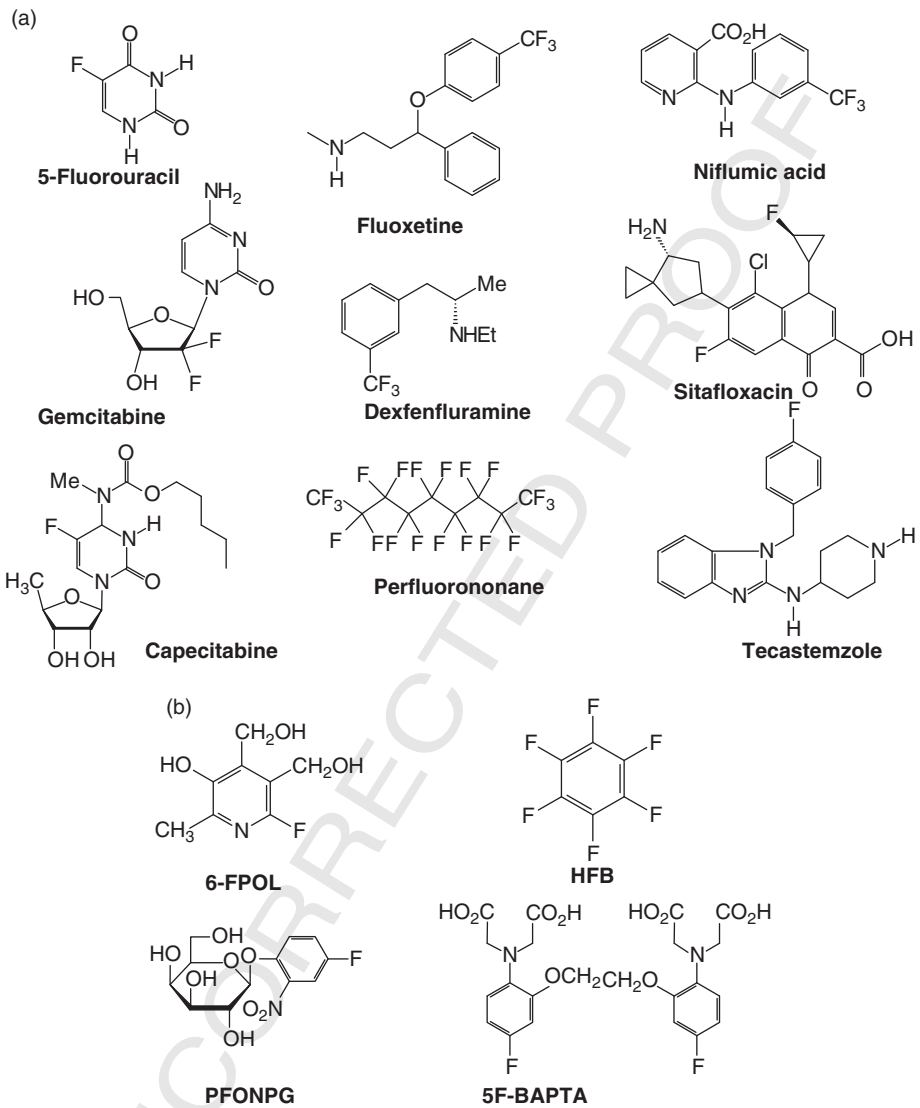

Fig. 1. Continued

series of fluoromethyl alanines (Table 3) [74]. The trifluoromethyl group is often considered to be equivalent to the introduction of an isopropyl group. Fluorine not only perturbs the electronic structure of a molecule, but also alters the hydrophobicity [75]. Indeed, in many cases, particularly for agrochemicals, fluorine is specifically added to reduce the water solubility of molecules, so they are retained more effectively on the waxy cuticle of plants [26]. Fluorine modifies lipophilicity and ability to cross membranes, such as the blood–brain barrier, which is pertinent to the extensive applications in anesthetics and psychiatric drugs [76].

UNCORRECTED PROOF

Comp. by: RMervin Date:19/11/07 Time:18:08:04 Stage:First Proof File Path://
pchns1301/WOMAT/Production/PRODENV/0000000001/0000006424/0000000016/
0000749453.3D Proof by: QC by: ProjectAcronym:bs:AFS Volume:00005

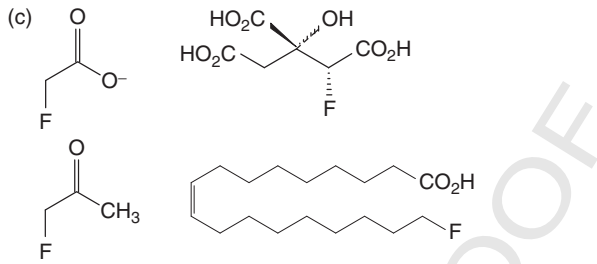

Fig. 1. (a) Representative fluorinated molecules. Pharmaceuticals for which clinical or preclinical *in vivo* NMR studies have been reported: 5-fluorouracil (5FU) [16,17,63], gemcitabine [65], and capecitabine [73] are anticancer drugs; fluoxetine [162] and dexfenfluramine [72] have neurological activity, sitafloxacin [66] is an antimicrobial, niflumic acid [67] is a nonsteroidal anti-inflammatory, tecastemzole [68] is an experimental antihistamine and perfluorononane has been proposed for GI imaging [69]. (b) Published ^{19}F NMR reporter molecules: 6-FPOL (6-fluoropyridoxol) is a pH reporter [11], hexafluorobenzene (HFB) is used for oximetry [10], PFONPG is a gene reporter for β-gal [294], and 5FBAPTA measures [Ca^{2+}] [295]. (c) Natural products incorporating fluorine atoms: fluoroacetate, fluorocitrate, fluoroacetone, and fluorooleic acid [4].

Fluorine chemistry has made major progress over the last 10–15 years and now many reagents are available for derivatization [24]. However, many require quite severe conditions using such materials as hydrogen fluoride [77], various metal halides such as SeF_4 [78], WF_6 [79], XeF_2 [80], and SbF_5 [81], or fluorine itself [82]. In some cases, a fluorine moiety may be introduced with *S*-ethyl trifluoroacetate (SETFA) [83] or trifluoroacetic anhydride [84]. It is often preferable to use a starting material that already includes a fluorine or multiple fluorine atoms, which may be introduced using relatively mild conditions, as explored extensively in the generation of fluorinated peptides [23].

While only a single isotope of fluorine is available for NMR, fluorine is finding increasing use as ^{18}F for PET (see other articles in this volume). While ^{18}F has a limited half-life ($t_{½} = 110$ min), it has found major application in the detection of tumors including Medicare reimbursed studies with FDG within the last 5 years. There is active interest in the pursuit of other ^{18}F agents to detect parameters such as hypoxia or mitosis [85–90]. The greatest strength of PET is that it may use nano to femtomolar concentrations, as opposed to the milli to micromolar concentrations required for NMR. However, ^{18}F simply provides a count of molecular concentration, that is, detecting radioactive decay with no indication of multiple substrates or metabolites. Thus, it may require rigorous HPLC or other analyses to strictly determine the fate of a drug. Meanwhile, ^{19}F can allow the detection of multiple agents, and metabolites simultaneously based on chemical shift. ^{19}F is indefinitely stable and the lack of radioactivity provides not only a long shelf life, but minimizes any issues of disposal of hazardous waste. Moreover, any fluorine MRI detection is readily correlated with the exquisite anatomy provided by routine proton MRI.

UNCORRECTED PROOF

Comp. by: RMervin Date:19/11/07 Time:18:08:07 Stage:First Proof File Path://
pchns1301/WOMAT/Production/PRODENV/0000000001/0000006424/0000000016/
0000749453.3D Proof by: QC by: ProjectAcronym:bs:AFS Volume:00005

Table 2. Fluorine-containing pharmaceuticals and agrochemicals [22,26,28]

Number of equivalent F-atoms	Molecular structure	Name	Use	Relevant references
1		Gefitinib ZD1839 Iressa®	Anticancer drug	[419,420]
1 + 1		Diflunisal Dolobid®	Anti-inflammatory drug	[182]
3		Flutamide Eulexin®	Anti-androgen drug	[181,421]
3		Flucarbazone	Herbicide	[422]

UNCORRECTED PROOF

Comp. by: RMervin Date:19/11/07 Time:18:08:09 Stage:First Proof File Path:// pchns1301/WOMAT/Production/PRODENV/0000000001/0000006424/0000000016/ 0000749453.3D Proof by: QC by: ProjectAcronym:bs:AFS Volume:00005

[423]

Bistrifluron

Insecticide

3 + 3+ 2

[424]

Roflumilast

Anti-inflammatory(asthma) phosphodiesterase (PDE) 4 inhibitor

2

[425]

Hexaflumuron

Insecticide

2 + 2 + 2

[426]

Fulvestrant

Faslodex®

Anti-androgens drug

3 + 2

UNCORRECTED PROOF

Comp. by: RMervin Date:19/11/07 Time:18:08:11 Stage:First Proof File Path://
pchns1301/WOMAT/Production/PRODENV/0000000001/0000006424/0000000016/
0000749453.3D Proof by: QC by: ProjectAcronym:bs:AFS Volume:00005

3 + 2 + 2 + 1	[427]	Lufenuron	Insecticide	
6 + 3	[183]	T 0901317	Anticancer drug	
1	[428]	Fludarabine	Topoisomerase inhibitor	
1 + 1	[429]	Flutriafol	Fungicide	
1	[430]	Sarin	Toxicant	

UNCORRECTED PROOF

Comp. by: RMervin Date:19/11/07 Time:18:08:15 Stage:First Proof File Path://
pchns1301/WOMAT/Production/PRODENV/0000000001/0000006424/0000000016/
0000749453.3D Proof by: QC by: ProjectAcronym:bs:AFS Volume:00005

Table 3. ^{19}F NMR pH indicators

Reporter	Structure	pK_a	$\delta_{F(acid)}$* (ppm)	$\delta_{F(base)}$* (ppm)	$\Delta\delta$ (ppm)	Reported applications
3-Fluoro-2-methyl alanine		8.5	−143.2	−145.3	2.05	Intracellular pH, perfused liver, lymphocytes [74]
3,3-Difluoro-2-methyl alanine		7.3	−53.95	−55.95	2.00	Figure 8 [74]
3,3,3-Trifluoro-2-methyl alanine		5.9	−0.25	−2.35	2.10	[74]
DFMO		6.4	4.60	4.30	0.30	[286]
6-FPOL		8.2	−9.84	−19.56	9.72	Transmembrane pH gradient, blood, heart, tumor [11,290]

UNCORRECTED PROOF

Comp. by: RMervin Date:19/11/07 Time:18:08:18 Stage:First Proof File Path:// pchns1301/WOMAT/Production/PRODENV/0000000001/0000006424/0000000016/ 0000749453.3D Proof by: QC by: ProjectAcronym:bs:AFS Volume:00005

6-FPAM		7.05	−9.19	−19.19	10.07	Transmembrane pH gradient, blood, heart, tumor [11,291]
6-FPOL-5-NH_2		8.0	−7.57	−19.55	11.98	[291]
6-FPOL-5-α-CF_3		7.6	−4.45	−14.09	9.64	[291]
PFONP		6.9	−44.44	−55.76	11.32	Transmembrane pH gradient, blood [294,374]
OFPNP		6.0	58.77	61.01	2.24	Extracellular pH [294]

UNCORRECTED PROOF

Comp. by: RMervin Date:19/11/07 Time:18:08:19 Stage:First Proof File Path:// pchns1301/WOMAT/Production/PRODENV/0000000001/0000006424/0000000016/ 0000749453.3D Proof by: QC by: ProjectAcronym:bs:AFS Volume:00005

5FNEAP-1	6.85	35.60**	24.70**	10.90	Extracellular pH [298]
N,N-(methyl-2-carboxyisopropyl)-4-fluoroaniline	6.8	−36.00	−49.50	13.50	*In vivo* pH measurement agents [297]
4-Fluoro benzene boronate (FBA)	8.7	−34.50	−43.50	8.80	*In vivo* pH measurement agents [431]
Fquene	6.7	11.82***	8.73***	3.09	Intracellular pH, liver of rats [296]

UNCORRECTED PROOF

Comp. by: RMervin Date:19/11/07 Time:18:08:21 Stage:First Proof File Path://
pchns1301/WOMAT/Production/PRODENV/0000000001/0000006424/0000000016/
0000749453.3D Proof by: QC by: ProjectAcronym:bs:AFS Volume:00005

PCF_3ONP		5.6	13.49	14.52	1.03	Extracellular pH [299]
CF_3POL		6.8	15.15	16.76	1.7	Extracellular pH [18]
ZK 150471		7.16	−52.74****	−62.87****	−10.13	*In vivo* pHe probe, tumor and tissue [301,303, 304]

Unless otherwise noted, dilute $CF_3CO_2^-$ was used as chemical shift reference

** tetrafluoroterphthalic acid was used as standard, though variously in the experimental section NaF and hexafluorobenzene were used as standards

*** chemicals shifts quoted with respect to 5FBAPTA

**** intramolecular chemical shift difference.

UNCORRECTED PROOF

Comp. by: RMervin Date:19/11/07 Time:18:08:22 Stage:First Proof File Path://
pchns1301/WOMAT/Production/PRODENV/0000000001/0000006424/0000000016/
0000749453.3D Proof by: QC by: ProjectAcronym:bs:AFS Volume:00005

NMR is a particularly facile approach to analysis requiring minimal sample preparation: mixtures, turbid media, and organisms including biopsy specimens or living plants and animals or even patients may be examined directly. Feasibility is governed by sample volume and the need for appropriate magnetic resonance systems and radio frequency (RF) coils [91,92]. For small specimens ($<$1 ml), magnetic fields exceed 22 T (950 MHz proton) and routine analysis is available at and above 7 T. These high field systems usually use vertical narrow bore magnets which can accommodate small samples of solutions (analytical and *in vitro* investigations) and sometimes mice. Small animal studies are most commonly performed in horizontal bore systems at 4.7 T, but increasingly systems are available at 7 and 9.4 T. Humans are now routinely studied at 3 T with research systems up to 12 T. Figure 1 shows representative drugs, which have been studied by ^{19}F NMR in clinical trials.

Proton NMR is potentially more versatile, since protons are essentially ubiquitous. However, this also provides a major drawback—crowded signals across limited chemical shift dispersion. Moreover, the water component of tissues can approach 70% water leading to signals approaching 80 M, as compared with mM metabolites. Elegant water suppression methods have evolved over the years, but often obliterate extended spectral windows around water or are limited to specific molecular structures exhibiting multiquantum detectability [93–95]. Lipid signals may also interfere with detection. Samples may be subjected to D_2O exchange, but this is perturbing. Deuterium enrichment is feasible providing up to 6,400-fold amplification [96], but the gyromagnetic ratio (γ) is much lower reducing ultimate sensitivity. Carbon is also ubiquitous in biological systems, but only 1.1% is NMR active as ^{13}C. This does provide the opportunity for selective isotopic enrichment and has proven fruitful for many studies [97], though ^{13}C can be expensive. Again, the gyromagnetic ratio is relatively low, precluding effective clinical studies at low fields.

The virtues of ^{19}F have led to the design and use of many reporter molecules in preclinical investigations (Table 1 and Fig. 1b). Since, there are few naturally occurring compounds containing fluorine, fluorinated molecules do not have to compete with background signal. Fluorine does occur extensively in bones and teeth, but the solid matrix causes very short T_2 values providing exceedingly broad signals, which can either be removed by deconvolution or electronic timing. Indeed, special rapid electronics are required for detecting solid state ^{19}F [98]. The spin lattice relaxation time T_1 can be quite long, but efficient use of rapid pulsing at the Ernst angle can accelerate spectral acquisition [99]. For aqueous solutions, relaxation agents, such as Gd-DTPA, can be added to accelerate relaxation [100–102], and indeed, this has been used to identify cellular compartmentation based on the ability of the contrast agent to relax extracellular material, but not intracellular [103]. Data acquisition efficiency can also be enhanced by interleaving or acquiring simultaneously ^{1}H and ^{19}F NMR providing both anatomical and pharmacological/physiological data simultaneously

UNCORRECTED PROOF

Comp. by: RMervin Date:19/11/07 Time:18:08:24 Stage:First Proof File Path://
pchns1301/WOMAT/Production/PRODENV/0000000001/0000006424/0000000016/
0000749453.3D Proof by: QC by: ProjectAcronym:bs:AFS Volume:00005

[91,92,104,105]. T_1 relaxation is extensively exploited with PFCs to measure pO_2, as described in detail in Section 3.1.1.

A few natural organofluorine compounds exist, most notably in plants (Fig. 1c). These are generally noted for their toxicity; most importantly, fluoroacetate enters the tricarboxylic acid (TCA) cycle and as fluorocitrate inhibits *cis*-aconitase [4,106,107]. Of course, toxicity provides an opportunity to generate specific poisons and fluoroacetate is widely used as a rodenticide providing opportunities for NMR [108]. ^{19}F NMR has been used for extensive studies of body fluids such as milk and urine with respect to xenobiotica [109–115].

Fluorine is increasingly used in industrial products ranging from fluoropolymers (e.g., Teflon) and liquid crystal components to anesthetics (e.g., isoflurane) to refrigerants and fire suppressants (halocarbons), numerous agrochemicals and several medicines [21,22,26,28]. While application of fluoro molecules will lead to increasingly crowded spectra, the large chemical shift range ensures that multiple molecules may be detected simultaneously. For example, in a study to investigate influence of tumor pH, on the anticancer drug 5FU in rat breast tumors, four molecules were detectable simultaneously (Fig. 2, the drug 5FU at -93.6 ppm, the extracellular pH reporter CF_3POL at -16.69 ppm, a chemical shift standard NaTFA (0 ppm) and two signals for the gaseous veterinary anesthetic isoflurane (-5.1, -10.99 ppm)). As noted above, we favor NaTFA as an internal standard for biological investigation, as compared with the IUPAC

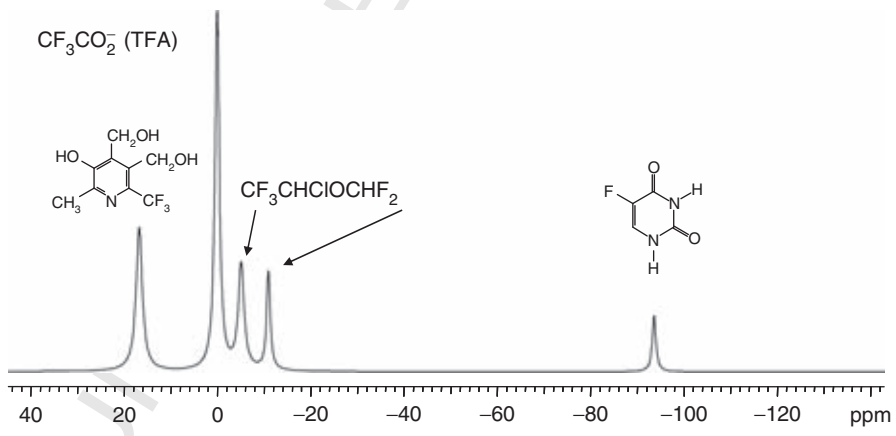

Fig. 2. Simultaneous detection of multiple fluorinated molecules *in vivo*. To explore the hypothesis that uptake of the anticancer drug 5FU by tumors is pH dependant, we infused 5FU (0.4 ml (50 mg/ml) IV), the extracellular pH reporter CF_3POL (400 mg/kg IP), and the chemical shift standard NaTFA (200 mg/kg IP) into an anesthetized rat (1% isoflurane) with a subcutaneous 13762NF breast tumor ($1.4 \times 1.5 \times 1.1$ cm). Thirty minutes after administration, all four molecules were detectable simultaneously in 17 min. At this stage, no metabolites of 5FU were detected.

Comp. by: RMervin Date:19/11/07 Time:18:08:25 Stage:First Proof File Path://
pchns1301/WOMAT/Production/PRODENV/0000000001/0000006424/0000000016/
0000749453.3D Proof by: QC by: ProjectAcronym:bs:AFS Volume:00005

standard ($CFCl_3$). In principle, the NaTFA was unnecessary here, since the isoflurane signals could have served as a secondary standard. However, it is important to note that the signals from anesthetics tend to have very short T_2^* [116–118], and thus, while they are visible in this pulse-acquire spectrum, they will tend to be ''lost'' in spin echo investigations, such as chemical shift imaging (CSI). While ^{19}F NMR investigations can generally be performed using existing ^{1}H equipment, some care is required, since probe and RF components may include fluorinated material which can give rise to spurious signals [119].

In the following sections, this review will separately consider industrial pharmacological and agrochemical agents (Section 2) followed by active (Section 3) and passive (Section 4) reporter molecules. Active reporter molecules may further be differentiated as those based on physical interaction with a substrate (Section 3.1) or those that undergo a chemical reaction (Section 3.2).

2. ^{19}F NMR FOR PHARMACOLOGY

Fluorine is often added to modulate biological activity of pharmaceuticals. Numerous reports describe changes in pK_a [74,75] (see also Table 3), lipophilicity [19,26,75], retention, resistance to degradation [22], enhanced binding [19,120] induced by selective incorporation of F atom or atoms. In other cases, F atoms have been used to probe molecular interactions or binding sites in order to enhance drug design, even if fluorine is ultimately not included in the drugs. It has been recognized that ^{19}F chemical shift is not only highly dependant on molecular structure and ionization, but also on the microenvironment. In early works, Dwek [121] and Gerig [122] reported the use of F moieties to probe interactions of oxy- and deoxyhemoglobin with cofactors such as diphosphoglycerate (DPG) under differential protonation [123]. Trifluoroacetylated chitotriose and *N*-trifluoroacetylglucosamine were used to probe active sites in lysozyme [124]. Many fluoro sugars have been used to study enzyme specificity, substrates, or inhibitors of enzymes such as glycogen phosphorylase and glucosidases [125–127].

Essentially, no background ^{19}F signal occurs and the sensitivity is sufficient to examine biological mixtures, for example, body fluids such as urine, blood, or milk for fluorinated metabolites [109–115,128,129]. This is being used both by academic laboratories and pharmaceutical companies to examine the fate of xenobiotica. In some cases, metabolites (degradation products or excretory bioconjugates) are derived from fluorine containing drugs; in other cases, ^{19}F labels may be added for the ADMET (absorption, distribution, metabolism, and excretion toxicity) process to learn about pathways, even though the labels are not included in the ultimate pharmaceuticals. In several cases, glucuronides have been identified as key detoxification products [130–132].

UNCORRECTED PROOF

Comp. by: RMervin Date:19/11/07 Time:18:08:26 Stage:First Proof File Path://
pchns1301/WOMAT/Production/PRODENV/0000000001/0000006424/0000000016/
0000749453.3D Proof by: QC by: ProjectAcronym:bs:AFS Volume:00005

2.1. Cancer chemotherapeutics

2.1.1. Fluoropyrimidines

With the significant developments in fluorination technology, inclusion of F atoms into pharmaceuticals and agrochemicals is becoming more feasible and popular [26,28]. Fluorine can yield subtle, but significant changes in drug activity [19,22,28]. The F atom is generally considered to have a structural size between H and OH, while CF_3 is similar to an isopropyl group [75]. The strong electronegativity can modulate electronic distributions influencing pK_a, particularly in proximity to delocalized aromatic structures [19,75]. F may be involved in hydrogen bonding altering binding and entry into enzyme pockets [23]. Many new industrial pharmaceuticals and agrochemicals incorporate a fluorine group providing a tool for NMR investigations. Figure 1 show drugs, which have been examined by ^{19}F NMR in clinical or advanced preclinical studies, while Table 2 shows diverse molecules including pharmaceuticals and agrochemicals, which could be strong candidates for ^{19}F NMR investigations, but for which reports are lacking in the public domain. Most studies to date have examined pharmacokinetics and metabolism of fluoropyrimidines, particularly 5-fluorouracil (5FU). 5FU was first developed in the 1950s and remains a primary drug in treatment of many cancers, but it has a narrow range of efficacy/toxicity [28,63,133]. Presumably, both response and toxicity are related to pharmacokinetics and there is interest in assessing dynamics of uptake, biodistribution, and metabolism. Patients with enhanced tumor retention of 5FU (''trappers'') may be expected to exhibit better response [134]. Such trapping is apparently a requisite, though not in itself sufficient for efficacy [17].

Given the importance and prevalence of 5FU, over 200 studies have reported ^{19}F NMR investigations in clinical trials and evaluation in animal models. Several detailed reviews consider metabolism, pharmacokinetics, and detectability of 5FU and its metabolites and the reader is referred to these [15–17,63]. 5FU requires anabolic conversion to nucleosides (e.g., FdUrd, FdUmp) and nucleotides for cytostatic activity, requiring the activity of various kinases and phosphorylases [17]. However, competing catabolic reactions convert 5FU to 5,6-dihydrofluorouracil (DHFU) and α-fluoro β-alanine (FBAL) in liver, in addition to several other molecules offering little toxicity [15,17,135]. FBAL is excreted by the kidneys. Localized NMR spectroscopy and low resolution CSI have examined pharmacokinetics [103,136–138]. NMR of excised tissue and body fluids has also provided insight into metabolism and can provide much higher sensitivity (e.g., μM). While studies *in vivo* are most attractive, studies of cultured cells can also provide important information.

The pharmacokinetics of 5FU are reported to be pH sensitive and thus, measurements of tumor pH may have prognostic value for drug efficacy. In tumors with lower pH, the retention of 5FU is considerably enhanced [139–141]. This has prompted

UNCORRECTED PROOF

Comp. by: RMervin Date:19/11/07 Time:18:08:27 Stage:First Proof File Path://
pchns1301/WOMAT/Production/PRODENV/0000000001/0000006424/0000000016/
0000749453.3D Proof by: QC by: ProjectAcronym:bs:AFS Volume:00005

investigations of the ability to alter pharmacokinetics by modulation of tumor pH to increase activity, for example, by breathing carbogen [142,143]. 5FU, its metabolites, and fluorinated pH reporter molecules can all be detected simultaneously by ^{19}F NMR (Fig. 2). Intriguingly, fluoronucleotides derived *in vivo* from 5FU exhibit sensitivity to changes in pH and could be used to measure intracellular pH (pHi), although the presence of a mixture of products may complicate interpretation [141,144,145].

Given the inherent dose-limiting toxicity of 5FU, various prodrugs and mixture formulations have been developed (e.g., capecitabine (Xeloda), Tegafur-uracil (Uftoral®), emitefur (3 (3-(6-benzoyloxy-3-cyano-2-pyridyloxycarbonyl)benzoyl)-1-ethoxymethyl-5-fluorouracil)) and ^{19}F NMR has played a role in analysis and development [16,63]. A new and potentially exciting application is assessment of prodrug therapy in conjunction with gene therapy; specifically, the use of cytosine deaminase (CD), to convert the relatively innocuous 5-fluorocytosine (5FC) to 5FU [146–150]. Several investigations have now reported ^{19}F NMR of the conversion of 5FC to 5FU based on the ^{19}F NMR chemical shift, $\Delta\delta = 2$ ppm [18,147,150,151].

Gemcitabine (Gemzar®) is a newer anticancer drug with a more favorable toxicity profile than 5FU. It comprises both sugar and pyrimidine moieties. In cells, it is phosphorylated and incorporated into DNA and to a lesser extent RNA, where it can inhibit DNA polymerases. It can also inhibit thymidine synthase. Given the significant clinical results and successful combination with radiotherapy, there is interest in optimizing activity based on ^{19}F NMR. Unlike 5FU, fluorine is now on the deoxyribosyl ring and the two geminal fluorines give rise to an AB quartet at -42 ppm ($\delta_{TFA} = 0$ ppm). This has been detected in human tumor xenografts by ^{19}F NMR following IP injection and kinetics have been investigated with respect to vasoactive drugs [65,152]. Metabolite signals have been observed in liver and bladder using CSI [153]. At low pH, the signals appear as an AB quartet, but they appear to collapse and broaden to a single signal at pH 8 (Fig. 3).

2.1.2. Other anticancer drugs

McSheehy *et al.* [154] presented a preliminary report of a novel thymidine synthase inhibitor, ZD9331, where both parent and metabolite peaks were detected at 4.7 T. Brix *et al.* [155] evaluated a trifluoromethylated derivative of 3-aminobenzamide, an inhibitor of poly(ADP-ribo) polymerase1 (PARP-1), as a potential radio sensitizer in Dunning prostate rat tumors and using CSI, detected separate signals from liver, muscle, and tumor revealing maximum tissue signals after 2 days. Spees *et al.* [156] followed pharmacokinetics of fluorine-labeled methotrexate in sensitive and resistant tumor xenografts in mice and found an inverse correlation between surviving fraction and area under the curve.

UNCORRECTED PROOF

Comp. by: RMervin Date:19/11/07 Time:18:08:28 Stage:First Proof File Path:// pchns1301/WOMAT/Production/PRODENV/0000000001/0000006424/0000000016/ 0000749453.3D Proof by: QC by: ProjectAcronym:bs:AFS Volume:00005

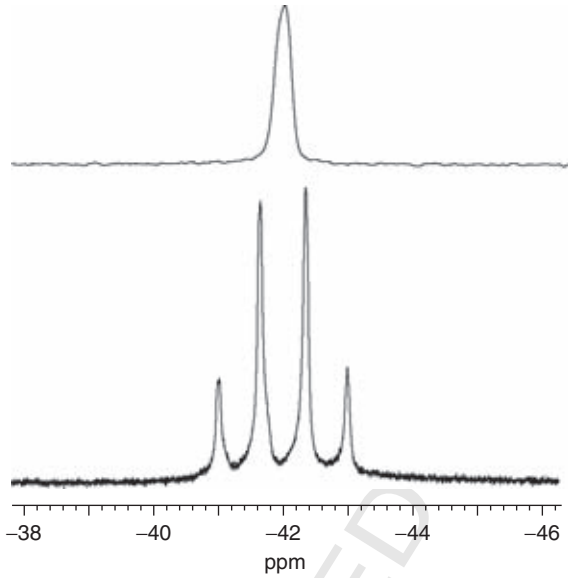

Fig. 3. ^{19}F NMR of gemcitabine. Lower spectrum shows a solution of gemcitabine hydrochloride at pH 3.2. For comparison, the upper spectrum was obtained in the presence of sodium hydroxide at pH 8.4. Each spectrum required about 1 min at 376 MHz (9.4 T) (data acquired in collaboration with Dr. Peter Peschke, DKFZ, Heidelberg, Germany).

2.2. Other drugs

Recognizing the exquisite sensitivity of ^{19}F NMR to microenvironment, inclusion of fluorine atoms in libraries of ligands has been used to probe molecular interactions based on changes in line width and chemical shift [157–160].

Following cancer chemotherapeutics, most *in vivo* ^{19}F NMR has examined psychiatric agents [14,161]. These can be particularly favorable when they incorporate a CF_3 moiety. Several reports investigated fluoxetine (Prozac) with studies ranging from biopsy tissue extracts to preclinical animal models and human volunteers [70,71,162]. The primary goal has been correlation of concentration with efficacy, for example, Henry *et al.* [70] explored the relative brain concentrations of *R* and *S* enantiomers versus a racemic mixture of fluoxetine in separate groups of patients. Other studies have examined fluvoxamine (a selective serotonin reuptake inhibitor—SSRI) to counter a possessive compulsive disorder [71,163]. Dexfenfluramine has been observed at brain concentrations $<10\ \mu$M [72]. ^{19}F NMR of trifluoperazine revealed multiple metabolites in rat brain extracts, but these were too weak and unresolved *in vivo* at 4.7 T [164]. Such studies have provided a single unlocalized spectrum corresponding to whole brain volume and lines are generally quite broad (2–3 ppm). Sassa *et al.* [165] used ^{19}F chemical shift imaging to detect haloperidol decanoate in schizophrenic patients.

UNCORRECTED PROOF

Comp. by: RMervin Date:19/11/07 Time:18:08:29 Stage:First Proof File Path://
pchns1301/WOMAT/Production/PRODENV/0000000001/0000006424/0000000016/
0000749453.3D Proof by: QC by: ProjectAcronym:bs:AFS Volume:00005

Other studies have examined fluoroquinolone antibiotics (fleroxacin) [166], antimicrobials (sitafloxacin) [66], nonsteroidal anti-inflammatory (niflumic acid [67]), and anti-histamines (tecastemizole [68]). However, the tecastemizole was only detected from 3 of 23 patients and the retention was found to be much shorter than the psychotropic drugs such as fluoxetine. Attempts to detect dexamethasone in the eye at 1.5 T failed [167]. PFCs have been used as a tamponade in eye surgery and residual PFC has been detected in patients at 1.5 T [168,169]. Indeed, this allowed pO_2 measurements based on spin lattice relaxation, as discussed in detail in Section 3.1.1.1. The PFC emulsion synthetic blood substitute Fluosol was proposed as a method of modulating tumor oxygenation [170] and it could be detected from surrounding tissues as long as 1 year after administration and tumor resection [171]. Perfluorononane has been used to explore GI tract in man and mice at 1.5 T [69]. This may provide insight into GI function or serve as a model for all drug delivery.

Many gaseous anesthetics are fluorinated, for example, halothane, enflurane isoflurane, sevoflurane, and desflurane. NMR studies of fluorinated anesthetics form some of the earliest *in vivo* applications of ^{19}F NMR [172–174]. Issues regarding the use of anesthetics are site of anesthetic action, duration of residence in the brain, and toxicity of metabolic byproducts. The results have been a source of debate and controversy. Wyrwicz and coworkers [175] addressed the issue of residence times of anesthetics in the brain and observed signals for prolonged durations after cessation of anesthesia. Global spectroscopy is straightforward, but anesthetics have a short transverse relaxation time (T_2^*) and signals may be lost in localized spectroscopy or imaging approaches. Very few clinical studies have reported ^{19}F NMR of anesthetics in the brain, though Menon *et al.* [13] demonstrated the feasibility of such studies and found halothane signal up to 90 min after the withdrawal of anesthetic. Lockwood *et al*. [176] studied isoflurane kinetics and showed biphasic elimination with decay halftimes of 9.5 and 130 min. Selinsky *et al*. [177,178] have studied the metabolism of volatile anesthetics showing generation of potentially toxic metabolites such as methoxydifluoroacetate, dichloroacetate, and fluoride ion from methoxyflurane.

The ability to detect drugs *in vivo* depends on multiple considerations. Obviously, the concentration at which drugs are administered is important together with the tendency to localize or clear from tissues. One would also expect multiple fluorine atoms to provide enhanced signal-to-noise over a single fluorine atom. Of course, they must be spectrally equivalent. Table 2 shows multiple diverse commercial molecules from the pharmaceutical and agrochemical fields, each of which has one or more fluorine atoms. Although no particular *in vivo* fluorine NMR has been reported, they are clearly prime candidates. Indeed, ^{19}F NMR has been exploited to assess pesticides as contaminants in food [179]: in oils and wine levels >1 mg/l, while in food extracts detection levels may approach parts per billion [180]. In particular, we note that some agents have multiple equivalent fluorine atoms. Flutamide [181] has a trifluoromethyl

UNCORRECTED PROOF

Comp. by: RMervin Date:19/11/07 Time:18:08:30 Stage:First Proof File Path://
pchns1301/WOMAT/Production/PRODENV/0000000001/0000006424/0000000016/
0000749453.3D Proof by: QC by: ProjectAcronym:bs:AFS Volume:00005

group and while there appear to be no references to *in vivo* NMR, ^{19}F NMR has been used to investigate drug formulation [181,182]. Bistrifluoron has two trifluoromethyl groups, but they are spectrally nonequivalent. By contrast, T009317 [183] has a hydroxyditrifluoromethylisopropyl group and would be expected to give high NMR sensitivity.

To obtain detectable signals (spectra, or images), sufficient fluorinated probe must be administered, though the concentration of probe in studies of living organisms should be as low as possible to avoid physiological perturbations or toxic side effects. For pharmaceuticals, fluorine labels are added for development, but their ultimate presence depends on optimal drug activity. By contrast, for reporter molecules, the fluorine atom is the key to efficacy and design is optimized for NMR detectability.

3. ACTIVE REPORTER MOLECULES

Many reporter molecules have been designed specifically to exploit fluorine chemical shift, coupling, or relaxation to reveal physiological parameters. Active agents typically fall into three categories: (i) molecules which enjoy a physical interaction, for example, PFCs, which exhibit exceptional gas solubility and reveal oxygen tension based on modification of relaxation parameters (Section 3.1.1); (ii) ligands designed to trap/bind specific entities, such as ions, specifically, but reversibly, for example, H^+ (pH) (Section 3.1.2), metal ions (Ca^{2+}, Mg^{2+}) (Section 3.1.3); and (iii) molecules which undergo irreversible chemical interaction modifying their structure, as revealed by a change in chemical shift (Section 3.2). These are represented by gene reporter molecules (Section 3.2.3), where substrates are cleaved by specific enzyme activity, and hypoxia agents (Section 3.2.2), which are modified by reductases and trapped. There are also passive agents, which occupy and hence reveal a space, compartment, or volume, for example, tumor blood volume (Section 4).

3.1. Physical interactions

3.1.1. In vivo *oximetry*

Oxygen is vital to the well being of normal mammalian tissues and deficits are associated with myocardial infarct, stroke, diabetic neuropathy, and cancer. In each case, lack of oxygen is associated with poor prognosis and a clinical goal is often to enhance tissue oxygenation. There is increasing evidence that hypoxia influences such critical characteristics as angiogenesis, tumor invasion, and metastasis [184–187]. Moreover, it has long been appreciated that hypoxic tumor cells are more resistant to radiotherapy [188]. Given that hypoxic tumors are more resistant to certain therapies, it becomes important to assess tumor oxygenation as part of therapeutic planning [189]. Patients could be stratified

UNCORRECTED PROOF

Comp. by: RMervin Date:19/11/07 Time:18:08:31 Stage:First Proof File Path://
pchns1301/WOMAT/Production/PRODENV/0000000001/0000006424/0000000016/
0000749453.3D Proof by: QC by: ProjectAcronym:bs:AFS Volume:00005

according to baseline hypoxia to receive adjuvant interventions designed to modulate pO_2, or more intense therapy as facilitated by intensity modulated radiation therapy (IMRT). Tumors, which do not respond to interventions, may be ideal candidates for hypoxia selective cytotoxins (e.g., tirapazamine [190]).

Thus, there is a vital need to be able to measure tissue pO_2 and many diverse technologies have been presented, as reviewed previously [10,191,192]. Some, such as near infrared spectroscopy and blood oxygen level dependent (BOLD) contrast MRI provide an indication of vascular oxygenation [2,193,194]. PET has been used to examine oxygen extraction fraction and hence metabolic activity based on uptake of $^{15}O_2$, but the half-life of oxygen-15 is exceedingly short ($t_{1/2} \sim 2$ min) [195,196]. Other modalities provide an indication of hypoxia [197,198]. In many cases, there is a desire to measure pO_2 directly and this may be achieved using polarographic electrodes [199,200], fiber optic probes [201], free radical probes with electron spin resonance (ESR) [191,202], or PFC probes with NMR [9,10], as described below.

3.1.1.1. PFC pO_2 reporters

NMR oximetry is based on the paramagnetic influence of dissolved oxygen on the ^{19}F NMR spin lattice relaxation rate of a PFC, as reviewed previously [10]. The solubility of gas, notably oxygen, in PFCs occurs as an ideal gas liquid mixture and thus, R_1 varies linearly with pO_2, as predicted by Henry's Law [5,10,203]. R_1 is sensitive to temperature, and magnetic field, but importantly, R_1 of PFCs is essentially unresponsive to pH, CO_2, charged paramagnetic ions, mixing with blood, or emulsification [204–206] and for the PFC emulsion of perfluorotributylamine (PFTB) (Oxypherol), we have shown that calibration curves obtained in solution are valid *in vivo* [207]. At any given magnetic field (B_o) and temperature (T)

$$R_1 = A + B\,pO_2, \tag{1}$$

where A is the anoxic relaxation rate and B represents the sensitivity of the reporter molecule to the paramagnetic contribution of oxygen and the ratio $\eta = B/A$ has been proposed as a sensitivity index [208]. Several PFCs have been used successfully for NMR oximetry and characteristics are summarized in Table 4. A particular PFC molecule may have multiple ^{19}F NMR resonances, and each resonance has a characteristic R_1 response to pO_2 and temperature [9,62]. Many PFCs (e.g., PFTB, perflubron (often referred to as perfluorooctylbromide [PFOB]) and Therox^{TM} (F44-E)) have several ^{19}F NMR resonances, which can be exploited to provide additional information in spectroscopic studies, but complicate effective imaging [209–211]. PFCs with a single resonance provide optimal signal-to-noise ratio (SNR) and simplify imaging: two agents hexafluorobenzene (HFB) [10,36,200,212–217], and perfluoro-15-crown-5-ether (15C5) [218–221] have found extensive use. While most pO_2 investigations have exploited the R_1 sensitivity, R_2 is also sensitive as reported by Girard *et al*. [222].

UNCORRECTED PROOF

Comp. by: RMervin Date:19/11/07 Time:18:08:34 Stage:First Proof File Path://
pchns1301/WOMAT/Production/PRODENV/0000000001/0000006424/0000000016/
0000749453.3D Proof by: QC by: ProjectAcronym:bs:AFS Volume:00005

Table 4. ^{19}F NMR characteristics and applications of PFCs for tissue oximetry

Name	Structure	Sensitivity to pO_2[a]	Number of ^{19}F resonances	Applications
HFB		$A = 0.0835$; $B = 0.001876$	1	Rat breast tumor, prostate tumor, human lymphoma xenograft [10,214, 215,217,267,270] (Fig. 7)
Perfluoro-15-crown-5-ether		$A = 0.345$; $B = 0.0034$	1	Tumor cells, mouse tumor, spleen, liver, rat breast tumor, rat brain [218,247,254]
FC-43 (Oxypherol)	$CF_2CF_2CF_2CF_3$ | $CF_3CF_2CF_2CF_2NCF_2CF_2CF_2CF_2CF_3$	$A = 1.09$; $B = 0.00623$	4	Liver, spleen, lung, eye, tumors, heart [5,243,244,256]
PFTP (Fluosol)	$CF_2CF_2CF_3$ | $CF_3CF_2CF_2NCF_2CF_2CF_2CF_3$	$A = 0.301$; $B = 0.00312$	3	Rat spleen, lung, tumors, cells [232,252,406]

UNCORRECTED PROOF

F-44E (Therox)	$CF_3(CF_2)_3CH{=}CH(CF_2)_3CF_3$	$A = 0.2525$; $B = 0.16527$	4	Rat spleen, liver, aorta, mouse Tumors [235,253]
PFOB (Imagent, Oxygen)	$Br(CF_2)_7CF_3$	$A = 0.2677$; $B = 0.12259$	7	Rat heart, rat prostate tumor, rabbit liver, pig lungs, phantom [241,250,432,433]
PTBD	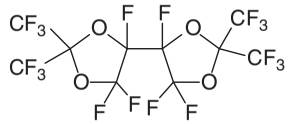	$A = 0.50104$; $B = 0.1672$	2	Phantom [434]

[a] R_1 (s^{-1}) $= A + B\,pO_2$ (Torr).
HFB, hexafluorobenzene.

UNCORRECTED PROOF

Comp. by: RMervin Date:19/11/07 Time:18:08:35 Stage:First Proof File Path://pchns1301/WOMAT/Production/PRODENV/0000000001/0000006424/0000000016/0000749453.3D Proof by: QC by: ProjectAcronym:bs:AFS Volume:00005

Comp. by: RMervin Date:19/11/07 Time:18:08:36 Stage:First Proof File Path://
pchns1301/WOMAT/Production/PRODENV/0000000001/0000006424/0000000016/
0000749453.3D Proof by: QC by: ProjectAcronym:bs:AFS Volume:00005

R_1 is sensitive to temperature and even a relatively small error in temperature estimate can introduce a sizable discrepancy into the apparent pO_2 based on some PFCs. The relative error introduced into a pO_2 determination by a 1 °C error in temperature estimate ranges from 8 Torr/°C for PFTB [207] to 3 Torr/°C for PFOB (perflubron) [223] or 15-Crown-5-ether [218] when pO_2 is actually 5 Torr. HFB exhibits remarkable lack of temperature dependence and the comparative error would be 0.1 Torr/°C [224]. Recognizing differential sensitivity of pairs of resonances within a single molecule to pO_2 and temperature, Mason *et al.* [207,225] patented a method to simultaneously determine both parameters by solving simultaneous equations. However, generally it is preferable for a pO_2 sensor to exhibit minimal response to temperature, since this is not always known precisely *in vivo* and temperature gradients may occur across tumors.

PFCs are extremely hydrophobic and do not dissolve in blood directly, but may be formulated as biocompatible emulsions for intravenous (IV) infusion. PFC emulsions have been developed commercially both as potential synthetic blood substitutes [226–229] and as ultrasound contrast agents [230,231]. Following IV infusion, a typical blood substitute emulsion circulates in the vasculature with a half-life of 12 h providing substantial clearance within 2 days [227]. Some investigators have examined tissue vascular pO_2, while PFC remained in the blood [206,232–235]. Flow can generate artifacts and correction algorithms have been proposed [236,237]. Primary clearance is by macrophage activity leading to extensive accumulation in the liver, spleen, and bone marrow [238,239]. This is ideal for investigating pO_2 in the liver or spleen, but a major shortcoming for other tissues, since animals may exhibit extensive hepatomegaly or splenomegaly though there is no apparent toxicity [227,238,240]. Long-term retention in tissues allows pO_2 measurements to be made *in vivo* and extensive studies have been reported in liver, spleen, abscess, perfused heart, and tumors [5,9,62,218,241–254].

3.1.1.2. Myocardial oxygenation

Due to motion, the heart is a particularly complex organ for measuring pO_2, yet understanding myocardial physiology with respect to infarcts has important implications for the clinical practice. Sponsored by the American Heart Association, we sought to develop a noninvasive approach for monitoring dynamic changes in myocardial oxygenation [243]. In Figs. 4 and 5, we present a case study demonstrating the ability to evaluate dynamic changes in myocardial oxygenation. Following IV or IP administration of PFC, some becomes sequestered in heart tissue. This is detectable using a surface coil placed over the heart of an open-chest rabbit, but for proof of principle investigations, we examined excised crystalloid perfused Langendorff rat hearts [243]. To achieve effective ^{19}F NMR signal, Sprague–Dawley rats were loaded with PFTB (Oxypherol: 1 ml/100g/day) for 9 days via tail vein injections. Hearts containing the sequestered PFC

UNCORRECTED PROOF

Comp. by: RMervin Date:19/11/07 Time:18:08:37 Stage:First Proof File Path://
pchns1301/WOMAT/Production/PRODENV/0000000001/0000006424/0000000016/
0000749453.3D Proof by: QC by: ProjectAcronym:bs:AFS Volume:00005

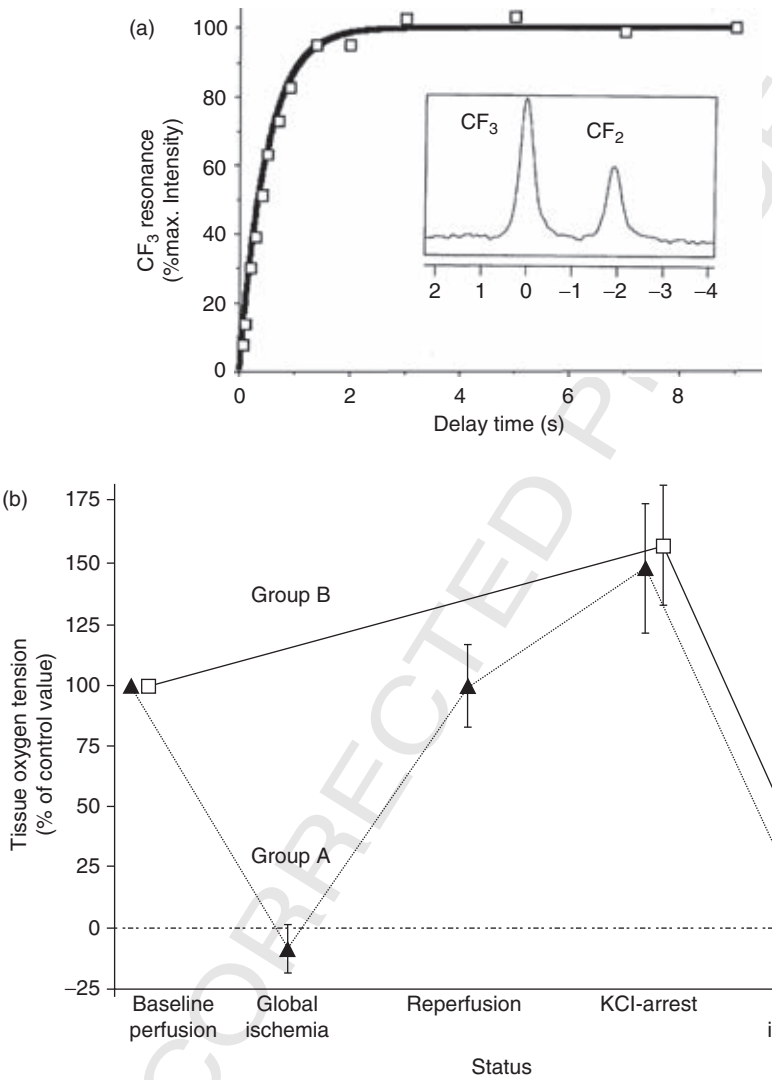

Fig. 4. Monitoring myocardial oxygenation using ^{19}F NMR of sequestered perfluorotributylamine. (a) Spin lattice relaxation (R_1) recovery curve obtained in 2 min for the CF_3 resonance from an isolated Langendorff perfused rat heart that had sequestered oxypherol. $R_1 = 2.11 \pm 0.08\,s^{-1}$ indicates 510 ± 30 Torr at 37 °C. Inset shows partial ^{19}F NMR spectrum with resolved downfield CF_3 and CF_2 resonances. (b) Steady-state R_1-measured pO_2 values of perfused rat hearts as percentage of normalized initial tissue pO_2 with respect to interventions. Hearts in Group A (▲) showed pO_2 equivalent to 0 Torr during total global ischemia (TGI), but returned to 100% upon reperfusion. KCl arrest resulted in increased tissue pO_2 from the excess available oxygen. Elevated pO_2 was observed in hearts in both Group B () (experiencing immediate arrest) and those in Group A (experiencing prior TGI). The previous ischemia experienced by Group A did not ''condition'' the hearts in terms of the

Comp. by: RMervin Date:19/11/07 Time:18:08:38 Stage:First Proof File Path://
pchns1301/WOMAT/Production/PRODENV/0000000001/0000006424/0000000016/
0000749453.3D Proof by: QC by: ProjectAcronym:bs:AFS Volume:00005

were excised and retrograde perfused by the Langendorff method at a pressure of 70 cm H_2O with modified Krebs–Henseleit buffer. A fluid-filled latex balloon was inserted into the left ventricle and connected to a pressure transducer to monitor developed pressure. Total global ischemia (TGI) was induced by halting flow to the aorta *in situ*. Cardiac arrest was induced by increasing the KCl in the perfusate to 20 mM.

In the absence of spatial selection, a ^{19}F NMR signal of PFTB could be obtained representing the whole heart in one pulse at 7 T using a volume coil [243]. Using a full T_1 relaxation sequence (e.g., Fig. 4), precise pO_2 values could be obtained. Global R_1 measurements provided an accuracy of 20–40 mmHg (Torr) and showed significant differences in cardiac tissue before and during ischemia ($p < 0.001$) and before and during KCl-induced cardiac arrest ($p < 0.001$, Fig. 4b). However, it was apparent that pO_2 changes occurred far more rapidly than could be assessed using a full T_1 curve. More rapid T_1 estimates are feasible using fewer recovery time delays on the relaxation curve, and indeed, a two-point comparison based on partial saturation allowed dynamic changes in pO_2 to be assessed with 1-s time resolution [243]. While any individual pO_2 estimate is less precise, the dynamics are apparent (Fig. 5). The decline in myocardial tissue pO_2 in KCl-arrested hearts undergoing ischemia was four to eight times slower than that of the normally beating hearts. Following the onset of ischemia, there was close correlation ($R = 0.93$) between the decline of pO_2 and developed pressure (Fig. 5e).

Global measurements related to TGI have some value, but clinical infarction is more likely to generate regional ischemia requiring spatial resolution for useful models. We have undertaken ^{19}F MRI of arrested hearts with respect to regional ischemia induced by ligation of the lower anterior descending (LAD) artery and found spatial heterogeneity of hypoxia [246]. However, acquisition times for the images were excessive (hours), so that monitoring pO_2 dynamics in the heart is restricted to preclinical studies. Use of a PFC with a single resonance could improve SNR and reduce imaging times. Targeting cardiac tissue directly could also improve SNR and this has been a goal of Wickline *et al*. [56].

3.1.1.3. Tumor oxygenation

The most extensive use of ^{19}F NMR oximetry has been to investigate tumor oxygenation with both acute studies of interventions and chronic studies of growth. Many investigations, including our own initial studies, used PFC emulsions to probe tumor oxygenation. Uptake and deposition of PFC emulsions in tumors is highly variable and heterogeneous with most signal occurring in well-perfused

R_1-measured pO_2. Global ischemia showed complete hypoxia for both groups with or without KCl arrest. Error bars represent one standard deviation of measurements from multiple hearts (data adapted from Ph.D. thesis of Himu Shukla, UT Southwestern 1994) [405].

UNCORRECTED PROOF

Comp. by: RMervin Date:19/11/07 Time:18:08:39 Stage:First Proof File Path:// pchns1301/WOMAT/Production/PRODENV/0000000001/0000006424/0000000016/ 0000749453.3D Proof by: QC by: ProjectAcronym:bs:AFS Volume:00005

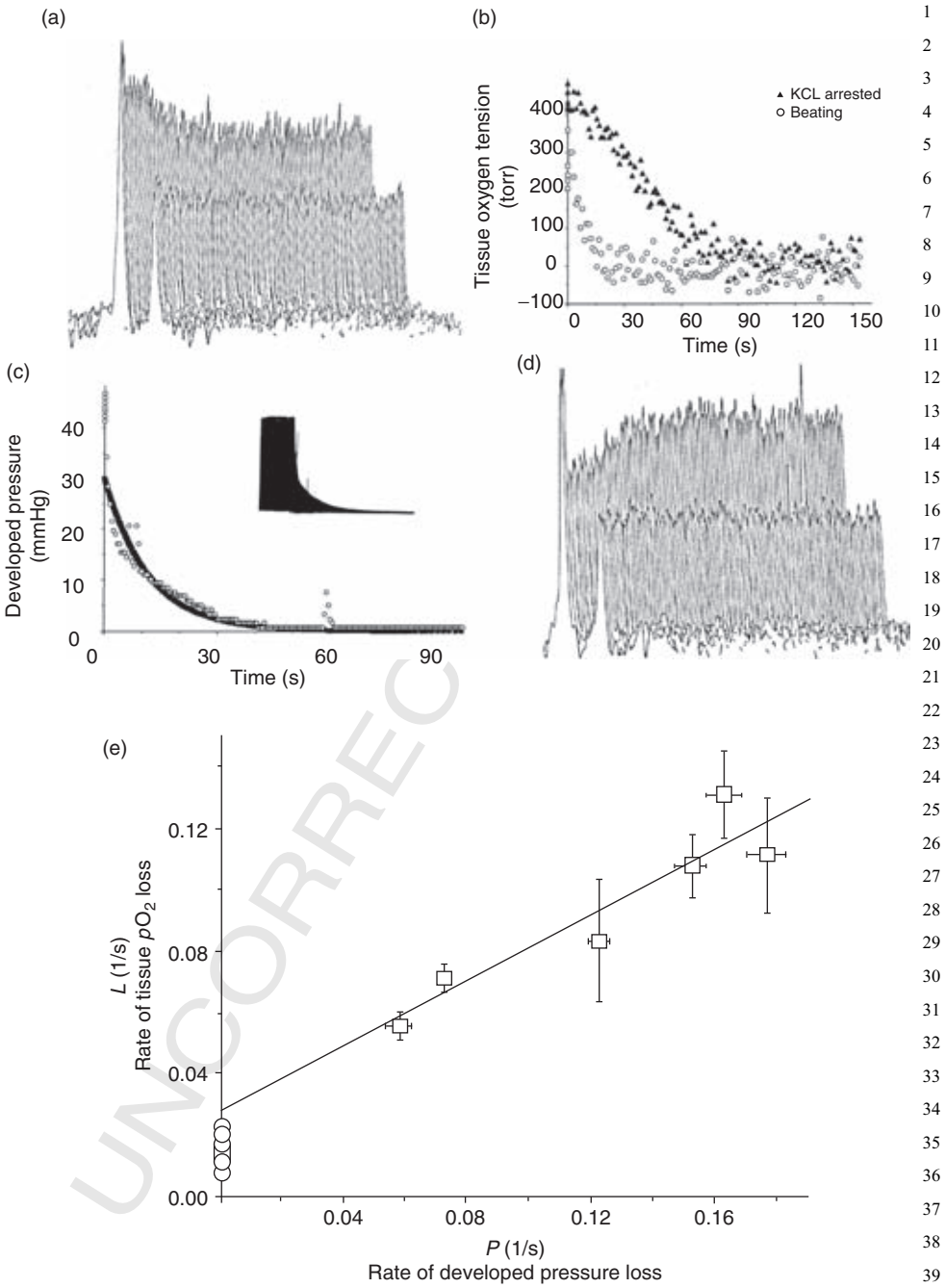

UNCORRECTED

Fig. 5. Correlation of myocardial oxygenation and developed pressure in excised Langendorff perfused rat hearts. (a) When NMR signals are acquired more rapidly than the time required for full relaxation, there is signal loss due to partial saturation. Comparing the

Comp. by: RMervin Date:19/11/07 Time:18:08:40 Stage:First Proof File Path://
pchns1301/WOMAT/Production/PRODENV/0000000001/0000006424/0000000016/
0000749453.3D Proof by: QC by: ProjectAcronym:bs:AFS Volume:00005

regions [242,254]. Indeed, pO_2 values measured soon after intravenous infusion, but following vascular clearance (typically 2 days), are generally high, approaching arterial pO_2 [242]. Thus, physiological measurements with respect to intervention are biased towards the well-perfused, well-oxygenated regions, which are often less important than hypoxic regions. Interestingly, following sequestration, PFC does not seem to redistribute within tissue, but remains associated with specific locations. Figure 6 shows residual PFC in the center of a tumor 18 days after systemic administration of Oxypherol. This was found to be essentially hypoxic tissue. When fresh PFC emulsion was administered and allowed to clear for two days, the original signal was still clearly delineated in shape, form, and intensity. However, a new signal was detected around the tumor periphery indicating the newly well-perfused regions. Such long-term tissue marking has been proposed as a form of noninvasive histology [255]. Long tissue retention has the advantage of facilitating chronic studies during tumor development and progressive tumor hypoxiation has been observed over many days [242,245].

To avoid the bias towards well-perfused regions and need to await vascular clearance, we developed an approach using direct intratumoral (IT) injection of neat PFC, which allows any region of interest in a tumor to be interrogated immediately [10]. Use of a fine needle ensures minimal tissue damage. Direct injection of neat PFC has been used by others to investigate retinal oxygenation [256–258] and cerebral oxygenation in the interstitial and ventricular spaces [221] and for the first time here, we show results in rat thigh muscle (Fig. 7).

We have identified HFB as an ideal reporter molecule [224]. Symmetry provides a single narrow ^{19}F NMR signal and the spin lattice relaxation rate is highly

---

intensity of a partially saturated signal to fully relaxed signal indicates R_1 and hence, pO_2. In (a), the larger CF_3 signal shows a decrease of about 15% compared with baseline under fully perfused, well-oxygenated conditions. Induction of TGI caused rapid loss of signal commensurate with increasing T_1 and reduced pO_2. Individual spectra were acquired in 1.1 s. The transition was complete within about 40 s. T_1 of the CF_3 resonance increased from 540–1240 ms causing the signal to decline from 86% to 68% accompanying TGI. The CF_2 resonance only changed from about 390 to 570 ms and this had minimal effect on signal intensity (SI) under these partial saturation conditions. (b) Dynamic data (the partial saturation spectra quantified using decay of the CF_3 resonance) from hearts made globally ischemic showed that an arrested heart (▲) consumed residual oxygen in the heart more slowly that a beating heart (). Note that the arrested heart started from a higher state of tissue oxygenation due to reduced oxygen demand. The monoexponential rate constants representing the loss of tissue pO_2 are: beating $L = 0.11\ s^{-1}$, arrested $L = 0.02\ s^{-1}$. (c) The pressure tracing of a perfused rat heart based on an intraventricular balloon catheter was digitized to quantitate the rate of ventricular pressure failure during ischemia. For this heart, a monoexponential curve fit to the pressure amplitude yielded a decay rate constant $P = 0.085\ s^{-1}$. (d) Reperfusion following 5 min TGI led to rapid reoxygenation of the rat hearts, revealed by increase in the CF_3 signal corresponding to shortening of T_1. (e) A strong linear relationship was found between the rate of heart tissue hypoxiation and ventricular pressure failure for rat hearts upon acute TGI ($r > 0.9$).

UNCORRECTED PROOF

Comp. by: RMervin Date:19/11/07 Time:18:08:41 Stage:First Proof File Path://
pchns1301/WOMAT/Production/PRODENV/0000000001/0000006424/0000000016/
0000749453.3D Proof by: QC by: ProjectAcronym:bs:AFS Volume:00005

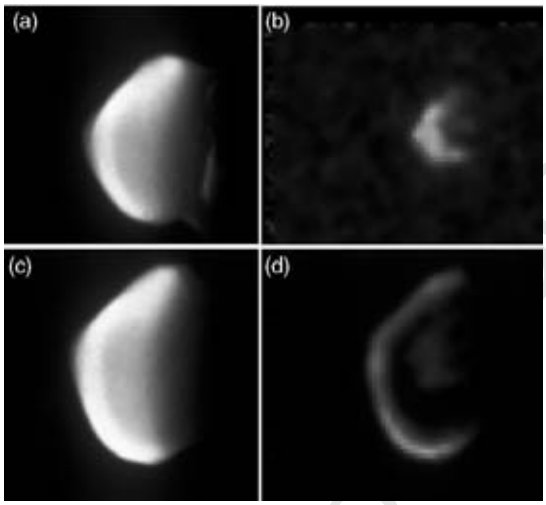

Fig. 6. *In vivo* MR histology. Following administration of Oxypherol (perfluorocarbon (PFC) blood substitute emulsion of perfluorotributylamine (PFTB)) to a Copenhagen rat bearing an AT1 tumor, ^{19}F NMR signal was initially detected around the tumor periphery [242]. Comparison of thin slices from 3D ^{1}H (a) and ^{19}F (b) MRI data sets obtained 18 days later showed that new tumor tissue grew around the labeled tissue and the ^{19}F label was exclusively in the central region and ^{19}F NMR oxygen tension measurements showed mean $pO_2 = 2.5$ Torr for a group of six such tumors. When fresh Oxypherol was administered (4×2.5 ml IV) and allowed to clear for 48 h, the new PFC was found around the tumor periphery, but the original signal was retained in the center (c) and (d). These data reveal the differential perfusion of tumor regions and tendency of IV administered reporters to target well-perfused regions (unpublished data obtained in collaboration with Drs. Anca Constantinescu and Peter Peschke).

sensitive to changes in pO_2, yet minimally responsive to temperature [224,259,260]. HFB also has a long spin–spin relaxation time (T_2), which is particularly important for imaging investigations. HFB is well characterized in terms of lack of toxicity [261,262], exhibiting no mutagenicity [263], teratogenicity or fetotoxicity [264], and the manufacturer's material data safety sheet indicates LD50 $>$ 25 g/kg (oral-rat) and LC50 95 g/m^3/2 h (inhalation-mouse). HFB had been proposed as a veterinary anesthetic and has been used in many species including ponies, sheep, cats, dogs, rats, and mice, but was abandoned due to its flammability [265]. Flammability is not a problem for NMR oximetry, where small quantities of liquid (typically, 50 μl) are injected directly into the tumor.

Initial studies used 10–20 μl HFB injected directly into the center or periphery of a tumor and pO_2 measurements indicated tumor heterogeneity [224,266]. Although data were acquired using nonlocalized spectroscopy, the highly localized signal ensured that regional pO_2 was measured. Subsequently, we developed an imaging approach: *FREDOM* (Fluorocarbon Relaxometry using Echo planar imaging for Dynamic Oxygen Mapping) [10], which typically provides

Comp. by: RMervin Date:19/11/07 Time:18:08:42 Stage:First Proof File Path://
pchns1301/WOMAT/Production/PRODENV/0000000001/0000006424/0000000016/
0000749453.3D Proof by: QC by: ProjectAcronym:bs:AFS Volume:00005

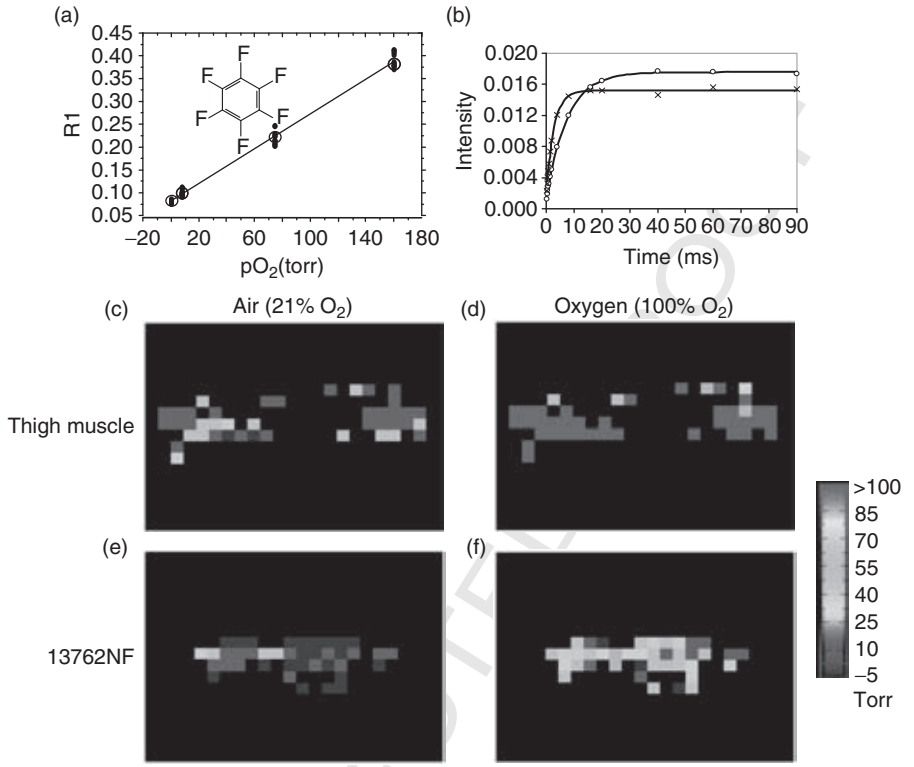

Fig. 7. *FREDOM*-tissue oxygen dynamics. A linear relationship is found between the spin lattice relaxation rate R_1 of hexafluorobenzene (HFB) and pO_2 (reprinted from *Methods in Enzymolology*, 386, Zhao D, Jiang L, Mason RP, Measuring Changes in Tumor Oxygenation., 378–418, Copyright (2004), with permission from Elsevier) [10]. ^{19}F NMR relaxation curves from a single voxel in rat leg muscle after direct administration of 50 μl HFB. Curves are shown during air breathing (circles; $T_1 = 7.37$ s, $pO_2 = 28$ Torr) and following switch to oxygen for about 20 min (crosses; $T_1 = 2.65$ s, $pO_2 = 156$ Torr), respectively. pO_2 map of rat thigh muscle during air berthing. Data obtained in 6.5 min, showing heterogeneity of baseline oxygenation. Mean $pO_2 = 20 \pm 1$ Torr. Following 20 min oxygen breathing, all the voxels in (c) showed increased pO_2 reaching a new mean $pO_2 = 158 \pm 6$ Torr. pO_2 map of 13762NF rat breast tumor, while rat breathed air (mean $pO_2 = 13 \pm 2$ Torr). Oxygenation is clearly lower than for muscle, above. During oxygen breathing, tumor pO_2 increased, though showing considerable heterogeneity of response with mean $pO_2 = 52 \pm 4$ Torr (See Colour Insert).

50–150 individual pO_2 measurements across a tumor simultaneously in about 6.5 min with a precision of 1–3 Torr in relatively hypoxic regions based on 50 μl injected dose (Fig. 7). In both muscle and tumor tissues, pO_2 heterogeneity is apparent when rats breathe air (pO_2 ranged from 0 to 100 Torr). Upon challenge with oxygen breathing, essentially all muscle regions showed a significant increase in oxygenation. Many tumors show little response to hyperoxic gas, but the 13762NF mammary tumor generally shows extensive response [217],

Comp. by: RMervin Date:19/11/07 Time:18:08:43 Stage:First Proof File Path://
pchns1301/WOMAT/Production/PRODENV/0000000001/0000006424/0000000016/
0000749453.3D Proof by: QC by: ProjectAcronym:bs:AFS Volume:00005

as seen in Fig. 7. We have used *FREDOM* to examine the effects of vascular targeting agents [36,267], vasoactive agents [215] and hyperoxic gases [10,200, 212–217,268–270]. We have shown that measurements are consistent with sequential determinations made using electrodes [271,272] and fiber optic probes (FOXY^{TM} and OxyLite®) [201,216]. Repeat measurements are highly reproducible and generally quite stable in tumors under baseline conditions. Results are also consistent with hypoxia estimates using the histological marker pimonidazole [212]. Most significantly, estimates of pO_2 and modulation of tumor hypoxia are found to be consistent with modified tumor response to irradiation [213,273]. Such prognostic capability could be important in the clinic, since it is known that relatively hypoxic tumors tend to be more aggressive and respond less well to radiation therapy [274–276]. Hitherto, we have lacked a ^{19}F MRI capability in our human systems in Dallas. However, Philips is promoting dual ^{19}F MRI capabilities on the new 3 T human systems [91,277] and we expect to be able to pursue translation of the *FREDOM* approach in the near future.

3.1.2. pH

pH is an important indicator of tissue health and acidosis may reflect ischemia and hypoxia. Historically, tumors were believed to be acidic (Warburg hypothesis) and the detection of neutral or basic environments by NMR led to initial controversy [278]. It was ultimately realized that ^{31}P NMR of endogenous inorganic phosphate (Pi) reflects primarily the cytosolic pH, which is often in the range 7.0–7.4, whereas tumor interstitial (pHe) may indeed be acidic, as previously observed using polarographic electrodes. This reversed pH gradient has important implications for partitioning of weak acid or base drugs, and thus, considerable effort has been applied to developing robust reporter molecules. ^{19}F NMR pH indicators (Table 3) represent three strategies: (i) development of molecules specifically designed for ^{19}F NMR, (ii) fluorinated analogues of existing fluorescent indicators, and (iii) exploitation of the ^{19}F NMR chemical shift sensitivity inherent in cytotoxic drugs. Many molecules exhibit chemical shift response to changes in pH, for example, the ^{19}F NMR resonance of 6-fluoropyridoxol (6-FPOL) [11,279]. On the NMR timescale, protonated and deprotonated moieties are generally in fast exchange, so that a single signal is observed representing the amplitude weighted mean of acid and base forms. pH is measured using the Henderson–Hasselbalch equation:

$$\mathrm{pH} = \mathrm{p}K_a + \log_{10}\left[\frac{\boldsymbol{\delta}_{obs} - \boldsymbol{\delta}_{acid}}{\boldsymbol{\delta}_{base} - \boldsymbol{\delta}_{obs}}\right] \quad (2)$$

where $\boldsymbol{\delta}_{acid}$ is the limiting chemical shift in acid, $\boldsymbol{\delta}_{base}$ is the limiting chemical shift in base, and $\boldsymbol{\delta}_{obs}$ is the chemical shift observed at a given pH. Due to the nonlinear form of the equation, greatest sensitivity is found close to the pK_a.

UNCORRECTED PROOF

Comp. by: RMervin Date:19/11/07 Time:18:08:44 Stage:First Proof File Path://
pchns1301/WOMAT/Production/PRODENV/0000000001/0000006424/0000000016/
0000749453.3D Proof by: QC by: ProjectAcronym:bs:AFS Volume:00005

Reporter molecules may readily access the interstitial compartment, but intracellular measurements are more difficult. Deutsch *et al*. [74,280] championed the use of ^{19}F NMR to measure intracellular pH primarily based on the series of agents 3-monofluoro-, 3,3-difluoro-, and 3,3,3-trifluoro-2-amino-2-methyl propanoic acid (Table 3). pH sensitivity is predicated on protonation of the amino group and it is immediately apparent that additional fluorine atoms influence the pK_a. These molecules have been successfully applied to pH measurements in cells [74,281–283] and isolated organs [74,284]. A significant problem is loading indicators into cells, but esters are relatively permeable, stable in water, and undergo nonspecific enzymatic hydrolysis intracellularly, liberating the pH-sensitive molecules [280]. This approach can lead to complex spectra including overlapping multiline ester and liberated free acid resonances from both intra- and extracellular compartments (Fig. 8) [285]. Widespread use of these molecules has been hindered by the problem of loading the indicators into cells and the relatively small chemical shift range approximately 2 ppm. Difluoromethyl ornithine (DFMO) represents another ^{19}F NMR sensitive amino acid, which is also a

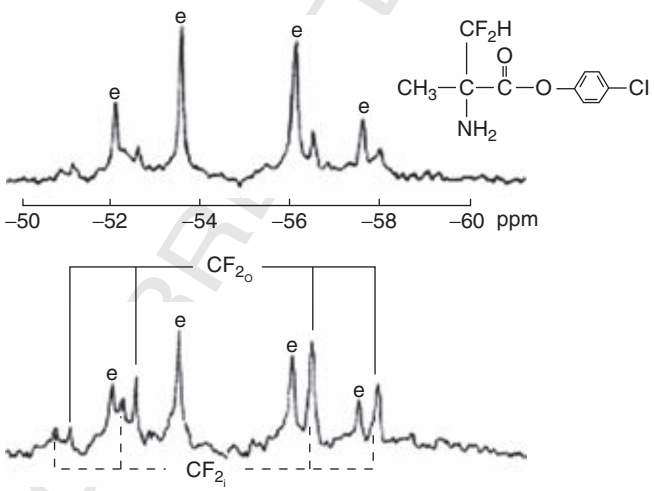

Fig. 8. pH measurement in cells. ^{19}F NMR of difluoromethylalanine *para*-chlorophenyl ester (1 mM) added to suspension of RINm5F cells (4% cytocrit). Spectra were taken at 4-min intervals (1,600 scans, 30° pulse, repetition rate = 5/s) with broadband proton decoupling. The resonances marked ''e'' arise from the ester form of the amino acid. The resonances in the lower spectrum marked ''o'' arise from extracellular free amino acid, whereas those marked ''i'' arise from intracellular free amino acid. Spectrum (a) 1–5 min; (b) 5–9 min after addition of ester to the cell suspension. The ester quartet (e) lines decreased in intensity, while the quartets of lines from the product of ester hydrolysis, intracellular difluoromethylalanine (CF_{2i}) and extracellular difluoromethylalanine (CF_{2e}), increased with time [partial figure reproduced from J. Taylor and C.J. Deutsch, ^{19}F nuclear magnetic resonance: measurements of [O_2] and pH in biological systems. *Biophys. J.* 1988; 53: 227–233 [406] with permission of the Biophysical Society].

UNCORRECTED PROOF

Comp. by: RMervin Date:19/11/07 Time:18:08:45 Stage:First Proof File Path://
pchns1301/WOMAT/Production/PRODENV/0000000001/0000006424/0000000016/
0000749453.3D Proof by: QC by: ProjectAcronym:bs:AFS Volume:00005

therapeutic drug. Unfortunately, its chemical shift response is even smaller and the chemical response is not monotonic, going though a reversal above the pK_a [286]. A large chemical shift range is important to ensure precise measurements of pH. When multiple cellular compartments are present there is less problem with signal overlap. Perhaps more importantly, any chemical shift perturbations due to other factors, such as susceptibly become less important [287–289]. Furthermore, the pK_a should be matched to the pH range of interest since the largest chemical shift response occurs close to the pK_a [74].

Aromatic reporter molecules tend to have a much larger chemical shift pH response. Analogs of vitamin B6, for example, 6-FPOL are highly sensitive to pH [11,279,290–292]. We showed that 6-FPOL itself readily enters cells and provides well-resolved resonances reporting both intra- and extracellular pH (pHi and pHe), simultaneously, in whole blood (Fig. 9) [279] and the perfused rat heart [290]. Ease of entry into blood cells may be related to facilitated transport, since vitamin B6 is naturally stored, transported, and redistributed by erythrocytes [293]. Intriguingly, most tumors cells show a single resonance only, suggesting that 6-FPOL does not enter. The somewhat basic pK_a = 8.2 is appropriate for investigations of cellular alkalosis, but it is not ideal for studies in the normal physiological range (6.5–7.5) [290].

Ring substitution allowed us to alter the pK_a and 6-fluoropyridoxamine (6-FPAM) offered superior characteristics with pK_a 7.05 [291]. As for 6-FPOL, we have observed intra- and extracellular signals in whole blood and perfused rat hearts [11,291] and in addition, specific tumor cells (Morris hepatoma

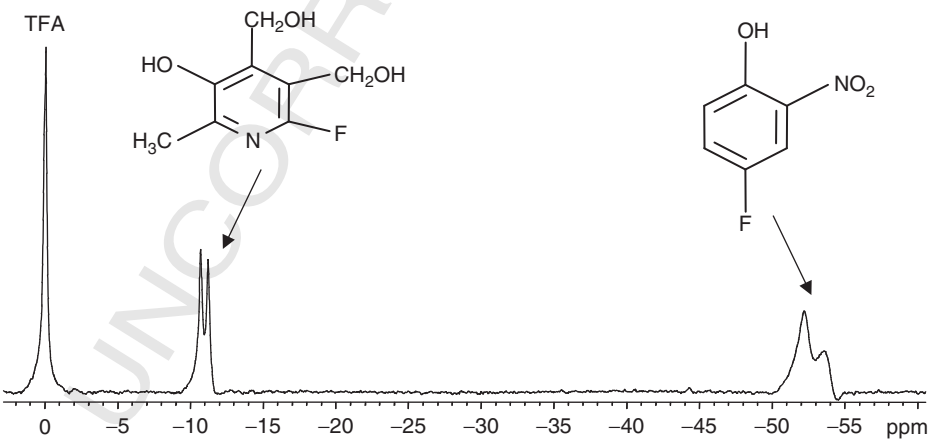

Fig. 9. Transmembrane pH gradient in red blood cells. ^{19}F NMR of 6-fluoropyridoxol (4.2 mg), PFONP (4.8 mg), and NaTFA in fresh wholerabbit blood (600 μl). Both pH indicators show split peaks arising from intra- and extracellular signals. Extracellular pH was measured using polarographic electrode pHe = 7.66 and compared with $pHe_{(PFONP)}$ = 7.55 and $pHe_{(FPOL)}$ = 7.55. ^{19}F NMR showed intracellular pH $pHi_{(PFONP)}$ = 7.16; $pHi_{(FPOL)}$ = 7.29.

UNCORRECTED PROOF

Comp. by: RMervin Date:19/11/07 Time:18:08:46 Stage:First Proof File Path://
pchns1301/WOMAT/Production/PRODENV/0000000001/0000006424/0000000016/
0000749453.3D Proof by: QC by: ProjectAcronym:bs:AFS Volume:00005

MH-Tk) showed uptake [18]. While modification of the 4-hydroxymethyl group to aminomethyl altered the pK_a favorably, the 5-isomer was minimally changed (Table 3) [291].

Noting the large chemical shift response of pyridines, we also explored fluorophenols as pH indicators. Like 6-FPOL, *p*-fluorophenols show a large chemical shift response $\Delta\delta$ 6.4–11.3 ppm, whereas *o*-fluorophenols have a smaller chemical shift range ($\sim$0.3–2.2 ppm) (Table 3) [294]. For comparison both 6-FPOL and PFONP (*p*-fluoro-*o*-nitrophenol) are shown to reveal pH gradients in whole blood giving comparable results and consistent with electrode measurements (Fig. 9). Fluorophenols must be used cautiously, since PFONP appears cytolytic for certain tumor cells and may act as an ionophore, by analogy with dinitrophenol.

Other aromatic pH reporters have been presented including analogs of fluorescent pH indicators. FQuene, a ^{19}F NMR sensitive analog of the fluorescent pH indicator quene-1, was used to measure intracellular pH in a perfused heart [295] and liver [296]. *o*-Methoxy-*N*-(2-carboxyisopropyl)-4-fluoroaniline has a chemical shift range approximately 17 ppm, but the pK_a (5.8) is less suitable for *in vivo* investigations. Modification to *N,N*-(methyl-2-carboxyisopropyl)-4-fluoroaniline [297] retained a substantial chemical shift range ($\Delta\delta$ 12 ppm) and produced a physiologically suitable pK_a (6.8), however, no biological studies have been reported. Metafluoro isomers showed considerably smaller chemical shift response to changes in pH. *N*-ethylaminophenol (NEAP) has been described with various analogs to detect pH or metal ions [298].

To enhance SNR, or reduce the required dose, a pH sensitive CF_3 moiety could be introduced in place of the F-atom. Trifluoromethylphenols show titration response, though by comparison with the fluorophenols (Table 3), the chemical shift response is typically smaller $\Delta\delta = 1.25$ ppm (*p*-CF_3ArOH, pK_a 8.5) to 0.4 ppm (*o*-CF_3-Ar, pK_a 7.92), as expected since electronic sensing must be transmitted through an additional C–C bond [299]. Importantly, the ^{19}F NMR signal occurs downfield from NaTFA, so that unlike 6-FPOL there is no interference from isoflurane signals [18]. While FPOL and FPAM provide both intra- and extracellular signals with varying ratios depending on cell type, 6-trifluoromethylpyridoxol (CF_3POL) is found to occur exclusively in the extracellular compartment, and thus reports pHe, or interstitial pH [18,300]. Frenzel *et al.* [301] have described a fluoroaniline sulfonamide (ZK150471) and its use has been demonstrated in mice and rats to investigate tumor pH [302,303]. This molecule is restricted to the extracellular compartment only [301,304], but combination with 31P NMR of Pi to determine pHi has been used to reveal the transmembrane pH gradient in mouse tumors [141]. A distinct problem with ZK150471 is that the pK_a differs in saline and plasma [304]. Most indicators require an additional chemical shift reference standard, for example, sodium trifluoroacetate, but NEAP [298], 6-FPOL-5-α-CF_3 [291], and ZK150471 [301] all have nontitrating intramolecular chemical shift references. pH measurements using 2-amino-3,3-difluoro-2-methyl propanoic acid is based on changes in the

UNCORRECTED PROOF

Comp. by: RMervin Date:19/11/07 Time:18:08:48 Stage:First Proof File Path://
pchns1301/WOMAT/Production/PRODENV/0000000001/0000006424/0000000016/
0000749453.3D Proof by: QC by: ProjectAcronym:bs:AFS Volume:00005

splitting of the AB quartet and this again avoids need for a chemical shift reference, but the splitting increases the complexity of the spectrum and reduces SNR (Fig. 8).

3.1.3. Metal ions

Since metal ions play key roles in cellular physiological processes many specific reporter molecules have been developed, mostly as fluorescent indicators incorporating extended aromatic and conjugated structures, where the wavelength of fluorescence depends upon specific binding of a metal ion. Several ^{19}F NMR reporters have been created by addition of fluorine atoms (Table 5).

Tsien [305] made an important breakthrough by establishing an approach for loading fluorescent metal ion chelators into cells using acetoxymethyl esters. He demonstrated 1,2-bis(*o*-aminophenoxy)ethane-*N,N,N′,N′*-tetraacetic acid (BAPTA) for detecting intracellular calcium ions and subsequently Metcalfe *et al*. [295] added *para*-fluoro atoms to the aromatic ring yielding a ^{19}F NMR responsive agent (5,5-difluoro-1,2-bis(*o*-aminophenoxy)ethane-*N,N,N′,N′*-tetraacetic acid (5FBAPTA)) (Table 5). Upon binding calcium, there is a change in chemical shift (Fig. 10).

Ideally, such a reporter molecule would have high specificity for the metal ion of interest. In fact, the F-BAPTA agents are found to bind several divalent metal ions, including Ca^{2+}, Zn^{2+}, Pb^{2+}, Fe^{2+}, and Mn^{2+} (Fig. 10) [306,307], but importantly, each metal ion chelate has an individual chemical shift, so that they can be detected simultaneously [308]. 5FBAPTA includes two fluorine atoms symmetrically placed to provide a single signal. Upon binding, there is slow exchange of Ca^{2+}, on and off the indicator, on the NMR timescale, so that separate signals are seen for the free and metal ion bound moieties, with chemical shifts of several ppm. Measurements are based on the signal ratio, avoiding the need for a chemical shift reference, in contrast to pH reporters, which are usually in the fast exchange regimen. Calcium concentration may be calculated from the formula [308]

$$[Ca^{2+}] = K_D \frac{[Ca - FBAPTA]}{[FBAPTA]} \quad (3)$$

However, the dissociation constant (K_D) does depend on pH, ionic strength, and the concentration of free Mg^{2+}, which need to be estimated independently. 5FBAPTA has been used extensively [308] in studies of cells [306,309,310], and the perfused beating heart, revealing calcium transients during the myocardial cycle (Fig. 11) [311–313]. Kirschenlohr *et al*. [313] reported that developed pressure in the perfused heart was reduced after addition of 5FBAPTA, but this could be reversed by including 50 μM $ZnCl_2$ in the perfusion medium.

UNCORRECTED PROOF

Comp. by: RMervin Date:19/11/07 Time:18:08:51 Stage:First Proof File Path://
pchns1301/WOMAT/Production/PRODENV/0000000001/0000006424/0000000016/
0000749453.3D Proof by: QC by: ProjectAcronym:bs:AFS Volume:00005

Table 5. ^{19}F NMR metal ions indicators[a]

Detected Ion	Agent	Structure	$\delta_{F(Ligand)}$ (ppm)	$\Delta\delta$ (ppm)	References
	5FBAPTA		2.08[b]		[307]
$[Ca^{2+}]$				5.8	
$[Zn^{2+}]$				3.7	
$[Pb^{2+}]$				4.6	
$[Cd^{2+}]$				4.8	
$[Hg^{2+}]$				5.3	
$[Co^{2+}]$				28.1	
$[Ni^{2+}]$				32.4	
$[Fe^{2+}]$				31.1	
	5FAPTRA		0.80[b]		[322]
$[Mg^{2+}]$				8.00	

UNCORRECTED PROOF

Comp. by: RMervin Date:19/11/07 Time:18:08:52 Stage:First Proof File Path://
pchns1301/WOMAT/Production/PRODENV/0000000001/0000006424/0000000016/
0000749453.3D Proof by: QC by: ProjectAcronym:bs:AFS Volume:00005

F-cryp-1	5.50	1.9	[410]	[Na^+]
F_4-Cage	−116.70	4.20 −13.5 −6.8 −4.2	[325]	[Li^+] [Na^+] [K^+] [Rb^+]
F_2-[2.1.1]-Cryptand	−100.70	28.53	[324]	[Li^+]
F_2-[3.1.1]-Cryptand	−105.80	−16.00	[324]	[Na^+]

UNCORRECTED PROOF

Comp. by: RMervin Date:19/11/07 Time:18:08:54 Stage:First Proof File Path://
pchns1301/WOMAT/Production/PRODENV/0000000001/0000006424/0000000016/
0000749453.3D Proof by: QC by: ProjectAcronym:bs:AFS Volume:00005

$[K^+]$	F_6-Carcerand		−110.50	−15.76	[325]
$[Rb^+]$	$(FN_2O_4)_2$		−124.46	5.40	[25,314]
$[Cs^+]$	$F(NO_4)_2$		−123.70	5.50	[25,314]
$[Ca^{2+}]$	F-[2.2.1]-Cryptand		−114.38	−11.90	[25,314]

UNCORRECTED PROOF

$[Sr^{2+}]$	HF-[3.1.1]-Cryptand	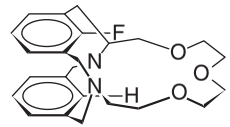	−110.38	−5.87	[324]
$[Ba^{2+}]$	$F(NO_5)_2$	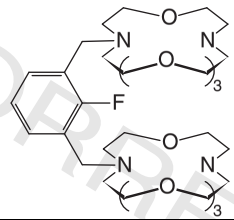	−123.78	7.90	[25,314]

[a] Unless otherwise noted, $CFCl_3$ was used as a chemical shift standard, solvent: CH_3CN.
[b] 6-Fluorotryptophan was used as a chemical shift standard.

UNCORRECTED PROOF

Comp. by: RMervin Date:19/11/07 Time:18:08:55 Stage:First Proof File Path://pchns1301/WOMAT/Production/PRODENV/0000000001/0000006424/0000000016/0000749453.3D Proof by: QC by: ProjectAcronym:bs:AFS Volume:00005

Comp. by: RMervin Date:19/11/07 Time:18:08:56 Stage:First Proof File Path://
pchns1301/WOMAT/Production/PRODENV/0000000001/0000006424/0000000016/
0000749453.3D Proof by: QC by: ProjectAcronym:bs:AFS Volume:00005

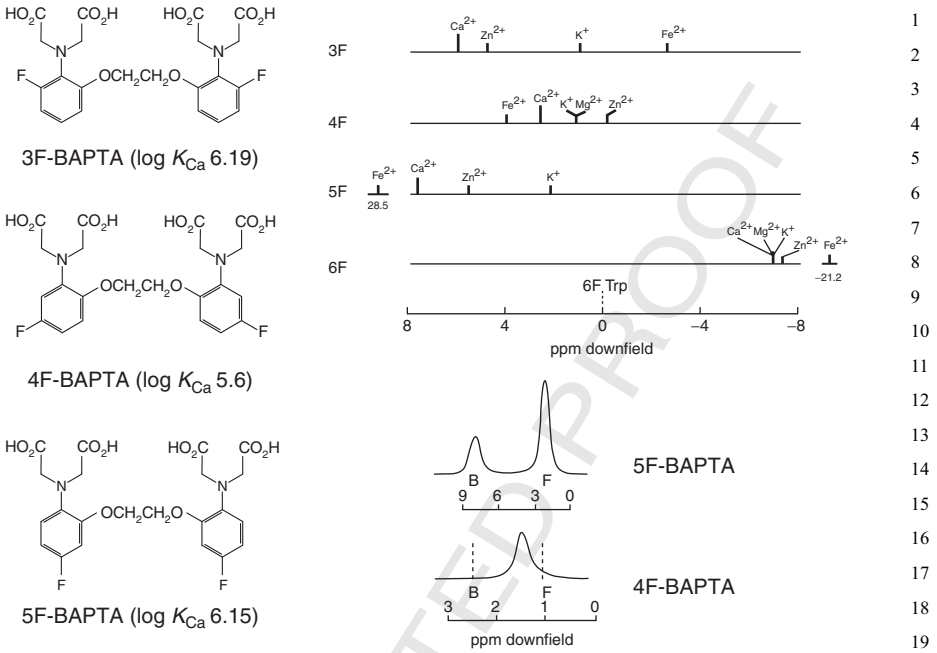

Fig. 10. Detection of $[Ca^{2+}]$ using ^{19}F NMR of F-BAPTA. Left: molecular structures of three F-BAPTA isomers with Ca^{2+} binding constants. Top right: chemical shifts of F-BAPTA isomers upon binding divalent metal ions with respect to F-tryptophan. Bottom right: ^{19}F NMR spectra of F-BAPTA in presence of Ca^{2+}. 5F-BAPTA is in slow exchange showing response for free and bound forms, whereas 4F-BAPTA is in fast exchange showing weighted average (modified from Smith et al., Proc. Natl. Acad. Sci. (USA) Biological Sciences 80, 7178–7182 (1983)—with permission [306]).

In an effort to find an optimal reporter, isomers and derivatives were developed (Fig. 10). 4FBAPTA has a somewhat lower binding constant $K_D = 0.7\ \mu M$, but exhibits fast exchange [308], so that the signals from the bound and unbound forms are averaged, and it is the absolute chemical shift, which is related to the ratio of the two components (Fig. 10).

Plenio and Diodone have also reported fluorocrown ethers (Table 5), which exhibit chemical shift response upon binding Ca^{2+} [314]. Of course, calcium could potentially be analyzed directly by ^{43}Ca NMR, however, its natural abundance is $<0.2\%$, its sensitivity is $<1\%$ that of ^{1}H, and being quadrupolar, it is liable to extensive line broadening [59]. Thus, the application of ^{19}F NMR with appropriately designed reporter molecules gives insight into cytosolic $[Ca^{2+}]$.

Magnesium ions are also involved in biological processes and occur in cells at millimolar concentrations [315]. Magnesium can be estimated based on the chemical shift difference of the resonances of adenosine triphosphate (ATP) using ^{31}P NMR [316–318], though ^{31}P NMR has intrinsically low signal-to-noise, exacerbated under many pathophysiological conditions, such as ischemia.

UNCORRECTED PROOF

Comp. by: RMervin Date:19/11/07 Time:18:08:57 Stage:First Proof File Path:// pchns1301/WOMAT/Production/PRODENV/0000000001/0000006424/0000000016/ 0000749453.3D Proof by: QC by: ProjectAcronym:bs:AFS Volume:00005

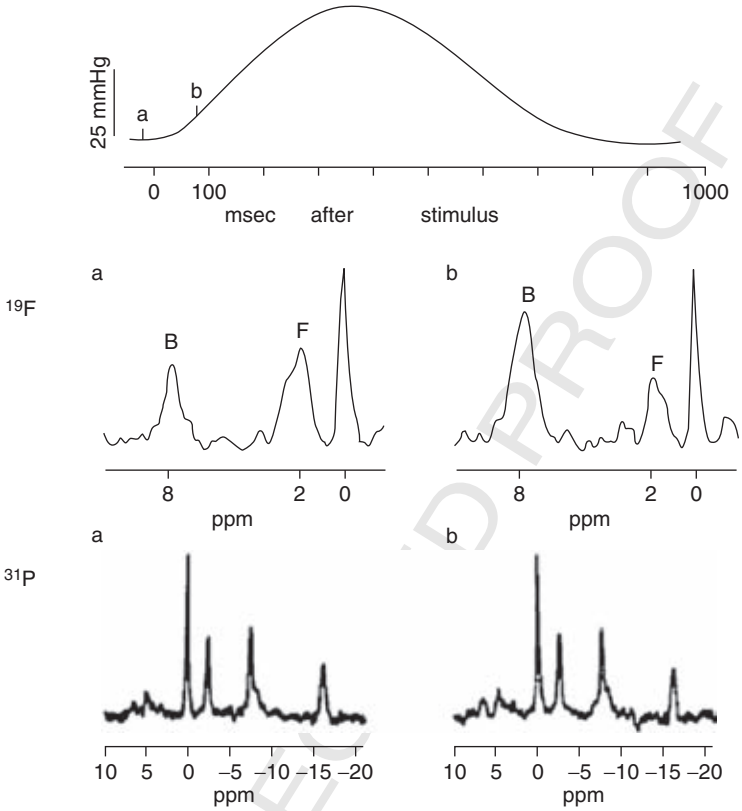

Fig. 11. Changes in gated NMR spectra during the cardiac cycle. Top panel: isovolumic left ventricular pressure in a ferret heart paced at 0.99 Hz in 8 mM [Ca^{2+}]. NMR spectra were acquired at the two times indicated on the pressure record: (a) 10 ms prior to stimulation; (b) 75 ms after stimulation. Middle panel shows gated ^{19}F NMR spectra (each from 800 acquisitions) recorded at (a) and (b), as indicated. The bound (B) and free (F) peaks of 5F-BAPTA exhibit distinct chemical shifts at approximately 8 and 2 ppm, respectively, downfield from a standard of 1 mM 6-Ftryptophan at 0 ppm. It appears that the free [Ca^{2+}] varied during the cardiac cycle. Bottom panel shows gated ^{31}P spectra (400 scans) acquired at times a and b in the same heart. The major peaks correspond to phosphocreatine (0 ppm), ATP (the three peaks upfield from phosphocreatine), and inorganic phosphate (the small peak at 4–5 ppm) (Reproduced from Marban *et al. Circ. Res.* 1988; 63: 673–678 [311] with permission of Lippincott, Williams & Wilkins).

There are many fluorescent indicators for detection of [Mg^{2+}] [319] and fluorinated NMR reporter have been proposed. The simplest is fluorocitrate [313], which shows a change in chemical shift upon binding Mg^{2+}. However, it is critical that the reporter molecule be used as the + isomer only, which has relatively little toxicity [320]. Levy *et al*. [8,321] developed the *o*-aminophenol-*N,N,O*-triacetic acid (APTRA) structure both for fluorescent application and by incorporation of fluorine atoms for ^{19}F NMR, which have been used in the perfused rat heart [322].

Comp. by: RMervin Date:19/11/07 Time:18:08:58 Stage:First Proof File Path://
pchns1301/WOMAT/Production/PRODENV/0000000001/0000006424/0000000016/
0000749453.3D Proof by: QC by: ProjectAcronym:bs:AFS Volume:00005

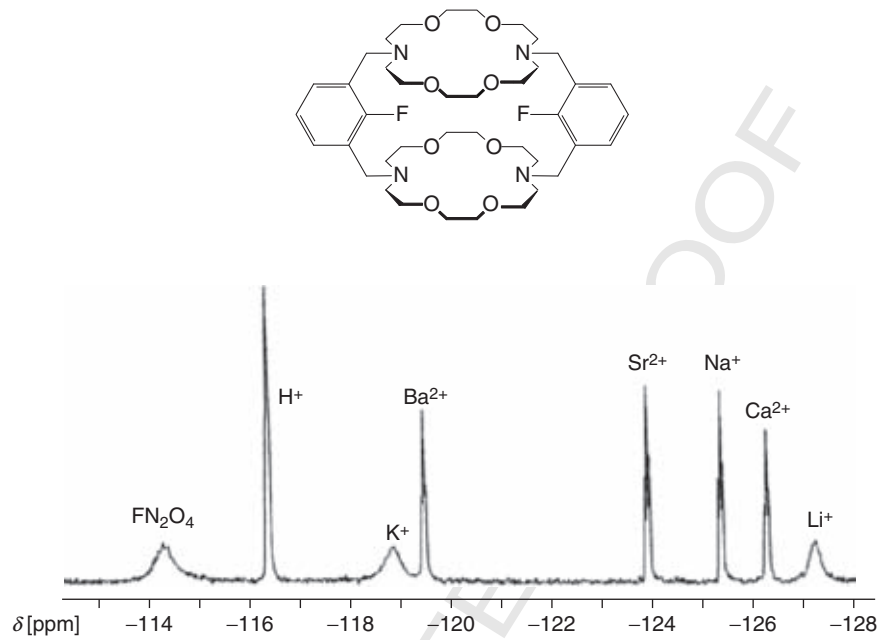

Fig. 12. ^{19}F NMR spectrum of FN_2O_4 ligand with mixture of mono- and divalent cations: Li^+, Na^+, K^+, Rb^+, Mg^{2+}, Ca^{2+}, Sr^{2+}, and Ba^{2+}. Due to slow exchange all species are detected simultaneously (reprinted with permission from Plenio and Diodone, JACS 118, 356–367 [314], Copyright 1996 American Chemical Society).

While indicators are normally designed for a specific ion they often also interact with other ions, for example, FBAPTA provides a unique chemical shift with many divalent metal ions (Fig. 10) [306,307] and has been used to estimate [Zn^{2+}], [Pb^{2+}] [323], and [Cd^{2+}] [307]. Plenio and Diodone [314,324] have developed series of fluorocyclophanes and fluoro crown ethers to explore specific cation binding (e.g., K^+, Li^+, Na^+, Ba^{2+}, Sr^{2+}, Ca^{2+}) though in many cases, multiple ions may be bound (Table 5 and Fig. 12). Takemura [325] reported macrocycles designed to bind K^+, NH_4^+, and Ag^+. In addition to the metal binding ligands shown in Table 5, many others have been reported, but these were selected since they exhibit particularly large chemical shift responses.

While most reporter molecules have been designed to interact with cations, Plenio and Diodone [326] reported fluorine containing cryptands, which interact with perchlorate. London and Gabel [327] reported fluorobenzene boronic acid, which interacted with specific sugars.

3.1.4. Caveats

A number of criteria are pertinent to the development and exploitation of reporter molecules. The fluorine NMR spectrum must respond to interaction with the ion of interest, for example, through the formation of a second signal, as in the slow

Comp. by: RMervin Date:19/11/07 Time:18:08:59 Stage:First Proof File Path://
pchns1301/WOMAT/Production/PRODENV/0000000001/0000006424/0000000016/
0000749453.3D Proof by: QC by: ProjectAcronym:bs:AFS Volume:00005

exchange regime, or chemical shift in a fast exchange regime. For many ions, agents should be water soluble, although a degree of lipophilicity may help in transport. The reporter molecule must reach the cellular compartment of interest. Some molecules penetrate cells directly, while for others, this is facilitated using acetoxymethyl esters. A critical issue for intracellular interrogation is loading the reporter molecule into cells. The tetra-carboxylates do not penetrate cells, however, derivatization as acetoxymethyl esters, which has been very widely used in association with analogous fluorescent indicators provides a more lipophilic entity, which can equilibrate across cell membranes [305]. These esters are specifically designed so that intracellular esterases cleave the acetoxymethyl ester, releasing the charged reporter molecule, which is then essentially trapped in the intracellular compartment. The release of acetic acid and formaldehyde are considered to be relatively innocuous. In other cases, specific cellular exclusion is important, so that any signal can unambiguously be attributed to the extracellular or interstitial compartment in a tissue. Such measurements would be analogous to electrode measurements.

It is critical that the reporter molecule not perturb the system under investigation. For ions, there is inevitably some binding and complexation. Provided there is sufficient reservoir of the ions, there can be rapid re-equilibration, and the concentration may give a realistic indication of the free concentration. In unregulated systems, this may be less reliable. The binding constant must be compatible with the typical concentration encountered *in vivo*. Ideally, the reporter ligand is highly selective for the ion of interest and of course the molecule should exhibit minimal toxicity. Signals should be narrow to enhance both the signal-to-noise and spectral resolution.

3.2. Chemical interactions

In the previous section, we considered reporter molecules, which interact reversibly in a physical sense, for example, solvation of gas, protonation, or binding of metal ion by a ligand. Other reporter molecules reveal activity based on irreversible bond cleavage to release a distinct product. This may be more akin to the metabolism of drugs, but these reporters can be tailored to interrogate specific biological processes.

3.2.1. Metabolism of FDG

Steric and electrostatic considerations allow a fluorine atom to replace a hydroxyl group in many sugars, while retaining enzyme substrate activity. Many tumors are characterized by a high glycolytic rate and FDG is a fluorinated glucose analogue used in PET to measure metabolic activity [328]. It is particularly useful for staging tumors and monitoring metastases. FDG is recognized by glucose transporters and enters cells where it is effectively phosphorylated, trapping it

UNCORRECTED PROOF

Comp. by: RMervin Date:19/11/07 Time:18:09:00 Stage:First Proof File Path://
pchns1301/WOMAT/Production/PRODENV/0000000001/0000006424/0000000016/
0000749453.3D Proof by: QC by: ProjectAcronym:bs:AFS Volume:00005

intracellularly, but phosphorylated FDG (FDG-6-P) is not a substrate for phosphofructose isomerase. FDG accumulates in metabolically active cells, such as tumors, brain, and myocardium. FDG PET is currently the method of choice for detecting many cancer metastases and differentiating recurrent disease from scar tissue. While PET can assess retention with great sensitivity, it provides no metabolic information, whereas ^{19}F NMR can be used to differentiate individual metabolites from anabolic and catabolic processes. Of course, NMR studies typically require mM concentrations as opposed to nM/μM for PET and thus, metabolic fates may differ, but 2-FDG has been used in metabolic studies using ^{19}F NMR [329–332]. The 3-fluoro-3-deoxy-D-glucose isomer (3-FDG) has also been used in the eye, particularly with respect to exploring onset of cataracts [333,334]. It is a poor substrate for hexokinase and the binding affinity of phosphohexose isomerase is low relative to glucose, but it has been used to probe aldose reductase activity in brain [335].

NMR not only provides spectral resolution for a given nucleus allowing multiple fluorine-labeled substrates to be observed simultaneously together with metabolic products, but other nuclei may also be detected. In particular, ^{13}C and ^{2}H NMR have been used extensively to probe metabolism, both confirming well-known pathways (e.g., glycolysis) and revealing novel detoxification products of xenobiotica [96,97,336,337]. ^{13}C NMR may be considered preferable for such studies since isotopic enrichment is less perturbing than introduction of a fluorine label. As for ^{19}F NMR, ^{13}C NMR normally has minimal background signal, since the natural abundance of ^{13}C is only 1.1% allowing almost 100-fold enrichment. Isotopomer analysis can reveal substrate preferences and mechanisms of enzyme activity and kinetic isotope effects are minimal for ^{13}C, though may be sizable for ^{2}H-examined substrates [338].

3.2.2. Hypoxia

While FDG has a role in detecting tumors, a new thrust is characterizing tumors so as to individualize therapy and optimize outcome. To this end, hypoxia is recognized as a critical characteristic. In Section 3.1.1, we described ^{19}F NMR methods for measuring pO_2. As an alternative approach, fluoronitroimidazoles have been used to detect hypoxia. Nitroimidazoles are bioreductive agents that are reduced by intracellular reductases to generate reactive intermediates. In the presence of oxygen, the intermediates are rapidly reoxidised and may clear from cells, but under hypoxic conditions they become covalently bound to cellular constituents, indicating the presence of cellular hypoxia. Nitroimidazoles have been used extensively in the past as hypoxic cell radiosensitizers [339] and more recently have gained a role as markers of tumor hypoxia [85,340–344]. EF5 and pimonidazole are widely used to assess hypoxia in histological analysis of biopsy specimens [198,345–347], but noninvasive approaches would be preferable for therapeutic prognosis. Retention of ^{18}F misonidazole in hypoxic tumors has been

UNCORRECTED PROOF

Comp. by: RMervin Date:19/11/07 Time:18:09:01 Stage:First Proof File Path://
pchns1301/WOMAT/Production/PRODENV/0000000001/0000006424/0000000016/
0000749453.3D Proof by: QC by: ProjectAcronym:bs:AFS Volume:00005

observed using PET. Given the importance of hypoxia other PET and SPECT sensitive agents have been proposed and tested (e.g., Cu-ATSM [348,349] and iodinated azomycin galactoside (IAZG) [350]), but nonradioactive approaches would be preferable.

Fluorine-19 labels have been introduced into the nitroimidazole structure providing NMR-sensitive agents [351,352]. Studies have reported the fluorinated nitroimidazoles CCI-103F [353], Ro 07–0741 [354], and SR4554 [351,355,356], which contain 6, 1, and 3 fluorine atoms per molecule, respectively (Table 6). Subsequent to administration, a washout period sufficient for elimination of unbound marker is required, since there is apparently no difference detectable *in vivo* in the chemical shifts of the parent molecule and the metabolites [351]. Li *et al*. [357] investigated the predictive potential of CCI-103F retention as an indicator of tumor radiosensitivity and found a weak correlation indicating that factors other than hypoxia are involved and glutathione concentration may be pertinent [351].

Aboagye *et al*. [358] found increased retention of SR4554 in hypoxic tumors, but no linear correlation with pO_2. Lack of correlation with pO_2 measurements [355,358] and pimonidazole uptake [351] suggest that additional factors influence hypoxia marker retention and indeed blood flow/perfusion has been implicated [351]. Robinson and Griffiths found differential uptake of SR4554 in diverse tumors known to exhibit different levels of hypoxia. Surprisingly, there was no retention detected in C6 gliomas, which are widely reported to have extensive hypoxia (Fig. 13). Trapping is predicated on nitroreductase activity, which may be lacking in some tumors. Unlike radiochemical approaches, which detect all labeled molecules, NMR offers potential benefits, but added complexity. Diverse adducts, and metabolites may exhibit multiple chemical shifts, each at very low concentration. There is also concern that polymeric adducts may have exceedingly short T_2, so that they become essentially invisible for many NMR sequences [359]. The biggest problem with ^{19}F hypoxia agents is that they merely provide a qualitative impression of hypoxia rather than a definitive pO_2. Seddon *et al.* [356] reported a correlation between retention of SR4554 and pO_2, but a Phase I clinical ^{19}F NMR study [356] required infusion at doses of 400–1600 mg/m^2, which could have adverse side effects.

3.2.3. Enzyme reporters

A ^{19}F atom can be substituted for a hydroxyl group in sugars with little overall structural perturbation. As such, fluorosugars were widely used to explore mechanisms of enzyme activity [124,126,360]. We adopted a different strategy by including ^{19}F into the aglycon moiety of a substrate to detect β-galactosidase activity (Figs. 1 and 14 and Table 7) [294]. This provides insight into activity of the lacZ gene, which has historically been the most popular reporter gene in molecular biology.

UNCORRECTED PROOF

Comp. by: RMervin Date:19/11/07 Time:18:09:02 Stage:First Proof File Path://pchns1301/WOMAT/Production/PRODENV/0000000001/0000006424/0000000016/0000749453.3D Proof by: QC by: ProjectAcronym:bs:AFS Volume:00005

Table 6. ^{19}F NMR hypoxia indicators

Name	Structure	Number of F atoms	Application
CCI 103F	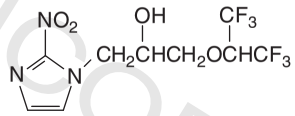	6	Tumors, cells [353,413]
RO 070741	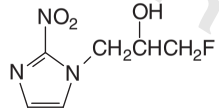	1	Tumors, cells [354]
SR4554	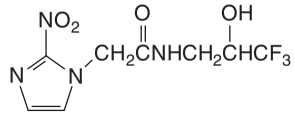	3	Tumors, cells [355,356,351]
NLTQ-1	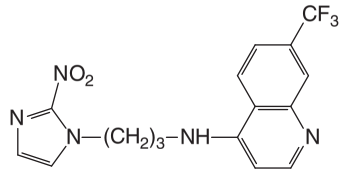	3	Tumors, cells [435]
3,3-Difluorochlorambucil	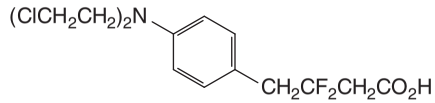	2 ABq	Tumors, cells [354]

UNCORRECTED PROOF

Comp. by: RMervin Date:19/11/07 Time:18:09:03 Stage:First Proof File Path://
pchns1301/WOMAT/Production/PRODENV/0000000001/0000006424/0000000016/
0000749453.3D Proof by: QC by: ProjectAcronym:bs:AFS Volume:00005

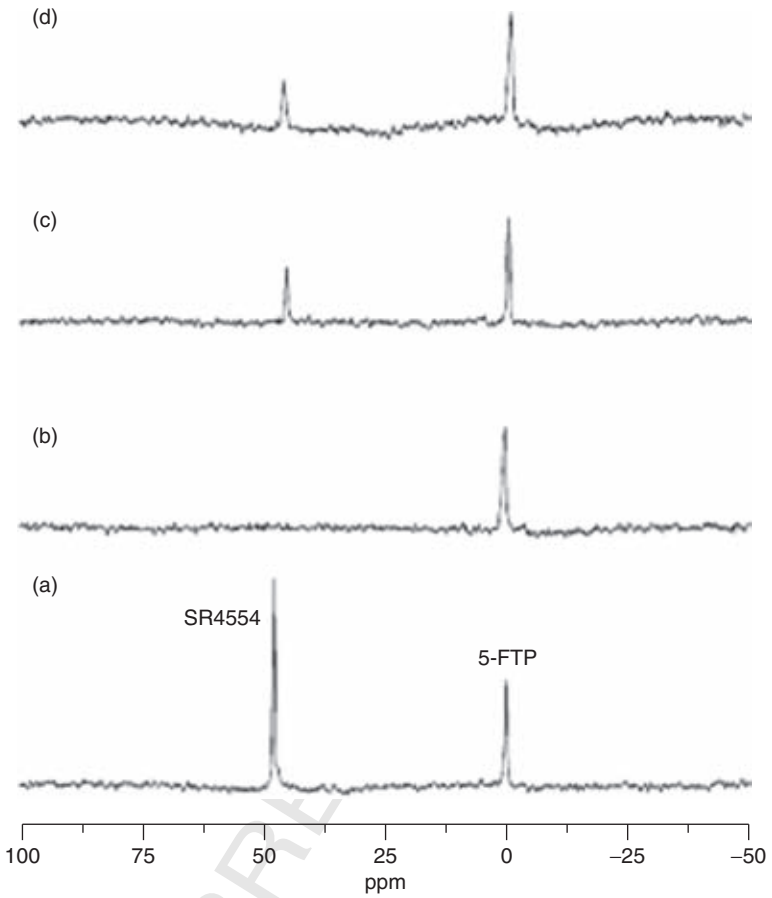

Fig. 13. ^{19}F NMR of hypoxia reporter SR4554 in tumors. ^{19}F NMR spectra obtained from (a) a vial containing 6 mg/ml SR4554 resonating at ca. 45 ppm relative to a 5-fluorotryptophan (5-FTP) external standard; (b) a wild-type C6 glioma; (c) a RIF-1 fibrosarcoma; and (d) an HT29 colon adenocarcinoma all acquired 45 min after administration of 180 mg/kg SR4554 IP. The degree of retention of the reduced adducts of SR4554, measured by ^{19}F MRS, affords a noninvasive assessment of tumor hypoxia. No ^{19}F resonance was detected in C6 gliomas, although they are expected to exhibit considerable hypoxia. The RIF-1 fibrosarcoma grown in C3H mice and HT29 colon adenocarcinoma grown in nude mice showed clear ^{19}F resonances from SR4554 (reproduced with permission from Robinson and Griffiths, *Phil. Trans. R. Soc. London B Biol. Sci*. 359, 987–996, Fig. 6 (2004) [351]).

Gene therapy holds great promise for the treatment of diverse diseases. However, widespread implementation is hindered by difficulties in assessing the success of transfection in terms of spatial extent, gene expression, and longevity of expression. The development of noninvasive reporter techniques based on appropriate molecules and imaging modalities may help to assay gene expression and this is often achieved by including a reporter gene in tandem with the

Comp. by: RMervin Date:19/11/07 Time:18:09:04 Stage:First Proof File Path://
pchns1301/WOMAT/Production/PRODENV/0000000001/0000006424/0000000016/
0000749453.3D Proof by: QC by: ProjectAcronym:bs:AFS Volume:00005

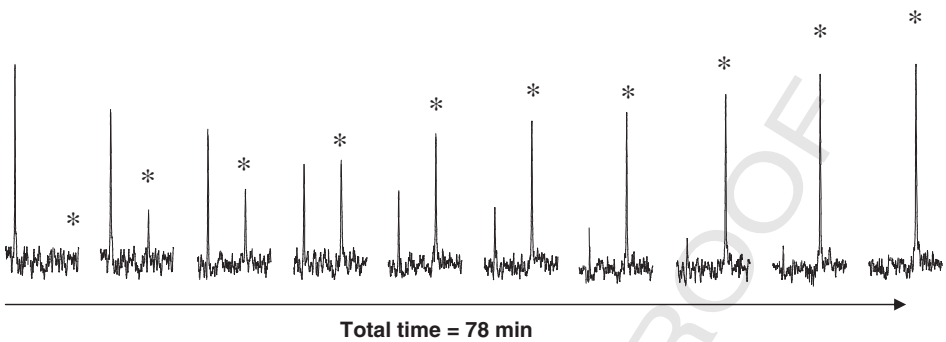

Fig. 14. Detection of β-galactosidase activity in cells using ^{19}F NMR. Sequential ^{19}F NMR spectra of Lncap C4–2 prostate cancer cells transiently transfected with *lacZ* (1.0′ 10^7) in phosphate buffered saline (PBS) (0.1 M, pH = 7.4, 700 ml) at 37 °C following addition of GFPOL (1.84 mg, 5.27 mmol). ^{19}F NMR spectra were acquired in 102 s each, and enhanced with an exponential line broadening 40 Hz. In each spectrum, GFPOL occurs on the left with liberated FPOL aglycon appearing at right (∗).

therapeutic gene [38,361]. Currently, reporter genes associated with optical imaging are most popular (e.g., BLI of luciferase [38,362] and fluorescent imaging of GFP and longer wavelength variants [45], since they are cheap modalities, and highly sensitive results are rapidly available. These techniques are very useful in superficial tissues and have extensive applications in mice, but application to larger bodies is limited by depth of light penetration. For deeper tissues and larger animals, nuclear medicine approaches based on thymidine kinase or the sodium iodine symporter (hNIS) have been used [49,363]. For cancer, thymidine kinase has the advantage that the gene serves not only as a reporter, but gene products can themselves have therapeutic value [146]. CD activates the minimally toxic 5-fluorocytosine (5FC) to the highly toxic 5-fluorouracil (5FU) [146,147]. The conversion of 5FC to 5FU causes a ^{19}F NMR chemical shift approximately 1.5 ppm, hence, revealing gene activity, which has been demonstrated in a number of systems *in vivo* [147,150].

We have focused on substrates for lacZ, recognizing its popularity as a reporter gene. Given the popularity of lacZ [364–366] diverse reporter agents are commercially available, but mostly for optical and histological applications (e.g., X-gal, *o*-nitrophenylgalactopyranoside (ONPG), S-Gal™, and S-Galacton-Star™) [367–369]. Recently, ^{1}H MRI [370], fluorescent [371], and radionuclide [372] substrates have been presented for *in vivo* work, prompting us to consider ^{19}F NMR active analogs. It appeared that introduction of a fluorine atom into the popular colorimetric biochemical indicator *ortho*-nitrophenyl β-galactopyranoside (ONPG) could produce a strong candidate molecule. Fluoronitrophenol galactosides were used by Yoon *et al*. [373], to explore β-gal activity, but they placed the fluorine atom on the sugar moiety, which would be expected to provide much

UNCORRECTED PROOF

Comp. by: RMervin Date:19/11/07 Time:18:09:07 Stage:First Proof File Path://
pchns1301/WOMAT/Production/PRODENV/0000000001/0000006424/0000000016/
0000749453.3D Proof by: QC by: ProjectAcronym:bs:AFS Volume:00005

Table 7. ^{19}F NMR lacZ gene reporters[a]

Reporter	Structure	$\delta_{F(Substrate)}$ (ppm)	$\delta_{F(aglycone)}$ (ppm)	$\Delta\delta$ (ppm)	References
PFONPG		−42.87	−52.71	−9.84	[294,374]
OFPNPG		−54.93	−61.04	−6.11	[294,375]
OFONPG		−50.67	−58.67	−8.00	[294]
PCF_3ONPG		13.40	14.54	1.14	[299]

UNCORRECTED PROOF

Comp. by: RMervin Date:19/11/07 Time:18:09:08 Stage:First Proof File Path://
pchns1301/WOMAT/Production/PRODENV/0000000001/0000006424/0000000016/
0000749453.3D Proof by: QC by: ProjectAcronym:bs:AFS Volume:00005

I-						
GFPOL		−3.22	−11.21	−8.00	[377]	
GDUFPOL		−2.85	−12.16	−9.31	[378]	

[a] NaTFA was used as a chemical shift standard in PBS (0.1 M, pH = 7.4) buffer at 37 °C.

UNCORRECTED PROOF

Comp. by: RMervin Date:19/11/07 Time:18:09:09 Stage:First Proof File Path://
pchns1301/WOMAT/Production/PRODENV/0000000001/0000006424/0000000016/
0000749453.3D Proof by: QC by: ProjectAcronym:bs:AFS Volume:00005

ess chemical shift response to cleavage and they do not appear to have used ^{19}F NMR in these investigations.

Our prototype molecule 4-fluoro-2-nitrophenyl β-D-galactopyranoside (PFONPG, Table 7) proved effective as a substrate for β-galactosidase [374]. It provides a single ^{19}F NMR signal with a narrow line width and good stability in solution. It is stable in normal wild-type cells and whole blood, but exposure to the enzyme or cells transfected to express β-galactosidase causes rapid cleavage in line with anticipated levels of transfection [374]. Upon cleavage of the glycosidic bond, a chemical shift difference $\Delta\delta > 3.6$ ppm is observed, though the chemical shift of the product may have a range of about 9 ppm, since the released aglycone is pH sensitive and the pK_a is in the physiological range. Significantly, there is no overlap between the chemical shift of the substrate and the product and the chemical shift difference is sufficient to permit chemical shift selective imaging to reveal distribution of each entity separately [375].

To seek optimal ^{19}F NMR reporters, we synthesized diverse agents and the broad range of substrate structures is consistent with enzyme promiscuity (lack of substrate specificity) (Table 7). The released aglycone PFONP is somewhat toxic and can cause lysis of fragile cells. We have synthesized series of analogues with the fluorine atom placed at various locations on the phenolic ring and incorporating alternate substituents, such as Cl and Br [294]. Each adduct and aglycone provides a unique chemical shift allowing ready comparison of susceptibility to enzyme activity. The chemical shift accompanying cleavage depends strongly on the orientation of the F-atom with largest response for *para*-F and less for *ortho*-F. The rate of cleavage was closely related to the pK_a of the aglycone [294] commensurate with enzyme studies reported previously [376].

One approach to reducing toxicity is introduction of a trifluoromethyl (CF_3) reporter group, as opposed to the single F-atom to enhance signal-to-noise. The chemical shift response is much smaller (Table 7), due to transmission of the electron density redistribution through an additional carbon–carbon bond [299]. Spectroscopic detection is still feasible *in vivo* and deconvolution allows CSI, but it is unlikely to be feasible *in vivo* [299]. Toxicity may also be altered by using alternate aglycons, such as the pH reporter 6-FPOL [11]. 3-*O*-(β-D-galactopyranosyl)-6-fluoropyridoxol (GFPOL) is found to be a much less good substrate and reactivity is much slower [377]. It is also less water soluble. However, we have found that water solubility may be enhanced by polyglycosylation of the hydroxymethyl arms [378]. The polyglycosylated substrate was also highly reactive for β-gal, but when galactose was used for all sugar residues multiple products were rapidly generated causing complex spectra. Differential glycosylation using glucose or mannose as the secondary sugars overcame this problem [378].

Given the different chemical shifts of individual substrates and products, we believe there will be opportunities to use multiple reporters simultaneously. Indeed, we have investigated using 4-fluoro-2-nitrophenyl β-D-galactopyranoside (PFONPG) and 2-fluorine-4-nitrophenyl β-D-galactopyranoside (OFPNPG) as

UNCORRECTED PROOF

Comp. by: RMervin Date:19/11/07 Time:18:09:10 Stage:First Proof File Path://
pchns1301/WOMAT/Production/PRODENV/0000000001/0000006424/0000000016/
0000749453.3D Proof by: QC by: ProjectAcronym:bs:AFS Volume:00005

substrates simultaneously to differentiate wild type and lacZ expressing tumors in mice [379].

4. PASSIVE REPORTER MOLECULES

Many active ^{19}F NMR reporter molecules have been designed, developed, and exploited, but other methods use a passive approach. In essence, fluorinated molecules occupy a space and a signal magnitude provides an indication of anatomical properties such as lung volume, bowel function, vascular volume, or flow.

PFCs exhibit remarkable gas solubility, and based on the high carrying capacity for oxygen and carbon dioxide, have been developed in emulsion form as synthetic blood substitutes [231]. PFCs may also be relevant as pure liquids. In a classic experiment, Clark and Gollan [380] submersed a living mouse in PFC liquid and far from drowning, it inhaled the PFC facilitating effective oxygen transport to the lungs. Thus, PFCs have potential application as surfactants to aid breathing in extremely premature infants, as explored in clinical trials [381]. PFC may be administered as liquid or aerosols. Thomas *et al*. [382,383] applied ^{19}F MRI to show the extent of lung filling. Further, by applying relaxation measurements (as described in Section 3.1), they could estimate regional pO_2 in the lungs of mice, rats, dogs, and pigs [208,383]. Various PFCs and PFC emulsions have been introduced into the lung as aerosols, sometimes with animals under forced ventilation, following thorocotomy [383]. The ^{19}F signal provides an opportunity to image lungs. By contrast ^{1}H MRI is handicapped by lack of water signal. In a novel approach, Huang *et al*. [384] applied ^{1}H MRI to the water in a PFC emulsion and found considerably enhanced structural information. Liquid and aerosol ventilation can be stressful, whereas inhalation of inert gas may be more practical, as shown by proof of principal using CF_4 or C_2F_6 [385]. More recent studies used SF_6 with potential application for detection of lung cancer, emphysema, or allograft rejection [386,387]. Gas detection does require special MR instrumentation, due to the exceedingly short T_1 and T_2 relaxation.

Increasing awareness of colon cancer demands improved screening. Traditional barium meals provide contrast in CT, and virtual colonoscopy is competing with traditional fiber optic probes [388]. MR procedures have lagged behind CT, but several potential contrast agents have been presented, ranging from paramagnetic zeolite formulations [389] and ferric ammonium citrate [390] to PFC emulsions [391,392] and recently images were shown in mice based on perfluorononane [69].

Angiogenesis is associated with tumor development and many clinical trials have found correlations between vascular density and prognosis. Traditional analysis required biopsy and histology, with CD31 antibodies to provide blood vessel counts [393], and dyes such as India ink or Hoechst 33342 to reveal

UNCORRECTED PROOF

Comp. by: RMervin Date:19/11/07 Time:18:09:11 Stage:First Proof File Path://
pchns1301/WOMAT/Production/PRODENV/0000000001/0000006424/0000000016/
0000749453.3D Proof by: QC by: ProjectAcronym:bs:AFS Volume:00005

perfusion [394]. ^{19}F NMR provides a robust indication of vascular volume *in vivo* based on intravenous PFC emulsions, which are retained in the vasculature for a period of hours [395,396]. Noninvasive measurements revealed acute modulation of tumor blood volume and have provided validation of noninvasive NIR methods [397,398]. This approach has also been applied to other organs and tissues, for example, demonstrating reactive hyperemia in muscles [399]. Studies have validated signal using traditional radioisotope-labeled approaches and dyes [400].

Fluorinated gases (e.g., trifluoromethane (FC-23) and chlorofluoromethane (FC-22)) have been used to examine cerebral blood flow based on inflow and outflow kinetics, sometimes with pulsed delivery to facilitate compartmental analysis [401,402]. The observation that HFB clears from tumors over a period of hours suggests this could provide insight into tissue perfusion [224,266].

5. POTENTIAL INNOVATIONS AND IMPROVEMENTS

Implementation and application of ^{19}F MRI in the clinic awaits further developments. As described above, many reporter molecules have been presented and are undergoing further refinement and evaluation. Sensitivity can be enhanced incrementally by exploiting molecular symmetry as emphasized in Table 2: bis-fluorine atoms can enhance SNR twofold, a CF_3 group threefold, a bis-CF_3 sixfold and tris-CF_3 ninefold. Perhaps the most satisfying increase in SNR is gained by better targetability and localization following systemic delivery. Widespread utility of agents will depend on ready commercial availability. Other sensitivity gains can arise from enhanced radiofrequency coils and parallel imaging (e.g., SMASH or SENSE technologies [403,404]) and higher magnetic field. While ^{19}F MRI on human NMR systems is feasible, it still remains to be established as part of a routine commercial inventory. Clearly, use and need will stimulate widespread provision and availability which could occur quite rapidly.

6. CONCLUSIONS

Since there is essentially no ^{19}F NMR background signal in tissues, fluorinated drugs, and reporter molecules may be detected without interference. Huge diversity of application has been demonstrated in the biochemical and small animal areas, with some limited clinical application. To date, clinical application is hindered by the lack of availability of clinical ^{19}F NMR, but manufacturers are increasingly recognizing the value of including such capability. Given that ^{19}F NMR offers the potential to investigate many diverse parameters (Table 1), it will become increasingly available and useful in the future.

UNCORRECTED PROOF

Comp. by: RMervin Date:19/11/07 Time:18:09:13 Stage:First Proof File Path://
pchns1301/WOMAT/Production/PRODENV/0000000001/0000006424/0000000016/
0000749453.3D Proof by: QC by: ProjectAcronym:bs:AFS Volume:00005

ACKNOWLEDGMENTS

Supported in part by the Cancer Imaging Program, NCI Pre-ICMIC P20 CA086354, and IDEA awards from the DOD Breast Cancer Initiative DAMD 17-99-1-9381, and 17-03-1-0343 and . NMR experiments were conducted at the Mary Nell and Ralph B. Rogers NMR Center, an NIH BTRP facility #P41-RR02584. We are grateful to Drs. Mark Jeffrey, Himu Shukla, and Peter Peschke, for collegial support and allowing us to include unpublished collaborative studies here. Melody Simmons provided expert assistance in preparing this manuscript. Over the past 15 years, our development of expertise in ^{19}F NMR has been supported by the NIH, Department of Defense Breast and Prostate Cancer Initiatives, the American Cancer Society, the American Heart Association, and The Whitaker Foundation.

REFERENCES

[1] Z. Zhang, S.A. Nair, T.J. McMurry, Gadolinium meets medicinal chemistry: MRI contrast agent development, Curr. Med. Chem. 12 (2005) 751–778.
[2] C. Baudelet, B. Gallez, Current issues in the utility of blood oxygen level dependent MRI for the assessment of modulations in tumor oxygenation, Curr. Med. Imag. Rev. 1 (2005) 229–243.
[3] D. Liebfritz, J.D. de Certaines, W.M.M.J. Bovee, F. Podo Water Suppression, Pergamon, Oxford, 1992, pp. 149–168.
[4] D. O'Hagan, D.B. Harper, Fluorine-containing natural products, J. Fluorine Chem. 100 (1999) 127–133.
[5] S.R. Thomas, C.L. Partain, R.R. Price,J.A. Patton, M.V. Kulkarni, A.E.J. James (Eds.), The Biomedical Applications of Fluorine-19 NMR, Vol. 2, W.B. Saunders Co., London, 1988, pp. 1536–1552.
[6] B.S. Selinsky, C.T. Burt, L.J. Berliner, J. Reuben (Eds.), *In Vivo* ^{19}F NMR, Vol. 11, Plenum, New York, 1992, pp. 241–276.
[7] M.J.W. Prior, R.J. Maxwell, J.R. Griffiths, M. Rudin (Eds.), Fluorine-^{19}F NMR Spectroscopy and Imaging *In-Vivo*, Springer-Verlag, Berlin, 1992, pp. 103–130.
[8] R.E. London, R.J. Gillies (Eds.), *In Vivo* NMR Studies Utilizing Fluorinated NMR Probes Academic, San Diego, 1994, pp. 263–277.
[9] R.P. Mason, Non-invasive physiology: ^{19}F NMR of perfluorocarbon, Artif. Cells Blood Substit. Immobil. Biotechnol. 22 (1994) 1141–1153.
[10] D. Zhao, L. Jiang, R.P. Mason, Measuring changes in tumor oxygenation, Meth. Enzymol. 386 (2004) 378–418.
[11] R.P. Mason, Transmembrane pH gradients *in vivo*: Measurements using fluorinated vitamin B6 derivatives, Curr. Med. Chem. 6 (1999) 481–499.
[12] P.M.J. McSheehy, L.P. Lemaire, J.R. Griffiths, D.M. Grant, in: R.K. Harris (Eds.), Fluorine-19 MRS: Applications in Oncology, Wiley, Chichester, 1996, pp. 2048–2051.
[13] D.K. Menon, Fluorine-19 MRS: General Overview and Anesthesia R.K. Harris (Eds.), Wiley, Chichester, 1995, pp. 2052–2063.
[14] T.J. Passe, H.C. Charles, P. Rajagopalan, K.R. Krishnan, Nuclear magnetic resonance spectroscopy: A review of neuropsychiatric applications, nuclear magnetic resonance spectroscopy: A review of neuropsychiatric applications, Prog. Neuropsychopharmacol. Biol. Psychiatry 19 (1995) 541–563.

UNCORRECTED PROOF

Comp. by: RMervin Date:19/11/07 Time:18:09:14 Stage:First Proof File Path://
pchns1301/WOMAT/Production/PRODENV/0000000001/0000006424/0000000016/
0000749453.3D Proof by: QC by: ProjectAcronym:bs:AFS Volume:00005

[15] P. Bachert, Pharmacokinetics using fluorine NMR *in vivo*, Prog. Nucl. Magn. Reson. Spectrosc. 33 (1998) 1–56.
[16] R. Martino, M. Malet-Martino, V. Gilard, Fluorine nuclear magnetic resonance, a privileged tool for metabolic studies of fluoropyrimidine drugs, Curr. Drug Metab. 1 (2000) 271–303.
[17] W. Wolf, C.A. Presant, V. Waluch, 19F-MRS studies of fluorinated drugs in humans, Adv. Drug Deliv. Rev. 41 (2000) 55–74.
[18] J.X. Yu, V. Kodibagkar, W. Cui, R.P. Mason, ^{19}F: A versatile reporter for non-invasive physiology and pharmacology using magnetic resonance, Curr. Med. Chem. 12 (2005) 818–848.
[19] H.J. Bohm, D. Banner, S. Bendels, M. Kansy, B. Kuhn, K. Muller, U. Obst-Sander, M. Stahl, Fluorine in medicinal chemistry, Chembiochem 5 (2004) 637–643.
[20] I. Ojima, Use of fluorine in the medicinal chemistry and chemical biology of bioactive compounds—A case study on fluorinated taxane anticancer agents, Chembiochem 5 (2004) 628–635.
[21] W.R. Dolbier, Fluorine chemistry at the millennium, J. Fluorine Chem. 126 (2005) 157–163.
[22] B.K. Park, N.R. Kitteringham, P.M. O'Neill, Metabolism of fluorine-containing drugs, Annu. Rev. Pharmacol. Toxicol. 41 (2001) 443–470.
[23] C. Jackel, B. Koksch, Fluorine in peptide design and protein engineering, Eur. J. Org. Chem. 2005(21) (2005) 4483–4503. Au4
[24] M. Shimizu, T. Hiyama, Modern synthetic methods for fluorine-substituted target molecules, Angew. Chem. Int. Ed. 44 (2005) 214–231.
[25] H. Plenio, The coordination chemistry of fluorine in fluorocarbons, Chembiochem 5 (2004) 650–655.
[26] P. Jeschke, The unique role of fluorine in the design of active ingredients for modern crop protection, Chembiochem 5 (2004) 570–589.
[27] F.M.D. Ismail, Important fluorinated drugs in experimental and clinical use, J. Fluorine Chem. 118 (2002) 27–33.
[28] C. Isanbor, D. O'Hagan, Fluorine in medicinal chemistry: A review of anti-cancer agents, J. Fluorine Chem. 127 (2006) 303–319.
[29] C.E. Oyiliagu, M. Novalen, L.P. Kotra, Fluorine containing molecules for peptidomimicry: A chemical act to modulate enzymatic activity, Mini-Rev. Organic Chem. 3 (2006) 99–115.
[30] M. Zanda, Trifluoromethyl group: An effective xenobiotic function for peptide backbone modification, New J. Chem. 28 (2004) 1401–1411.
[31] http://www.nibib.nih.gov/in Vol. 2006.
[32] http://imaging.cancer.gov/in Vol. 2007.
[33] http://www.molecularimaging.org.
[34] http://www.ismrm.org/.
[35] http://interactive.snm.org/in Vol. 2007.
[36] R.P. Mason, S. Ran, P.E. Thorpe, Quantitative assessment of tumor oxygen dynamics: Molecular Imaging for Prognostic Radiology, J. Cell. Biochem. 87(Suppl.) (2002) 45–53.
[37] J.A. Karam, R.P. Mason, K.S. Koeneman, P.P. Antich, E.A. Benaim, J.T. Hsieh, Molecular imaging in prostate cancer, J. Cell. Biochem. 90 (2003) 473–483.
[38] C.H. Contag, B.D. Ross, It's not just about anatomy: *In vivo* bioluminescence imaging as an eyepiece into biology, J. Magn. Reson. Imaging 16 (2002) 378–387.
[39] R. Kumar, S. Jana, Positron emission tomography: An advanced nuclear medicine imaging technique from research to clinical practice, Methods Enzymol. 385 (2004) 3–19.
[40] http://probes.invitrogen.com/handbook/in Vol. 2007.
[41] http://www.cri-inc.com/products/maestro.aspin Vol. 2007.
[42] M. Oldham, H. Sakhalkar, T. Oliver, Y.M. Wang, J. Kirpatrick, Y.T. Cao, C. Badea, G.A. Johnson, M. Dewhirst, Three-dimensional imaging of xenograft tumors using optical computed and emission tomography, Med. Phys. 33 (2006) 3193–3202.

UNCORRECTED PROOF

Comp. by: RMervin Date:19/11/07 Time:18:09:15 Stage:First Proof File Path://
pchns1301/WOMAT/Production/PRODENV/0000000001/0000006424/0000000016/
0000749453.3D Proof by: QC by: ProjectAcronym:bs:AFS Volume:00005

[43] G. Zacharakis, H. Kambara, H. Shih, J. Ripoll, J. Grimm, Y. Saeki, R. Weissleder, V. Ntziachristos, Volumetric tomography of fluorescent proteins through small animals *in vivo*, Proc. Natl. Acad. Sci. USA 102 (2005) 18252–18257.
[44] A.M. Derfus, W.C.W. Chan, S.N. Bhatia, Probing the cytotoxicity of semiconductor quantum dots, Nano Lett. 4 (2004) 11–18.
[45] R. Hoffman, Green fluorescent protein imaging of tumour growth, metastasis, and angiogenesis in mouse models, Lancet Oncol. 3 (2002) 546–556.
[46] C.H. Contag, S.D. Spilman, P.R. Contag, M. Oshiro, B. Eames, P. Dennery, D.K. Stevenson, D.A. Benaron, Visualizing gene expression in living mammals using a bioluminescent reporter, Photochem. Photobiol. 66 (1997) 523–531.
[47] E. Richer, N. Slavine, M.A. Lewis, E. Tsyganov, G.C. Gellert, Z. Gunnur Dikmen, V. Bhagwandin, J.W. Shay, R.P. Mason, P.P. Antich, Society of Molecular Imaging (St. Louis) 2004.
[48] F. Blankenberg, W.C. Eckelman, H.W. Strauss, M.J. Welch, A. Alavi, C. Anderson, S. Bacharach, R.G. Blasberg, M.M. Graham, W. Weber, Role of radionuclide imaging in trials of antiangiogenic therapy. [Review], Acad. Radiol. 7 (2000) 851–867.
[49] U. Haberkorn, W. Mier, M. Eisenhut, Scintigraphic imaging of gene expression and gene transfer, Curr. Med. Chem. 12 (2005) 779–794.
[50] D. Vranjesevic, J.E. Filmont, J. Meta, D.H. Silverman, M.E. Phelps, J. Rao, P.E. Valk, J. Czernin, Whole-body (18)F-FDG PET and conventional imaging for predicting outcome in previously treated breast cancer patients, J. Nucl. Med. 43 (2002) 325–329.
[51] Y. Seo, B.L. Franc, R.A. Hawkins, K.H. Wong, B.H. Hasegawa, Progress in SPECT/CT imaging of prostate cancer, Technol. Cancer Res. Treat. 5 (2006) 329–336.
[52] C. Love, A.S. Din, M.B. Tomas, T.P. Kalapparambath, C. Palestro, Radionuclide bone imaging: An illustrative review, Radiographics 23 (2003) 341–358.
[53] E. Cherin, R. Williams, A. Needles, G.W. Liu, C. White, A.S. Brown, Y.Q. Zhou, F.S. Foster, Ultrahigh frame rate retrospective ultrasound microimaging and blood flow visualization in mice *in vivo*, Ultrasound Med. Biol. 32 (2006) 683–691.
[54] M. Tepel, P. Aspelin, N. Lameire, Contrast-induced nephropathy: A clinical and evidence-based approach, Circulation 113 (2006) 1799–1806.
[55] H. Mishima, T. Kobayashi, M. Shimizu, Y. Tamaki, M. Baba, In vivo F-19 chemical shift imaging with FTPA and antibody-coupled FMIQ, J. Magn. Reson. Imaging 1 (1991) 705–709.
[56] A.M. Morawski, P.M. Winter, X. Yu, R. Fuhrhop, M.J. Scott, F. Hockett, J.-D. Robertson, P.J. Gaffney, G.M. Lanza, S.A. Wickline, Quantitative ''magnetic resonance immunohistochemistry'' with ligand-targeted (19)F nanoparticles, Magn. Reson. Med. 52 (2004) 1255–1262.
[57] M. Higuchi, N. Iwata, Y. Matsuba, K. Sato, K. Sasamoto, T.C. Saido, F-19 and H-1 MRI detection of amyloid beta plaques *in vivo*, Nat. Neurosci. 8 (2005) 527–533.
[58] R.K. Harris, E.D. Becker, S.M. Cabral de Menezes, R. Goodfellow, P. Granger, NMR nomenclature. Nuclear spin properties and conventions for chemical shifts (IUPAC Recommendations 2001), Pure Appl. Chem. 73 (2001) 1795–1818.
[59] F.A. Bovey, Nuclear Magnetic Resonance Spectroscopy, Academic Press, San Diego,1988, p. 653.
[60] J.W. Emsley, L. Phillips, Fluorine chemical shifts, Prog. Nucl. Magn. Reson. Spectrosc. 7 (1971) 1–520.
[61] J.W. Emsley, L. Phillips, V. Wray, Fluorine coupling constants, Prog. Nucl. Magn. Reson. Spectrosc. 10 (1976) 83–756.
[62] H.P. Shukla, R.P. Mason, D.E. Woessner, P.P. Antich, A comparison of three commercial perfluorocarbon emulsions as high field NMR probes of oxygen tension and temperature, J. Magn. Reson. Series B. 106 (1995) 131–114.
[63] H.W.M. van Laarhoven, C.J.A. Punt, Y.J.L. Kamm, A. Heerschap, Monitoring fluoropyrimidine metabolism in solid tumors with *in vivo* 19F magnetic resonance spectroscopy, Crit. Rev. Oncol./Hematol. 56 (2005) 321–343.

UNCORRECTED PROOF

Comp. by: RMervin Date:19/11/07 Time:18:09:16 Stage:First Proof File Path://
pchns1301/WOMAT/Production/PRODENV/0000000001/0000006424/0000000016/
0000749453.3D Proof by: QC by: ProjectAcronym:bs:AFS Volume:00005

[64] M.C. Malet-Martino, J.P. Armand, A. Lopez, J. Bernadou, J.P. Beteille, M. Bon, R. Martino, Evidence for the importance of 5′-deoxy-5-fluorouridine catabolism in humans from ^{19}F nuclear magnetic resonance spectrometry, Cancer Res. 46 (1986) 2105–2112.

[65] A.W. Blackstock, H. Lightfoot, L.D. Case, J.E. Tepper, S.K. Mukherji, B.S. Mitchell, S. G. Swarts, S.M. Hess, Tumor uptake and elimination of 2′,2′-difluoro-2′-deoxycytidine (gemcitabine) after deoxycytidine kinase gene transfer: Correlation with *in vivo* tumor response, Clin. Cancer Res. 7 (2001) 3263–3268.

[66] G.S. Payne, D.J. Collins, P. Loynds, G. Mould, P.S. Murphy, A.S.K. Dzik-Jurasz, P. Kessar, N. Haque, M. Yamaguchi, S. Atarashi, M.O. Leach, Quantitative assessment of the hepatic pharmacokinetics of the antimicrobial sitafloxacin in humans using *in vivo* F-19 magnetic resonance spectroscopy, Br. J. Clin. Pharmacol. 59 (2005) 244–248.

[67] D. Bilecen, A.C. Schulte, A. Kaspar, E. Kustermann, J. Seelig, D. von Elverfeldt, K. Scheffler, Detection of the non-steroidal anti-inflammatory drug niflumic acid in humans: A combined F-19-MRS *in vivo* and *in vitro* study, NMR Biomed. 16 (2003) 144–151.

[68] E. Schneider, N.R. Bolo, B. Frederick, S. Wilkinson, F. Hirashima, L. Nassar, I. K. Lyoo, P. Koch, S. Jones, J. Hwang, Y. Sung, R.A. Villafuerte, G. Maier, R. Hsu, R. Hashoian, P.F. Renshaw, Magnetic resonance spectroscopy for measuring the biodistribution and *in situ in vivo* pharmacokinetics of fluorinated compounds: Validation using an investigation of liver and heart disposition of tecastemizole, J. Clin. Pharm. Ther. 31 (2006) 261–273.

[69] R. Schwarz, A. Kaspar, J. Seelig, B. Kunnecke, Gastrointestinal transit times in mice and humans measured with ^{27}Al and ^{19}F nuclear magnetic resonance, Magn. Reson. Med. 48 (2002) 255–261.

[70] M.E. Henry, M.E. Schmidt, J. Hennen, R.A. Villafuerte, M.L. Butman, P. Tran, L.T. Kerner, B. Cohen, P.F. Renshaw, A comparison of brain and serum pharmacokinetics of R-fluoxetine and racemic fluoxetine: A 19-F MRS study, Neuropsychopharmacology 30 (2005) 1576–1583.

[71] W.L. Strauss, A.S. Unis, C. Cowan, G. Dawson, S.R. Dager, Fluorine magnetic resonance spectroscopy measurement of brain fluvoxamine and fluoxetine in pediatric patients treated for pervasive developmental disorders, Am. J. Psychiatry 159 (2002) 755–760.

[72] J.D. Christensen, D.A. Yurgelun-Todd, S.M. Babb, S.A. Gruber, B.M. Cohen, P.F. Renshaw, Measurement of human brain dexfenfluramine concentration by ^{19}F magnetic resonance spectroscopy, Brain Res. 834 (1999) 1–5.

[73] Y.L. Chung, H. Troy, I.R. Judson, R. Leek, M.O. Leach, M. Stubbs, A.L. Harris, J.R. Griffiths, Noninvasive measurements of capecitabine metabolism in bladder tumors overexpressing thymidine phosphorylase by fluorine-19 magnetic resonance spectroscopy, Clin. Cancer Res. 10 (2004) 3863–3870.

[74] C.J. Deutsch, J.S. Taylor, R.K. Gupta (Eds.), ^{19}F NMR Measurements of Intracellular pH CRC Press, Boca Raton, 1987, pp. 55–73.

[75] B.E. Smart, Fluorine substituent effects (on bioactivity), J. Fluorine Chem. 109 (2001) 3–11.

[76] G. Gerebtzoff, X. Li-Blatter, H. Fischer, A. Frentzel, A. Seelig, Halogenation of drugs enhances membrane binding and permeation, Chembiochem 5 (2004) 676–684.

[77] B.A. Shainyan, Y.S. Danilevich, A.A. Grigor'eva, Y.A. Chuvashev, Electrochemical fluorination of benzamide and acetanilide in anhydrous HF and in acetonitrile, Russian J. Org. Chem. (Trans. Zh. Organ. Khim.). 40 (2004) 513–517.

[78] G.A. Olah, M. Nojima, I. Kerekes, Synthetic methods and reactions. I. Seleniuum tetrafluoride and its pyridine complex. Convenient fluorinating agents for fluorination of ketones, aldehydes, amides, alcohols, carboxylic acids, and anhydrides, J. Am. Chem. Soc. 96 (1974) 925–927.

UNCORRECTED PROOF

Comp. by: RMervin Date:19/11/07 Time:18:09:17 Stage:First Proof File Path://
pchns1301/WOMAT/Production/PRODENV/0000000001/0000006424/0000000016/
0000749453.3D Proof by: QC by: ProjectAcronym:bs:AFS Volume:00005

[79] A. Haas, T. Maciej, Fluorination by tungsten hexafluoride, J. Fluorine Chem. 20 (1982) 581–587.
[80] T.B. Patrick, L. Zhang, Q. Li, Rearrangement and double fluorination in the deiodinative fluorination of neopentyl iodide with xenon difluoride, J. Fluorine Chem. 102 (2000) 11–15.
[81] G.G. Belen'kii, V.A. Petrov, P.R. Resnick, Electrophilic, catalytic alkylation of polyfluoroolefins by some fluoroalkanes, J. Fluorine Chem. 108 (2001) 15–20.
[82] K. Adachi, Y. Ohira, G. Tomizawa, S. Ishihara, S. Oishi, Electrophilic fluorination with N,N′-difluoro-2,2′-bipyridinium salt and elemental fluorine, J. Fluorine Chem. 120 (2003) 173–183.
[83] V. Mehta, P.V. Kulkarni, R.P. Mason, A. Constantinescu, P.P. Antich, Novel molecular probes for ^{19}F magnetic resonance imaging: Synthesis & characterization of fluorinated polymers, Bioorg. Med. Chem. Lett. 2 (1992) 527–532.
[84] J. Joubert, S. Roussel, C. Christophe, T. Billard, B.R. Langlois, T. Vidal, Trifluoroacetamides from amino alcohols as nucleophilic trifluoromethylating reagents, Angew. Chem. Int. Ed. 42 (2003) 3133–3136.
[85] J.S. Rasey, J.J. Casciari, P.D. Hofstrand, M. Muzi, M.M. Graham, L.K. Chin, Determining hypoxic fraction in a rat glioma by uptake of radiolabeled fluoromisonidazole, Radiat. Res. 153 (2000) 84–92.
[86] W.R. Dolbier Jr., A.R. Li, C.J. Koch, C.Y. Shiue, A.V. Kachur, [18F]-EF5, a marker for PET detection of hypoxia: Synthesis of precursor and a new fluorination procedure, Appl. Radiat. Isot. 54 (2001) 73–80.
[87] C.S. Yap, J. Czernin, M.C. Fishbein, R.B. Cameron, C. Schiepers, M.E. Phelps, W.A. Weber, Evaluation of thoracic tumors with ^{18}F-fluorothymidine and ^{18}F-fluorodeoxyglucose-positron emission tomography, Chest 129 (2006) 393–401.
[88] P. Zanzonico, J. Campa, D. Polycarpe-Holman, G. Forster, R. Finn, S. Larson, J. Humm, C. Ling, Animal-specific positioning molds for registration of repeat imaging studies: Comparative microPET imaging of F18-labeled fluoro-deoxyglucose and fluoro-misonidazole in rodent tumors, Nucl. Med. Biol. 33 (2006) 65–70.
[89] N.J. Spratt, U. Ackerman, H.J. Tochon-Danguy, G.A. Donnan, D.W. Howells, Characterization of fluoromisonidazole binding in stroke, Stroke 37 (2006) 1862–1867.
[90] J. Bussink, E.G.C. Troost, P. Laverman, M. Philippens, J. Lok, O.C. Boerman, J. Kaanders, A.J. van der Kogel, Characterization of human squamous cell head and neck carcinoma xenografts using 18F-FLT and 18F-MISO autoradiography and immunohistochemistry, Radiother. Oncol. 78 (2006) S33–S33.
[91] J. Keupp, P.C. Mazurkewitz, I. Gräßlin, T. Schaeffter, Proc. Intl. Soc. Mag. Reson. Med. 2006, p. 102.
[92] G. Schnur, R. Kimmich, R. Lietzenmayer, Hydrogen/Fluorine retuning tomography. Applications to ^{1}H image-guided volume-selective ^{19}F spectroscopy and relaxometry of perfluorocarbon emulsions in tissue, Magn. Reson. Med. 13 (1990) 478–489.
[93] J. Sanders, B. Hunter, Modern NMR Spectroscopy, Oxford University Press, New York 1987, p. 308.
[94] R.P. Mason, G. Cha, G.H. Gorrie, E.E. Babcock, P.P. Antich, Glutathione in whole blood: A novel determination using double quantum coherence transfer proton NMR spectroscopy, FEBS Lett. 318 (1993) 30–34.
[95] R.E. Hurd, D.M. Freeman, Metabolite specific proton magnetic-resonance imaging, Proc. Natl. Acad. Sci. USA 86 (1989) 4402–4406.
[96] R.P. Mason, J.K.M. Sanders, *In vivo* enzymology: A deuterium NMR study of formaldehyde dismutase in Pseudomonas putida F61a and Staphylococcus aureus, Biochemistry 28 (1989) 2160–2168.
[97] R.P. Mason, J.K.M. Sanders, A. Crawford, B.K. Hunter, Formaldehyde metabolism by *E. coli*: Detection using *in vivo* ^{13}C NMR spectroscopy of S-(hydroxymethyl) glutathione as a transient intracellular intermediate, Biochemistry 25 (1986) 4504–4507.
[98] R.F. Code, J.E. Harrison, K.G. McNeill, M. Szyjkowski, *In vivo* ^{19}F spin relaxation in index finger bones, Mag. Reson. Med. 13 (1990) 358–369.

UNCORRECTED PROOF

Comp. by: RMervin Date:19/11/07 Time:18:09:19 Stage:First Proof File Path://
pchns1301/WOMAT/Production/PRODENV/0000000001/0000006424/0000000016/
0000749453.3D Proof by: QC by: ProjectAcronym:bs:AFS Volume:00005

[99] D.W.J. Klomp, H.W.M. van Laarhoven, A.P.M. Kentgens, A. Heerschap, Optimization of localized F-19 magnetic resonance spectroscopy for the detection of fluorinated drugs in the human liver, Magn. Reson. Med. 50 (2003) 303–308.
[100] A.V. Ratner, S. Quay, H.H. Muller, B.B. Simpson, R. Hurd, S.W. Young, ^{19}F relaxation rate enhancement and frequency shift with Gd-DTPA, Invest. Radiol. 24 (1989) 224–227.
[101] V.D. Mehta, R.P. Mason, P.V. Kulkarni, P. Lea, A. Constantinescu, P.P. Antich, E.H. Emram(Eds.), ^{19}F MR Characterization of Fluorinated Proteins and Relaxation Rate Enhancement with Gd-DTPA for Faster Imaging, Plenum, New York, 1995, pp. 305–313.
[102] H. Lee, R.R. Price, G.E. Holburn, C.L. Partain, M.D. Adams, W.P. Cacheris, *In-Vivo* F-19 MR-Imaging—Relaxation Enhancement with Gd-DTPA, J. Magn. Reson. Imaging 4 (1994) 609–613.
[103] G. Brix, M.E. Bellemann, L. Gerlach, U. Haberkorn, Intra- and extracellular fluorouracil uptake: Assessment with contrast-enhanced metabolic F-19 MR imaging, Radiology 209 (1998) 259–267.
[104] B.S.Y. Li, G.S. Payne, D.J. Collins, M.O. Leach, H-1 decoupling for *in vivo* F-19 MRS studies using the time-share modulation method on a clinical 1.5 T NMR system, Magn. Reson. Med. 44 (2000) 5–9.
[105] R.D. Kendrick, C.S. Yannoni, High-Power H-1-F-19 Excitation in a Multiple-Resonance Single-Coil Circuit, J. Magn. Reson. 75 (1987) 506–508.
[106] H.B. Lantum, R.B. Baggs, D.M. Krenitsky, M.W. Anders, Nephrotoxicity of chlorofluoroacetic acid in rats, Toxicol. Sci. 70 (2002) 261–268.
[107] B. Hassel, U. Sonnewald, G. Unsgard, F. Fonnum, NMR-spectroscopy of cultured astrocytes—Effects of glutamine and the gliotoxin fluorocitrate, J. Neurochem. 62 (1994) 2187–2194.
[108] R.L. Frost, R.W. Parker, J.V. Hanna, Detection of the pesticide compound-1080 (sodium monofluoroacetate) using F-19 nuclear magnetic-resonance spectroscopy, Analyst 114 (1989) 1245–1248.
[109] O. Corcoran, J.C. Lindon, R. Hall, I.M. Ismail, J.K. Nicholson, The potential of F-19 NMR spectroscopy for rapid screening of cell cultures for models of mammalian drug metabolism, Analyst 126 (2001) 2103–2106.
[110] M. Spraul, M. Hofmann, I.D. Wilson, E. Lenz, J.K. Nicholson, J.C. Lindon, Coupling of Hplc with F-19-NMR and H-1-NMR spectroscopy to investigate the human urinary-excretion of flurbiprofen metabolites, J. Pharm. Biomed. Anal. 11 (1993) 1009–1015.
[111] M.E. Bollard, E. Holmes, C.A. Blackledge, J.C. Lindon, I.D. Wilson, J.K. Nicholson, H-1 and F-19-nmr spectroscopic studies on the metabolism and urinary excretion of mono- and disubstituted phenols in the rat, Xenobiotica 26 (1996) 255–273.
[112] A. Preiss, J. Kruppa, J. Buschmann, C. Mugge, The determination of trifluoroacetic acid in rat milk samples by F-19-NMR spectroscopy and capillary gas chromatography, J. Pharm. Biomed. Anal. 16 (1998) 1381–1385.
[113] M. Tugnait, E.M. Lenz, M. Hofmann, M. Spraul, I.D. Wilson, J.C. Lindon, J.K. Nicholson, The metabolism of 2-trifluormethylaniline and its acetanilide in the rat by ^{19}F NMR monitored enzyme hydrolysis and ^{1}H/^{19}F HPLC-NMR spectroscopy, J. Pharm. Biomed. Anal. 30 (2003) 1561–1574.
[114] C.J. Duckett, J.C. Lindon, H. Walker, F. Abou-Shakra, I.D. Wilson, J.K. Nicholson, Metabolism of 3-chloro-4-fluoroaniline in rat using [C-14]-radiolabelling, F-19-NMR spectroscopy, HPLC-MS/MS, HPLC-ICPMS and HPLC-NMR, Xenobiotica 36 (2006) 59–77.
[115] C.A. Blackledge, J.K. Nicholson, J.A. Evans, C. Rodgers, I.D. Wilson, Application of H-1- and F-19-NMR spectroscopy in the investigation of the urinary and biliary excretion of 3,5-, 2,4-ditrifluoromethylbenzoic and pentafluorobenzoic acids in rat, Xenobiotica 32 (2002) 605–613.

UNCORRECTED PROOF

Comp. by: RMervin Date:19/11/07 Time:18:09:20 Stage:First Proof File Path://
pchns1301/WOMAT/Production/PRODENV/0000000001/0000006424/0000000016/
0000749453.3D Proof by: QC by: ProjectAcronym:bs:AFS Volume:00005

[116] B.W. Dubois, A.S. Evers, 19F-NMR spin-spin relaxation (T2) method for characterizing volatile anesthetic binding to proteins. Analysis of isoflurane binding to serum albumin, Biochemistry. 31 (1992) 7069–7076.
[117] W.M. Chew, M.E. Moseley, P.A. Mills, D. Sessler, R. Gonzalez-Mendez, T.L. James, L. Litt, Spin-echo fluorine magnetic resonance imaging at 2 T: *In vivo* spatial distribution of halothane in the rabbit head, Magn. Reson. Imaging 5 (1987) 51–56.
[118] D.K. Menon, G.G. Lockwood, C.J. Peden, I.J. Cox, J. Sargentoni, J.D. Bell, G.A. Coutts, J.G. Whitwam, *In-vivo* F-19 magnetic-resonance spectroscopy of cerebral halothane in postoperative-patients—preliminary-results, Magn. Reson. Med. 30 (1993) 680–684.
[119] E.E. Babcock, J.T. Vaughan, B. Lesan, R.L. Nunnally, Multinuclear NMR investigations of probe construction materials at 4.7-T, Magn. Reson. Med. 13 (1990) 498–503.
[120] T.A. Morinelli, A.K. Okwu, D.E. Mais, P.V. Halushka, V. John, C.K. Chen, J. Fried, Difluorothromboxane-A2 and stereoisomers—stable derivatives of thromboxane-A2 with differential-effects on platelets and blood-vessels, Proc. Natl.Acad. Sci. USA 86 (1989) 5600–5604.
[121] R.A. Dwek, R.A. Dwek (Eds.), The Use of Fluorine-19 as a Detecting Shift Probe, Clarendon, Oxford, 1975, pp. 158–173.
[122] J.T. Gerig, Fluorine magnetic resonance of fluorinated ligands, Meth. Enzymol. 177 (1989) 3–23.
[123] W.H. Huestis, M.A. Raftery, Study of cooperative interactions in hemoglobin using fluorine nuclear magnetic resonance, Biochemistry 11 (1972) 1648–1654.
[124] F. Millett, M.A. Raftery, Fluorine-19 nuclear magnetic resonance study of the binding of trifluoroacetylglucosamine oligomers to lysozyme, Biochemistry 11 (1972) 1639–1643.
[125] S.G. Withers, K. Rupitz, I.P. Street, 2-Deoxy-2-fluoro-D-glycosyl fluorides—a new class of specific mechanism-based glycosidase inhibitors, J. Biol. Chem. 263 (1988) 7929–7932.
[126] S.G. Withers, I.P. Street, M.D. Percival, Fluorinated carbohydrates as probes of enzyme specificity and mechanism, ACS Symposium Series 374 (1988) 59–77.
[127] W.G. Stirtan, S.G. Withers, Phosphonate and alpha-fluorophosphonate analogue probes of the ionization state of pyridoxal 5′-phosphate (PLP) in glycogen phosphorylase, Biochemistry 35 (1996) 15057–15064.
[128] P. Szczecinski, D. Bartusik, F-19 NMR measurements—A potential tool for the determination of amino acids in body fluids, Pol. J. Chem. 77 (2003) 321–328.
[129] L.A. Sylvia, J.T. Gerig, Fluorine NMR-studies of the metabolism of flumecinol (3-trifluoromethyl-alpha-ethylbenzhydrol), Drug Metab. Dispos. 21 (1993) 105–113.
[130] U. Sidelmann, S.H. Hansen, C. Gavaghan, A.W. Nicholls, H.A.J. Carless, J.C. Lindon, I.D. Wilson, J.K. Nicholson, Development of a simple liquid chromatographic method for the separation of mixtures of positional isomers and anomers of synthetic 2-, 3- and 4-fluorobenzoic acid glucuronides formed via acyl migration reactions, J. Chromatogr. B: Biomed. Sci. Appl. 685 (1996) 113–122.
[131] G.B. Scarfe, M. Tugnait, I.D. Wilson, J.K. Nicholson, Studies on the metabolism of 4-fluoroaniline and 4-fluoroacetanilide in rat: Formation of 4-acetamidophenol (paracetamol) and its metabolites via defluorination and N-acetylation, Xenobiotica 29 (1999) 205–216.
[132] M.K. Ellis, J.L. Naylor, T. Green, M.A. Collins, Identification and quantification of fluorine-containing metabolites of 1-chloro-2,2,2-trifluoroethane (Hcfc133a) in the rat by F-19-Nmr spectroscopy, Drug Metab. Dispos. 23 (1995) 102–106.
[133] C. Heidelberger, Fluorinated pyrimidines, a new class of tumour-inhibitory compounds, Nat. Chem. Biol. 179 (1957) 663–666.
[134] C.A. Presant, W. Wolf, V. Waluch, C. Wiseman, P. Kennedy, D. Blayney, R.R. Brechner, Association of intratumoral pharmacokinetics of fluorouracil with clinical response, Lancet 343 (1994) 1184–1187.

UNCORRECTED PROOF

Comp. by: RMervin Date:19/11/07 Time:18:09:21 Stage:First Proof File Path://
pchns1301/WOMAT/Production/PRODENV/0000000001/0000006424/0000000016/
0000749453.3D Proof by: QC by: ProjectAcronym:bs:AFS Volume:00005

[135] G.F.J. Peters, Fluorouracil: Biochemistry and pharmacology, J. Clin. Oncol. 6 (1988) 1653–1664.
[136] G. Brix, M.E. Bellemann, U. Haberkorn, L. Gerlach, W.J. Lorenz, Assessment of the biodistribution of 5-fluorouracil as monitored by ^{18}F PET and ^{19}F MRI: A comparative animal study, Nucl. Med. Biol. 23 (1996) 897–906.
[137] G. Brix, M.E. Bellemann, L. Gerlach, U. Haberkorn, Direct detection of intratumoral 5-fluorouracil trapping using metabolic F-19 MR imaging, Magn. Reson. Imaging 17 (1999) 151–155.
[138] G. Brix, M.E. Bellemann, U. Haberkorn, L. Gerlach, P. Bachert, W.J. Lorenz, Mapping the biodistribution and catabolism of 5-fluorouracil in tumor-bearing rats by chemical-shift selective F-19 MR-imaging, Magn. Reson. Med. 34 (1995) 302–307.
[139] J.L. Guerquin-Kern, F. Leteurtre, A. Croisy, J.M. Lhoste, pH dependence of 5-fluorouracil uptake observed by *in vivo* ^{31}P and ^{19}F NMR spectroscopy, Cancer Res. 51 (1991) 5770–5773.
[140] A.S.E. Ojugo, P.M.J. McSheehy, M. Stubbs, G. Alder, C.L. Bashford, R.J. Maxwell, M.O. Leach, I.R. Judson, J.R. Griffiths, Influence of pH on the uptake of 5-fluorouracil into isolated tumour cells, Br J. Cancer 77 (1998) 873–879.
[141] P.M.J. McSheehy, S.P. Robinson, A.S.E. Ojugo, E.O. Aboagye, M.B. Cannell, M.O. Leach, I.R. Judson, J.R. Griffiths, Carbogen breathing increases 5-Fluorouracil uptake and cytotoxicity in hypoxic Rif-1 tumors: A magnetic resonance study *in vivo*, Cancer Res. 58 (1998) 1185–1194.
[142] J.R. Griffiths, D.J.O. McIntyre, F.A. Howe, P.M.J. McSheehy, A.S.E. Ojugo, L.M. Rodrigues, P. Wadsworth, N.M. Price, F. Lofts, G. Nicholson, K. Smid, P. Noordhuis, G.J. Peters, M. Stubbs, Issues of normal tissue toxicity in patient and animal studies—Effect of carbogen breathing in rats after 5-fluorouracil treatment, Acta Oncol. 40 (2001) 609–614.
[143] H. van Laarhoven, G. Gambarota, J. Lok, M. Lammens, Y. Kamm, T. Wagener, C. Punt, A. van der Kogel, A. Heerschap, Proc. Intl. Soc. Mag. Reson. Med. (Seattle) 2006, p. 1766.
[144] P.E. Sijens, N.J. Baldwin, T.C. Ng, Multinuclear MR investigation of the metabolic response of murine RIF-1 tumor to 5-fluorouracil chemotherapy, Magn. Reson. Med. 19 (1991) 337–385.
[145] N.W. Lutz, W.E. Hull, Assignment and pH dependence of the 19F-NMR resonances from the fluorouracil anabolites involved in fluoropyrimidine chemotherapy, NMR Biomed. 12 (1999) 237–248.
[146] S.O. Freytag, M. Khil, H. Stricker, J. Peabody, M. Menon, M. DePeralta-Venturina, D. Nafziger, J. Pegg, D. Paielli, S. Brown, K. Barton, M. Lu, E. Aguilar-Cordova, J.H. Kim, Phase I study of replication-competent adenovirus-mediated double suicide gene therapy for the treatment of locally recurrent prostate cancer, Cancer Res. 62 (2002) 4968–4976.
[147] L.D. Stegman, A. Rehemtulla, B. Beattie, E. Kievit, T.S. Lawrence, R.G. Blasberg, J.G. Tjuvajev, B.D. Ross, Noninvasive quantitation of cytosine deaminase transgene expression in human tumor xenografts with *in vivo* magnetic resonance spectroscopy, Proc. Natl. Acad. Sci. USA 96 (1999) 9821–9826.
[148] L.D. Stegman, A. Rehemtulla, D.A. Hamstra, D.J. Rice, S.J. Jonas, K.L. Stout, T.L. Chenevert, B.D. Ross, Diffusion MRI detects early events in the response of a glioma model to the yeast cytosine deaminase gene therapy strategy, Gene Ther. 7 (2000) 1005–1010.
[149] M. Aghi, C.M. Kramm, T.C. Chou, X.O. Breakefield, E.A. Chiocca, Synergistic anticancer effects of ganciclovir/thymidine kinase and 5-fluorocytosine/cytosine deaminase gene therapies, J. Natl. Cancer Inst. 90 (1998) 370–380.
[150] H. Corban-Wilhelm, W.E. Hull, G. Becker, U. Bauder-Wust, D. Greulich, J. Debus, Cytosine deaminase and thymidine kinase gene therapy in a dunning rat prostate

UNCORRECTED PROOF

Comp. by: RMervin Date:19/11/07 Time:18:09:22 Stage:First Proof File Path://
pchns1301/WOMAT/Production/PRODENV/0000000001/0000006424/0000000016/
0000749453.3D Proof by: QC by: ProjectAcronym:bs:AFS Volume:00005

tumour model: Absence of bystander effects and characterisation of 5-fluorocytosine metabolism with ^{19}F-NMR spectroscopy, Gene Ther. 9 (2002) 1564–1575.

[151] T. Dresselaers, J. Theys, L. Dubois, W. Landuyt, P. Van Hecke, P. Lambin, Proc. Intl. Soc. Mag. Reson. Med. (2006) p. 3175.

[152] G.O. Cron, N. Beghein, R. Ansiaux, B. Gallez, Proc. Intl. Soc. Mag. Reson. Med. (Seattle) 2006, p. 1764.

[153] M.E. Bellemann, U. Haberkorn, L. Gerlach, J. Blatter, G. Brix, Proceedings of the 7th Scientific Meeting ISMRM (Philadelphia, PA), (1999) p. 1352.

[154] P.M.J. McSheehy, A.S.E. Ojugo, M.O. Leach, I.R. Judson, J.R. Griffiths, Proceedings of the 7th Annual Meeting ISMRM (Philadelphia) (1999), p. 1347.

[155] G. Brix, A. Schlicker, W. Mier, P. Peschke, M.E. Bellemann, Biodistribution and pharmacokinetics of the F-19-labeled radiosensitizer 3-aminobenzamide: Assessment by F-19 MR imaging, Magn. Reson. Imaging 23 (2005) 967–976.

[156] W.M. Spees, T.P.F. Gade, G.L. Yang, W.P. Tong, W.G. Bornmann, R. Gorlick, J.A. Koutcher, An F-19 magnetic resonance-based *in vivo* assay of solid tumor methotrexate resistance: Proof of principle, Clin. Cancer Res. 11 (2005) 1454–1461.

[157] T. Tengel, T. Fex, H. Emtenas, F. Almqvist, I. Sethson, J. Kihlberg, Use of F-19 NMR spectroscopy to screen chemical libraries for ligands that bind to proteins, Org. Biomol. Chem. 2 (2004) 725–731.

[158] T. Tarrago, S. Frutos, R.A. Rodriguez-Mias, E. Giralt, Identification by F-19 NMR of traditional chinese medicinal plants possessing prolyl oligopeptidase inhibitory activity, Chembiochem 7 (2006) 827–833.

[159] S. Frutos, T. Tarrago, E. Giralt, A fast and robust F-19 NMR-based method for finding new HIV-1 protease inhibitors, Bioorg. Med. Chem. Lett. 16 (2006) 2677–2681.

[160] L.P. Yu, P.J. Hajduk, J. Mack, E.T. Olejniczak, Structural studies of Bcl-xL/ligand complexes using F-19 NMR, J. Biomol. NMR 34 (2006) 221–227.

[161] M. Bartels, K. Albert, Detection of psychoactive drugs using 19F MR spectroscopy, J. Neural Transm. Gen Sect. 99 (1995) 1–6.

[162] N.R. Bolo, Y. Hode, J.P. Macher, Long-term sequestration of fluorinated compounds in tissues after fluvoxamine or fluoxetine treatment: A fluorine magnetic resonance spectroscopy study *in vivo*, MAGMA 16 (2004) 268–276.

[163] W.L. Strauss, M.E. Layton, S.R. Dager, Brain elimination half-life of fluvoxamine measured by ^{19}F magnetic resonance spectroscopy, Am. J. Psychiatry 155 (1998) 380–384.

[164] D.M. Lindquist, M. Dachtler, R.M. Hawk, C.N. Karson, K. Albert, R.A. Komoroski, Contribution of trifluoperazine metabolites to the *in vivo* F-19 NMR spectrum of rat brain, Magn. Reson. Med. 43 (2000) 756–759.

[165] T. Sassa, T. Suhara, H. Ikehira, T. Obata, F. Girard, S. Tanada, Y. Okubo, 19F-magnetic resonance spectroscopy and chemical shift imaging for schizophrenic patients using haloperidol decanoate, Psychiatry Clin. Neurosci. 56 (2002) 637–642.

[166] P. Jynge, T. Skjetne, I. Gribbestad, C.H. Kleinbloesem, H.F.W. Hoogkamer, O. Antonsen, J. Krane, O.E. Bakoy, K.M. Furuheim, O.G. Nilsen, *In vivo* tissue pharmacokinetics by fluorine magnetic-resonance spectroscopy—a study of liver and muscle disposition of fleroxacin in humans, Clin. Pharmacol. Ther. 48 (1990) 481–489.

[167] O. Saether, A. Midelfart, O. Risa, O. Haraldseth, J. Krane, Proton decoupled F-19 NMR spectroscopy of drugs used in eye treatment, Spectrosc. Lett. 39 (2006) 135–144.

[168] B. Gewiese, W. Noske, A. Schilling, D. Stiller, K. Wolf, M. Foerster, Human eye: Visualization of perfluorodecalin with F-19 MR imaging, Radiology 185 (1992) 131–133.

[169] C. Wilson, B. Berkowitz, B. McCuen, C. Charles, Measurement of preretinal pO_2 in the vitrectomized human eye using 19F NMR, Arch. Ophthalmol. 110 (1992) 1098–1100.

UNCORRECTED PROOF

Comp. by: RMervin Date:19/11/07 Time:18:09:23 Stage:First Proof File Path://
pchns1301/WOMAT/Production/PRODENV/0000000001/0000006424/0000000016/
0000749453.3D Proof by: QC by: ProjectAcronym:bs:AFS Volume:00005

[170] R.P. Mason, E.E. Babcock, R.L. Nunnally, Proceedings of the XIII International Congress of Magnetic Resonance in Biological Systems (Madison, WI) 1988.
[171] R. Nunnally, P. Antich, P. Nguyen, E. Babcock, G. McDonald, R. Mason, Fluosol adjuvant therapy in human cancer: Examinations *in vivo* of perfluorocarbons by F-19 NM, in: Proceedings of the SMRM 7th Meeting San Francisco, 1988, p. 342.
[172] A.M. Wyrwicz, C.B. Conboy, Multiecho ^{19}F NMR imaging of halothane in rabbit brain, Proceedings of the 7th SMRM San Francisco 1988, p. 597.
[173] T. Takeda, K. Makita, S. Ishikawa, K. Kaneda, K. Yokoyama, K. Amaha, Uptake and elimination of sevoflurane in rabbit tissues - an *in vivo* magnetic resonance spectroscopy study, Can. J. Anaesth. 47 (2000) 579–584.
[174] Y. Xu, P. Tang, W.G. Zhang, L. Firestone, P.M. Winter, F-19 nuclear-magnetic-resonance imaging and spectroscopy of sevoflurane uptake, distribution, and elimination in rat-brain, Anesthesiology 83 (1995) 766–774.
[175] P.N. Venkatasubramanian, Y.J. Shen, A.M. Wyrwicz, *In vivo* ^{19}F one-dimensional chemical shift imaging study of isoflurane uptake in rabbit brain, NMR Biomed. 6 (1993) 377–382.
[176] G.G. Lockwood, D.P. Dob, D.J. Bryant, J.A. Wilson, J. Sargentoni, S. M. SapsedByrne, D.N.F. Harris, D.K. Menon, Magnetic resonance spectroscopy of isoflurane kinetics in humans. 1. Elimination from the head, Br. J. Anaesth. 79 (1997) 581–585.
[177] B.S. Selinsky, M.E. Perlman, R.E. London, *In vivo* nuclear magnetic resonance studies of hepatic methoxyflurane metabolism. I. Verification and quantitation of methoxydifluoroacetate, Mol. Pharmacol. 33 (1988) 559–566.
[178] B.S. Selinsky, M.E. Perlman, R.E. London, *In vivo* nuclear magnetic-resonance studies of hepatic methoxyflurane metabolism. 2. A reevaluation of hepatic metabolic pathways, Mol. Pharmacol. 33 (1988) 567–573.
[179] E.P. Mazzola, A.P. Borsetti, S.W. Page, D.W. Bristol, Determination of pesticide-residues in foods by F-19 fourier-transform nuclear magnetic-resonance spectroscopy, J. Agric. Food Chem. 32 (1984) 1102–1103.
[180] R.D. Mortimer, B.A. Dawson, Using F-19 Nmr for trace analysis of fluorinated pesticides in food-products, J. Agric. Food. Chem. 39 (1991) 1781–1785.
[181] Z. Zuo, G. Kwon, B. Stevenson, J. Diakur, L.I. Wiebe, Flutamide—Hydroxypropyl-beta-cyclodextrin complex: Formulation, physical characterization, and absorption studies using the Caco-2 *in vitro* model, J. Pharm. Pharm. Sci. 3 (2000) 220–227.
[182] M. Masson, J.F. Sigurjonsdottir, S. Jonsdottir, T. Loftsson, Examination of F-19-NMR as a tool for investigation of drug-cyclodextrin complexes, Drug Dev. Ind. Pharm. 29 (2003) 107–112.
[183] J. Fukuchi, J.M. Kokontis, R.A. Hiipakka, C.P. Chuu, S. Liao, Antiproliferative effect of liver X receptor agonists on LNCaP human prostate cancer cells, Cancer Res. 64 (2004) 7686–7689.
[184] E.K. Rofstad, T. Danielsen, Hypoxia-induced metastasis of human melanoma cells: Involvement of vascular endothelial growth factor-mediated angiogenesis, Br. J. Cancer 80 (1999) 1697–1707.
[185] M. Höckel, P. Vaupel, Tumor hypoxia: Definitions and current clinical, biologic, and molecular aspects, J. Natl. Cancer Inst. 93 (2001) 266–276.
[186] J. Folkman, Angiogenesis and apoptosis, Semin. Cancer Biol. 13 (2003) 159–167.
[187] H.J. Knowles, A.L. Harris, Hypoxia and oxidative stress in breast cancer. Hypoxia and tumourigenesis. [Review], Breast Cancer Res. 3 (2001) 318–322.
[188] L. Gray, A. Conger, M. Ebert, S. Hornsey, O. Scott, The concentration of oxygen dissolved in tissues at time of irradiation as a factor in radiotherapy, Br. J. Radiol. 26 (1953) 638–648.
[189] J.L. Tatum, G.J. Kelloff, R.J. Gillies, J.M. Arbeit, J.M. Brown, K.S. Chao, J.D. Chapman, W.C. Eckelman, A.W. Fyles, A.J. Giaccia, R.P. Hill, C.J. Koch, M.C. Krishna, K.A. Krohn, J.S. Lewis, R.P. Mason, G. Melillo, A.R. Padhani,

UNCORRECTED PROOF

Comp. by: RMervin Date:19/11/07 Time:18:09:25 Stage:First Proof File Path://
pchns1301/WOMAT/Production/PRODENV/0000000001/0000006424/0000000016/
0000749453.3D Proof by: QC by: ProjectAcronym:bs:AFS Volume:00005

G. Powis, J.G. Rajendran, R. Reba, S.P. Robinson, G.L. Semenza, H.M. Swartz, P. Vaupel, D. Yang, B. Croft, J. Hoffman, G. Liu, H. Stone, D. Sullivan, Hypoxia: Importance in tumor biology, noninvasive measurement by imaging, and value of its measurement in the management of cancer therapy, Int. J. Radiat. Biol. 82 (2006) 699–757.

[190] J.M. Brown, Exploiting the hypoxic cancer cell: Mechanisms and therapeutic strategies, Mol. Med. Today 6 (2000) 157–162.

[191] H.M. Swartz, J.F. Dunn, J.F. Dunn, H.M. Swartz (Eds.), Measurements of Oxygen in Tissues: Overview and Perspectives on Methods, Vol. 530, Kluwer Academic, New York, 2003, pp. 1–12.

[192] H.B. Stone, J.M. Brown, T. Phillips, R.M. Sutherland, Oxygen in human tumors: Correlations between methods of measurement and response to therapy, Radiat. Res. 136 (1993) 422–434.

[193] H. Liu, Y. Gu, J.G. Kim, R.P. Mason, Near infrared spectroscopy and imaging of tumor vascular oxygenation, Methods Enzymol. 386 (2004) 349–378.

[194] R.P. Mason, Non-Invasive assessment of kidney oxygenation: A role for BOLD MRI, Kidney Int. 70 (2006) 10–11.

[195] S.H. Yee, K. Lee, P.A. Jerabek, P.T. Fox, Quantitative measurement of oxygen metabolic rate in the rat brain using microPET imaging of briefly inhaled 15O-labelled oxygen gas, Nucl. Med. Commun. 27 (2006) 573–581.

[196] J.P. Coles, T.D. Fryer, P.G. Bradley, J. Nortje, P. Smielewski, K. Rice, J.C. Clark, J.D. Pickard, D.K. Menon, Intersubject variability and reproducibility of 15O PET studies, J. Cereb. Blood Flow Metab. 26 (2006) 48–57.

[197] C.J. Koch, Measurement of absolute oxygen levels in cells and tissues using oxygen sensors and 2-nitroimidazole EF5, Methods Enzymol. 352 (2002) 3–31.

[198] J.A. Raleigh, S.C. Chou, G.E. Arteel, M. Horsman, Comparison among pimonidazole binding oxygen electrode measurements, and radiation response in C3H mouse tumors, Radiat. Res. 151 (1999) 580–589.

[199] C. Song, I. Lee, T. Hasegawa, J. Rhee, S. Levitt, Increase in pO_2 and radiosensitivity of tumors by Fluosol and carbogen, Cancer Res. 47 (1987) 442–446.

[200] J.G. Kim, D. Zhao, A. Constantinescu, R.P. Mason, H. Liu, Interplay of tumor vascular oxygenation and tumor pO_2 observed using NIRS, oxygen needle electrode, and ^{19}F MR pO_2 mapping, J. Biomed. Opt. 8 (2003) 53–62.

[201] Y. Gu, V. Bourke, J.G. Kim, A. Constantinescu, R.P. Mason, H. Liu, Dynamic response of breast tumor oxygenation to hyperoxic respiratory challenge monitored with three oxygen-sensitive parameters, Appl. Opt. 42 (2003) 1–8.

[202] B. Gallez, C. Baudelet, B.F. Jordan, Assessment of tumor oxygenation by electron paramagnetic resonance: Principles and applications, NMR Biomed. 17 (2004) 240–262.

[203] P. Parhami, B.N. Fung, Fluorine-19 relaxation study of perfluorochemicals as oxygen carriers, J. Phys. Chem. 87 (1983) 1928–1931.

[204] S.R. Thomas, R.G. Pratt, R.W. Millard, R.C. Samaratunga, Y. Shiferaw, L.C. Clark Jr., R.E. Hoffmann, Evaluation of the influence of the aqueous phase bioconstituent environment on the F-19 T1 of perfluorocarbon blood substitute emulsions, J. Magn. Reson. Imag. 4 (1994) 631–635.

[205] C.S. Lai, S. Stair, H. Miziorko, J.S. Hyde, Effect of oxygen and the spin label TEMPO-Laurate on ^{19}F and proton relaxation rates of the perfluorochemical blood substitute FC-43 emulsion, J. Magn. Reson. 57 (1984) 447–452.

[206] D. Eidelberg, G. Johnson, D. Barnes, P.S. Tofts, D. Delpy, D. Plummer, W.I. McDonald, ^{19}F NMR imaging of blood oxygenation in the brain, Magn. Reson. Med. 6 (1988) 344–352.

[207] R.P. Mason, H.P. Shukla, P.P. Antich, *In vivo* oxygen tension and temperature: Simultaneous determination using ^{19}F spectroscopy of perfluorocarbon, Magn. Reson. Med. 29 (1993) 296–302.

UNCORRECTED PROOF

Comp. by: RMervin Date:19/11/07 Time:18:09:26 Stage:First Proof File Path://
pchns1301/WOMAT/Production/PRODENV/0000000001/0000006424/0000000016/
0000749453.3D Proof by: QC by: ProjectAcronym:bs:AFS Volume:00005

[208] S.R. Thomas, R.G. Pratt, R.W. Millard, R.C. Samaratunga, Y. Shiferaw, A.J. McGoron, K.K. Tan, *In vivo* pO_2 imaging in the porcine model with perfluorocarbon F-19 NMR at low field, Magn. Reson. Imaging 14 (1996) 103–114.
[209] R.P. Mason, N. Bansal, E.E. Babcock, R.L. Nunnally, P.P. Antich, A novel editing technique for ^{19}F MRI: Molecule-specific imaging, Magn. Reson. Imaging 8 (1990) 729–736.
[210] E.E. Babcock, R.P. Mason, P.P. Antich, Effect of homonuclear J modulation on ^{19}F spin-echo images, Magn. Reson. Med. 17 (1991) 178–188.
[211] C.H. Sotak, P.S. Hees, H.N. Huang, M.H. Hung, C.G. Krespan, S. Raynolds, A new perfluorocarbon for use in fluorine-19 MRI and MRS, Magn. Reson. Med 29 (1993) 188–195.
[212] D. Zhao, S. Ran, A. Constantinescu, E.W. Hahn, R.P. Mason, Tumor oxygen dynamics: Correlation of *in vivo* MRI with histological findings, Neoplasia 5 (2003) 308–318.
[213] D. Zhao, A. Constantinescu, C.H. Chang, E.W. Hahn, R.P. Mason, Correlation of tumor oxygen dynamics with radiation response of the dunning prostate R3327-HI tumor, Radiat. Res. 159 (2003) 621–631.
[214] D. Zhao, C. Constantinescu, E.W. Hahn, R.P. Mason, Differential oxygen dynamics in two diverse Dunning prostate R3327 rat tumor sublines (MAT-Lu and HI) with respect to growth and respiratory challenge, Int. J. Radiat. Oncol. Biol. Phys. 53 (2002) 744–756.
[215] D. Zhao, A. Constantinescu, L. Jiang, E.W. Hahn, R.P. Mason, Prognostic radiology: Quantitative assessment of tumor oxygen dynamics by MRI, Am. J. Clin. Oncol. 24 (2001) 462–466.
[216] D. Zhao, A. Constantinescu, E.W. Hahn, R.P. Mason, Tumor oxygen dynamics with respect to growth and respiratory challenge: Investigation of the dunning prostate R3327-HI tumor, Radiat. Res. 156 (2001) 510–520.
[217] Y. Song, A. Constantinescu, R.P. Mason, Dynamic breast tumor oximetry: The development of prognostic radiology, Technol. Cancer Res. Treat. 1 (2002) 471–478.
[218] B.J. Dardzinski, C.H. Sotak, Rapid tissue oxygen tension mapping using ^{19}F inversion-recovery echo-planar imaging of Perfluoro-15-crown-5-ether, Magn. Reson. Med. 32 (1994) 88–97.
[219] Z. Wang, M.Y. Su, O. Nalcioglu, Applications of dynamic contrast enhanced MRI in oncology: Measurement of tumor oxygen tension, Technol. Cancer Res. Treat. 1 (2002) 29–38.
[220] B.J.P. van der Sanden, A. Heerschap, L. Hoofd, A.W. Simonetti, K. Nicolay, A. van der Toorn, W.N.M. Colier, A.J. van der Kogel, Effect of carbogen breathing on the physiological profile of human glioma xenografts, Magn. Reson. Med. 42 (1999) 490–499.
[221] T.Q. Duong, C. Iadecola, S.G. Kim, Effect of hyperoxia, hypercapnia, and hypoxia on cerebral interstitial oxygen tension and cerebral blood flow, Magn. Reson. Med. 45 (2001) 61–70.
[222] F. Girard, P. Poulet, I.J. Namer, J. Steibel, J. Chambron, Localized T-2 measurements using an osiris-CPMG method—application to measurements of blood oxygenation and transverse relaxation free of diffusion effect, NMR Biomed. 7 (1994) 343–348.
[223] R.P. Mason, H.P. Shukla, P.P. Antich, Oxygent: A novel probe of tissue oxygen tension, Biomater. Artif. Cells Immobilization. Biotechnol. 20 (1992) 929–935.
[224] R.P. Mason, W. Rodbumrung, P.P. Antich, Hexafluorobenzene: A sensitive ^{19}F NMR indicator of tumor oxygenation, NMR Biomed. 9 (1996) 125–134.
[225] R.P. Mason, P.P. Antich, Application of ^{19}F MR to Non Invasively Assess pO_2 and Temperature *In Vivo* with Rapid Time Resolution (Ed. US patent No.5, 562), 1995.
[226] J.G. Riess, Overview of progress in the fluorocarbon approach to *in vivo* oxygen delivery, Biomater. Artif. Cells Immobilization Biotech. 20 (1992) 183–202.
[227] R.J. Kaufman, J. Goldstein (Ed.), Medical Oxygen Transport Using Perfluorochemicals Butterworth-Heinemann, N.Y., 1991, pp. 127–158.

UNCORRECTED PROOF

Comp. by: RMervin Date:19/11/07 Time:18:09:27 Stage:First Proof File Path://
pchns1301/WOMAT/Production/PRODENV/0000000001/0000006424/0000000016/
0000749453.3D Proof by: QC by: ProjectAcronym:bs:AFS Volume:00005

[228] T.F. Zuck, J.G. Riess, Current status of injectable oxygen carriers. [Review], Crit. Rev. Clin. Lab. Sci. 31 (1994) 295–324.
[229] M.P. Krafft, Fluorocarbons and fluorinated amphiphiles in drug delivery and biomedical research, Adv. Drug Deliv. Rev. 47 (2001) 209–228.
[230] E.G. Schutt, D.H. Klein, R.M. Mattrey, J.G. Riess, Injectable microbubbles as contrast agents for diagnostic ultrasound imaging: The key role of perfluorochemicals, Angew. Chem. Int. Ed. 42 (2003) 3218–3235.
[231] J.G. Riess, Oxygen carriers (“blood substitutes”)—raison d’etre, chemistry, and some physiology, Chem. Rev. 101 (2001) 2797–2920.
[232] J.E. Fishman, P.M. Joseph, T.F. Floyd, B. Mukherji, H.S. Sloviter, Oxygen-sensitive ^{19}F NMR imaging of the vascular system *in vivo*, Magn. Reson. Imag. 5 (1987) 279–285.
[233] J.E. Fishman, P.M. Joseph, M.J. Carvlin, M. Saadi-Elmandjra, B. Mukherji, H.S. Sloviter, *In vivo* measurements of vascular oxygen tension in tumors using MRI of a fluorinated blood substitute, Invest. Radiol. 24 (1989) 65–71.
[234] D. Eidelberg, G. Johnson, P.S. Tofts, J. Dobbin, H.A. Crockard, D. Plummer, ^{19}F imaging of cerebral blood oxygenation in experimental middle cerebral artery occlusion: Preliminary results, J. Cereb. Blood Flow Metab. 8 (1988) 276–281.
[235] U. Noth, S.P. Morrissey, R. Deichmann, H. Adolf, C. Schwarzbauer, J. Lutz, A. Haase, *In vivo* measurement of partial oxygen pressure in large vessels and in the reticuloendothelial system using fast 19F-MRI, Magn. Reson. Med. 34 (1995) 738–745.
[236] K.M. Hoard, Measurement of Flow Rates Using Surface Coil Nuclear Magnetic Resonance Vol. MSc. University of Arlington, Arlington, 1989.
[237] T. Higuchi, S. Naruse, Y. Horikawa, K. Hirakawa, C. Tanaka, *In vivo* measurement of the partial pressure of oxygen in brain tissue using 19F NMR, in: Proceedings of the 7th SMRM, 1988, p. 435.
[238] R.P. Mason, P.P. Antich, E.E. Babcock, J.L. Gerberich, R.L. Nunnally, Perfluorocarbon imaging *in vivo*: A ^{19}F MRI study in tumor-bearing mice, Magn. Reson. Imag. 7 (1989) 475–485.
[239] R.F. Mattrey, D.C. Long, Potential role of PFOB in diagnostic imaging, Invest. Radiol. 23 (1988) s298–301.
[240] W.I. Rosenblum, M.G. Hadfield, A.J. Martinez, P. Schatzki, Alterations of liver and spleen following intravenous infusion of fluorocarbon emulsions, Arch. Pathol. Lab. Med. 100 (1976) 213–217.
[241] R.P. Mason, P.P. Antich, Tumor oxygen tension: Measurement using Oxygent^{TM} as a ^{19}F NMR probe at 4.7 T, Artif. Cells Blood Substit. Immobil. Biotechnol. 22 (1994) 1361–1367.
[242] R.P. Mason, P.P. Antich, E.E. Babcock, A. Constantinescu, P. Peschke, E.W. Hahn, Non-invasive determination of tumor oxygen tension and local variation with growth, Int. J. Radiat. Oncol. Biol. Phys. 29 (1994) 95–103.
[243] R.P. Mason, F.M.H. Jeffrey, C.R. Malloy, E.E. Babcock, P.P. Antich, A noninvasive assessment of myocardial oxygen tension: ^{19}F NMR spectroscopy of sequestered perfluorocarbon emulsion, Magn. Reson. Med. 27 (1992) 310–317.
[244] R.P. Mason, R.L. Nunnally, P.P. Antich, Tissue oxygenation: A novel determination using ^{19}F surface coil spectroscopy of sequestered perfluorocarbon emulsion, Magn. Reson. Med. 18 (1991) 71–79.
[245] N.J. Baldwin, T.C. Ng, Oxygenation and metabolic status of KHT tumors as measured simultaneously by ^{19}F magnetic resonance imaging and ^{31}P magnetic resonance spectroscopy, Magn. Reson. Imaging 14 (1996) 541–551.
[246] H.P. Shukla, R.P. Mason, N. Bansal, P.P. Antich, Regional myocardial oxygen tension: ^{19}F MRI of sequestered perfluorocarbon, Magn. Reson. Med. 35 (1996) 827–833.
[247] B.P.J. van der Sanden, A. Heerschap, A.W. Simonetti, P.F.J.W. Rijken, H.P.W. Peters, G. Stüben, A.J. van der Kogel, Characterization and validation of non-invasive oxygen

UNCORRECTED PROOF

Comp. by: RMervin Date:19/11/07 Time:18:09:28 Stage:First Proof File Path://
pchns1301/WOMAT/Production/PRODENV/0000000001/0000006424/0000000016/
0000749453.3D Proof by: QC by: ProjectAcronym:bs:AFS Volume:00005

tension measurements in human glioma xenografts by ^{19}F-MR relaxometry, Int. J. Radiat. Oncol. Biol. Phys. 44 (1999) 649–658.

[248] H.T. Tran, Q. Guo, D.J. Schumacher, R.B. Buxton, R.F. Mattrey, ^{19}F chemical shift imaging technique to measure intracellular pO_2 *in vivo* using perflubron, Acad. Radiol. 2 (1995) 756–761.

[249] K.G. Helmer, S. Han, C.H. Sotak, On the correlation between the water diffusion coefficient and oxygen tension in RIF-1 tumors, NMR Biomed. 11 (1998) 120–130.

[250] B.R. Barker, R.P. Mason, N. Bansal, R.M. Peshock, Oxygen tension mapping by ^{19}F echo planar NMR imaging of sequestered perfluorocarbon, J. Magn. Reson. Imaging 4 (1994) 595–602.

[251] X. Fan, J.N. River, M. Zamora, H.A. Al-Hallaq, G.S. Karczmar, Effect of carbogen on tumor oxygenation: Combined fluorine-19 and proton MRI measurements, Int. J. Radiat. Oncol. Biol. Phys. 54 (2002) 1202–1209.

[252] S.K. Holland, R.P. Kennan, M.M. Schaub, M.J. D'Angelo, J.C. Gore, Imaging oxygen tension in liver and spleen by ^{19}F NMR, Magn. Reson. Med. 29 (1993) 446–458.

[253] P.S. Hees, C.H. Sotak, Assessment of changes in murine tumor oxygenation in response to nicotinamide using ^{19}F NMR relaxometry of a perfluorocarbon emulsion, Magn. Reson. Med. 29 (1993) 303–310and erratum 329 716 (1993).

[254] D.J.O. McIntyre, C.L. McCoy, J.R. Griffiths, Tumour oxygenation measurements by ^{19}F MRI of perfluorocarbons, Curr. Sci. 76 (1999) 753–762.

[255] P.P. Antich, R.P. Mason, A. Constantinescu, P. Peschke, E.W. Hahn, MRI staining: A novel approach to tumor architecture using perfluorocarbons, Proc. Soc. Nucl. Med. 35(5) (1994) 216P.

[256] B.A. Berkowitz, C.A. Wilson, D.L. Hatchell, Oxygen kinetics in the vitreous substitute perfluorotributylamine: A 19F NMR study *in vivo*, Invest. Ophthalmol. Vis. Sci. 32 (1991) 2382–2387.

[257] C.A. Wilson, B.A. Berkowitz, D.L. Hatchell, Oxygen kinetics in preretinal perfluorotributylamine, Exp. Eye Res. 55 (1992) 119–126.

[258] W. Zhang, Y. Ito, E. Berlin, R. Roberts, B.A. Berkowitz, Role of hypoxia during normal retinal vessel development and in experimental retinopathy of prematurity, Invest. Ophthalmol. Vis. Sci. 44 (2003) 3119–3123.

[259] J.J. Delpuech, M.A. Hamza, G. Serratice, M.J. Stébé, Fluorocarbons as oxygen carriers. I. An NMR study of oxygen solutions in hexafluorobenzene, J. Chem. Phys. 70 (1979) 2680–2687.

[260] M.A. Hamza, G. Serratice, M.J. Stebe, J.J. Delpuech, Solute-solvent interactions in perfluorocarbon solutions of oxygen. An NMR study, J. Am. Chem. Soc. 103 (1981) 3733–3738.

[261] I.M.C.M. Rietjens, A. Steensma, C. den Besten, G. van Tintelen, J. Haas, B. van Ommen, P.J. van Bladeren, Comparative biotransformation of hexachlorobenzene and hexafluorobenzene in relation to the induction of porphyria, Eur. J. Pharmacol. 293 (1995) 292–299.

[262] Y.S. Gorsman, T.A. Kapitonenko, Pharmacology and toxicology of hexafluorobenzene, Izv. Estestvennonauchu. Inst. Pevinsk. 15 (1973) 155–163.

[263] K.M. Mortelmans, V.F. Simmon, ''*In vitro*'' microbiological mutagenicity assays of eight fluorocarbon taggant samples, Gov. Rep. Announce. Index. (US). 81 (1981) 2555–2587.

[264] K.D. Courtney, J.E. Andrews, Teratogenic evaluation and fetal deposition of hexabromobenzene (HBB) and hexafluorobenzene (HFB) in CD-1 mice, J. Environ. Sci. Health B 19 (1984) 83–94.

[265] L.W. Hall, S.R.K. Jackson, G.M. Massey, A. Arias, R. Llaurado,M.A. Nalda, J.N. Lunn (Eds.), Hexafluorobenzene in veterinary anaesthesia, Excerpta Medica, Oxford, 1975, pp. 201–204.

[266] S. Hunjan, R.P. Mason, A. Constantinescu, P. Peschke, E.W. Hahn, P.P. Antich, Regional tumor oximetry: ^{19}F NMR spectroscopy of hexafluorobenzene, Int. J. Radiat. Oncol. Biol. Phys. 40 (1998) 161–171.

UNCORRECTED PROOF

Comp. by: RMervin Date:19/11/07 Time:18:09:30 Stage:First Proof File Path://
pchns1301/WOMAT/Production/PRODENV/0000000001/0000006424/0000000016/
0000749453.3D Proof by: QC by: ProjectAcronym:bs:AFS Volume:00005

[267] D. Zhao, L. Jiang, E.W. Hahn, R.P. Mason, Tumor physiological response to combretastatin A4 phosphate assessed by MRI, Int. J. Radiat. Oncol. Biol. Phys 62 (2005) 872–880.

[268] D. Le, R.P. Mason, S. Hunjan, A. Constantinescu, B.R. Barker, P.P. Antich, Regional tumor oxygen dynamics: ^{19}F PBSR EPI of hexafluorobenzene, Magn. Reson. Imaging, 15 (1997) 971–981.

[269] S. Hunjan, D. Zhao, A. Constantinescu, E.W. Hahn, P.P. Antich, R.P. Mason, Tumor oximetry: Demonstration of an enhanced dynamic mapping procedure using fluorine-19 echo planar magnetic resonance imaging in the Dunning prostate R3327-AT1 rat tumor, Int. J. Radiat. Oncol. Biol. Phys. 49 (2001) 1097–1108.

[270] M. Xia, V. Kodibagkar, H. Liu, R.P. Mason, Tumour oxygen dynamics measured simultaneously by near infrared spectroscopy and ^{19}F magnetic resonance imaging in rats, Phys. Med. Biol. 51 (2006) 45–60.

[271] R.P. Mason, S. Hunjan, A. Constantinescu, Y. Song, D. Zhao, E.W. Hahn, P.P. Antich, P. Peschke, J.F. Dunn, H.M. Swartz (Eds.), Tumor oximetry: Comparison of ^{19}F MR EPI and electrodes, Vol. 530, Kluwer, New York, 2003, pp. 19–28.

[272] R.P. Mason, A. Constantinescu, S. Hunjan, D. Le, E.W. Hahn, P.P. Antich, C. Blum, P. Peschke, Regional tumor oxygenation and measurement of dynamic changes, Radiat. Res. 152 (1999) 239–249.

[273] V. Bourke, J. Gilio, D. Zhao, A. Constantinescu, V. Kodibagkar, L. Jiang, E.W. Hahn, R.P. Mason, Radiat. Res. Meeting (St. Louis, Mo), 2004.

[274] E.K. Rofstad, K. Sundfor, H. Lyng, C.G. Trope, Hypoxia-induced treatment failure in advanced squamous cell carcinoma of the uterine cervix is primarily due to hypoxia-induced radiation resistance rather than hypoxia-induced metastasis, Br. J. Cancer 83 (2000) 354–359.

[275] A.W. Fyles, M. Milosevic, R. Wong, M.C. Kavanagh, M. Pintile, A. Sun, W. Chapman, W. Levin, L. Manchul, T.J. Keane, R.P. Hill, Oxygenation predicts radiation response and survival in patients with cervix cancer, Radiother. Oncol. 48 (1998) 149–156.

[276] M. Höckel, K. Schlenger, B. Aral, M. Mitze, U. Schäffer, P. Vaupel, Hypoxia and radiation response in human tumors, Semi. Radiat. Oncol. 6 (1996) 3–9.

[277] J. Keupp, T. Schaeffter, Proc. Intl. Soc. Mag. Reson. Med. (Seattle) 2006, p. 916.

[278] J.R. Griffiths, Are cancer cells acidic? Br. J. Cancer 64 (1991) 425–427.

[279] V.D. Mehta, P.V. Kulkarni, R.P. Mason, A. Constantinescu, S. Aravind, N. Goomer, P.P. Antich, 6-Fluoropyridoxol: A novel probe of cellular pH using ^{19}F NMR spectroscopy, FEBS Lett. 349 (1994) 234–238.

[280] C.J. Deutsch, J.S. Taylor, Intracellular pH measured by ^{19}F NMR, Ann. N. Y. Acad. Sci. 508 (1987) 33–47.

[281] C. Deutsch, J.S. Taylor, D.F. Wilson, Regulation of intracellular pH of human peripheral blood lymphocytes as measured by ^{19}F NMR, Proc. Natl. Acad. Sci. USA 79 (1982) 7944–7948.

[282] C. Deutsch, J.S. Taylor, M. Price, pH homeostasis in human lymphocytes: Modulation by ions and mitogen, J. Cell Biol. 98 (1984) 885–894.

[283] T. Kashiwagura, C.J. Deutsch, J. Taylor, M. Erecinska, D.F. Wilson, Dependence of gluconeogenesis, urea synthesis, and energy metabolism of hepatocytes on intracellular pH, J. Biol. Chem. 259 (1984) 237–243.

[284] W.J. Thoma, K. Ugurbil, pH and compartmentation of isolated perfused rat liver studied by ^{19}F and ^{31}P NMR, NMR Biomed. 1 (1988) 95–100.

[285] J.S. Taylor, C.J. Deutsch, Fluorinated α-methylamino acids as ^{19}F NMR indicators of intracellular pH, Biophys. J. 43 (1983) 261–267.

[286] A. Joseph, C. Davenport, L. Kwock, C.T. Burt, R.E. London, Fluorine-19 NMR studies of tumor-bearing rats treated with difluoromethylornithine, Magn. Reson. Med. 4 (1987) 137–143.

[287] R.E. London, S.A. Gabel, Determination of membrane potential and cell volume by ^{19}F NMR using trifluoroacetate and trifluoroacetamide probes, Biochemistry 28 (1989) 2378–2382.

UNCORRECTED PROOF

Comp. by: RMervin Date:19/11/07 Time:18:09:31 Stage:First Proof File Path://
pchns1301/WOMAT/Production/PRODENV/0000000001/0000006424/0000000016/
0000749453.3D Proof by: QC by: ProjectAcronym:bs:AFS Volume:00005

[288] A.S.L. Xu, J.R. Potts, P.W. Kuchel, The phenomenon of separate intracellular and extracellular resonances of difluorophosphate in P-31 and F-19 Nmr-spectra of erythrocytes, Magn. Reson. Med. 18 (1991) 193–198.

[289] A.S.L. Xu, A.R. Waldeck, P.W. Kuchel, Transmembrane F-19 Nmr chemical-shift difference of fluorinated solutes in liposomes, erythrocytes and erythrocyte-ghosts, NMR Biomed. 6 (1993) 136–143.

[290] S. Hunjan, R.P. Mason, V.D. Mehta, P.V. Kulkarni, S. Aravind, V. Arora, P.P. Antich, Simultaneous intra- and extra-cellular pH measurement using ^{19}F NMR of 6-Fluoropyridoxol, Magn. Reson. Med. 39 (1998) 551–556.

[291] S. He, R.P. Mason, S. Hunjan, V.D. Mehta, V. Arora, R. Katipally, P.V. Kulkarni, P.P. Antich, Development of novel ^{19}F NMR pH indicators: Synthesis and evaluation of a series of fluorinated vitamin B_6 analogs, Bioorg. Med. Chem. 6 (1998) 1631–1639.

[292] W. Korytnyk, R.P. Singh, Proton magnetic resonance spectra of compounds in the vitamin B_6 group, J. Am. Chem. Soc. 85 (1963) 2813–2817.

[293] K. Yamada, M. Tsuji, Transport of vitamin B6 in human erythrocytes, J. Vitaminol. 16 (1970) 237–242.

[294] J.X. Yu, P. Otten, Z. Ma, W. Cui, L. Liu, R.P. Mason, A novel NMR platform for detecting gene transfection: Synthesis and evaluation of fluorinated phenyl β-D-Galactosides with potential application for assessing LacZ gene expression, Bioconjug. Chem. 15 (2004) 1334–1341.

[295] J.C. Metcalfe, T.R. Hesketh, G.A. Smith, Free cytosolic Ca^{2+} measurements with fluorine labelled indicators using ^{19}F NMR, Cell Calcium 6 (1985) 183–195.

[296] J.S. Beech, R.A. Iles, ^{19}F NMR indicators of hepatic intra cellular pH *in vivo*, Biochem. Soc. Trans. 15 (1987) 871–872.

[297] C.J. Deutsch, J.S. Taylor, New class of ^{19}F pH indicators: Fluoroanilines, Biophys. J. 55 (1989) 799–804.

[298] C.K. Rhee, L.A. Levy, R.E. London, Fluorinated o-aminophenol derivatives for measurement of intracellular pH, Bioconjug. Chem. 6 (1995) 77–81.

[299] J.X. Yu, L. Liu, V.D. Kodibagkar, W. Cui, R.P. Mason, Synthesis and evaluation of novel enhanced gene reporter molecules: Detection of β-Galactosidase activity using ^{19}F NMR of trifluoromethylated Aryl β-D-galactopyranosides, Bioorg. Med. Chem. 14 (2006) 326–333.

[300] W. Cui, P. Otten, J. Yu, V. Kodibagkar, R.P. Mason, Proc. ISMRM (Toronto, Canada) 2003, p. 675.

[301] T. Frenzel, S. Koszler, H. Bauer, U. Niedballa, H.J. Weinmann, Noninvasive *in vivo* pH measurement using a fluorinated pH probe and fluorine-19 magnetic resonance spectroscopy, Invest. Radiol. 29 (1994) S220–222.

[302] T. Miyazawa, Y. Aoki, K. Akagi, M. Takahashi, B. Fritz-Zieroth, T. Frenzel, H.J. Weinmann, Application of ZK150 471, a fluorinated pH probe for ^{19}F MRS, to *in vivo* pH measurement after hyperthermic treatment of tumors in mice, Acad. Radiol. 3 (1996) S363–S364.

[303] A.S. Ojugo, P.M. McSheehy, D.J. McIntyre, C. McCoy, M. Stubbs, M.O. Leach, I.R. Judson, J.R. Griffiths, Measurement of the extracellular pH of solid tumours in mice by magnetic resonance spectroscopy: A comparison of exogenous (19)F and (31)P probes, NMR Biomed. 12 (1999) 495–504.

[304] Y. Aoki, K. Akagi, Y. Tanaka, J. Kawai, M. Takahashi, Measurement of intratumor pH by pH indicator used in ^{19}F MR spectroscopy, Invest. Radiol. 31 (1996) 680–689.

[305] R.Y. Tsien, A non-disruptive technique for loading calcium buffers and indicators into cells, Nature 290 (1981) 527–528.

[306] G.A. Smith, R.T. Hesketh, J.C. Metcalfe, J. Feeney, P.G. Morris, Intracellular calcium measurements by F-19 Nmr of fluorine-labeled chelators, Proc. Natl. Acad. Sci. USA 80 (1983) 7178–7182.

UNCORRECTED PROOF

Comp. by: RMervin Date:19/11/07 Time:18:09:32 Stage:First Proof File Path://
pchns1301/WOMAT/Production/PRODENV/0000000001/0000006424/0000000016/
0000749453.3D Proof by: QC by: ProjectAcronym:bs:AFS Volume:00005

[307] J. Benters, U. Flogel, T. Schafer, D. Leibfritz, S. Hechtenberg, D. Beyersmann, Study of the interactions of cadmium and zinc ions with cellular calcium homoeostasis using F-19-NMR spectroscopy, Biochem. J. 322 (1997) 793–799.
[308] R.K. Gupta, R.J. Gillies, R.K. Gupta (Ed.), ^{19}F NMR Measurement of Intracellular Free Calcium Ions In Intact Cells and Tissues, Vol. 2, CRC, Boca Raton, 1987, pp. 45–53.
[309] F.A. Schanne, J.R. Moskal, R.K. Gupta, Effect of lead on intracellular free calcium ion concentration in a presynaptic neuronal model: 19F-NMR study of NG108–15 cells, Brain Res. 503 (1989) 308–311.
[310] F.A. Schanne, T.L. Dowd, R.K. Gupta, J.F. Rosen, Lead increases free Ca^{2+} concentration in cultured osteoblastic bone cells: Simultaneous detection of intracellular free Pb^{2+} by ^{19}F NMR, Proc. Nal. Acad. Sci. USA 86 (1989) 5133–5135.
[311] E. Marban, M. Kitakaze, V.P. Chacko, M.M. Pike, Ca-2+ transients in perfused hearts revealed by gated F-19 NMR-spectroscopy, Circ. Res. 63 (1988) 673–678.
[312] H. Kusuoka, P.H. Backx, M.C. Camilion de Hurtado, M. Azan-Backx, E. Marban, H.E. Cingolani, Relative roles of intracellular Ca^{2+} and pH in shaping myocardial contractile response to acute respiratory alkalosis, Am. J. Physiol. 265 (1993) H1696–1703.
[313] H.L. Kirschenlohr, J.C. Metcalfe, P.G. Morris, G.C. Rodrigo, G.A. Smith, Ca-2+ Transient, Mg-2+, and pH Measurements in the cardiac cycle by F-19 NMR, Proc. Natl. Acad. Sci. USA 85 (1988) 9017–9021.
[314] H. Plenio, R. Diodone, Covalently bonded fluorine as a σ-donor for groups I and I metal ions in partially fluorinated macrocycles, JACS 118 (1996) 356–367.
[315] J.L. Noronha, G.M. Matuschak, Magnesium in critical illness: Metabolism, assessment, and treatment, Intensive Care Med. 28 (2002) 667–679.
[316] R.K. Gupta, P. Gupta, R.K. Gupta (Ed.), ^{31}P NMR Measurement of Intracellular Free Magnesium in Cells and Organisms, Vol. 2, CRC, Boca Raton, 1987, pp. 34–43.
[317] E. Weller, P. Bachert, H.M. Meinck, B. Friedmann, P. Bartsch, H. Mairbaurl, Lack of effect of oral Mg-supplementation on Mg in serum, blood cells, and calf muscle, Med. Sci. Sports Exerc. 30 (1998) 1584–1591.
[318] C.V. Odvina, R.P. Mason, C.Y.C. Pak, Prevention of thiazide-induced hypokalemia without magnesium depletion by potassium-magnesium citrate, Am. J. Ther. 13 (2006) 101–108.
[319] E. Murphy, Measurement of intracellular ionized magnesium, Miner. Electrolyte Metab. 19 (1993) 250–258.
[320] B. Tecle, J.E. Casida, Enzymatic defluorination and metabolism of fluoroacetate, fluoroacetamide, fluoroethanol, and (-)-erythro-fluorocitrate in rats and mice examined by ^{19}F and ^{13}C NMR, Chem. Res. Toxicol. 2 (1989) 429–435.
[321] L.A. Levy, E. Murphy, B. Raju, R.E. London, Measurement of cytosolic free magnesium concentration by ^{19}F NMR, Biochemistry 27 (1988) 4041–4048.
[322] E. Murphy, C. Steenbergen, L.A. Levy, B. Raju, R.E. London, Cytosolic free magnesium levels in ischemic rat-heart, J. Biol. Chem. 264 (1989) 5622–5627.
[323] G.J. Long, J.F. Rosen, F.A.X. Schanne, Lead activation of protein-kinase-C from rat-brain - determination of free calcium, lead, and zinc by F-19-Nmr, J. Biol. Chem. 269 (1994) 834–837.
[324] H. Plenio, J. Hermann, R. Diodone, The coordination chemistry of fluorocarbons: Difluoro-m-cyclophane-based fluorocryptands and their group I and II metal ion complexes, Inorg. Chem. 36 (1997) 5722–5729.
[325] H. Takemura, H. Kariyazono, M. Yasutake, N. Kon, K. Tani, K. Sako, T. Shinmyozu, T. Inazu, Syntheses of macrocyclic compounds possessing fluorine atoms in their cavities: Structures and complexation with cations, Eur. J. Org. Chem. 1 (2000) 141–148.
[326] H. Plenio, R. Diodone, A fluorine-containing cryptand for the complexation of anions and the utility of F-19 Nmr-spectroscopy for the determination of host guest association, Z. Naturforsch. Section. B-. J. Chem. Sci. 50 (1995) 1075–1078.

UNCORRECTED PROOF

Comp. by: RMervin Date:19/11/07 Time:18:09:33 Stage:First Proof File Path://
pchns1301/WOMAT/Production/PRODENV/0000000001/0000006424/0000000016/
0000749453.3D Proof by: QC by: ProjectAcronym:bs:AFS Volume:00005

[327] R.E. London, S.A. Gabel, F-19 NMR-studies of fluorobenzeneboronic acids.1. Interaction kinetics with biologically significant, JACS 116 (1994) 2562–2569.
[328] J.S. Fowler, N.D. Volkow, G.J. Wang, Y.S. Ding, 2-deoxy-2-[18F]fluoro-D-glucose and alternative radiotracers for positron emission tomography imaging using the human brain as a model, Semin. Nucl. Med. 34 (2004) 112–121.
[329] T. Nakada, I.L. Kwee, C.B. Conboy, J. Neurochem. 46 (1986) 198.
[330] T. Nakada, I.L. Kwee, P.J. Card, N.A. Matwiyoff, B.V. Griffey, R.H. Griffey, F-19 NMR imaging of glucose-metabolism, Magn. Reson. Med. 6 (1988) 307–313.
[331] T. Nakada, I.L. Kwee, B.V. Griffey, R.H. Griffey, F-19 Mr imaging of glucose-metabolism in the rabbit, Radiology 168 (1988) 823–825.
[332] B.A. Berkowitz, J.J.H. Ackerman, Proton decoupled fluorine nuclear-magnetic-resonance spectroscopy *in situ*, Biophys. J. 51 (1987) 681–685.
[333] M.J. Lizak, K. Mori, P.F. Kador, Determination of aldose reductase activity in the eye by localized magnetic resonance spectroscopy, J. Ocul. Pharmacol. Ther. 17 (2001) 475–483.
[334] E.F. Secchi, M.J. Lizak, S. Sato, P.F. Kador, 3-Fluoro-3-deoxy-D-galactose: A new probe for studies on sugar cataract, Curr. Eye Res. 18 (1999) 277–282.
[335] I.L. Kwee, H. Igarashi, T. Nakada, Aldose reductase and sorbitol dehydrogenase activities in diabetic brain: *In vivo* kinetic studies using F-19 3-FDG NMR in rats, Neuroreport 7 (1996) 726–728.
[336] R.G. Shulman, D.L. Rothman, C-13 NMR of intermediary metabolism: Implications for systemic physiology, Annu. Rev. Physiol. 63 (2001) 15–48.
[337] F.M.H. Jeffrey, A. Rajagopal, C.R. Malloy, A.D. Sherry, C-13-Nmr - a simple yet comprehensive method for analysis of intermediary metabolism, Trends Biochem. Sci. 16 (1991) 5–10.
[338] R.P. Mason, J.K.M. Sanders, A. Cornish, *In vivo* enzymology—C-13 Nmr measurement of a kinetic isotope effect for methanol oxidation in methylosinus-trichosporium Ob3b, FEBS Lett. 216 (1987) 4–6.
[339] I.J. Stratford, G.E. Adams, G.G. Steel, G.E. Adams,A. Horwich (Eds.), Radiation Sensitizers and Bioreductive Drugs, Elsevier, Amsterdam, 1989, pp. 145–162.
[340] S.S. Foo, D.F. Abbott, N. Lawrentschuk, A.M. Scott, Functional imaging of intratumoral hypoxia, Mol. Imaging. Biol. 6 (2004) 291–305.
[341] A. Franko, C. Koch, D. Boisvert, Distribution of misonidazole adducts in gliosarcoma tumors and spheroids: Implications for oxygen distribution, Cancer Res. 52 (1992) 3831–3837.
[342] J.R. Ballinger, Imaging hypoxia in tumors, Semin. Nucl. Med. 31 (2001) 321–329.
[343] R.J. Hodgkiss, Use of 2-nitroimidazoles as bioreductive markers for tumour hypoxia, Anticancer Drug Des. 13 (1998) 687–702.
[344] J.G. Rajendran, K.A. Krohn, Imaging hypoxia and angiogenesis in tumors, Radiol. Clin. North Am. 43 (2005) 169–187.
[345] S.M. Evans, S. Hahn, D.R. Pook, W.T. Jenkins, A.A. Chalian, P. Zhang, C. Stevens, R. Weber, G. Weinstein, I. Benjamin, N. Mirza, M. Morgan, S. Rubin, W.G. McKenna, E.M. Lord, C.J. Koch, Detection of hypoxia in human squamous cell carcinoma by EF5 binding, Cancer Res. 60 (2000) 2018–2024.
[346] C.J. Koch, S.M. Hahn, K.J. Rockwell, J.M. Covey, W.G. McKenna, S.M. Evans, Pharmacokinetics of EF5 [2-(2-nitro-1-H-imidazol-1-yl)-N-(2,2,3,3,3-pentafluoropropyl) acetamide] in human patients: Implications for hypoxia measurements *in vivo* by 2-nitroimidazoles, Cancer Chemother. Pharmacol. 48 (2001) 177–187.
[347] A.S.E. Ljungkvist, J. Bussink, P.F.J.W. Rijken, J.A. Raleigh, J. Denekamp, A.J. Van Der Kogel, Changes in tumor hypoxia measured with a double hypoxic marker technique, Int. J. Radiat. Oncol. Biol. Phys. 48 (2000) 1529–1538.
[348] J.S. Lewis, D.W. McCarthy, T.J. McCarthy, Y. Fujibayashi, M.J. Welch, Evaluation of Cu-64-ATSM in vitro and *in vivo* in a hypoxic tumor model, J. Nucl. Med. 40 (1999) 177–183.

Au5

UNCORRECTED PROOF

Comp. by: RMervin Date:19/11/07 Time:18:09:34 Stage:First Proof File Path://
pchns1301/WOMAT/Production/PRODENV/0000000001/0000006424/0000000016/
0000749453.3D Proof by: QC by: ProjectAcronym:bs:AFS Volume:00005

[349] F. Dehdashti, P.W. Grigsby, M.A. Mintun, J.S. Lewis, B.A. Siegel, M.J. Welch, Assessing tumor hypoxia in cervical cancer by positron emission tomography with 60Cu-ATSM: Relationship to therapeutic response-a preliminary report, Int. J. Radiat. Oncol. Biol. Phys. 55 (2003) 1233–1238.

[350] J.D. Chapman, E.L. Engelhardt, C.C. Stobbe, R.F. Schneider, G.E. Hanks, Measuring hypoxia and predicting tumor radioresistance with nuclear medicine assays, Radiother. Oncol. 46 (1998) 229–237.

[351] S.P. Robinson, J.R. Griffiths, Current issues in the utility of ^{19}F nuclear magnetic resonance methodologies for the asssessment of tumour hypoxia, Philos. Trans. R. Soc. Lond. B Biol. Sci. 359 (2004) 987–996.

[352] D. Procissi, F. Claus, J. Koziorowski, P. Burgman, C. Matei, S. Thakur, C. Ling, J.A. Koutcher, Proc. Intl. Soc. Mag. Reson. Med. 2006, p. 1260.

[353] J.M. Cline, G.L. Rosner, J.A. Raleigh, D.E. Thrall, Quantification of CCI-103F labeling heterogeneity in canine solid tumors, Int. J. Radiat. Oncol. Biol. Phys. 37 (1997) 655–662.

[354] P. Workman, R.J. Maxwell, J.R. Griffiths, Noninvasive MRS in New Anticancer Drug Development, NMR Biomed. 5 (1992) 270–272.

[355] B.M. Seddon, R.J. Maxwell, D.J. Honess, R. Grimshaw, F. Raynaud, G.M. Tozer, P. Workman, Validation of the fluorinated 2-nitroimidazole SR-4554 as a noninvasive hypoxia marker detected by magnetic resonance spectroscopy, Clin. Cancer Res. 8 (2002) 2323–2335.

[356] B.M. Seddon, G.S. Payne, L. Simmons, R. Ruddle, R. Grimshaw, S. Tan, A. Turner, F. Raynaud, G. Halbert, M.O. Leach, I. Judson, P. Workman, A phase I study of SR-4554 via intravenous administration for noninvasive investigation of tumor hypoxia by magnetic resonance spectroscopy in patients with malignancy, Clin. Cancer Res. 9 (2003) 5101–5112.

[357] S.J. Li, G.Y. Jin, J.E. Moulder, Prediction of tumor radiosensitivity by hexafluoromisonidazole retention monitored by [H-1]/[F-19] magnetic-resonance spectroscopy, Cancer Commun. 3 (1991) 133–139.

[358] E.O. Aboagye, R.J. Maxwell, M.R. Horsman, A.D. Lewis, P. Workman, M. Tracy, J.R. Griffiths, The relationship between tumour oxygenation determined by oxygen electrode measurements and magnetic resonance spectroscopy of the fluorinated 2-nitroimidazole SR-4554, Br. J. Cancer 77 (1998) 65–70.

[359] H.W. Salmon, D.W. Siemann, Utility of ^{19}F MRS detection of the hypoxic cell marker EF5 to assess cellular hypoxia in solid tumors, Radiother. Oncol. 73 (2004) 359–366.

[360] J.K. Fairweather, M. Faijes, H. Driguez, A. Planas, Specificity studies of bacillus 1,3–1,4-beta-glucanases and application to glycosynthase-catalyzed transglycosylation, Chembiochem 3 (2002) 866–873.

[361] T. Ichikawa, D. Hogemann, Y. Saeki, E. Tyminski, K. Terada, R. Weissleder, E.A. Chiocca, J.P. Basilion, MRI of transgene expression: Correlation to therapeutic gene expression, Neoplasia (New York) 6 (2002) 523–530.

[362] Z. Paroo, R.A. Bollinger, D.A. Braasch, E. Richer, D.R. Corey, P.P. Antich, R.P. Mason, Validating bioluminescence imaging as a high-throughput, quantitative modality for assessing tumor burden, Mol. Imaging 3 (2004) 117–124.

[363] J.G. Tjuvajev, M. Doubrovin, T. Akhurst, S. Cai, J. Balatoni, M.M. Alauddin, R. Finn, W. Bornmann, H. Thaler, P.S. Conti, R.G. Blasberg, Comparison of radiolabeled nucleoside probes (FIAU, FHBG, and FHPG) for PET imaging of HSV1-tk gene expression, J. Nucl. Med. 43 (2002) 1072–1083.

[364] A. Kruger, V. Schirrmacher, R. Khokha, The bacterial lacZ gene: An important tool for metastasis research and evaluation if new cancer therapies, Cancer Metastasis Rev. 17 (1999) 285–294.

[365] I.G. Serebriiskii, E.A. Golemis, Uses of lacZ to study gene function: Evaluation of beta-galactosidase assays employed in the yeast two-hybrid system, Anal. Biochem. 285 (2000) 1–15.

UNCORRECTED PROOF

Comp. by: RMervin Date:19/11/07 Time:18:09:36 Stage:First Proof File Path://
pchns1301/WOMAT/Production/PRODENV/0000000001/0000006424/0000000016/
0000749453.3D Proof by: QC by: ProjectAcronym:bs:AFS Volume:00005

[366] J.R. Beckwith, D. Zipser, The Lactose Operon Cold Spring Harbor Laboratory, Cold Spring Harbor, 1970, p. 435.
[367] J. Kawaguchi, V. Wilson, P.J. Mee, Visualization of whole-mount skeletal expression patterns of LacZ reporters using a tissue clearing protocol, Biotechniques 32 (2002) 68–73.
[368] K. Heuermann, J. Cosgrove, S-Gal: An autoclavable dye for color selection of cloned DNA inserts, Biotechniques 30 (2001) 1142–1147.
[369] I. Bronstein, B. Edwards, J.C. Voyta, 1,2-Dioxetanes—novel chemi-luminescent enzyme substrates—applications to immunoassays, J. Chemilum. Biolum. 4 (1989) 99–111.
[370] A.Y. Louie, M.M. Huber, E.T. Ahrens, U. Rothbacher, R. Moats, R.E. Jacobs, S.E. Fraser, T.J. Meade, *In vivo* visualization of gene expression using magnetic resonance imaging, Nat. Biotechnol. 18 (2000) 321–325.
[371] C.H. Tung, Q. Zeng, K. Shah, D.E. Kim, D. Schellingerhout, R. Weissleder, *In vivo* imaging of beta-galactosidase activity using far red fluorescent switch, Cancer Res. 64 (2004) 1579–1583.
[372] K.H. Lee, S.S. Byun, J.H. Choi, J.Y. Paik, Y.S. Choe, B.T. Kim, Targeting of lacZ reporter gene expression with radioiodine-labelled phenylethyl-beta-d-thiogalacto-pyranoside, Eur. J. Nucl. Med. Mol. Imaging 31 (2004) 433–438.
[373] S. Yoon, H.G. Kim, K.H. Chun, J.E.N. Shin, 4-deoxy-analogs of p-nitrophenyl β-D-galactopyranosides for specificity study with b-galactosidase from escherichia coli, Bull. Korean Chem. Soc. 17 (1996) 599–604.
[374] W. Cui, P. Otten, Y. Li, K. Koeneman, J. Yu, R.P. Mason, A novel NMR approach to assessing gene transfection: 4-fluoro-2-nitrophenyl-β-D-galactopyranoside as a prototype reporter molecule for β-galactosidase, Magn. Reson. Med. 51 (2004) 616–620.
[375] V.D. Kodibagkar, J. Yu, L. Liu, H.P. Hetherington, R.P. Mason, Imaging b-galactosidase activity using ^{19}F chemical shift imaging of LacZ gene-reporter molecule 2-fluoro-4-nitrophenol-β-D-galactopyranoside, Magn. Reson. Imaging 24 (2006) 959–962.
[376] J.P. Richard, J.G. Westerfeld, S. Lin, Structure-reactivity relationships for beta-galactosidase (Escherichia coli, lac Z). 1. Bronsted parameters for cleavage of alkyl beta-D-galactopyranosides, Biochemistry 34 (1995) 11703–11712.
[377] J.X. Yu, Z. Ma, Y. Li, K.S. Koeneman, L. Liu, R.P. Mason, Synthesis and evaluation of a novel gene reporter molecule: Detection of β-galactosidase activity using ^{19}F NMR of a fluorinated vitamin B6 conjugate, Med. Chem. 1 (2005) 255–262.
[378] J.X. Yu, R.P. Mason, Synthesis and characterization of novel lacZ gene reporter molecules: Detection of b-galactosidase activity using ^{19}F NMR of polyglycosylated fluorinated vitamin B6, J. Med. Chem. 49 (2006) 1991–1999.
[379] V. Kodibagkar, J. Yu, L. Liu, R.P. Mason, 2006, in press.
[380] L.C. Clark Jr., F. Gollan, Survival of mammals breathing organic liquids equilibrated with oxygen at atmospheric pressure, Science 152 (1966) 1755–1756.
[381] J.S. Greenspan, W.W. Fox, S.D. Rubenstein, M.R. Wolfson, S.S. Spinner, T.H. Shaffer, Partial liquid ventilation in critically ill infants receiving extracorporeal life support. Philadelphia Liquid Ventilation Consortium, Pediatrics 99 (1997) E2.
[382] S.R. Thomas, L.C. Clark Jr., J. Ackerman, R.G. Pratt, R.E. Hoffmann, L.J. Busse, R.A. Kinsey, R.C. Samaratunga, MRI imaging of the lung using liquid perfluorocarbons, J. Comput. Asst. Tomogr. 10 (1986) 1–9.
[383] S.R. Thomas, L. Gradon, S.E. Pratsinis, R.G. Pratt, G.P. Fotou, A.J. McGoron, A.L. Podgorski, R.W. Millard, Perfluorocarbon compound aerosols for delivery to the lung as potential ^{19}F magnetic resonance reporters of regional pulmonary pO_2, Invest. Radiol. 32 (1997) 29–38.
[384] M.Q. Huang, Q. Ye, D.S. Williams, C. Ho, MRI of lungs using partial liquid ventilation with water-in-perfluorocarbon emulsions, Magn. Reson. Med. 48 (2002) 487–492.
[385] E. Heidelberger, P.C. Lauterbur, 1982, pp. 70–71.

UNCORRECTED PROOF

Comp. by: RMervin Date:19/11/07 Time:18:09:37 Stage:First Proof File Path://
pchns1301/WOMAT/Production/PRODENV/0000000001/0000006424/0000000016/
0000749453.3D Proof by: QC by: ProjectAcronym:bs:AFS Volume:00005

[386] D.O. Kuethe, V.C. Behr, S. Begay, Volume of rat lungs measured throughout the respiratory cycle using F-19 NMR of the inert gas SF_6, Magn. Reson. Med. 48 (2002) 547–549.

[387] J. Ruiz-Cabello, J.M. Perez-Sanchez, R.P. de Alejo, I. Rodriguez, N. Gonzalez-Mangado, G. Peces-Barbas, M. Cortijo, Diffusion-weighted F-19-MRI of lung periphery: Influence of pressure and air-SF_6 composition on apparent diffusion coefficients, Resp. Physiol. Neurobiol. 148 (2005) 43–56.

[388] W.F. Remy, R.W. Geenen, S.M. Hussain, F. Cademartiri, J.W. Poley, P.D. Siersema, G.P. Krestin, CT and MR colonography: Scanning techniques, postprocessing, and emphasis on polyp detection, Radiograph. 24 (2004) e18.

[389] D.L. Rubin, K.L. Falk, M.J. Sperling, M. Ross, S. Saini, B. Rothman, F. Shellock, E. Zerhouni, D. Stark, E.K. Outwater, U. Schmiedl, L.C. Kirby, J. Chezmar, T. Coates, M. Chang, J.M. Silverman, N. Rofsky, K. Burnett, J. Engel, S.W. Young, A multicenter clinical trial of Gadolite Oral Suspension as a contrast agent for MRI. [Clinical Trial. Clinical Trial, Phase II. Clinical Trial, Phase III, J. Magn. Reson. Imaging 7 (1997) 865–872.

[390] S. Hirohashi, H. Uchida, K. Yoshikawa, N. Fujita, K. Ohtomo, Y. Yuasa, Y. Kawamura, O. Matsui, Large scale clinical evaluation of bowel contrast agent containing ferric ammonium citrate in MRI, Magn. Reson. Imaging 12 (1994) 837–846.

[391] G.S.I. Bisset, K.H. Emery, M.P. Meza, N.K. Rollins, S. Don, J.S. Shorr, Perflubron as a gastrointestinal MR imaging contrast agent in the pediatric population, Pediatr. Radiol. 26 (1996) 409–415.

[392] R.F. Mattrey, M.A. Trambert, J.J. Brown, S.W. Young, J.N. Bruneton, G.E. Wesbey, Z.N. Balsara, Perflubron as an oral contrast agent for MR imaging: Results of a phase III clinical trial, Radiology 191 (1994) 841–848.

[393] B. Uzzan, P. Nicolas, M. Cucherat, G.Y. Perret, Microvessel density as a prognostic factor in women with breast cancer: A systematic review of the literature and meta-analysis, Cancer Res. 64 (2004) 2941–2955.

[394] S.P. Robinson, P.F. Rijken, F.A. Howe, P.M. McSheehy, B.P. van der Sanden, A. Heerschap, M. Stubbs, A.J. Van Der Kogel, J.R. Griffiths, Tumor vascular architecture and function evaluated by non-invasive susceptibility MRI methods and immunohistochemistry, J. Magn. Reson. Imaging. 17 (2003) 445–454.

[395] T.L. Ceckler, S.L. Gibson, R. Hilf, R.G. Bryant, In situ assessment of tumor vascularity using fluorine NMR imaging, Magn. Reson. Med. 13 (1990) 416–433.

[396] K.L. Meyer, P.M. Joseph, B. Mukherji, V.A. Livolsi, R. Lin, Measurement of vascular volume in experimental rat-tumors by F-19 magnetic-resonance-imaging, Invest. Radiol. 28 (1993) 710–719.

[397] T. Sogabe, T. Imaizumi, T. Mori, M. Tominaga, K. Koga, Y. Yabuuchi, Effects of vasodilators on the signal intensity of perfluorocarbon monitored by *in vivo* F-19-NMR spectroscopy, Magn. Reson. Imaging 15 (1997) 341–345.

[398] Y. Gu, R.P. Mason, H. Liu, Estimated fraction of tumor vascular blood contents sampled by near infrared spectroscopy and ^{19}F magnetic resonance spectroscopy, Opt. Express. 13 (2005) 1724–1733.

[399] B. Authier, Reactive hyperemia monitored on rat muscle using perfluorocarbons and F-19 NMR, Magn. Reson. Med. 8 (1988) 80–83.

[400] N.J. Baldwin, Y. Wang, T.C. Ng, *In situ* ^{19}F MRS measurement of RIF-1 tumor blood volume: Corroboration by radioisotope-labeled [^{125}I]-albumin and correlation to tumor size, Magn. Reson. Imaging 14 (1996) 275–280.

[401] J.R. Ewing, C.A. Branch, S.C. Fagan, J.A. Helpern, R.T. Simkins, S.M. Butt, K.M. A. Welch, Fluorocarbon-23 measure of cat cerebral blood flow by NMR, Stroke 21 (1990) 100–106.

[402] S.M. Eleff, M.D. Schnall, L. Ligetti, M. Osbakken, V.H. Subramanian, B. Chance, J.S. Leigh, concurrent measurements of cerebral blood-flow, sodium, lactate, and

UNCORRECTED PROOF

Comp. by: RMervin Date:19/11/07 Time:18:09:38 Stage:First Proof File Path://
pchns1301/WOMAT/Production/PRODENV/0000000001/0000006424/0000000016/
0000749453.3D Proof by: QC by: ProjectAcronym:bs:AFS Volume:00005

high-energy phosphate-metabolism using F-19, Na-23, H-1, and P-31 nuclear magnetic-resonance spectroscopy, Magn. Reson. Med. 7 (1988) 412–424.

[403] J.S. van den Brink, Y. Watanabe, C.K. Kuhl, T. Chung, R. Muthupillai, M. Van Cauteren, K. Yamada, S. Dymarkowski, J. Bogaert, J.H. Maki, C. Matos, J.W. Casselman, R.M. Hoogeveen, Implications of SENSE MR in routine clinical practice, Eur. J. Radiol. 46 (2003) 3–27.

[404] K.P. Pruessmann, M. Weiger, M.B. Scheidegger, P. Boesiger, SENSE: Sensitivity encoding for fast MRI, Magn. Reson. Med. 42 (1999) 952–962.

[405] H.P. Shukla, Application of Perfluorocarbon Emulsions as Fluorine-19 Nuclear Magnetic Resonance Molecular Probes of Cardiac Tissue Oxygen Tension, University of Texas Southwestern Graduate School of Biomedical Sciences, 1994Ph.D..

[406] J. Taylor, C.J. Deutsch, ^{19}F nuclear magnetic resonance: Measurements of [O_2] and pH in biological systems, Biophys. J. 53 (1988) 227–233.

[407] Q. Guo, R.F. Mattrey, C. Guclu, R.B. Buxton, O. Nalcioglu, Monitoring of pO2 by spin-spin relaxation rate 1/T2 of 19F in a rabbit abscess model, Artif Cells Blood Substit. Immobil. Biotechnol. 22 (1994) 1449–1454.

[408] J.J. Delpuech, M.A. Hamza, G. Serratrice, Determination of oxygen by a nuclear magnetic-resonance method, J. Magn. Reson. 36 (1979) 173–179.

[409] N. Raghunand, R.J. Gillies, pH and chemotherapy, Novartis Foundation Symposium 240 (2001) 199–211.

[410] G.A. Smith, P.G. Morris, T.R. Hesketh, J.C. Metcalfe, Design of an indicator of intracellular free Na^+ concentration using ^{19}F-NMR, Biochim. Biophys. Acta 889 (1986) 72–83.

[411] R. Ramasamy, P. Zhao, W.L. Gitomer, A.D. Sherry, C.R. Malloy, Determination of chloride potential in perfused rat hearts by NMR spectroscopy, Am. J. Physiol. 263 (1993) H1958–1962.

[412] A.A. Bobko, S.V. Sergeeva, E.G. Bagryanskaya, A.L. Markel, V.V. Khramtsov, V.A. Reznikov, N.G. Kolosova, 19F NMR measurements of NO production in hypertensive ISIAH and OXYS rats, Biochem. Biophys. Res. Commun. 330 (2005) 367–370.

[413] J. Raleigh, A. Franko, D. Kelly, L. Trimble, P. Allen, Development of an *in vivo* 19F MR method for measuring oxygen deficiency in tumors, Magn. Reson. Med 22 (1991) 451–466.

[414] A. Daugherty, N.N. Becker, L.A. Scherrer, B.E. Sobel, J.J.H. Ackerman, J.W. Baynes, S.R. Thorpe, Non-invasive detection of protein-metabolism *In vivo* by NMR-spectroscopy—Application of a novel F-19-containing residualizing label, Biochem. J. 264 (1989) 829–835.

[415] B.A. Berkowitz, J.T. Handa, C.A. Wilson, Perfluorocarbon temperature measurement using ^{19}F NMR, NMR Biomed 5 (1992) 65–68.

[416] T.Q. Duong, J.J.H. Ackerman, H.S. Ying, J.J. Neil, Evaluation of extra- and intracellular apparent diffusion in normal and globally ischemic rat brain via F-19 NMR, Magn. Reson. Med. 40 (1998) 1–13.

[417] C. Thomas, C. Counsell, P. Wood, G.E. Adams, Use of F-19 nuclear-magnetic-resonance spectroscopy and hydralazine for measuring dynamic changes in blood perfusion volume in tumors in mice, J. Natl. Cancer Inst. 84 (1992) 174–180.

[418] R.L. Nunnally, E.E. Babcock, S.D. Horner, R.M. Peshock, Fluorine-19 NMR spectroscopy and imaging investigations of myocardial perfusion and cardiac function, Magn. Reson. Imaging 3 (1985) 399–405.

[419] R. Tibes, J. Trent, R. Kurzrock, Tyrosine kinase inhibitors and the dawn of molecular cancer therapeutics, Ann. Rev. Pharmacol. Toxicol. 45 (2005) 357.

[420] M.H. Cohen, G.A. Williams, R. Sridhara, G. Chen, R. Pazdur, FDA drug approval summary: Gefitinib (ZD1839) (Iressa(R)) Tablets, Oncologist 8 (2003) 303–306.

[421] R. Neri, Pharmacology and pharmacokinetics of flutamide, Urology 34 (1989) 19–21.

[422] R. Eliason, J.J. Schoenau, A.M. Szmigielski, W.M. Laverty, Phytotoxicity and persistence of flucarbazone-sodium in soil, Weed Sci. 52 (2004) 857–862.

UNCORRECTED PROOF

Comp. by: RMervin Date:19/11/07 Time:18:09:39 Stage:First Proof File Path://
pchns1301/WOMAT/Production/PRODENV/0000000001/0000006424/0000000016/
0000749453.3D Proof by: QC by: ProjectAcronym:bs:AFS Volume:00005

[423] J.K. Moon, J.H. Kim, S. Rhee, G. Kim, H. Yun, B.J. Chung, S. Lee, Y. Lim, Structural investigation of bistrifluron using X-ray crystallography, NMR spectroscopy, and molecular modeling, Bull. Korean Chem. Soc. 23 (2002) 1545–1547.

[424] P. Christie, Roflumilast: A selective phosphodiesterase 4 inhibitor, Drugs Today 41 (2005) 667–675.

[425] K.A. Haagsma, M.K. Rust, Effect of hexaflumuron on mortality of the Western subterranean termite (Isoptera: Rhinotermitidae) during and following exposure and movement of hexaflumuron in termite groups, Pest. Manag. Sci. 61 (2005) 517–531.

[426] A. Howell, Fulvestrant ('Faslodex'): Current and future role in breast cancer management, Crit. Rev. Oncol. Hematol. 57 (2006) 265–273.

[427] K.A. Santora, M. Zakson-Aiken, C. Rasa, W. Shoop, Development of a mouse model to determine the systemic activity of potential flea-control compounds, Vet. Parasitol. 104 (2002) 257–264.

[428] E. Van Den Neste, S. Cardoen, F. Offner, F. Bontemps, Old and new insights into the mechanisms of action of two nucleoside analogs active in lymphoid malignancies: Fludarabine and cladribine (Review), Int. J. Oncol. 27 (2005) 1113–1124.

[429] C. Blasco, G. Font, J. Manes, Y. Pico, Solid-phase microextraction liquid chromatography/tandem mass spectrometry to determine postharvest fungicides in fruits, Anal. Chem. 75 (2003) 3606–3615.

[430] A.W. Abu-Qare, M.B. Abou-Donia, Sarin: Health effects, metabolism, and methods of analysis, Food Chem. Toxicol. 40 (2002) 1327–1333.

[431] R.E. London, S.A. Gabel, F-19 NMR-studies of fluorobenzeneboronic acids.1. Interaction kinetics with biologically significant ligands, J. Am. Chem. Soc. 116 (1994) 2562–2569.

[432] R.F. Mattrey, D.J. Schumacher, H.T. Tran, Q. Guo, R.B. Buxton, The use of Imagent in diagnostic imaging research and ^{19}F magnetic resonance for pO_2 measurements, Biomater. Artif. Cells Immobization Biotechnol. 20 (1992) 917–920.

[433] S. Laukemper-Ostendorf, A. Scholz, K. Burger, C.P. Heussel, M. Schmittner, N. Weiler, K. Markstaller, B. Eberle, H.U. Kauczor, M. Quintel, M. Thelen, W. G. Schreiber, 19F-MRI of perflubron for measurement of oxygen partial pressure in porcine lungs during partial liquid ventilation, Magn. Reson. Med. 47 (2002) 82–89.

[434] C.H. Sotak, P.S. Hees, H.H. Huang, M.H. Hung, C.G. Krespan, S. Reynolds, A new perfluorocarbon for use in fluorine-19 magnetic resonance spectroscopy, Magn. Reson. Med. 29 (1993) 188–195.

[435] M.V. Papadopoulou, R. Pouremad, M.K. Rao, M. Ji, W.D. Bloomer, *In vitro* evaluation of 4-[3-(2-nitro-1-imidazolyl)-propylamino]-7-trifluoromethylquinoline hydrochloride (NLTQ-1), a new bioreductive agent as a hypoxia marker by F-19-magnetic resonance spectroscopy (F-19-MRS), *In Vivo* 15 (2001) 365–371.

UNCORRECTED PROOF

Blood Oxygen Level Dependent (BOLD) and Gd-DTPA dynamic contrast enhanced (DCE) MRI: comparison of two prostate tumor sublines exhibiting different vascular development

Lan Jiang[1], Dawen Zhao[1], Eric W. Hahn[1], Albert J. van der Kogel[2], Johan Bussink[2], Peter Peschke[3], and Ralph P. Mason[1]

[1]Department of Radiology, UT Southwestern Medical Center, Dallas, TX
[2]Department of Radiation Oncology, University Medical Center Nijmegen, Netherlands,
[3]German Cancer Research Center, Heidelberg, Germany

Running title: BOLD and DCE MRI assessment of prostate tumors

Contact information:
Ralph P Mason, Ph.D., CSci, CChem
Department of Radiology
UT Southwestern Medical Center at Dallas
5323 Harry Hines Blvd
Dallas, TX 75390-9058 USA
Email: Ralph.Mason@UTSouthwestern.edu
Tel: 214-648-8926
FAX: 214-648-2991

Key Words: BOLD, DCE, prostate tumor, oxygen, hypoxia

Abstract

Background: Tumor microcirculation and oxygenation play important roles in the responsiveness of tumors to cytotoxic treatment. Dynamic Contrast-Enhanced (DCE) MRI based on the transport properties of Gd-DTPA provides an indication of vascular perfusion and permeability. Blood Oxygenation Level Dependent (BOLD) MRI contrast in response to challenge with hyperoxic gas is sensitive to tumor vascular oxygenation, blood flow, and vascular volume.

Methods: This study investigates correlations and differences between BOLD and DCE MRI acquired in immediate succession in two Dunning prostate R3327 rat tumor sublines (AT1 and H) noted for their different growth rates and vascular maturity. Tumors were imaged serially during respiratory oxygen challenges and Gd-DTPA injection at 4.7 Tesla using echo planar imaging (EPI). Both BOLD and DCE revealed intra and inter tumor heterogeneity. A pharmacokinetic model and histology were used to assess characteristics of the tumor vasculature.

Results: The mean permeability, *Kep*, showed no significant difference between tumor regions or types. However, the regional semi-quantitative response (ΔSI) accompanying BOLD or DCE MRI in the two sublines was markedly different in accord with histology.

Conclusion: This study further validates the use of DCE and BOLD MRI for characterizing the vascular compartments and differentiating tumors with diverse vascular characteristics.

Introduction

Imaging provides the opportunity to non-invasively characterize tumors with three primary goals: identification of tumors, prognosis of potential tumor development, and the longitudinal response to therapy. Tumors comprise heterogeneous populations of stromal and tumor cells that differ in their growth rates and sensitivity to therapeutic agents. Owing to this diversity, marked regional differences are also observed in microenvironmental characteristics, such as oxygenation status and microcirculation. Heterogeneity may be spatial and temporal and imaging allows non-invasive repeat assessment. It may be particularly valuable in prostate cancer, which is often a heterogeneous multi-focal disease with the potential development ranging from aggressive metastatic spread to indolent stasis. A major goal of Urology/Radiology is to be able to differentiate patients who need immediate aggressive therapy from those better served by watchful waiting.

Proton MRI not only provides non-invasive assessment of detailed tumor anatomy, but specific MRI techniques may give an indication of tumor angiogenesis and pathophysiological state (1-4). Dynamic Contrast Enhanced MRI based on the transport properties of small paramagnetic contrast agents, such as Gd-DTPA, provides an indication of tumor perfusion and vessel permeability. There have been many semi quantitative reports together with increasingly sophisticated pharmacokinetic models to monitor tumor vascular function (5-8). Another approach exploits intrinsic contrast based on Blood Oxygenation Level Dependent (BOLD) signal in response to inhaling hyperoxic gas, such as oxygen or carbogen (5% CO_2, 95% O_2). The conversion of paramagnetic deoxyhemoglobin to diamagnetic oxyhemoglobin influences the MR signal, particularly in T_2^* weighted images (9). However, the BOLD effect is also

sensitive to changes in blood flow and vascular volume, and hence, the term FLOOD (Flow and oxygen level dependent) has been introduced (10). To date, there have been limited reports of the use of the BOLD effect to characterize tumors (11-20). Still fewer reports have examined BOLD and DCE together in the same tumors consecutively or in conjunction with histology (13,21).

We hypothesize that the combined application of BOLD and DCE MRI can provide additional insight into tumor pathophysiology. In this study, we test this notion in two syngeneic rat prostate tumor sublines noted for their differences in growth rates and vascular maturity.

Materials and Methods

Experiments were approved by the UT-Southwestern Institutional Animal Care and Use Committee.

Animal model

Two sublines of the Dunning prostate R3327 adenocarcinoma were selected: H, a well-differentiated, hormone dependent slow-growing tumor with a volume doubling time (VDT) of 16 days, and the AT1, an anaplastic and faster-growing subline with a VDT of 5 days (22-24). Tumor tissues were originally obtained from Dr. J. T. Isaacs (Johns Hopkins University, Baltimore, MD). Eight tumors of each subline were implanted in a skin pedicle surgically created on the foreback of adult male syngeneic Copenhagen-2331 rats, as described in detail previously (25). Tumors were allowed to grow to about 1 cm^3 and were investigated by MRI. The rats were anesthetized with ketamine hydrochloride 200 μl (100 mg/ml) IP, and maintained with air and isoflurane (1.3%; 1 dm^3/min). A heparin tipped catheter (27 G butterfly, Abbott Labs, Chicago, IL)

was placed in the right tail vein. The body temperature of rats was maintained with a circulating warm-water blanket. A reference capillary phantom containing saline was placed adjacent to selected tumors.

MRI technique

A size-matched single turn solenoid volume coil was placed around the tumor and MR experiments were performed using a 4.7 T horizontal bore system with actively shielded gradients (GE Omega with Acustar®, Bruker, Fremont, CA). Vascular oxygen dynamics were assessed using BOLD contrast ^{1}H MRI in a coronal section parallel to the rat body acquired using a series of spin echo planar images sensitive to both T_1 and T_2^* with a field of view 40×40 mm, matrix 32×32, and thickness 2 mm. We previously used this pulse burst saturation recovery MBEST sequence for both ^{19}F MRI oximetry and ^{1}H contrast studies (15,26). Initial saturation is non-slice selective, thereby saturating signal throughout the tumor and minimizing in-flow effects. Here, we used a constant recovery time τ = 500 ms (≡ TR) and TE = 33.5 ms. Each experiment included a series of fifty-six consecutive echo planar images obtained at 5 s intervals. Baseline stability was measured for up to 5 mins, while the rat breathed air. For BOLD contrast measurements, baseline was assessed for 25 s (images 1 to 5) before respiratory challenge with oxygen (1 dm^3/min) for a period of 255 s (images 6 to 56). Following a re-equilibration period of breathing air (15 minutes), a new baseline was measured for 25 s and then a bolus of Gd-DTPA (125 μl 0.1 mmol/kg, Magnevist™, Berlex) was injected manually via the tail vein catheter *in situ* over 1 s. A further series of echo planar images was acquired without changing animal position.

Relative signal intensity

Changes in signal intensity and model fitting were assessed on a voxel-by-voxel basis. Initial inspection showed occasional signal spikes, and thus, a pre filter was applied removing any data points, which deviated from the mean signal intensity by more than three standard deviations of the complete curve. The baseline signal intensity, SI_b, of each voxel was defined as the average of the five initial images under baseline conditions. The relative signal intensity changes of each tumor voxel with respect to each intervention (breathing oxygen or Gd-DTPA injection) were analyzed statistically using the equation:

$$\text{Relative Signal Intensity}\,(\Delta SI) = \left(SI_E - SI_b\right)/SI_b \cdot 100\%, \quad (1)$$

where SI_E refers to the enhanced signal intensity of the voxel. Image normalization yielded voxel-by-voxel signal intensity changes from baseline values expressed as a percentage change. Mean (ΔSI) is directly related to area under the curve (AUC). Each tumor was also divided into peripheral and central regions. The peripheral region occupied the two outermost voxels of the tumor. The boundary occupied a single voxel width and the remaining area was considered to be central.

Pharmacokinetic modeling

Contrast enhancement was quantified using the Brix two-compartment model (27) to assess the vascular permeability, *Kep*. For a bolus injection:

$$\frac{SI_E}{SI_0} = 1 + A^H \cdot K_{ep}\left(\frac{e^{-K_{ep}\,t} - e^{-K_{el}\,t}}{K_{el} - K_{ep}}\right) \quad (2)$$

where A^H is a parameter that depends on properties of the tissue, the MR sequence, and the infusion rate; SI_E is signal intensity after injection of contrast agent;

SI_0 is the signal intensity before injection; *Kep* is the rate constant between extravascular extracellular space (EES) and plasma, which is effected by microvascular permeability; K_{el} is the elimination rate of tracer from the central compartment. We have previously shown that ΔSI is proportional to [Gd-DTPA] using this pulse sequence in gel phantoms at 4.7 T (15).

Histology

Pimonidazole hydrochloride (Hypoxyprobe-1; NPI, Belmont, MA) was injected into the tail vein at a dose of 60 mg/kg. Ninety minutes later the blue fluorescent dye Hoechst 33342 (Molecular Probes, Eugene, OR) was injected via the tail vein of anesthetized rats at a concentration of 10 mg/kg in 0.9% saline (0.1 ml), and the tumors were excised 1 min later. For immunohistochemistry, the tissues were immediately immersed in liquid nitrogen and stored at -80 ^{o}C. Tumor sections were double-stained for hypoxia (pimonidazole) and vasculature (CD31). Pimonidazole was detected with a polyclonal rabbit-anti-pimonidazole (gift J. A. Raleigh) and donkey-anti-rabbit F(ab')2 Alexa488 (Molecular Probes, Eugene, Oregon). For staining of the blood vessels, mouse anti rat CD31 monoclonal antibody (1:20; Serotec, Raleigh, NC) and HRP-conjugated goat anti mouse secondary antibody Cy3.

Grey-scale images were acquired with a high-resolution camera (12 bit, 1300x1300 pixels) on a fluorescence microscope (Axioskop, Zeiss, Weesp, The Netherlands) using a computer-controlled motorized stepping stage. The recorded fields were combined to a composite gray scale image. Using different filter sets, multiple scans yielded composite images. To capture hypoxia and vascular parameters, whole tumor sections were scanned sequentially three times at 100x magnification with a UV filter set for the Hoechst 33342 signal, as well as filter sets for the Alexa488 and Cy3

signals. Each scan consisted of 144 (12X12) fields of 1.2 mm^2 (the maximum on this system), which comprised approximately 1/2-1/3 of the tumor sections evaluated in this study.

Statistics

Data processing used IDL software with programs written by us. Image display used a commercial graph display and analysis package (SIGMAPLOT 2000). All results are presented as mean ± s.e. Comparisons between the groups were performed using an Analysis of Variance (ANOVA) with significance set at $p< 0.01$ (Statview, SAS, Carey, NC). Data were assessed in terms of individual voxels, tumor regions, tumors, and the whole tumor group with respect to interventions based on numerical values.

Results

^{1}H MRI showed distinct heterogeneity in signal intensity across tumors of each type (Fig. 1) with mean signal stability during repeat measurements under baseline conditions (variation <2%, Fig. 2). Both tumor types showed significant regionally heterogeneous changes in the BOLD signal contrast with respect to oxygen inhalation (Fig. 1a) or Gd-DTPA infusion (Fig. 1b). In response to oxygen inhalation, mean signal intensity increased significantly, though there was a delay of about 40 s after switching gases. The mean signal intensity for the groups of tumors increased rapidly to a plateau of about 40% (AT1) (Fig 2a) and 30% (H) (Fig 2b) above baseline. Following Gd-DTPA infusion, signal intensity rapidly increased above baseline to a peak 50% for the AT1 tumors (Fig 2a) and 70% for the H tumors (Fig 2b) and then settled to equilibrium at values of 30% and 50% above baseline.

To further examine the spatial heterogeneity evident in Fig. 1, the regional response of each tumor was examined by dividing the tumors into central (mean area 18±1% for AT1 tumors, 24±2% for H tumors) and peripheral regions (60 ±2% for AT1 tumors, 55±3% for H tumors). As a group, the AT1 tumors showed a significantly higher response in the periphery compared to the center with both BOLD and DCE ((p<0.0001), Table 1, Fig. 3a and b). The group of H tumors showed the opposite effect for both interventions, but with a particularly large DCE in the tumor center (Table 1, Fig. 3c and d). Considering individuals, five of eight AT1 tumors showed significantly higher response to oxygen in the peripheral region compared to that in the central region (p<0.01). Of these, three tumors also showed significantly greater responses to Gd-DTPA in the peripheral region (p<0.01). Conversely, for the H tumors, four of eight showed a significantly higher BOLD response in the central region (p<0.01), but only one of eight showed a significantly higher response in the peripheral region (p<0.01). For DCE contrast, four H tumors showed significantly higher central response (p<0.01).

Tumors may also be considered in terms of the fate of individual voxels, *i.e*., spatial heterogeneity. For BOLD the response was delayed relative to DCE with minimal change after 20 s, but by 125 s after switching gas about 90% of the AT1 tumor regions had responded by > 20% (Fig. 4a). H tumors behaved similarly (Fig 4b). By comparison, for DCE the signal had changed by more than 20% in more than 70% of the tumor regions in the AT1 tumors within 20 s of administering Gd-DTPA (Fig. 4c). More than 30% of the voxels had changed more than 60% within 125 s, though intriguingly about one third showed a signal decline rather than increase. H tumors showed a rather similar time course, but the fraction of responding tumor was larger (~90% showed > 20% change after 20 s; Fig 4d). Intriguingly, about as many voxels showed a signal

decrease of >20%, as showed such an increase in response to either intervention in both tumor types. Signal loss was generally restricted to a 20 to 40% range, whereas 20% of voxels showed >80% signal gain in response to either intervention in both tumor types. The pharmacokinetic parameter mean *Kep* showed no consistent significant regional differences in either individual tumors or between tumor types. (Table 1, Fig. 5).

Immunohistochemistry showed that the undifferentiated AT1 tumors had lower vascular density, were more poorly perfused, and were substantially more hypoxic with more extensive micro-necroses in the center than in peripheral regions (Fig. 6a). H tumors showed more extensive well-perfused vasculature, overall greater homogeneity, and small regions of hypoxia towards the center of the tumor (Fig. 6b).

Following a single bolus of Gd-DTPA signal enhancement persisted in both tumor sublines for many minutes (Figs. 3 and 4c and d). The BOLD effect can also be made to persist by continuously breathing hyperoxic gas (Figs. 3 and 4a and b). However, if the inhaled gas was returned to air, the signal perturbation rapidly returned to baseline (data not shown). Within 1 min, the mean signal was no longer significantly different from baseline and over 75 % of voxels returned to baseline within 95 s.

Discussion

Tumors of both sublines responded to respiratory challenge and Gd-DTPA infusion (Figs. 1 and 2). As expected, the oxygen response was relatively delayed due to transport of oxygen to the rat, then progressively into lungs, blood, and finally tumor. In most cases, the initial kinetic curves for BOLD were similar to DCE after the initial delay, suggesting that each intervention interrogates a similar flow pattern, presumably

first-pass through major vessels. After the initial delay, the BOLD response rises to a plateau, whereas DCE peaks and then settles to a lower value.

The peripheral regions of many of these AT1 tumors showed significantly greater and more rapid response to each intervention (Fig. 3). The marked heterogeneity between center and periphery in AT1 tumors observed here coincides with previous reports based on vascular and metabolic observations (15,28-32). Several H tumors showed the opposite behavior with substantially greater BOLD and DCE response in the center than the periphery, although in some cases there was no significant difference. The magnitude of response is expected to relate to vascular extent and indeed is corroborated by the histology (Fig. 6). We have previously found that AT1 tumors are significantly less well oxygenated than size matched H tumors and have significantly greater hypoxic fraction (23). Using the hot spot method, we also found that vascular density of AT1 tumors was significantly lower (23). Based on high-resolution gray-scale images of approximately half the surface of each section, we now find extensive hypoxia (pimonidazole binding) throughout the AT1 tumors. H tumors showed much less hypoxia, and mostly localized towards the center, with extensive perfusion (Hoechst) of blood vessels (CD31). Robinson *et al.* (12) previously showed that tumor MRI signal response to breathing carbogen or infusion of the blood pool agent NCI100150 was much greater in GH3 prolactinoma than RIF-1 tumors and this matched the extent of perfused vessels as judged by histology. However, they used separate cohorts of animals for each study. Here, we studied the same tumors for both BOLD and DCE sequentially in individual tumors for comparison.

Trying to differentiate tumor types by non-invasive imaging is a goal of many studies. The shape of DCE curves appears valuable in assessing breast cancer (27,33)

and response to therapy (34). There appears to be prognostic value for BOLD response to hyperoxic gas breathing in patients with locally advanced breast cancer undergoing preoperative chemotherapy (35). Others have shown the feasibility of using a BOLD response to identify chemically induced cholangioma from hepatocellular carcinoma in mice (36). Prostate cancer has often proved a greater challenge due to its multi focal nature. In the clinic Padhani *et al.* (37) found differences using DCE MRI of GD-DTPA between tumor and peripheral zone, but not central gland in patients. There was a weak correlation between tumor stage and vascular permeability assessed, but no significant correlation with Gleason score of PSA levels. Turnbull *et al.* (38) found significant kinetic contrast differences between tumor and fibromuscular benign prostatic hyperplasia.

BOLD MRI can be technically more challenging in the clinical setting, since patients wear a facemask and contrast changes may be much smaller. Nonetheless, we have successfully performed studies of the prostate in normal human volunteers (28). Taylor *et al.* (18) succeeded with four cancer patients and Diergarten *et al.* (39) examined a group of 32 patients finding significantly different signal enhancement between biopsy proven carcinoma of the prostate and the contra lateral normal side.

Meanwhile, several studies have shown differences between prostate tumor types based on dynamic MRI in animal models often noting that macromolecular contrast agents were more effective than small molecules such as Gd-DTPA. Based on the endothelial transfer constant (K^{PS}) Gossman *et al*. (40) could separate the more aggressive MAT-LyLu from PAP subline of the Dunning prostate R3327 syngeneic rat tumor systems at 1.5 T. Several investigators have worked with tumors in small animals at 4.7 T. Fan *et al.* (41) used spectroscopic imaging to differentiate benign Dunning prostate R3327- AT2.1 from metastatic AT3.1 based on image texture, tumor edge

morphology and change in T_2* following administration of the super paramagnetic particulate agent NC100150 (Clariscan). Bhujwalla *et al*. (42) found that metastatic prostate tumors formed vasculature with significantly higher permeability or vascular volume as assessed with albumin-GD-DTPA infusion. We have ourselves previously investigated the R3327-AT1 and H tumors using NMR oximetry and histology (23). While neither tumor is metastatic, they are characterized by substantially different growth rates (5 vs. 16 day volume doubling times) and levels of cellular differentiation. Both small and large H tumors had significantly higher mean and median pO_2, lower hypoxic fraction (HF_5 and HF_{10}), and better response to breathing hyperoxic gas, as judged by ^{19}F NMR oximetry. Hot spot analysis showed significantly lower vascular density and greater overall pimonidazole uptake in AT1 tumors, as confirmed here. Here, we now report differences in magnitude of both DCE and BOLD responses, but not K_{ep}, provided that tumors were divided into central and peripheral regions (Table 1).

It is important to establish tumor characteristics, which can be used to monitor growth and response to therapy. While some authors favor more complex models with three or more compartments, we used a two-compartment model, which is mathematically stable during fitting and for which most clinical experience exists. The quality of the curve-fitting procedure is critical for model-based parametric methods that rely on fitting the data to a complex dynamic curve. For example, the *K*ep value is highly influenced by the accuracy of curve fitting algorithm, the blood flow, and the signal intensity curve. If the signal intensity curves of voxels are negative or unstable, the curve fitting fails or results in too high a *Kep* value. We found that some voxels did not show increased signal during DCE, but our fitting algorithm required that each voxel have a mean value (AUC) greater than zero with DCE contrast. Thus, it was necessary

to filter out negative data in calculating K_{ep}. For K_{ep} regression analysis threshholding criteria were set such that K_{ep} <10 min^{-1}, K_{ep}(error) <5 min^{-1}, and ratio K_{ep}(error)/K_{ep} < 0.8 min^{-1}, Clearly, this issue needs to be further investigated and will markedly depend on the signal/noise ratio and the temporal resolution of the images and also on the model. Here, we found no significant differences between K_{ep} in central and peripheral regions of either tumor type or between tumor types.

Loss of signal accompanying intervention may be rationalized on the basis of a "steal effect" for BOLD investigations, as reported by others (13,43). It is less clear why signal intensity should decrease for extended periods following gadolinium DTPA infusion, though this phenomenon has been reported by Peller *et al.* (13). Our MRI pulse sequence is sensitive to both T_1 and T_2* effects (15). While Gd-DTPA is expected to increase signal by shortening T_1, it can reduce the signal by shortening T_2*, although we do not believe that local concentrations are sufficient to cause T_2* shortening in our investigations. A bolus of Gd-DTPA can cause T_2* signal loss, but this would most likely be a transient effect rather than long-term. Magnet or signal drift must be considered, but when a capillary phantom was included it showed central signal stability better than 5% during Gd-DTPA studies. We also tested infusion of saline and found minimal signal response.

Many investigators have used carbogen rather than oxygen to examine the effects of hyperoxic gas inhalation. Historically, carbogen has been favored in the clinic, since the CO_2 component is vasoactive, minimizing oxygen associated hypotension and potentially increasing blood flow to tumors. Indeed, carbogen is used in the highly successful ARCON clinical trial for head and neck cancer (44). Some investigators reported a differential response to oxygen or carbogen in rodent tumors, notably mouse

xenografts (16), but our studies, in general, have shown similar response to either gas on the basis of vascular oxygenation assessed by near infrared (NIR) of ΔHbO_2 (45-47) or *FREDOM* NMR oximetry of pO_2 (48-50). Rates of signal change with BOLD or DCE observed here closely match our previous observations using non-localized (global) interrogation of Dunning prostate R3327-AT1 rat tumors by near-infrared spectroscopy with respect to switching gas under similar conditions (51).

Conclusion

Overall, both techniques showed significant differences between the tumor types based on regional analysis and may be relevant to future clinical investigations. Macromolecular contrast agents might prove even more definitive, but they are not yet routinely used in the clinic. We previously found that the BOLD changes were rapidly reversible upon return to air breathing and this could allow rapid assessment of acute response during interventions.

Acknowledgements

We are grateful to Dr. Roddy McColl for valuable discussions and members of the MR Cancer Listserver (in particular, Dr. Yanping Lou, Abbott labs) for suggesting the IV infusion protocol. This work was supported in part by NIH R01 CA79515/EB002762 and DOD Prostate Initiative IDEA award PC050766 (W81XWH-06-1-0149). MR investigations were performed at the Mary Nell and Ralph B. Rogers Magnetic Resonance Center, an NIH BTRP Facility P41-RR02584, and in conjunction with the Cancer Imaging Program (Pre-ICMIC) P20 CA86354 and SAIRP U24 CA126608A.

References

1. Taylor JS, Tofts PS, Port R, Evelhoch JL, Knopp M, Reddick WE, Runge VM and Mayr N.(1999) MR imaging of tumor microcirculation: promise for the new millennium. J Magn Reson Imaging **10**:903-907.
2. Hawighorst H, Knapstein PG, Knopp MV, Weikel W, Brix G, Zuna I, Schönberg SO, Essig M, Vaupel P and van Kaick G.(1998) Uterine cervical carcinoma: comparison of standard and pharmacokinetic analysis of time-intensity curves for assessment of tumor angiogenesis and patient survival. *Cancer Res* **58**:3598-3602.
3. Turetschek K, Preda A, Novikov V, Brasch RC, Weinmann HJ, Wunderbaldinger P and Roberts TP.(2004) Tumor microvascular changes in antiangiogenic treatment: assessment by magnetic resonance contrast media of different molecular weights. J Magn Reson Imaging **20**:138-144.
4. Knopp MV, Weiss E, Sinn HP, Mattern J, Junkermann H, Radeleff J, Magener A, Brix G, Delorme S, Zuna I and van Kaick G.(1999) Pathophysiologic basis of contrast enhancement in breast tumors. J Magn Reson Imaging **10**: 260-266.
5. Tofts PS, Brix G, Buckley DL, Evelhoch JL, Henderson E, Knopp MV, Larsson HB, Lee TY, Mayr NA, Parker GJ, Port RE, Taylor J and Weisskoff RM.(1999) Estimating kinetic parameters from dynamic contrast-enhanced T(1)-weighted MRI of a diffusable tracer: standardized quantities and symbols. J Magn Reson Imaging **10**:223-223.
6. Cao Y, Brown SL, Knight RA, Fenstermacher JD and Ewing JR.(2005) Effect of intravascular-to-extravascular water exchange on the determination of blood-to-

tissue transfer constant by magnetic resonance Imaging. Magn Reson Med **53**:282-293.

7. Su MY, Jao JC and Nalcioglu O.(1994) Measurement of vascular volume fraction and blood-tissue permeability constants with a pharmacokinetic model - studies in rat muscle tumors with dynamic Gd-DTPA enhanced MRI. Magn Reson Med **32**:714-724.

8. Collins DJ and Padhani AR.(2004) Dynamic magnetic resonance imaging of tumor perfusion. IEEE Eng Med Biol **23**:65-83.

9. Ogawa S, Menon RS, Tank DW, Kim S-G, Ellermann JM and Ugurbil K.(1993) Functional brain mapping by blood oxygenation level-dependent contrast magnetic resonance imaging. Biophys J **64**:803-812.

10. Howe FA, Robinson SP, Rodrigues LM and Griffiths JR.(1999) Flow and oxygenation dependent (FLOOD) contrast MR imaging to monitor the response of rat tumors to carbogen breathing. Magn Reson Imaging ***17***:1307-1318.

11. Robinson SP, Rodrigues LM, Ojugo ASE, McSheey PMJ, Howe FA and Griffiths JR.(1997) The response to carbogen breathing in experimental tumour models monitored by gradient-recalled echo magnetic resonance imaging. Br J Cancer **75**(7):1000-1006.

12. Robinson SP, Rijken PF, Howe FA, McSheehy PM, van der Sanden BP, Heerschap A, Stubbs M, Van Der Kogel AJ and Griffiths JR.(2003) Tumor vascular architecture and function evaluated by non-invasive susceptibility MRI methods and immunohistochemistry. J Magn Reson Imaging **17**:445-454.

13. Peller M, Weissfloch L, Stehling MK, Weber J, Bruening R, Senekowitsch-Schmidtke R, Molls M and Reiser M.(1998) Oxygen-induced MR signal changes in murine tumors. Magn Reson Imaging **16**:799-809.

14. Fan X, River JN, Zamora M, Al-Hallaq HA and Karczmar GS.(2002) Effect of carbogen on tumor oxygenation: combined fluorine-19 and proton MRI measurements. Int J Radiat Oncol Biol Phys **54**:1202-1209.

15. Jiang L, Zhao D, Constantinescu A and Mason RP.(2004) Comparison of BOLD contrast and Gd-DTPA Dynamic Contrast Enhanced imaging in rat prostate tumor. Magn Reson Med **51**:953-960.

16. van der Sanden BJP, Heerschap A, Hoofd L, Simonetti AW, Nicolay K, van der Toorn A, Colier WNM and van der Kogel AJ.(1999) Effect of carbogen breathing on the physiological profile of human glioma xenografts. Magn Reson Med ***42***:490-499.

17. Baudelet C and Gallez B.(2002) How does blood oxygen level-dependent (BOLD) contrast correlate with oxygen partial pressure (pO_2) inside tumors? Magn Reson Med **48**:980-986.

18. Taylor NJ, Baddeley H, Goodchild KA, Powell ME, Thoumine M, Culver LA, Stirling JJ, Saunders MI, Hoskin PJ, Phillips H, Padhani AR and Griffiths JR.(2001) BOLD MRI of human tumor oxygenation during carbogen breathing. JMRI **14**:156-163.

19. Mazurchuk R, Zhou R, Straubinger RM, Chau RI and Grossman Z.(1999) Functional magnetic resonance (fmr) imaging of a rat brain tumor model: Implications for evaluation of tumor microvasculature and therapeutic response. Magn Reson Imaging **17**: 537-548.

20. Abramovitch R, Frenkiel D and Neeman M.(1998) Analysis of subcutaneous angiogenesis by gradient echo magnetic resonance imaging. Magn Reson Med **39**:813-824.

21. Rijpkema M, Kaanders JH, Joosten FB, van der Kogel AJ and Heerschap A.(2002) Effects of breathing a hyperoxic hypercapnic gas mixture on blood oxygenation and vascularity of head-and-neck tumors as measured by magnetic resonance imaging. Int J Radiat Oncol Biol Phys **53**:1185-1191.

22. Tennant TR, Kim H, Sokoloff M and Rinker-Schaeffer CW.(2000) The Dunning model. Prostate **43**:295-302.

23. Zhao D, Ran S, Constantinescu A, Hahn EW and Mason RP.(2003) Tumor oxygen dynamics: correlation of in vivo MRI with histological findings. Neoplasia **5**(4):308-318.

24. Lohr F, Wenz F, Flentje M, Peschke P and Hahn E.(1993) Measurement of proliferative activity of three different sublines of Dunning rat prostate tumor R3327. Strahlenther Onkol **169**:438-445.

25. Hahn EW, Peschke P, Mason RP, Babcock EE and Antich PP.(1993) Isolated tumor growth in a surgically formed skin pedicle in the rat: A new tumor model for NMR studies. Magn Reson Imaging **11**:1007-1017.

26. Zhao D, Jiang L and Mason RP.(2004) Measuring Changes in Tumor Oxygenation. *Methods Enzymol* **386**:378-418.

27. Port RE, Knopp MV, Hoffmann U, Milker-Zabel S and Brix G.(1999) Multicompartment analysis of gadolinium chelate kinetics: blood-tissue exchange in mammary tumors as monitored by dynamic MR imaging. J Magn Reson Imaging **10**:233-241.

28. Karam JA, Mason RP, Koeneman KS, Antich PP, Benaim EA and Hsieh JT.(2003) Molecular imaging in prostate cancer. J Cell Biochem **90**:473-483.

29. Mason RP, Antich PP, Babcock EE, Constantinescu A, Peschke P and Hahn EW.(1994) Non-invasive determination of tumor oxygen tension and local variation with growth. Int J Radiat Oncol Biol Phys **29**: 95-103.

30. Delorme S, Peschke P, Zuna I and Van Kaick G.(1999) Sensitivity of color Doppler sonography: an experimental approach. Ultrasound Med Biol **25**:541-547.

31. Zhao D, Jiang L, Hahn EW and Mason RP.(2005) Continuous low-dose (Metronomic) chemotherapy on rat prostate tumors evaluated using MRI *in vivo* and comparison with histology. *Neoplasia* **7**:678-687.

32. Fink C, Kiessling F, Bock M, Lichy MP, Misselwitz B, Peschke P, Fusenig NE, Grobholz R and Delorme S.(2003) High-resolution three-dimensional MR angiography of rodent tumors: Morphologic characterization of intratumoral vasculature. Journal of Magnetic Resonance Imaging **18**(1):59-65.

33. Choyke PL, Dwyer AJ and Knopp MV.(2003) Functional tumor imaging with dynamic contrast-enhanced magnetic resonance imaging. J Magn Reson Imaging **17**:509-520.

34. Hayes C, Padhani AR and Leach MO.(2002) Assessing changes in tumour vascular function using dynamic contrast-enhanced magnetic resonance imaging. NMR in Biomed **15**:154-163.

35. Jiang L, McColl R, Weatherall P, Tripathy D and Mason RP.(2005) Blood Oxygenation Level Dependent (BOLD) contrast MRI for early evaluation of breast cancer chemotherapy. Breast Cancer Res Treat **94**(Suppl. 1):S257-S258

36. Thomas CD, Chenu E, Walczak C, Plessis MJ, Perin F and Volk A.(2003) Morphological and carbogen-based functional MRI of a chemically induced liver tumor model in mice. Magn Reson Med **50**:522-530.

37. Padhani AR, Gapinski CJ, Macvicar DA, Parker GJ, Suckling J, Revell PB, Leach MO, Dearnaley DP and Husband JE.(2000) Dynamic contrast enhanced MRI of prostate cancer: correlation with morphology and tumour stage, histological grade and PSA. Clin Radiol **55**:99-109.

38. Turnbull LW, Buckley DL, Turnbull LS, Liney GP and Knowles AJ.(1999) Differentiation of prostatic carcinoma and benign prostatic hyperplasia: correlation between dynamic Gd-DTPA-enhanced MR imaging and histopathology. J Magn Reson Imaging **9**:311-316.

39. Diergarten T, Martirosian P, Kottke R, Vogel U, Stenzl A, Claussen CD and Schlemmer HP.(2005) Functional characterization of prostate cancer by integrated magnetic resonance imaging and oxygenation changes during carbogen breathing. Invest Radiol **40**:102-109.

40. Gossmann A, Okuhata Y, Shames DM, Helbich TH, Roberts TP, Wendland MF, Huber S and Brasch RC.(1999) Prostate cancer tumor grade differentiation with dynamic contrast-enhanced MR imaging in the rat: comparison of macromolecular and small-molecular contrast media--preliminary experience. Radiology **213**:265-272.

41. Fan X, River JN, Zamora M, Tarlo K, Kellar K, Rinker-Schaeffer C and Karczmar GS.(2001) Differentiation of nonmetastatic and metastatic rodent prostate tumors with high spectral and spatial resolution MRI. Magn Reson Med **45**:1046-1055.

42. Bhujwalla ZM, Artemov D, Natarajan K, Ackerstaff E and Solaiyappan M.(2001) Vascular differences detected by MRI for metastatic versus nonmetastatic breast and prostate cancer xenografts. Neoplasia (New York) **3**:143-153.

43. Landuyt W, Hermans R, Bosmans H, Sunaert S, Beatse E, Farina D, Meijerink M, Zhang H, Van Den Bogaert W, Lambin P and Marchal G.(2001) BOLD contrast fMRI of whole rodent tumour during air or carbogen breathing using echo-planar imaging at 1.5 T. Eur Radiol **11**:2332-2340.

44. Kaanders JHAM, Wijffels KIEM, Marres HAM, Ljungkvist ASE, Pop LAM, van den Hoogen FJA, de Wilde PCM, Bussink J, Raleigh JA and van der Kogel AJ.(2002) Pimonidazole binding and tumor vascularity predict for treatment outcome in head and neck cancer. *Cancer Res* **62**:7066-7074.

45. Gu Y, Bourke V, Kim JG, Constantinescu A, Mason RP and Liu H.(2003) Dynamic Response of Breast Tumor Oxygenation to Hyperoxic Respiratory Challenge Monitored with Three Oxygen-Sensitive Parameters. Applied Optics **42**:1-8.

46. Liu H, Song Y, Worden KL, Jiang X, Constantinescu A and Mason RP.(2000) Noninvasive Investigation of Blood Oxygenation Dynamics of Tumors by Near-Infrared Spectroscopy. *Appl Optics* **39**(28):5231-5243.

47. Xia M, Kodibagkar V, Liu H and Mason RP.(2006) Tumour oxygen dynamics measured simultaneously by near infrared spectroscopy and ^{19}F magnetic resonance imaging in rats. *Phys Med Biol* **51**:45-60.

48. Hunjan S, Mason RP, Constantinescu A, Peschke P, Hahn EW and Antich PP.(1998) Regional tumor oximetry: ^{19}F NMR spectroscopy of hexafluorobenzene. Int J Radiat Oncol Biol Phys **40**(5):161-171.

49. Zhao D, Constantinescu C, Hahn EW and Mason RP.(2002) Differential oxygen dynamics in two diverse Dunning prostate R3327 rat tumor sublines (MAT-Lu and HI) with respect to growth and respiratory challenge. Int J Radiat Oncol Biol Phys **53**(3):744-756.

50. Zhao D, Constantinescu A, Hahn EW and Mason RP.(2001) Tumor oxygen dynamics with respect to growth and respiratory challenge: investigation of the Dunning prostate R3327-HI tumor. Radiat Res **156**:510-520.

51. Kim JG, Zhao D, Constantinescu A, Mason RP and Liu H.(2003) Interplay of Tumor Vascular Oxygenation and Tumor pO_2 Observed Using NIRS, Oxygen Needle Electrode, and ^{19}F MR pO_2 Mapping. J Biomed Optics **8**:53-62.

Table 1. The mean regional change in signal intensity (ΔSI) of individual tumors after oxygen inhalation or injection of contrast agent and pharmacokinetic analysis

		Tumor type	
		AT1[#]	H[#]
Number of tumors		8	8
Volume (cm^3)		3.3±1.6	2.4±0.5
Region (%)[@]	Periphery	60±2	55±2
	Center	18±1	24±2
(ΔSI) BOLD[+]	Mean	33±2	27±2
	Periphery	42±3*[‡]	20±1
	Center	23±2	42±3*[‡]
(ΔSI) DCE[+]	Mean	36±1	55±2[‡]
	Periphery	43±1*[‡]	31±1
	Center	24±1	124±6*[‡]
K_{ep} (min^{-1})	Mean	3.05±0.37	3.20±0.39
	Periphery	3.11±0.44	3.34±0.46
	Center	2.59±0.51	2.95±0.54

[@]: Percentage of whole tumor slice

+: Relative % signal change from baseline mean ± s.e.

[#] : $\frac{\sum_{T=1}^{n}\sum_{t=1}^{51}\overline{\Delta SI_{T,t}}}{n \cdot 51}$, where $\overline{\Delta SI}$ is the mean for each tumor (T) at each time point post intervention (t), n is the number of tumors in the group.

*: Mean value is significantly greater than that in other region of the same tumor subline, p<0.0001.

[‡]: Mean value is significantly greater than that in same region of other tumor subline, p<0.0001.

Figure Legends

Figure 1 Proton MRI of tumor vascular dynamics

^{1}H MRI signal intensity response to respiratory challenge and Gd-DTPA injection in representative Dunning prostate tumors. AT1 is shown in upper panels and H tumors in lower panels. ^{1}H MRI was obtained using a spin echo planar imaging sequence with T1-weighting providing sensitivity to changes in both T1 and T2* relaxation (TE= 33.5 ms, TR = 500 ms). Green line on center images indicates the boundary used to separate central and peripheral tumor regions.

a) BOLD with respect to hyperoxic gas challenge. Left: Control baseline images indicating considerable signal heterogeneity, while breathing air. Center: images acquired after 150 s breathing oxygen. Right: Contour maps showing changes in SI (150 s relative to baseline). The color scale indicates the magnitude of relative SI changes.

b) Dynamic contrast enhancement. Left: Control baseline images. Center: Images observed 70 s after Gd-DTPA infusion. Right: Contour maps showing changes in SI (70 s relative to baseline).

Figure 2 Comparison of vascular kinetics of two tumor types

Mean ^{1}H MRI signal intensity in response to oxygen inhalation (BOLD) (◆) and Gd-DTPA infusion (□) for groups of (a) AT1 tumors (n=8) and (b) H tumors (n=8). Lines indicate mean±SE. Dotted vertical lines show start of intervention. An immediate signal response is seen for Gd-DTPA, whereas the BOLD response is somewhat delayed (~ 40 s).

Figure 3 Comparison of regional vascular kinetics of AT1 and H tumors

The mean ^{1}H MR signal intensity in central region (C; filled symbols) and peripheral region (P, open symbols) in response to oxygen inhalation (BOLD) (upper) and Gd-DTPA infusion (DCE) (lower). The mean ΔSI of AT1 tumors (n=8) in BOLD and DCE was significantly higher in the peripheral regions than that in the central regions ($p<0.0001$) (a and b). For H tumors (n=8) the mean response to BOLD and DCE in the peripheral regions was significant lower than that in the central regions ($p<0.0001$) (c and d). Lines indicate mean$\pm$SE.

Figure 4 Magnitude of dynamic signal response to intervention

Variations in distribution of relative signal intensity in response to intervention for the two tumor sublines. BOLD response to breathing oxygen is shown in a and b for groups of AT1 and H subline tumors, respectively. A more rapid response is observed following Gd-DTPA infusion (c and d). Hotter colors represent a larger fractional volume of tumor as shown by scale.

Figure 5 Comparison of regional pharmacokinetic *Kep* of AT1 and H tumors

While individual tumors showed differences in the mean value of *Kep* in peripheral and central regions, the differences were neither consistent nor significant. a) AT1 tumors; b) H tumors. Bars indicate mean$\pm$SE; open periphery; shaded, center.

Figure 6 Comparison of microvasculature and hypoxia in AT1 and H tumors.

Vascular endothelium marked by CD-31 (red), perfused vessels marked by Hoechst dye 33342 (blue) and hypoxia by pimonidazole hydrochloride (green).

a) The AT1 tumor shows extensive hypoxia and many vessels appeared to be non-perfused. Near the tumor periphery, perfusion is more effective as revealed by the purple appearance of vessels (red overlapping blue).

b) The H tumor shows more extensive vascular endothelium, which is well perfused throughout the tumor. Hypoxia occurs distant to perfused vessels and is less extensive.

Figure 1a

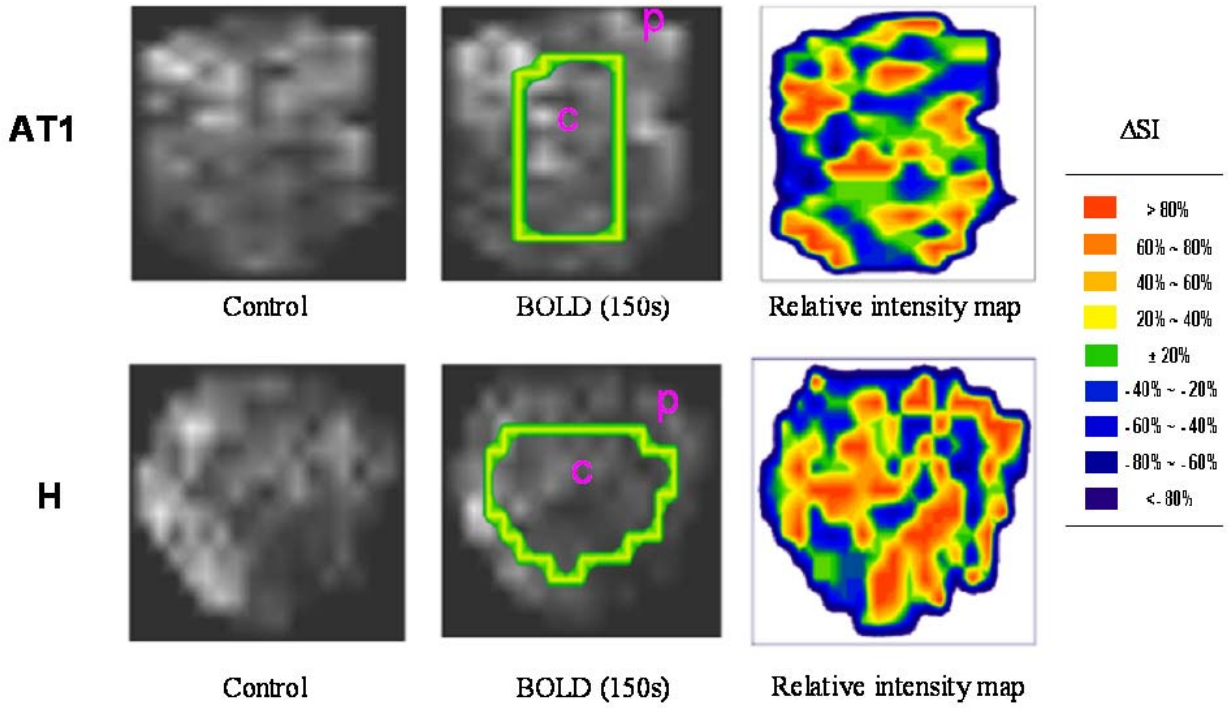
AT1
H
p
c
Control
BOLD (150s)
Relative intensity map
ΔSI
> 80%
60% ~ 80%
40% ~ 60%
20% ~ 40%
± 20%
-40% ~ -20%
-60% ~ -40%
-80% ~ -60%
<- 80%

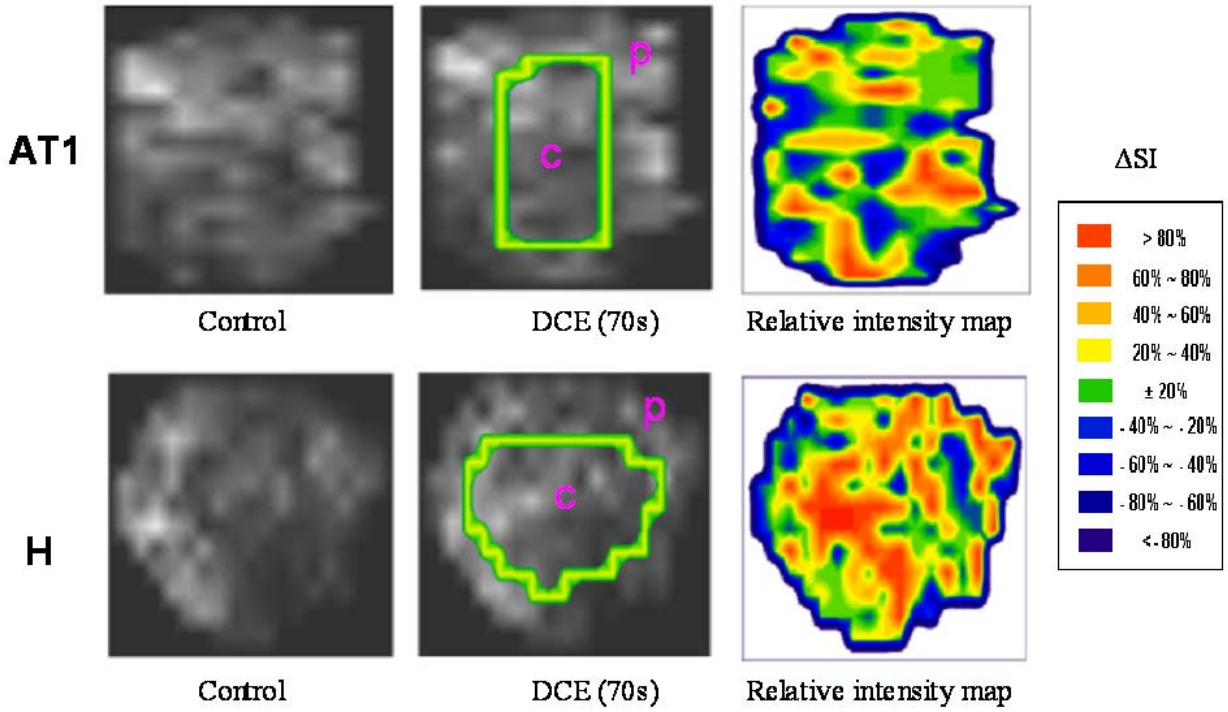
AT1
p
c
ΔSI
> 80%
60% ~ 80%
40% ~ 60%
20% ~ 40%
± 20%
- 40% ~ - 20%
- 60% ~ - 40%
- 80% ~ - 60%
< - 80%
Control
DCE (70s)
Relative intensity map
H
p
c
Control
DCE (70s)
Relative intensity map

Figure 1b

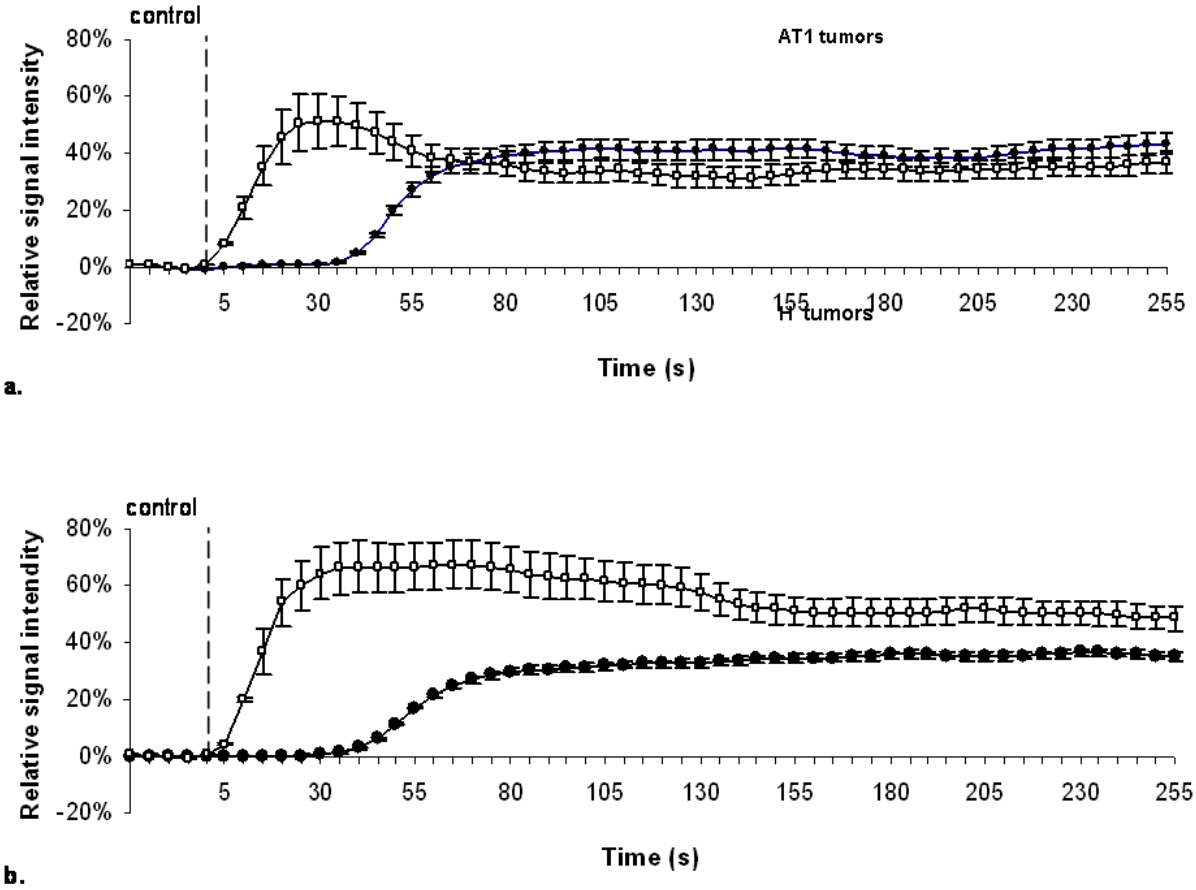
control
AT1 tumors
Relative signal intensity
80%
60%
40%
20%
0%
-20%
5
30
55
80
105
130
155
180
205
230
255
H tumors
Time (s)
a.
control
Relative signal intendity
80%
60%
40%
20%
0%
-20%
5
30
55
80
105
130
155
180
205
230
255
Time (s)
b.

Figure 2

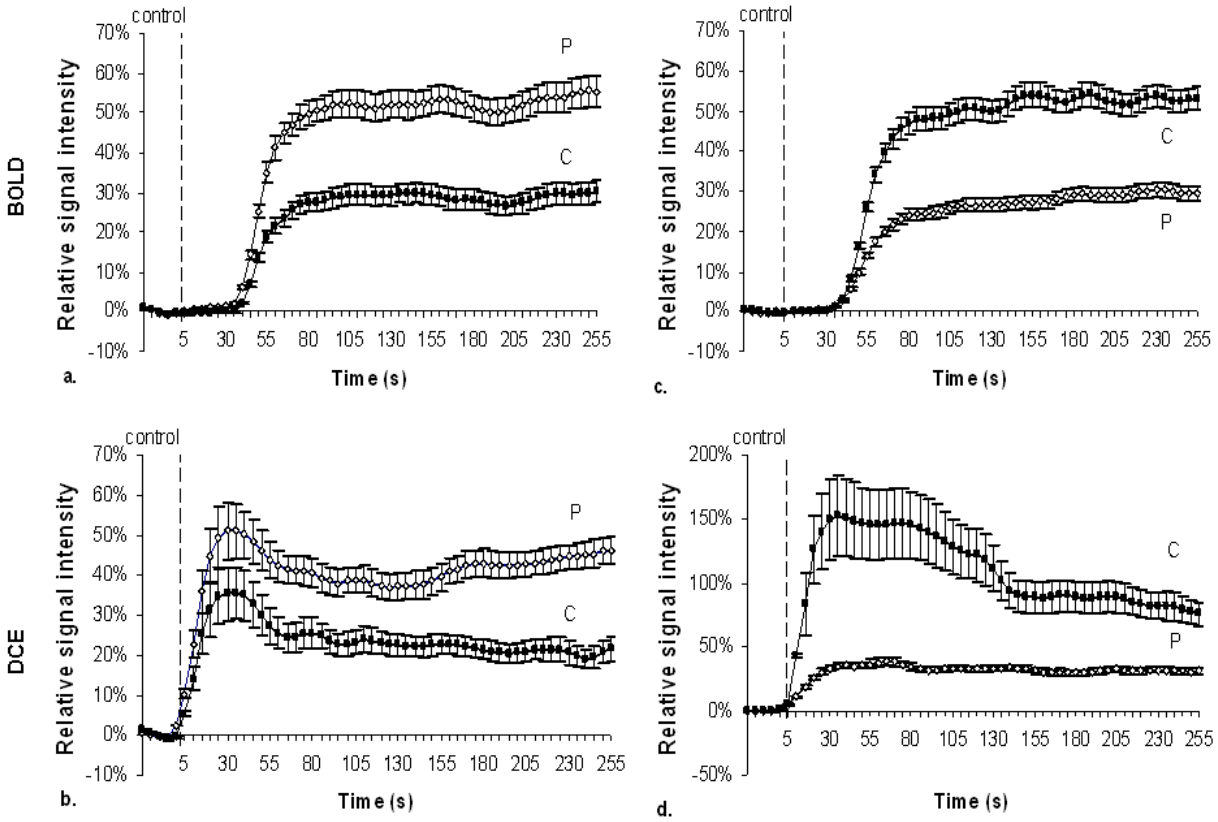

Figure 3

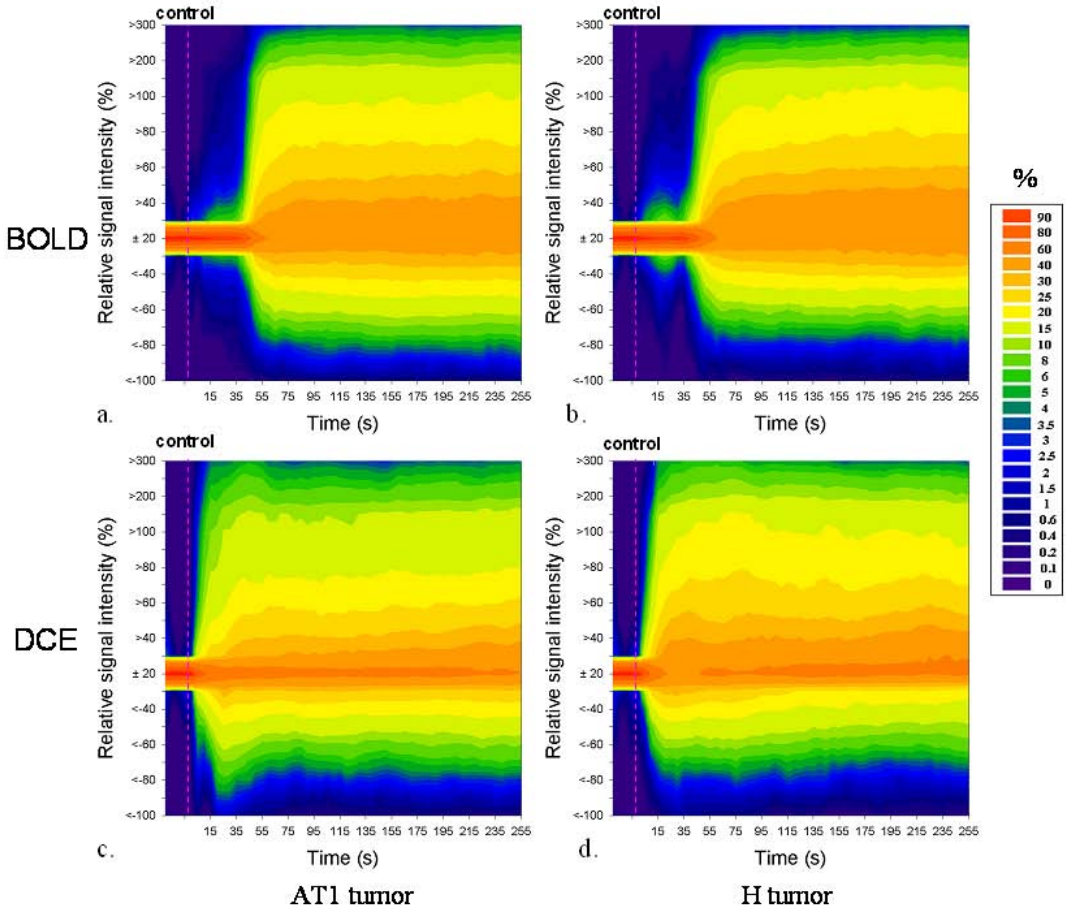
BOLD
DCE
control
Relative signal intensity (%)
Time (s)
a.
b.
c.
d.
AT1 tumor
H tumor
%
90
80
60
40
30
25
20
15
10
8
6
5
4
3.5
3
2.5
2
1.5
1
0.6
0.4
0.2
0.1
0

Figure 4

Figure 5

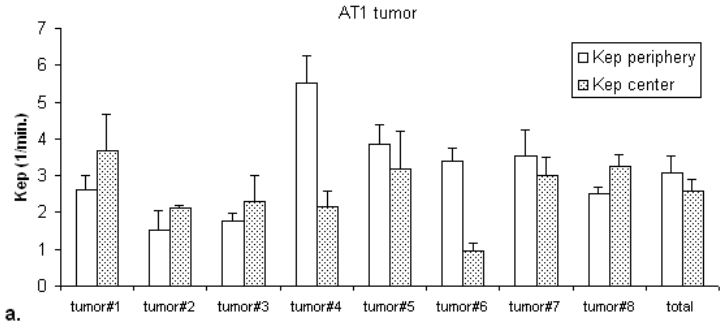
AT1 tumor
Kep periphery
Kep center
Kep (1/min.)
0
1
2
3
4
5
6
7
tumor#1
tumor#2
tumor#3
tumor#4
tumor#5
tumor#6
tumor#7
tumor#8
total

a.

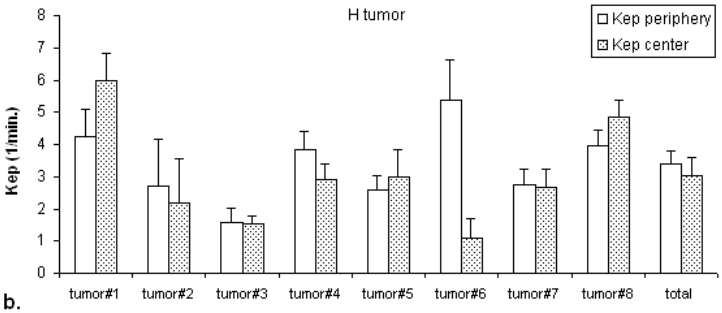
H tumor
Kep periphery
Kep center
Kep (1/min.)
0
1
2
3
4
5
6
7
8
tumor#1
tumor#2
tumor#3
tumor#4
tumor#5
tumor#6
tumor#7
tumor#8
total

b.

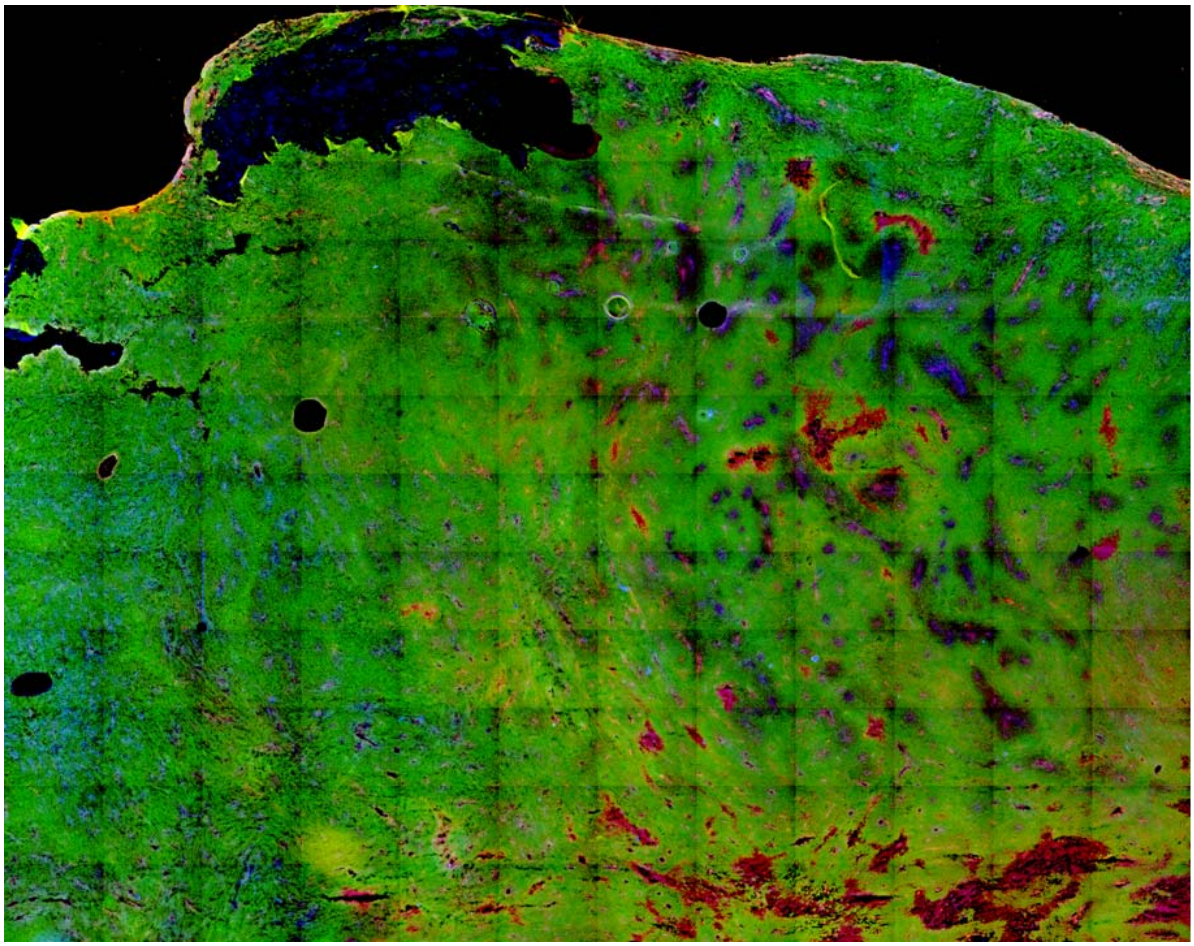

Figure 6a

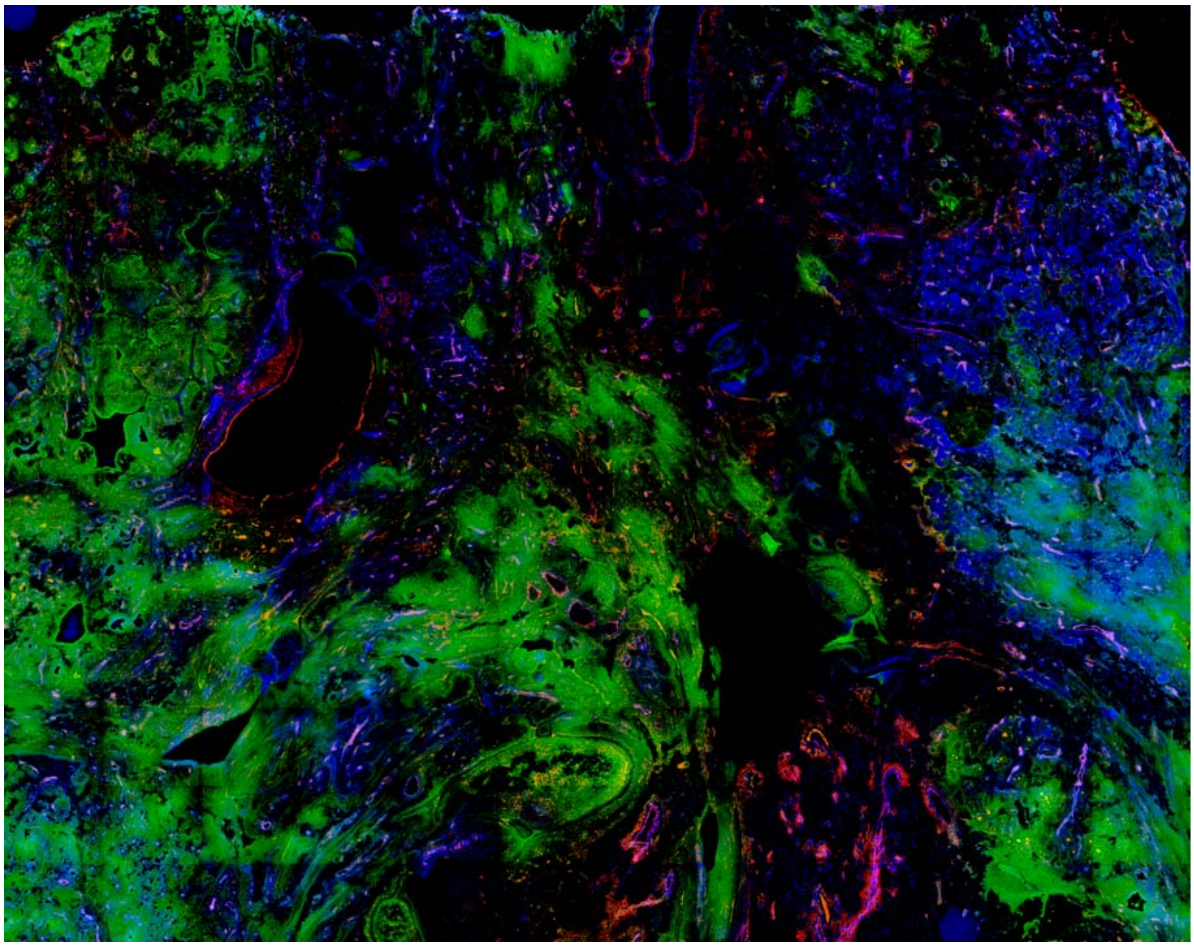

Figure 6b

Poster #: P32-12

UT SOUTHWESTERN MEDICAL CENTER

Bavituximab: Optimizing Therapeutic Strategies for Prostate Cancer Based on Dynamic MR Tumor Oximetry

Ralph P. Mason[1], Weina Cui[1], Dawen Zhao[1], Albert J. van der Kogel[3] and Johan Bussink[3] Jesús Pacheco Torres[1,4], Jennifer McAnally[1], Linda Watkins[2], Peter Peschke[5,] and Philip Thorpe[2,]

Cancer Imaging Program, Departments of [1]Radiology, and [2]Pharmacology, The University of Texas Southwestern Medical Center, Dallas, TX;

[3]Department of Radiation Oncology, University Medical Center Nijmegen, Netherlands; [4]Instituto de Investigaciones Biomédicas "Alberto Sols" CSIC/UAM, Madrid, Spain;

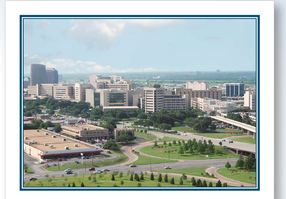

Introduction

Targeting tumor vasculature promises a new effective therapy for prostate cancer, since a blood supply is required for the tumor to grow and develop. We proposed a new approach, using the novel antibody 3G4 (now called bavituximab), which targets phosphatidylserine (PS) expressed on tumor vasculature (1,2). In collaboration with Peregrine Pharmaceuticals, this agent is being developed for clinical trials. Normally, PS exclusively resides on the cytosolic leaflet of the plasma membrane. However, in tumors PS becomes externalized and provides a target (Figure 1). Bavituximab has previously been shown to target various tumors and induce vascular damage and tumor regression with minimal accompanying toxicity. The current goal is to evaluate the dynamic effects of bavituximab on prostate tumor pathophysiology, so as to optimize combination with additional drugs for synergistic therapeutic response.

Methods

Magnetic resonance imaging is used to follow the induction and development of tumor vascular damage *in vivo* in diverse syngeneic rat tumors (Dunning R3327-MAT-Lu, AT1, HI and H) known to exhibit differential vascular extent and growth rates (3). Specifically, we are examining changes in apparent diffusion coefficients (ADCs), perfusion and vascular leakiness based on dynamic contrast enhancement (DCE) and hypoiaxation based on NMR oximetry (FREDOM-Fluorocarbon Relaxometry using Echo planar imaging for Dynamic Oxygen Mapping) (4) using MRI at 4.7 T.

Figure 1

EXPOSURE OF AMINOPHOSPHOLIPIDS ON THE SURFACE OF TUMOR CELLS AND TUMOR ENDOTHELIAL CELLS

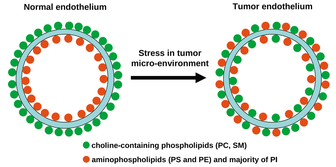

Figure 2

Differential histology apparent by H&E staining.

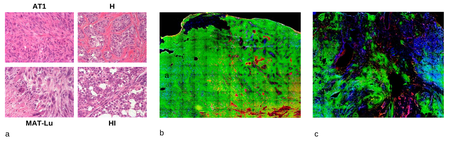

Comparison of histology and pathophysiology in prostate tumors.

a) Differential histology apparent by H&E staining. The H tumor is well differentiated with extensive glandular structure and stroma; the AT1 is undifferentiated; MAT-Lu shows giant cells and considerable necroses and the HI has well defined mucinous acini.

b) Perfusion, vasculature, and hypoxia in AT1 tumor. Extensive hypoxia is seen and many vessels appeared to be non-perfused. Near the tumor periphery, perfusion is more effective as revealed by the purple appearance of vessels (red overlapping blue). Vascular endothelium marked by CD-31 (red), perfused vessels marked by Hoechst dye 33342 (blue) and hypoxia by pimonidazole hydrochloride (green).

c) Perfusion, vasculature, and hypoxia in H tumor. There is more extensive vascular endothelium, which is well perfused throughout the tumor. Hypoxia occurs distant to perfused vessels and is less extensive.

Results

Figure 3

Apparent diffusion maps obtained by ^{1}H MRI of Dunning prostate R3327 tumors.

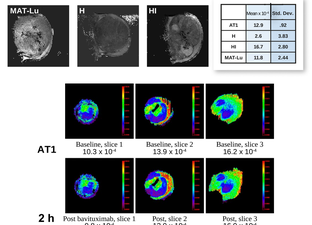

	Mean x 10^{-4}	Std. Dev.
AT1	12.9	.92
H	2.6	3.83
HI	16.7	2.80
MAT-Lu	11.8	2.44

Each image represents a slice of a tumor observed *in vivo* presenting diffusion maps obtained with 4 b-value diffusion gradients (MR parameters, FOV = 30 mm, TR = 2,300 ms, TE= 50 ms, in plane resolution 230 µm, slice thickness 2 mm with a total acquisition time of 20 mins). Respective maps are shown for R3327-MAT-Lu, H, and HI tumors in gray scale. Mean (±SD) values for ADC values in the respective tumor types are presented in Table.

Maps are shown in color for AT1 tumor for three consecutive image slices. Distinct baseline heterogeneity is apparent with mean ADC ranging from 10.2×10^{-4} to 16.2×10^{-4} mm^2/s. The lower images show the same slices 2 h after administration of 2.5 mg/kg bavituximab. There were no significant acute changes.

Figure 4

DCE before and after Bavituximab in a AT1 tumor

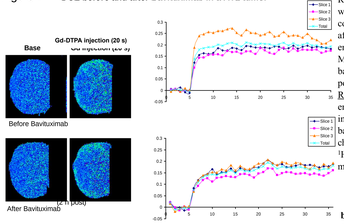

DCE before and after Bavituximab in an H tumor

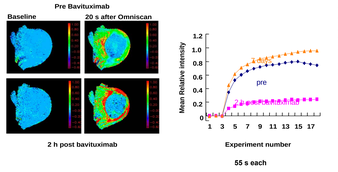

a) DCE for AT1 tumor. Top left Relative signal intensity map for T1-weighted MRI pre therapy and before contrast agent. Top center: 4 mins after contrast showing peripheral enhancement; Bottom left baseline MRI 2 h after administration of bavituximab; Bottom center 4 mins post contrast, 2 h after bavituximab. Right curves show mean signal enhancement for three representative image slices before and 2 h after bavituximab. There were no significant changes. DCE was performed using ^{1}H MRI at 4.7 T with Omniscan (0.1 mmol /kg (~250 µl)

b) DCE for H tumor. Top left Relative signal intensity map for T1 weighted MRI pre therapy and before contrast agent. Top center: 4 mins after contrast showing strong peripheral enhancement; Bottom left baseline MRI 2 h after administration of bavituximab; Bottom center 4 mins post contrast, 2 h after bavituximab. Right: Mean signal intensity kinetics for the single slice shown following infusion of contrast agent. 7 days post (yellow). On most occasions DCE indicated considerably lower signal response in the H tumors 2 h after bavituximab.

Figure 5

Acute response of tumor oxygenation to bavituximab

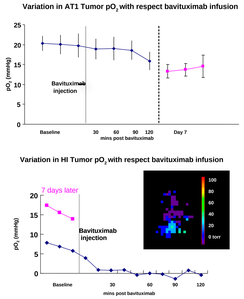

a) Tumor pO_2 was assessed in AT1 tumor using FREDOM following intra tumoral injection of the reporter molecule hexafluorobenzene (50 µl). No acute changes were observed due to bavituximab administration.

b) Tumor pO_2 was assessed in HI tumor indicating hypoxiation 2 h after bavituximab IP. Typical baseline pO_2 map inset showing heterogeneity. In plane voxel dimensions 1.25 mm.

Figure 6

Growth curves and bavituximab induced histological changes in AT 1 tumors.

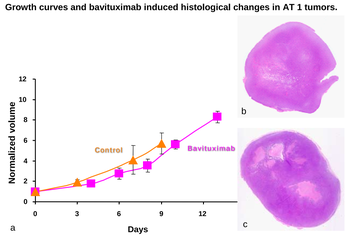

Growth curves for groups of control and bavituximab-treated AT1 tumors. Bavituximab treated tumors (n=6; 2.5 mg/kg IP thrice weekly starting on day 0) show a marginally slower growth rate than control tumors (n=4). H&E stains of Dunning prostate R3327-AT1 tumors; b) control tumor and c) tumor after 8 days bavituximab showing induction of extensive necrosis.

Figure 7

Bavituximab Localized to Vasculature of Rat AT1 Tumor after I.V. Injection

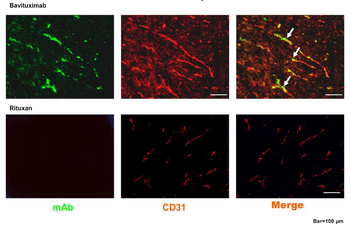

Rats were injected i.v. with bavituximab or rituximab as control. After 24 h the rats were exsanguinated and their tumors were removed. Panels show blood vessels in a frozen sections of tumor at low magnification.

Figure 8

Growth curves for bavituximab-treated Dunning prostate R3327-H tumors

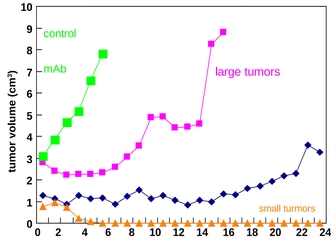

Bavituximab treated tumors received 2.5 mg/kg IP thrice weekly starting on day 1 and showed significant growth delay.

Impact

Bavituximab targets the tumor vasculature ensuring ease of access. It is reported to have little or no toxicity and is in Phase 1 clinical trials. Our data suggest little acute effect on any of the parameters investigated for perfusion, diffusion, and oxygenation, although the relative perfusion of the slow growing H tumors appears depressed after 2 h. In the faster growing tumors we have observed development of distinct central necroses, though tumor periphery continues to grow making therapeutic control difficult to analyze and suggesting the need for a secondary combined therapeutic approach. However, in the small slow growing H tumors (which many consider to be an optimal model for human prostate cancer) there was obvious tumor control, with distinct size reduction and some tumors "melting away".

Acknowledgements

This work was supported by DOD Prostate Initiative IDEA award PC050766 (W81XWH-06-1-0149). MR investigations were performed at the Mary Nell and Ralph B. Rogers Magnetic Resonance Center, an NIH BTRP Facility P41-RR02584, and in conjunction with the Cancer Imaging Program (Pre-ICMIC) P20 CA86354 and SAIRP U24 CA126608A.

References

1. Ran S, Downes A, Thorpe PE. Increased exposure of anionic phospholipids on the surface of tumor blood vessels. *Cancer Res* 2002; 62:6132-6140.

2. Huang X, Bennett M, Thorpe PE. A monoclonal antibody that binds anionic phospholipids on tumor blood vessels enhances the antitumor effect of docetaxel on human breast tumors in mice. *Cancer Res* 2005;65(10):4408-4416.

3. Zechmann CM, Woenne EC, Brix G, Radzwill N, Ilg M, Bachert P, Peschke P, Kirsch S, Kauczor HU, Delorme S, Semmler W, Kiessling F. Impact of stroma on the growth, microcirculation, and metabolism of experimental prostate tumors. *Neoplasia* 2007;9(1):57-67.

4. Zhao D, Jiang L, Mason RP. Measuring Changes in Tumor Oxygenation. *Methods Enzymol* 2004;386:378-418.

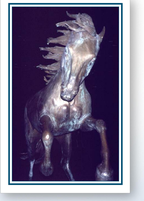

DOCENT-Dynamic Oxygen Challenge Evaluated by NMR T1 and T2* of Tumors

Dawen Zhao[1], Jesús Pacheco Torres[1,2], Peter Peschke[3] and Ralph P. Mason[1]

[1]Department of Radiology, University of Texas Southwestern Medical Center, Dallas, TX,
[2]Instituto de Investigaciones Biomédicas "Alberto Sols" Madrid, Spain,
[3]German Cancer Center, Heidelberg, Germany

Introduction

Hypoxia inhibits tumor response to radiation therapy. Thus, many techniques are being developed to assess hypoxia or quantitative pO_2 (1). We have been developing NMR approaches to measuring oxygen tension dynamics (2). Using *FREDOM* (Fluorocarbon Relaxometry using Echo planar imaging for Dynamic Oxygen Mapping) we have demonstrated differential size dependent hypoxia among diverse Dunning prostate tumor lines. Importantly, hypoxic tumors were found to respond less well to irradiation, and indeed, direct correlations were found between the volume doubling time following radiation and pO_2 (3, 4). We are currently evaluating *PISTOL* (Proton Imaging of Silane for Tissue Oxygen Levels) as a potential ^{1}H MRI alternative (5). However, such measurements require introduction of a reporter molecule. Prompted by the report of Matsumoto *et al*. (6) we are exploring the ability to evaluate tumor hypoxia based on the response of tumor T1 and T2* weighted water signals to hyperoxic gas breathing.

Methods

We examined Dunning prostate R3327-AT1 and HI tumors. When tumors reached ~1 cm diameter MR measurements were performed under general anesthesia at 4.7 T. We previously characterized these tumors using *FREDOM* in terms of response to hyperoxic gas challenge (Figures 1-4).

Using quantitative ^{19}F NMR oximetry we are able to categorize tumors according to baseline hypoxia and response to hyperoxic gas breathing into three types: 1) well oxygenated and responsive; 2) hypoxic, but responsive to oxygen challenge, and 3) hypoxic and resistant to modulation (Figures 3 and 4).

Here, series of interleaved T1- and T2*-weighted proton (water) images were acquired during transition from air to carbogen breathing to assess ability to detect tumor response. Measurements were repeated when tumors were >2 cm diameter.

Results

- Tumors known from ^{19}F MRI to be well oxygenated (small HI and AT1) showed a large response in both T1 and T2* signal with respect to breathing carbogen.
- Tumors known to be hypoxic, but responsive to hyperoxic gas challenge (large HI) showed a large response in both T1 and T2* signal with respect to breathing carbogen.
- Tumors known to be hypoxic and not to respond to hyperoxic gas breathing (large AT1) showed very small response in T1 or T2* weighted images in response to breathing carbogen.

For further information, you may contact
Ralph.Mason@UTSouthwestern.edu

FREDOM (Fluorine Relaxometry using Echo planar imaging for Dynamic Oxygen Mapping)

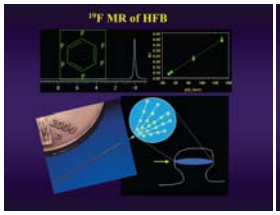

Figure 1 ^{19}F NMR oximetry
Tumor pO_2 may be measured quantitatively using *FREDOM* (Fluorocarbon Relaxometry using Echo planar imaging for Dynamic Oxygen Mapping). This is based on the reporter molecule hexafluorobenzene (HFB), which has a single ^{19}F NMR signal and linear response of the spin lattice relaxation rate (R1) to pO_2. HFB is administered into tissue using a fine needle (32G) and distributed to sample multiple regions (2).

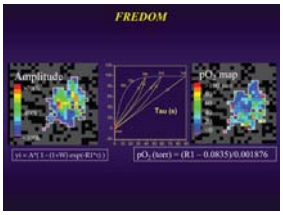

Figure 2 *FREDOM* (Fluorocarbon Relaxometry using Echo planar imaging for Dynamic Oxygen Mapping)
^{19}F MRI provides maps of HFB. Varying a recovery time reveals spin lattice recovery, the rate of which is related to local pO_2. Based on curve fitting and the linear relationship between R1 and pO_2, maps of tumor oxygenation are acquired in 6.5 mins each, with typical resolution 1.25 mm in plane and 1-3 torr precision under relatively hypoxic conditions (2).

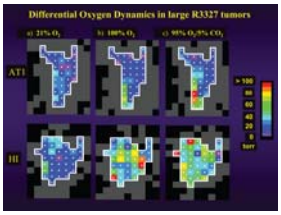

Figure 3 Differential Oxygen Dynamics in large R3327 tumors
Dynamic oxygenation changes observed in Dunning prostate rat tumors in response to breathing oxygen or carbogen. Both AT1 and HI tumors show similar baseline patterns of oxygenation in large tumors, but very different response to hyperoxic gas breathing. In the AT1, only initially well oxygenated regions respond, whereas in the HI tumor essentially all regions become well oxygenated.

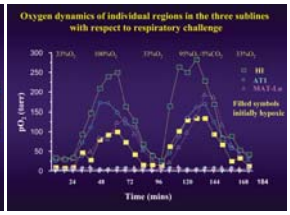

Figure 4 Differential Oxygen Dynamics in individual voxels
In three different Dunning prostate tumor sublines we observe that well oxygenated regions respond to hyperoxic gas breathing. In most lines (here AT1 and MAT-Lu) those regions which are poorly oxygenated respond little, whereas those in the HI tumor show a remarkable increase in pO_2.

The Influence of Hyperoxic Gas Breathing on Reponse to Radiation

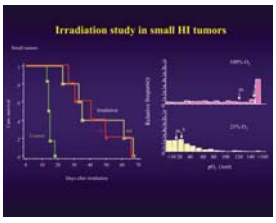

Figure 5 Tumor responses to irradiation
Small HI tumors, which are well oxygenated respond to irradiation. Here, a single dose of 30 Gy (half the TCD_{50}) was applied and the time to double in size was observed. Tumors on rats breathing air or oxygen showed a significant growth delay compared with controls. Baseline hypoxic fraction was small HF_{10}<25% (3).

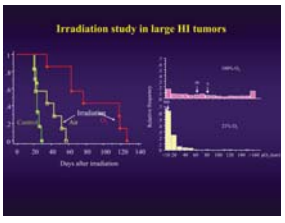

Figure 6 Modulating tumor response to irradiation
Large HI tumors exhibit extensive hypoxia. However, it is essentially eliminated by breathing oxygen resulting in excellent response to irradiation. Here a single dose of 30 Gy was applied and the time to double in size was observed. Tumors on rats breathing air showed little benefit over controls. Baseline hypoxic fraction was high HF_{10}>65%. However, breathing oxygen essentially eliminated the hypoxic fraction HF_{10}<20% and these tumors showed a significant growth delay compared with controls or irradiated air breathing animals (3).

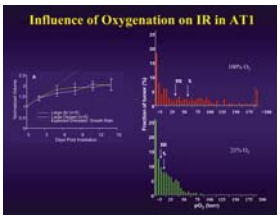

Figure 7 Tumor response to irradiation
Large AT1 tumors exhibit HF_{10} > 40% and this responds little to breathing oxygen. In this case breathing oxygen has negligible effect on response to single dose of radiation (4).

DOCENT

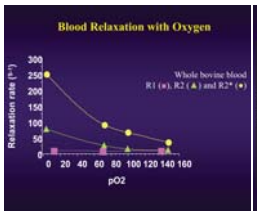

Figure 8 Blood relaxation with oxygen
Relationship between NMR relaxation parameters R1 (■), R2 (▲) and R2* (●) and pO_2 in aliquots of fresh bovine blood observed by MRI at 4.7 T (7)

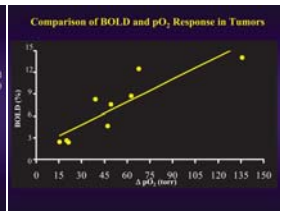

Figure 9 Comparison of BOLD and pO_2 response in tumors
For a group of 13762NF rat breast tumors a strong relationship was found between mean BOLD signal response and change in mean pO_2 in response to breathing oxygen.

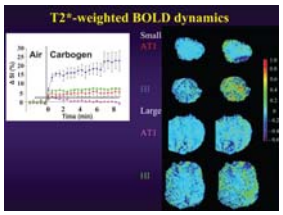

Figure 10 BOLD response to carbogen breathing
BOLD (T2*-weighted) signal response was examined in groups of Dunning prostate AT1 and HI tumors, known to exhibit differential response based on ^{19}F MRI (above). Small HI, AT1 and large HI tumors all showed a substantial signal response (>2%), which was particularly large for the small HI tumors (>10%). Large AT1 tumors showed a significantly smaller response.

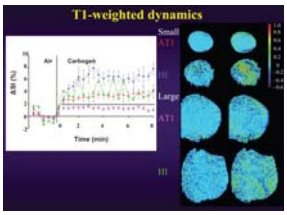

Figure 11 T1 responses to carbogen breathing
Interleaved with the T2* response in Figure 10, T1-weighted signal response was also examined in the groups of Dunning prostate AT1 and HI tumors. As for T2* small HI, AT1 and large HI tumors all showed a large signal response, while large AT1 tumors showed a significantly smaller response.

Conclusions

These preliminary data suggest that T1 and T2* weighted signal response to carbogen challenge reveals unresponsive hypoxic tumors. Since such measurements are entirely non-invasive they appear worthy of further exploration and correlation with response to therapy.

Acknowledgements

Investigations were supported in part by DOD Prostate Cancer Initiative IDEA award W81XWH-06-1-0149 (PC050766), The Southwestern Small Animal Imaging Resource (SW-SAIR) under NIH SAIRP U24 CA126608 and The Advanced Imaging Research Center, a BTRP facility #P41-RR02584

References

1. Tatum, J. L., Kelloff, G. J., Gillies, R. J., Arbeit, J. M., Brown, J. M., Chao, K. S., Chapman, J. D., Eckelman, W. C., Fyles, A. W., Giaccia, A. J., Hill, R. P., Koch, C. J., Krishna, M. C., Krohn, K. A., Lewis, J. S., Mason, R. P., Melillo, G., Padhani, A. R., Powis, G., Rajendran, J. G., Reba, R., Robinson, S. P., Semenza, G. L., Swartz, H. M., Vaupel, P., Yang, D., Croft, B., Hoffman, J., Liu, G., Stone, H., and Sullivan, D. Hypoxia: Importance in tumor biology, noninvasive measurement by imaging, and value of its measurement in the management of cancer therapy. Int. J. Radiat. Biol., 82: 699 - 757, 2006.
2. Zhao, D., Jiang, L., and Mason, R. P. Measuring Changes in Tumor Oxygenation. Methods Enzymol, 386: 378-418, 2004.
3. Zhao, D., Constantinescu, A., Chang, C.-H., Hahn, E. W., and Mason, R. P. Correlation of Tumor Oxygen Dynamics with Radiation Response of the Dunning Prostate R3327-HI Tumor. Radiat. Res., 159: 621-631, 2003.
4. Bourke, V. A., Zhao, D., Gilio, J., Chang, C.-H., Jiang, L., Hahn, E. W., and Mason, R. P. Correlation of Radiation Response with Tumor Oxygenation in the Dunning Prostate R3327-AT1 Tumor. Int. J. Radiat. Oncol. Biol. Phys., 67: 1179-1186, 2007.
5. Kodibagkar, V. D., Cui, W., Merritt , M. E., and Mason, R. P. A novel ^{1}H NMR approach to quantitative tissue oximetry using hexamethyldisiloxane. Magn. Reson. Med., 55: 743-748, 2006.
6. Matsumoto, K., Bernardo, M., Subramanian, S., Choyke, P., Mitchell, J. B., Krishna, M. C., and Lizak, M. J. MR assessment of changes of tumor in response to hyperbaric oxygen treatment. Magn. Reson. Med., 56: 240-246, 2006.
7. Mason, R. P. Non-invasive assessment of kidney oxygenation: a role for BOLD MRI. Kidney International, 70: 9-11, 2006.